Physics of liquid jets

Jens Eggers[1] **and Emmanuel Villermaux**[2,3]

[1] School of Mathematics, University of Bristol, University Walk, Bristol BS8 1TW, UK
[2] IRPHE, Université de Provence, Aix-Marseille I, Technopôle de Château-Gombert,
49, rue Frédéric Joliot-Curie 13384 Marseille Cedex 13, France

Abstract

Jets, i.e. collimated streams of matter, occur from the microscale up to the large-scale structure of the universe. Our focus will be mostly on surface tension effects, which result from the cohesive properties of liquids. Paradoxically, cohesive forces promote the *breakup* of jets, widely encountered in nature, technology and basic science, for example in nuclear fission, DNA sampling, medical diagnostics, sprays, agricultural irrigation and jet engine technology. Liquid jets thus serve as a paradigm for free-surface motion, hydrodynamic instability and singularity formation leading to drop breakup. In addition to their practical usefulness, jets are an ideal probe for liquid properties, such as surface tension, viscosity or non-Newtonian rheology. They also arise from the last but one topology change of liquid masses bursting into sprays. Jet dynamics are sensitive to the turbulent or thermal excitation of the fluid, as well as to the surrounding gas or fluid medium. The aim of this review is to provide a unified description of the fundamental and the technological aspects of these subjects.

(Some figures in this article are in colour only in the electronic version)

Contents

[3] Also at: Institut Universitaire de France.

List of symbols

Q	flow rate
g	acceleration of gravity
h	jet radius
ρ	density
γ	surface tension
λ	wavelength
x	dimensionless wave number
We	Weber number
Oh	Ohnesorge number
ν	kinematic viscosity
Bo	Bond number
$\boldsymbol{v}$	velocity
κ	mean curvature
σ	stress tensor
p	pressure
ϕ	velocity potential
$\boldsymbol{n}$	normal vector
$\boldsymbol{t}$	tangent vector
λ	viscosity ratio
η	shear viscosity
k	wave number
m	azimuthal wave number
ω	growth rate
ρ_a	outer density
p_a	outer pressure
δ	penetration depth
η_a	outer viscosity
e	film thickness
σ	elongation rate
ρ_1	liquid density
ρ_2	gas density
v_1	liquid velocity
v_2	gas velocity
$\boldsymbol{E}$	electric field
ϵ_0	permittivity of free space
σ_0	surface charge
V	electric potential
N	magnetic Bond number
S	Swirl number
C_D	drag coefficient
$\mathcal{G}$	constant of gravity
ξ	ligament diameter
L	ligament length
ν_s	kinematic viscosity of solvent
ν_p	kinematic viscosity of polymer
b	extensibility parameter of polymer
λ_p	time scale of polymer
ν_e	extensional viscosity
Γ	surfactant concentration
Pe	Peclet number
β	surface activity number

1. Introduction

1.1. Scope and motivation

A jet is a stream of matter having a more or less columnar shape. They are encountered in an extremely large variety of situations, spanning a broad range of physical length scales, hence the wide scope of this review.

Jets occur on the scale of the universe as well as on subatomic length scales and have attracted attention both for their potential practical use and for their heuristic interest, demonstrating some key phenomena of physics and applied mathematics. Our focus will be on the *breakup* of jets, most often driven by surface tension. In the first stage, one investigates the jet's stability; in the case of instability one is ultimately interested in the resulting *fragment sizes*. The motivation is essentially twofold:

On one hand, these studies are motivated by practical questions and applications. Among them, illustrated below, one can mention: understanding and explaining the large-scale structure of the universe and the support of galaxy clusters (figure 1), improving and optimizing liquid jet propulsion, diesel engine technology, manufacturing (figure 2), agricultural sewage and irrigation (figure 3), powder technology, ink-jet printing (figure 4), medical diagnostics or DNA sampling and nuclear fission. Jets are also present in our everyday environment in kitchens, showers, pharmaceutical sprays and cosmetics, and are also used for our entertainment (figure 3), and for our security, for example to inflate air bags or to help firemen.

On the other hand, jet dynamics probes a wide range of physical properties, such as liquid surface tension, viscosity or non-Newtonian rheology and density contrast with its environment. Jets are also sensitive, on very small scales (typically nanometres) to thermal fluctuations (see figure 5). On very large scales, on the other hand, gravitational interactions are important. The basic flow state can be both laminar and turbulent. The carrying fluid can be electrically charged, or magnetic. Nearly all classical physics comes into play in jet dynamics, and articulating the different effects in a sound picture remains in several cases a challenging exercise.

For all these applications or academic situations, the recurrent questions are: will the jet break, and if so, how long will it take? How sensitive is the jet to, e.g. background turbulence, or the presence of a dense, viscous outer medium in relative motion? How does viscosity affect the ultimate stages of the separation between two droplets? After breakup, how disperse in size will the fragments be? If they are, how can the size distribution be made narrower, or broader?

Experimentally, various laboratory techniques, and notably high-speed digital cinematography in recent years, have revived the subject. Minute details of the breakup process can now be documented in real time, as well as the structure of the resulting spray, thus providing us with a rich source of information for comparison with theory.

On the analytical side, the most basic tool is linear stability analysis around the cylindrical base state. However, there are many important features of the break-up process for which non-linear effects are dominant. Numerically, this remains
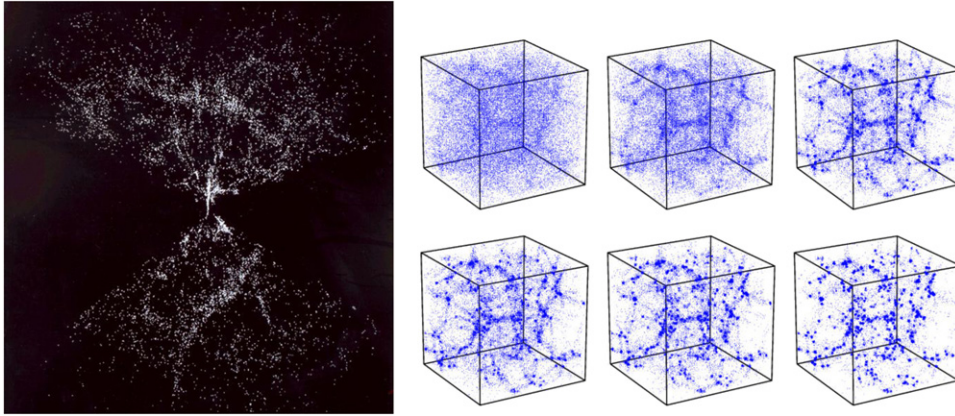
Figure 1. Studies of the large-scale structure of the cosmos indicate that the universe consists mostly of voids (90%), with filaments and sheets of galaxies comprising the rest. In the image on the left (Smithsonian Astrophysical Observatory, 1993), each of the 11 000 dots are individual galaxies. Our own Milky Way galaxy is at the centre. The outer radius is 450 million light years away. Obstruction by the plane of the Milky Way caused the missing pie-shaped sectors. The image above is less than 5% of the distance to the edge of the observable universe. (Right) Numerical simulation of the 'filamentarization' of the mass support in the universe, interacting by gravitation, and the subsequent breakup of filaments.

Figure 2. (Left) A jet of tap water falling into a sink. The jet is too thick and its falling time too short for breakup to occur, yet it has become rough. The continuous jet hits the sink floor, where it expands radially in the form of a thin sheet boarded by a hydraulic jump. (Right) Higher speed water jets are also used to cut tissues, meat, and even metal plates.

an extremely hard problem: one either has to focus on a detailed description of individual breakup events, using very high resolution. On the other hand, the complex geometry of a spray is hardly captured by existing codes due to the many degrees of freedom. The final, highly non-linear stages of breakup can be understood making use of scale invariance; an obvious example is visible from the conical shape of a French baguette (figure 4). The interpretation of the resulting drop size distribution, inherently large to jet breakup, requires statistical tools.

This review embraces all the aspects of jet breakup phenomenology in a progressive manner: we first present the physical mechanisms leading to breakup in various typical situations, each characterized by its own relevant ingredients. Second, we give a precise description of the corresponding breakup event, and then we describe how jet dynamics is at the core of spray formation and give a unified picture of atomization.

1.2. History

The earliest study of the behaviour of jets and of breakup was by Leonardo da Vinci in the Codex Leicester (cf figure 6). The same work also contains thoughts on the cohesion of fluids and its role for the formation of drops [2]:

> *'How water has tenacity in itself and cohesion between its particles. This is seen in the process of a drop becoming detached from the remainder, this remainder being stretched out as far as it can through the weight of the drop which is extending it; and after the drop has been severed from this mass the mass returns upwards with a movement contrary to the nature of heavy things'.*

Thus da Vinci notes correctly that the detachment of a drop falling from a tap is governed by the condition that gravity overcomes the cohesive (surface tension) forces. However, he
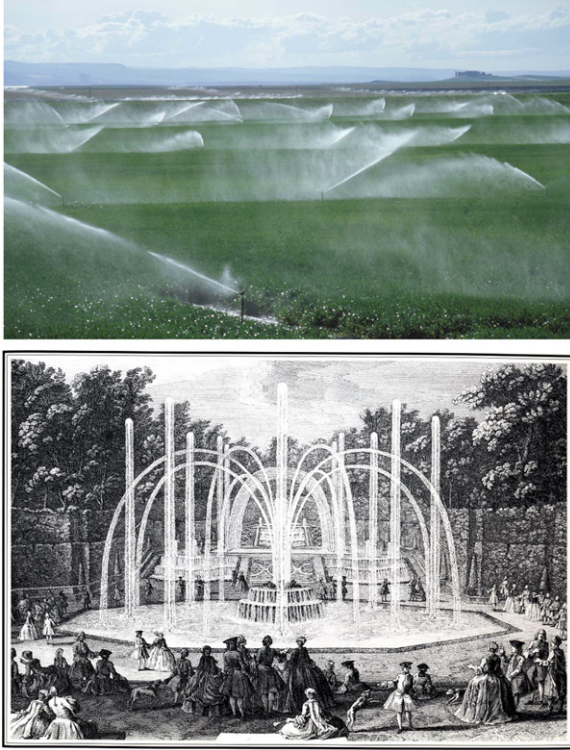
Figure 3. (Top) Sprays produced by jets are widely used in agricultural irrigation. The big drops from the rupture of the jet fall rapidly on the ground where they may damage the plants while smaller ones go with the wind, possibly across the field and farther, causing a loss of water, or pesticide. Controlling the drop size distribution remains a crucial issue in this context. (Bottom) The 'Bosquet des Trois Fontaines' in Le Nôtre's Versailles garden (1677). Engraving by Jean Rigaud.

then incorrectly goes on to assume that the same principle also governs the separation of the drop itself, which occurs once a sufficiently extended fluid neck has formed.

The same flawed argument was elaborated later by Mariotte [3], who claims that gravity is responsible for drop breakup (a jet which is projected upward does not break up); breakup occurs when the fluid thread has become as 'thin as a hair'. Thus both authors view the breakup of liquids and solids as related phenomena. Mariotte argues more quantitatively that a falling jet acquires a speed corresponding to free fall $v = \sqrt{2gx}$ at a distance x from the nozzle (neglecting the initial speed). Then if Q is the flow rate, mass conservation gives

$$h = \left[\frac{Q}{\pi \sqrt{2gx}} \right]^{1/2} \qquad (1)$$

for the radius h of the jet, making it increasingly thin as it falls. The ideas of da Vinci and Mariotte suggest that cohesive forces provide a certain tensile strength σ of water, which has to be overcome by gravity for the jet to break. Taking the value for the tensile strength of glass $\sigma = 10^8 \, \mathrm{N \, m^{-2}}$ as a conservative estimate, the thread can no longer support a drop of 1 ml volume when its cross sectional area has become $A = 10^{-5} \, \mathrm{cm^2}$. Taking $Q = 1 \, \mathrm{ml \, s^{-1}}$ in (1), the fluid thread can formally extend to a length of 100 km before it breaks!

The resolution of this problem had to wait another 100 years: in 1804–1805 Laplace [4] and Young [5] published their celebrated work, exhibiting the crucial role of the *mean curvature*, made up of contributions from both the axial and the radial curvature. The subtle point which leads to the fallacy of earlier authors is that surface tension can act in two different ways: while for a hanging drop it indeed acts like an elastic membrane, once a cylindrical shape is reached the radial curvature is *driving* the breakup! Namely, the system is driven towards a state having a smaller surface area, and thus towards a smaller jet radius, which eventually goes to zero. Thus paradoxically, the greater the cohesion between the particles (and thus the surface tension γ [6]), the faster breakup becomes.

Namely, if the fluid viscosity is neglected, by dimensional analysis a characteristic timescale of the motion is

$$\tau = \left[\frac{\rho h_0^3}{\gamma} \right]^{1/2}, \qquad (2)$$

where h_0 is the initial radius of the fluid cylinder. As h_0 decreases, the motion accelerates even more, and the radius h can be estimated to decrease according to $\dot{h} \propto h^{-1/2}$. Thus from integrating this expression one finds that h goes to zero in *finite* time, with a characteristic exponent of 2/3, see below. The time (2) estimates the total time for breakup to occur.

Although by the early 19th century, combining the effects of surface tension [4, 5] with the laws of fluid motion [7, 8], all that was needed for a mathematical description of jet breakup was at hand, some experimental progress came first, in particular in the work of Savart[4] [9]. Savart noted that breakup occurs spontaneously, independent of any external force or the direction in which the jet is projected, and thus must be a feature *intrinsic* to jet dynamics. To confirm breakup, Savart found that a 'thin object'[5] could be made to pass through the jet without getting wet. For more quantitative observation, Savart developed a stroboscopic technique, which allowed him to produce images such as figure 7. To this end he employed a continuous moving tape painted with alternating black and white stripes, against which the jet was viewed. In particular, Savart noticed the appearance of a smaller 'satellite' drop between two main ones, a feature which can only be understood by considering the non-linear dynamics of jet breakup, as we will see later.

The most unstable mode of breakup is best excited by allowing the vibrations produced by the impact of drops to be fed back to the vessel out of which the jet is flowing. This produces a definite resonance frequency f of the system, for which Savart formulated two laws [9, 10]: (a) f is inversely proportional to the nozzle radius h_0, and (b) proportional to the square root of the pressure head $\sqrt{\Delta p}$. By Bernoulli's law $\sqrt{\Delta p}$ is proportional to the jet velocity, hence both of Savart's laws are explained by the existence of a characteristic *wavelength* λ_{opt}, corresponding to resonance. Indeed, some years later Plateau, observing the decay of columns of fluid in density-matched surroundings (the so-called Plateau tank [11]) found

---

[4] Who worked as a 'préparateur' to Abbé Nollet, see figure 10.
[5] Savart must have handled well all manners of knives, owing to his training as a military surgeon.
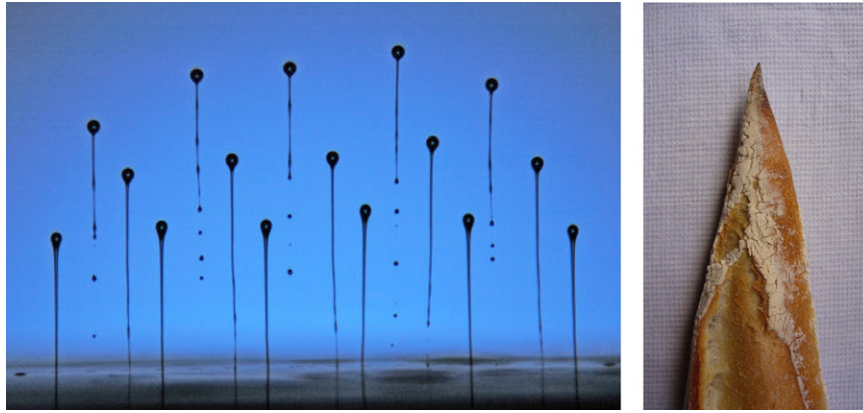
Figure 4. (Left) Drops emerging from a bank of ink-jet nozzles (just visible at the bottom of the picture). The image is about 2.3 mm across, the drop heads are 50 μm across and the tails are less than 10 μm wide (10 times thinner than a human hair). Although very small the drops are moving at around 6 m s^{-1} hence the need for a very short flash to freeze the motion (20 ns). Credit: Steve Hoath, Cambridge Engineering Department, Ink-jet Research Centre investigating the performance of ink-jet printers. (Right) A manifestation of breakup familiar to French gastronomes: the bread dough is initially shaped into a long circular ribbon. Before cooking them in the oven to make the celebrated 'baguettes de pain', the baker cuts the ribbon into disjoint pieces by stretching the dough at regular intervals. The extremity of the crunchy cooked baguette keeps the imprint of the singular breakup process (Courtesy Boulangerie Breteuil, Marseille).
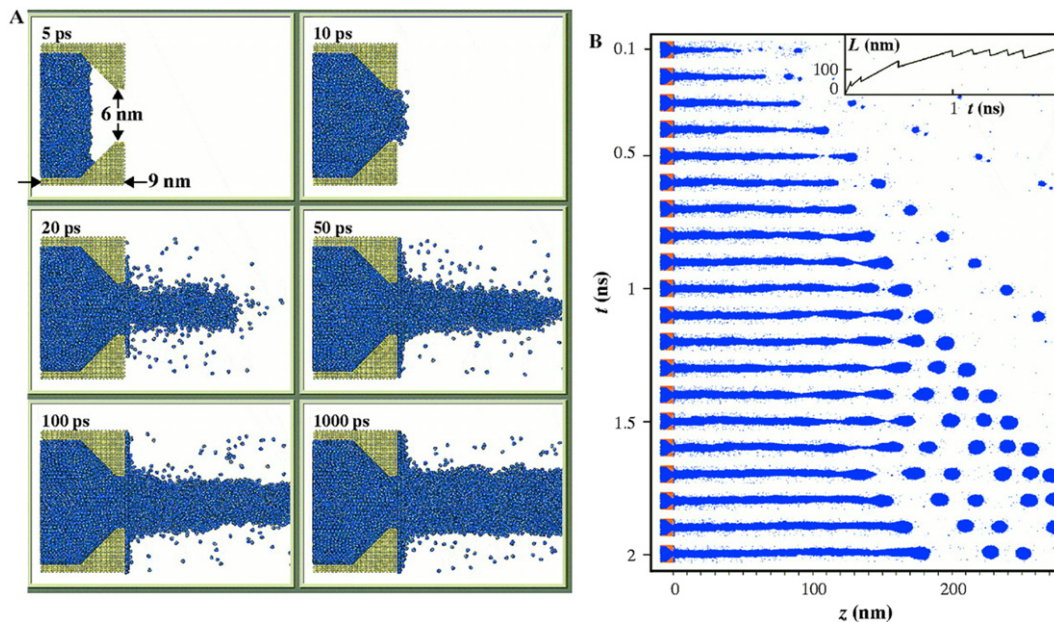

Figure 5. A MD simulation of a jet of propane coming out of a gold nozzle 6 nm in diameter (see section 4.5, figure 58). From [298]. Reprinted with permission from AAAS.

that perturbations are unstable if their wavelength λ is greater than a critical one λ_{cr}, whose value lies between $6h_0$ and $7.2h_0$ [12]. But only after Hagen [13] published the incorrect answer $\lambda_{cr}/h_0 = 2^{5/2} \approx 5.66$ did Plateau reveal [14] his 'perfectly rigorous' result, $\lambda_{cr}/h_0 = 2\pi \approx 6.28$, first demonstrated explicitly by Beer [15], and spelled out in detail in [16].

Plateau's observation is that a jet is unstable to any perturbation which reduces the surface area, thus finally recognizing the crucial role of surface energy (or surface tension) for jet breakup. However, the value of the 'optimal' wavelength λ_{opt} Plateau [12] deduces from Savart's measurements is $\lambda_{opt} = 8.76h_0$, significantly greater than $2\pi \approx 6.28$. Only Rayleigh [17,18] realized that to understand this 'overstretching', the jet *dynamics* has to be taken into account: among all unstable wavelengths $\lambda > \lambda_{cr}$, the one with

the fastest growth rate is selected. For inviscid jet dynamics, this gives $\lambda_{opt} = 9.01h_0$, in good agreement with Savart's data, taken some 50 years earlier! Rayleigh thus introduced the extremely fruitful method of linear stability to jet breakup, which will be the topic of section 3.

Of course, as soon as the perturbations are no longer small, non-linear effects become important, and eventually dominate close to breakup. The features of this non-linear dynamics were revealed in increasingly sophisticated experiments, among which those of Savart [9], Magnus [19], and Lenard [20] stand out. The photographs of figure 8 were obtained with an electric spark, triggered off the forgoing drop. The sequence demonstrates the satellite drop coming from an elongated neck, which pinches on either end. The form of the neck, on the other hand, is imposed by the asymmetry of the
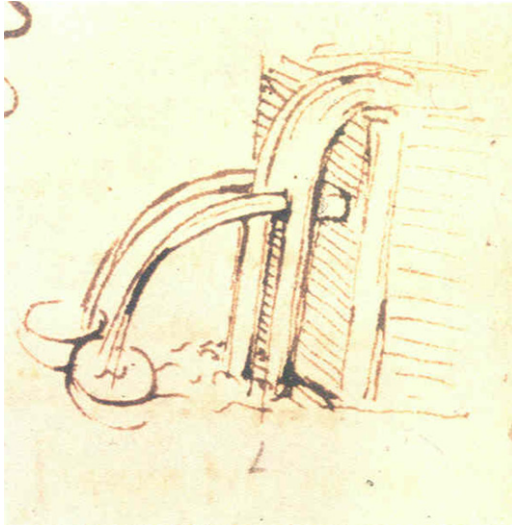
Figure 6. Sketch by Leonardo da Vinci [1] illustrating the impact of jets.
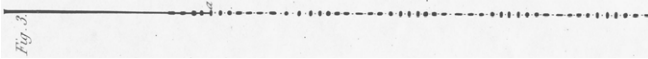

Figure 7. A figure from Savart's original paper [9], showing the breakup of a liquid jet 6 mm in diameter. It clearly shows the succession of main and satellite drops as well as drop oscillations.

profile close to the pinch point: on one side it is very flat, on the other it merges into the circular drop shape.

The ubiquity of satellite drops, invariably seen in both dripping and jetting experiments (cf figures 7 and 8), is thus understood from the nature of the breakup process: the profile has a *universal* shape, which in most cases is highly asymmetric [21]. Regardless of the initial conditions, such as the nozzle radius or the nature of the perturbation to the jet, the breakup behaviour stays the same. In the absence of any characteristic length scale, the profiles near breakup are self-similar, and characteristic quantities like the minimum thread radius $h_{\min}$ are described by power laws [21]. For example, in the case of small viscosity, the conically shaped neck seen in figure 8 is predicted to have an opening half-angle of 18.1° [22]. Dimensional analysis based on (2) predicts the minimum neck radius to follow the universal law $h_{\min} = 0.7(\gamma(t_0-t)^2/\rho)^{1/3}$, where t_0 denotes the time of breakup and γ/ρ the surface tension, divided by density. The scaling properties of solutions close to pinch-off will be the topic of section 4.

The intricate features of drop breakup were essentially well established with Lenard's work [20], and articles by Rayleigh [23] and Boyd [24] further popularized 'high-speed' photography using electrical sparks, see figure 9. However, in the absence of a theoretical framework in which to describe the non-linear aspects of free-surface flow, these considerable advances did not take hold. As reviewed in [25], similar shapes were rediscovered several times [23, 26–28], but not until self-similarity had been suggested as the basis for a theoretical description [28,29] could significant progress occur. It is these more recent developments that will form the bulk of section 4 of this review.

Although it was known from the beginning of the 20th century that many natural phenomena give rise to a multiplicity of drop sizes, in particular as applied to rain (see the remarkable observations of Bentley (1904) [30]), the quantitative study of sprays only started in the 1950s. This was motivated by the wide use of liquid propulsion for cars and aircraft, and concomitantly the development of appropriate measurement tools [31], as we review in section 5. The possible relation of the drop size distribution to jet or ligament dynamics was hinted at in that period, but a definite proof and quantitative study have emerged only recently [32].

Some more complex and exotic topics have also been explored widely during the 19th century and before. One such topic is the sensitivity of jets to electric field, making them easy to deflect [19]. As illustrated in figure 10, strong electric fields are capable of deforming a jet into singular shapes, modifying the character of breakup completely. The interaction of electric fields and fluid motion will be investigated in sections 3.9 and 4.7. Finally, in section 6 we will consider jets made up of non-Newtonian materials, for which forces are not proportional to deformation rates. Figure 11 shows a series of instantaneous images of jets of various granular materials, which appear to break up in a manner similar to that of fluids. Thus unconventional materials like sand, whose novel properties have generated widespread interest only recently, have already been investigated in imperial Russia.

2. Describing jets

This review is devoted almost entirely to hydrodynamic descriptions of jet decay. In this section we outline the description of a jet issuing into a dynamically inert medium in terms of the Navier–Stokes equation. Many important approximations are derived from it, such as the limiting cases of very small or very large viscosity, or the case of the jet geometry being slender.

2.1. Essential parameters

To set the stage, we discuss the dimensionless parameters controlling jet decay, neglecting the outer atmosphere (i.e. air). We assume that the driving is purely sinusoidal, so that the speed at the nozzle is

$$v_{\text{nozzle}} = v_0 + A \left(\frac{\gamma}{\rho h_0} \right)^{1/2} \sin(2\pi f t). \quad (3)$$

Here v_0 is the speed of the jet and h_0 its unperturbed radius. As an aside, h_0 is in general not equal to the nozzle radius, as the jet contracts for high jet speeds and expands for low speeds [35]. This effect depends on the fluid parameters as well as on the velocity profile in the nozzle, so to this day there is no complete theory for the effect [35–37]. The dimensionless perturbation amplitude A is multiplied by the capillary velocity $u_0 = (\gamma/(\rho h_0))^{1/2}$. By properly adjusting the driving frequency f, a wavelength $\lambda = v_0/f$ is chosen. In typical experimental situations the frequency is several kilohertz.
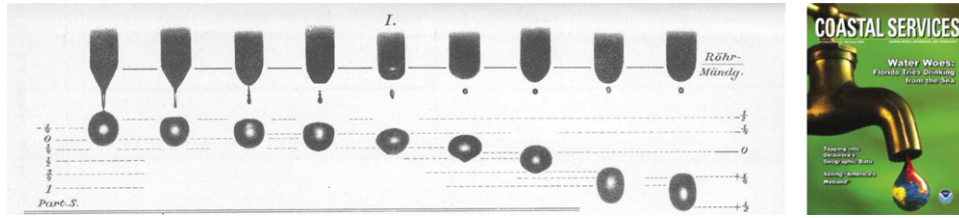
Figure 8. A sequence of pictures of a drop of water falling from a pipette [20], taken in 1887. For the first time, the sequence of events leading to satellite formation can be appreciated. The drop is observed to be almost spherical at the instant it is formed. On the right, an example of contemporary iconography of drop formation, bearing no resemblance to the shapes observed in nature.
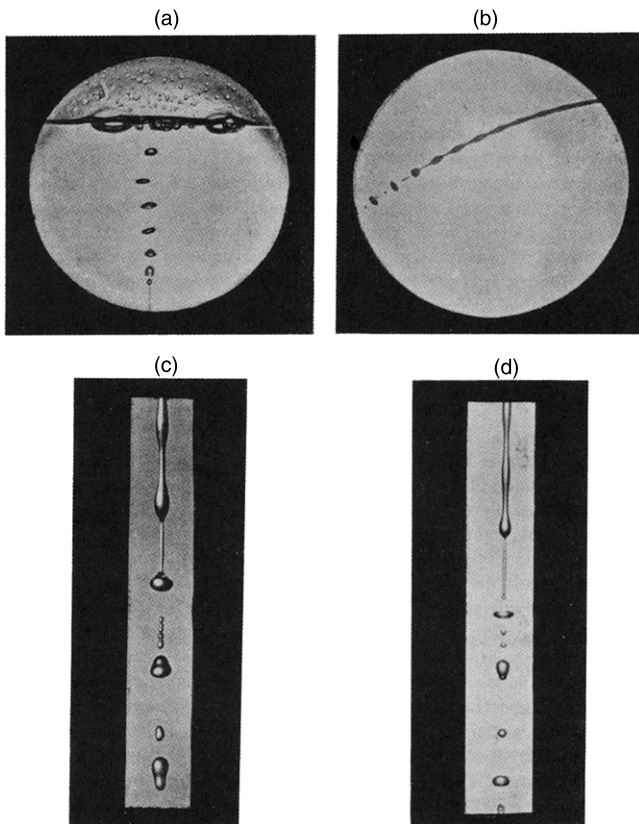

Figure 9. Plate I of Rayleigh's 'some applications of photography' (1891) [23] showing the destabilization of a jet of air into water (*a*) of a water jet in air (*b*). Rayleigh notes that the air jet destabilizes faster than the water jet. Details of the breakup process and the recoil of initially straight 'ligaments' between the drops, sometimes breaking themselves before they have recoiled (*c*) and (*d*).

Figure 10. Abbot Nollet himself demonstrating how a water jet disintegrates when it is charged. He notes that (at the location of the letter C) '...the main jet spreads and divides itself in several tiny jets' (from Abbé Nollet (1749) [33]).

The parameter most significant to jet decay is the reduced wavenumber

$$x = 2\pi h_0/\lambda. \tag{4}$$

At a resonance or 'Rayleigh' wave number $x = x_R$ [17, 18] perturbations grow fastest, and the distance between the nozzle and the first drop 'breakup length', is the shortest. For $x > 1$ or without driving the Rayleigh mode is selected from a spectrum of tiny initial perturbations by virtue of its dominant growth, but breakup becomes much more irregular.

The Weber number [38]

$$We = \rho h_0 v_0^2/\gamma \tag{5}$$

(sometimes denoted by β^2) measures the ratio of the kinetic energy of a drop issuing from the jet relative to its surface energy. The temporal perturbation on a jet is translated into space by convection with velocity v_j. As perturbations grow along the jet on a timescale given by (2), (5) measures how much a disturbance can grow from one swell to the next. Typical numbers are several hundred. The last parameter is the Ohnesorge number [39]

$$Oh = \nu\sqrt{\rho/h_0\gamma}, \tag{6}$$

which measures the relative importance of viscosity $\eta = \nu\rho$. For water and a jet diameter of 1 mm it is about 5×10^{-3}, but technologically relevant fluids cover a wide range of different
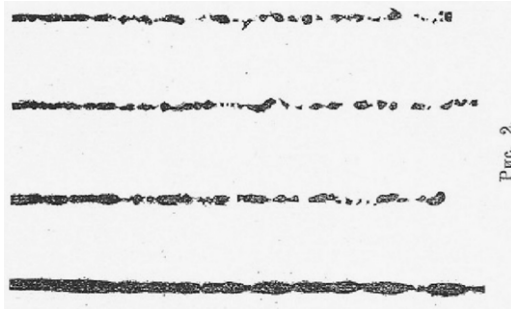
Figure 11. The breakup of different types of granular jets, among them sand and lycopodium powder, from [34]. Even in the absence of surface tension, denser 'drop' regions appear spontaneously.
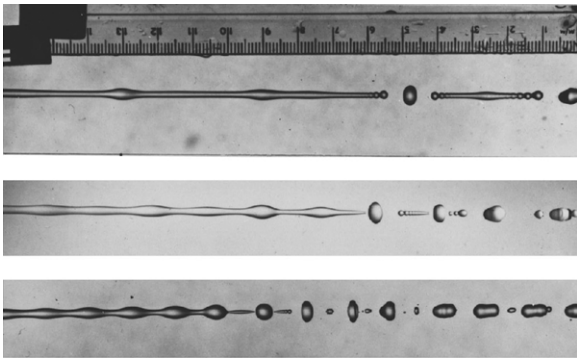

Figure 12. Photographs of a decaying jet [40] for three different frequencies of excitation. The bottom picture corresponds to $x = 0.683$, which is close to the Rayleigh mode. At longer wavelengths secondary swellings develop (middle picture, $x = 0.25$), which cause the jet to break up at twice the frequency of excitation. At the longest wavelength (top picture, $x = 0.075$) main and secondary swellings have become virtually indistinguishable. Reprinted with permission from Cambridge University Press.

viscosities. For example, in the case of glycerol Oh is increased to 2, and by mixing both fluids a wide range of different scaling behaviour can be explored. Finally, if the jet velocity is small 'dripping', gravity plays an important role, as measured by the dimensionless Bond number

$$Bo = \rho g h_0^2 / \gamma \qquad (7)$$

So, in the case of purely sinusoidal driving there are four dimensionless parameters governing jet decay: the driving amplitude A, the reduced wavenumber x, the Weber number We and the Ohnesorge number Oh. The range of possible dynamics in this huge parameter space has never been fully explored; the most dramatic effect is that of viscosity, i.e. by changing Oh. Figure 12 shows typical pictures of a decaying jet of water that is forced at a distinct wavelength. Increasing Oh significantly, for example by taking a glycerol–water mixture, the breakup process changes substantially. After the initial sinusoidal growth, a region develops where almost spherical drops are connected by thin threads of almost constant thickness, which now take quite a long time to break (see figure 13). In general, the thread will still break close to the swells. If the viscosity is increased further, the threads become so tenuous before they break at the end, that instead
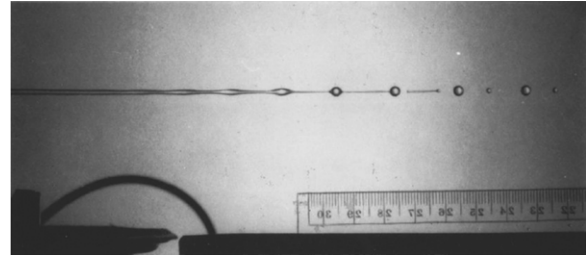

Figure 13. A photograph of a viscous jet [41] for a reduced wavenumber of $x = 0.268$ and $Oh = 0.5$. A thread has just broken at the ends and is contracting into a droplet.

they break at several places in between in what seems to be a random breakup process.

2.2. Hydrodynamic description

2.2.1. Navier–Stokes equation. The theoretical as well as the numerical challenge in the study of jets is to solve the full Navier–Stokes equation in the time-dependent fluid domain, subject to forcing at the boundary. Even in a fixed domain this is not a simple problem, but the main challenge here is to find an accurate description for the fluid boundary. The strength of the forcing is proportional to the mean curvature, which goes to infinity as the jet radius goes to zero, making jet breakup a very singular phenomenon.

The free surface moves with the local velocity; the most elegant and general way to describe this is to introduce a function $C(\boldsymbol{r}, t)$ which is defined in three-dimensional space, and which is constant exactly on the surface of the jet. If $\boldsymbol{v}(\boldsymbol{r}, t)$ is the three-dimensional velocity field, then the motion of the interface is described by the kinematic equation

$$\partial_t C + \boldsymbol{v} \cdot (\boldsymbol{\nabla} C) = 0. \qquad (8)$$

The motion of the interface does not depend on the definition of C, so there is great flexibility to define C according to a specific numerical technique or to endow it with a specific physical meaning.

The most important driving force of jet dynamics is the Laplace pressure, i.e. the pressure jump Δp across a curved interface, producing an increased pressure inside a convex surface:

$$\Delta p = \gamma \left(\frac{1}{R_1} + \frac{1}{R_2} \right) \equiv \gamma \kappa. \qquad (9)$$

Here R_1 and R_2 are the principal radii of curvature, and κ is (twice) the mean curvature. If $\boldsymbol{n}$ is the outward normal to the interface, then

$$\kappa = -\nabla_{\delta\Omega} \cdot \boldsymbol{n}, \qquad (10)$$

where ∇ is defined to be restricted to the surface $\delta\Omega$. If the jet is axisymmetric the surface may be defined by the height function $h(z, t)$, which gives the local radius of the jet. In this description, the kinematic equation (8) becomes

$$\partial_t h + v_z \partial h = v_r|_{r=h}, \qquad (11)$$

and the mean curvature is

$$\kappa = \frac{1}{h(1 + h'^2)^{1/2}} - \frac{h''}{(1 + h'^2)^{3/2}}, \qquad (12)$$
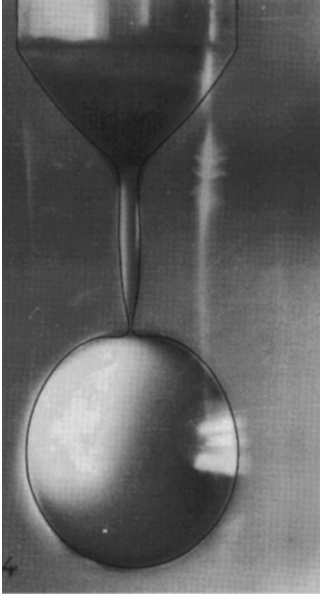
Figure 14. The shape of a drop of water falling from a nozzle at the first bifurcation [28]; the parameters are $Bo = 1.02$ and $Oh = 2.2 \times 10^{-3}$. The line is the result of a boundary integral computation [53]. Reprinted with permission from Cambridge University Press.

where the prime, as throughout this review, denotes the spatial derivative. If the jet develops overhangs, the free surface can of course no longer be written as $h(z, t)$, as it in fact generically occurs during pinching of a jet of small viscosity (Oh small), see figures 14 and 52 below.

The interior of the flow is described by the Navier–Stokes equation [42]

$$\partial_t v + (\nabla v)v = -\frac{1}{\rho}\nabla p + \nu \Delta v \tag{13}$$

for incompressible flow

$$\nabla v = 0. \tag{14}$$

On the free boundary pressure and viscous forces are balanced by capillary forces:

$$\sigma \cdot n = -\gamma \kappa n|_{\partial \Omega}, \tag{15}$$

where

$$\sigma = -pI + \eta[\nabla : v + (\nabla : v)^{\mathrm{T}}] \tag{16}$$

is the stress tensor and p is the pressure. With the velocity known, the interface is moved according to (8). The shape of the interface then couples back into the flow via the boundary condition (15).

2.2.2. Small viscosity: irrotational flow. In the limiting case of vanishing viscosity it is generally believed that little vorticity is generated at the free boundary [43]. Thus unless vorticity is introduced from elsewhere, the flow can be treated as irrotational, i.e. the velocity is given by the potential ϕ,

$$v(r, z) = \nabla \phi(r, z), \tag{17}$$

which obeys Laplace's equation

$$\Delta \phi = 0. \tag{18}$$

Since the Green function of (18) is known, the fluid motion in the interior can effectively be integrated exactly. Thus one ends up with an equation for the free surface alone (a so-called boundary integral method), which can be implemented numerically with very high accuracy. This method was developed in [44], and first applied to jet breakup by [45].

It is convenient to represent the surface in the Lagrangian form $x(\xi, t)$, where ξ is an arbitrary parametrization. For a known velocity field, the surface can then be advanced according to $\partial_t x(\xi, t) = v$. Using Laplace's formula for the pressure jump across the interface, Bernoulli's equation [42] results in an equation of motion for the potential on the free surface:

$$\partial_t \phi(\xi, t) = v^2/2 + \frac{\gamma}{\rho}\kappa \text{ on } \partial \Omega. \tag{19}$$

The velocity v on the right-hand side of (19) can be represented as (17), decomposing into tangential and normal components:

$$v = (\partial_n \phi)n + (\partial_s \phi)t. \tag{20}$$

The tangential derivative $\partial_s \phi$ can be evaluated from the knowledge of ϕ on the surface alone, but to compute $\partial_n \phi$ Laplace's equation comes into play. Namely, given (18) it follows from Green's second theorem that

$$2\pi \phi(r) = \text{P.V.} \int_{\partial \Omega} \left(\phi(r')\partial_n \frac{1}{|r - r'|} - \frac{\partial_{n'}\phi(r')}{|r - r'|} \right) ds', \tag{21}$$

where both r and r' lie on the surface. This is an integral equation which can be solved for $\partial_n \phi$ once ϕ is known on $\partial \Omega$. Thus (19)–(21) form a closed system by which the velocity on the surface can be updated, which in turn advances the interface.

Numerically more efficient implementations of the above scheme represent the velocity potential by a distribution of dipoles $\mu(\xi, t)$ on the surface [45–47]. The dipole distribution can then be used directly to calculate the normal component of the velocity field. All numerical implementations of the inviscid boundary integral equations suffer from a *non-linear* instability on the scale of the grid spacing, investigated for a model problem by Moore [48]. Therefore, some amount of artificial smoothing or damping is always needed [49, 50], typically a redistribution of grid points at every time step. It has been shown only very recently that the mathematical problem itself is well posed [51], thus the instability appears to be a numerical artefact. However, the mathematical result only applies to zero surface tension, and requires smooth initial data as well as additional assumptions on the pressure distribution.

A typical computation is shown in figure 14; note the turnover of the profile at bifurcation, explained by the similarity description of inviscid pinch-off, cf section 4.3. The boundary integral formulation allows for high accuracy; [52] followed pinching solutions through 7 orders of magnitude!

2.2.3. High viscosity: Stokes flow. We now come to the opposite case of Stokes flow, for which the rhs of (13) can be neglected. For the resulting linear equation the velocity and stress distribution of a point force [54] $f(r) = F\delta(r - r_p)$, i.e. the Green function in an infinite domain can be computed [54]:

$$v(r) = \frac{1}{\eta}J(r - r_p)F, \qquad \sigma(r) = K(r - r_p)F, \qquad (22)$$

where

$$J(r) = \frac{1}{8\pi}\left[\frac{I}{r} + \frac{rr}{r^3}\right], \qquad K(r) = -\frac{3}{4\pi}\frac{rrr}{r^5}. \qquad (23)$$

With this in mind the flow equations can again be reduced to a boundary integral description, as developed in [55] and [56].

The basic idea is that surface tension can be viewed as a distribution of point forces over the surface, with $F = \kappa n$. This leads to the integral equation

$$\frac{(1 + \lambda^{-1})}{2}v(x) = -\frac{\gamma}{\eta}\int_{\partial\Omega}\kappa J.n\,\mathrm{d}\sigma' + (1 - \lambda^{-1})\int_{\partial\Omega}v.K.n\,\mathrm{d}\sigma', \qquad (24)$$

where η/λ is the viscosity of the outer fluid. Thus for $\lambda = 1$ (fluid of the same viscosity everywhere) the velocity is simply a convolution of the boundary forcing with J. If for example $\lambda = \infty$ (no fluid in the exterior) the jump in viscosity introduces a stress discontinuity which is accounted for by the second integral of (24). This turns (24) into an integral equation for the velocity on the boundary, which can be used to advance the interface.

The impressive power of the viscous boundary integral method is illustrated in figure 15. The shape of the interface is a double-cone structure, to which we return in section 4.4. The viscosity of the outer fluid is much larger, so recoil of fluid necks is slow. As a result, necks break multiple times, and a complicated nested singularity structure forms. Equation (24), as it stands, is only valid for the motion of a jet in an unbounded fluid, disregarding, e.g., the effect of the nozzle. As described for example in [58], the method can be extended to handle the no-slip boundary condition at a solid wall, so the nozzle can be included as well. A boundary integral code was used in [59] to compute pinching profiles with very high accuracy, for a wide range of viscosity ratios λ. As an illustration of the resolution achievable, [60] studied the coalescence of drops, resolving features down to 10^{-12} relative to the drop radius.

2.3. Numerics: Navier–Stokes methods

If one cannot resort to boundary integral methods, both the accurate representation of the free surface as well as the solution of (13) in a time-varying domain become a significant challenge. In addition, the fluid may undergo topological transitions (both breakup and merging), in which case the identity of a surface changes.

Either the surface is represented directly, for example by surface markers ('front tracking'), or the surface is viewed as a movable object in a higher dimensional space ('front capturing'). The main advantage of the latter method is that it easily deals with topological transitions. For example, one
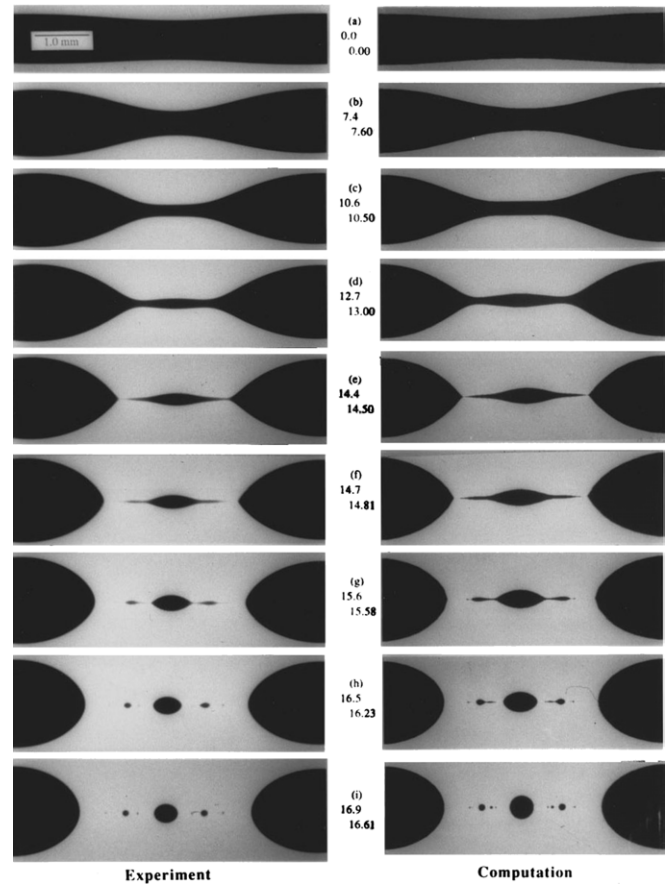
Figure 15. Time evolution of a cylinder of fluid suspended in another fluid. The viscosity ratio is $\lambda = 0.0067$, and the initial dimensionless wavenumber $x = 0.5$ [57]. Snapshots are taken at the times shown in the middle. Reprinted with permission from Cambridge University Press.

can use the advection equation (8) with a suitably defined smooth function C to represent the interface, which can be multiply connected. On the other hand, by tracking the surface directly, much higher accuracy can be attained; however when the topology changes, some amount of 'surgery' is required.

Secondly, the fluid occupies a time-dependent domain $\Omega(t)$. Hence either the computational domain deforms with Ω (Lagrangian approach) or the computational grid, occupying a larger domain, is stationary and the interface sweeps over it (Eulerian approach). Again, boundary conditions can be incorporated very reliably and accurately for Lagrangian schemes, since the computational grid respects the shape of the boundary. A Eulerian scheme, on the other hand, has much greater flexibility in representing a complex and multiply connected fluid domain.

For an overview of existing numerical schemes, see, for example, [50, 61–67]. Each of the computational philosophies named above can be implemented in different ways, and any combination of treating the surface on one hand, and the fluid motion on the other, is possible. The most accurate methods are those for which the grid is fitted to $\Omega(t)$, either by choosing appropriately defined computational elements [64], or by transforming to a fixed grid [68–70]. The code [64] was developed with particular emphasis on a detailed description

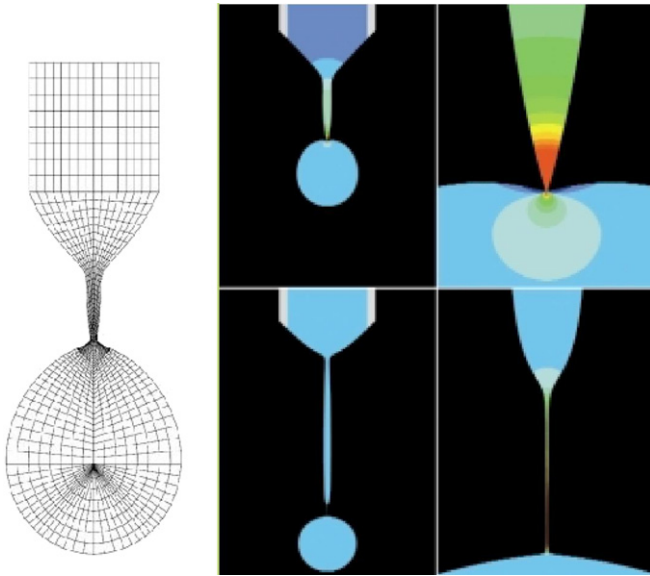**Figure 16.** Schematic of tessellation (left), and simulations of dripping (right). The nozzle radius is $R = 3.6$ mm, the top picture corresponds to water, the bottom to a 83% glycerol solution. Reprinted from [73]. Copyright 2002, with permission of John Wiley and Sons.

of pinch-off, and has been applied to a variety of dripping and jetting applications [71–75].

Equations (13)–(15) are solved using a Galerkin/finite difference method [76], decomposing the domain into elements as illustrated in figure 16. The flow is assumed to be axisymmetric, and different prescriptions are used in different parts of the flow, making the discretization highly specific to the problem at hand. As in an earlier implementation of the same method [77], the boundary conditions can be incorporated directly into the residual equations for each boundary element. Figure 16 shows typical result for dripping at low viscosity (top) and high viscosity (bottom). As revealed in the closeup, the interface *overturns* at low viscosities, while in the opposite case very long threads are formed.

The most popular *front capturing schemes* are the volume of fluid (VOF) [80] and the level set [81, 82] methods, or combinations thereof [61]. In the former, the interface is reconstructed from the fraction of each phase that exists within each computational cell; as a result, volume is conserved exactly. The level set method uses (8), with a function C chosen for computational convenience; typically, it is maintained as the signed distance from the free-surface. With either method, there is essentially no limit to the complexity of the free-surface shape, and breakup and merging events are handled automatically (which of course does not imply that they represent physical reality)! A number of well-known problems such as spurious currents are discussed in [62]. In addition, there are limits on stability which require the densities of both phases not to be too dissimilar [83]. An example illustrating the considerable power of front capturing schemes is that of a turbulent jet entering a gas atmosphere, as shown in figure 17. The dimension of the (uniform) mesh is $128 \times 128 \times 896$, the calculation time on a 14 processor machine was 3 weeks.

In spite of sophisticated techniques to reconstruct the surface, the accuracy of front capturing schemes is limited by the calculation of surface tension forces. The rate of convergence of these schemes is not well understood, and is often only linear [62]. For this reason methods have been developed that represent the surface by marker points [63, 84], so that the curvature can be computed with high accuracy based on the position of marker points. In addition, *adaptive* grid methods have been developed [63, 85], which refine the grid in the neighbourhood of the free surface. Thus the flow can be calculated more accurately as well. A number of codes are open source, such as SURFER [86] or Gerris [87].

Finally, there are numerical implementations which endow the interface or the fluid itself with some 'microscopic' structure. Only on an appropriately coarse-grained scale is the Navier–Stokes equation with a sharp interface recovered. Firstly, there are order parameter or Cahn–Hilliard models [88, 89], which also go by the name of 'diffuse interface models'. The two phases are distinguished by different values of an order parameter, which can be the density ρ, with a smooth tanh-like profile at the position of the interface. Surface tension emerges from the coupling between the velocity field and the order parameter, which results in a forcing concentrated in the interface region. The value of the surface tension is related to the free energy functional of the order parameter [90]. Evidently the resolution of this method is limited by the thickness of the interface, which in present implementations is much thicker than its true physical value of a few angstrom for a liquid–gas interface [90]. Secondly, lattice gas [91] and lattice Boltzmann (LB) methods [92] have been adopted to free surfaces as well [67, 93]. Since the strength of these methods lies in their flexibility to describe complex boundary conditions, they are probably best compared to front capturing methods. However, we are not aware of LB methods having been applied to complex free-surface flows yet.

2.4. Long-wavelength descriptions

Here we describe methods which have been used successfully to describe free surfaces for the case that perturbations have a wavelength much longer than the radial extension. Results are often highly quantitative, and play an important role in cases where full Navier–Stokes simulations are prohibitively expensive [75]. However, the greatest significance of long-wavelength models lies in the fact that they often capture the *exact* form of the solution near breakup. They thus form the basis for most analytical descriptions of jet breakup, see section 4.

The first two methods are applicable if the fluid motion is confined mainly to the inner (jet) fluid. Either the velocity field is represented directly by expanding in the radial variable, or it is exhausted in the radial direction by a set of basis functions. Slender-body analysis is widely used if the jet is dynamically inactive and the focus is on the description of the exterior motion. In that case one aims to represent the motion by a distribution of point singularities along the axis.
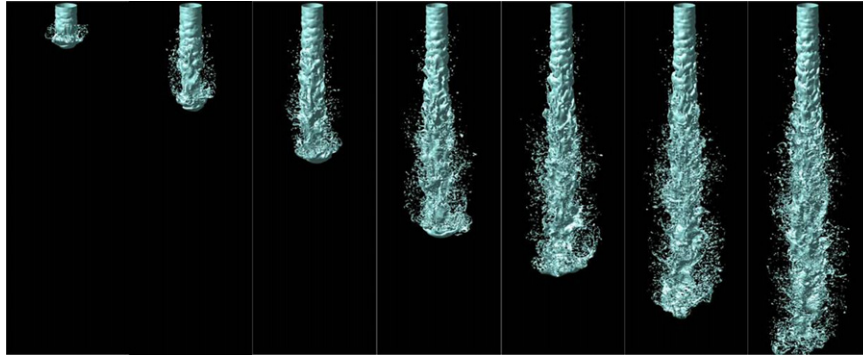
Figure 17. A numerical simulation of a turbulent jet of liquid ($\rho_{liq} = 696 \, \text{kg m}^{-3}$, $\eta_{liq} = 1.2 \times 10^{-3} \, \text{kg (ms)}^{-1}$) entering a gas atmosphere ($\rho_{gas} = 25 \, \text{kg m}^{-3}$, $\eta_{gas} = 10^{-5} \, \text{kg (ms)}^{-1}$) [78]. The surface tension is $\gamma = 0.06 \, \text{N m}^{-1}$, the jet speed is $v_{nozzle} = 100 \, \text{m s}^{-1}$, the turbulence intensity [79] is 0.05.

2.4.1. Radial expansion. The essential idea of this method goes back to Reynolds' lubrication theory [94]: if variations along the jet are slow, the flow field in the transversal direction can be described by a 'simple' function. The two main advantages are that the effective description becomes one-dimensional, and that the flow field no longer has to be solved over a time-varying domain. Detailed comparisons with experiments and simulations have shown that one-dimensional descriptions often are surprisingly accurate, even if the long-wavelength assumption is not well verified [95–97].

One-dimensional descriptions of jets and fibres have been used for a long time, elements of it going back to Trouton [98] and Weber [38]. Matovich and Pearson [99–101] developed equations for *steady* fibre spinning. In two pioneering papers, Markova and Shkadov [102] and Lee [103] developed one-dimensional *dynamical* equations for inviscid flow, see also [104]. They studied the non-linear dynamics of jet breakup numerically, using Fourier [102] and finite difference [103] methods. Unfortunately, the resulting models suffer from unphysical singularities at which the slope of the profile goes to infinity [105]. Viscosity was included by Green [106], but using an inherently one-dimensional description known as the Cosserat equations [107, 108]. Entov *et al* [109] and Renardy and Markovich [110, 111] included memory effects appropriate for the description of polymers, while Entov and Yarin [112–114] and Dewynne *et al* [115, 116] extended to the case of curved centrelines.

Reynolds' idea amounts to saying that a typical radial length scale ℓ_r of a solution one hopes to describe is much smaller that its longitudinal scale ℓ_z:

$$\ell_r = \epsilon \ell_z, \qquad (25)$$

where ϵ is a small number. Thus, if one expands the hydrodynamic fields in the radial direction:

$$v_z(r, z, t) = v_0(z, t) + v_2(z, t)(\epsilon r)^2 + \cdots,$$

$$v_r(r, z, t) = -v_0'(z, t)\frac{\epsilon r}{2} - v_2'(z, t)\frac{(\epsilon r)^3}{4} - \cdots, \qquad (26)$$

$$p(r, z, t) = p_0(z, t) + p_2(z, t)(\epsilon r)^2 + \cdots,$$

the higher-order terms will be of decreasing size. When studying the behaviour near breakup, we will discover that

ϵ is to be identified with the square root of the *time distance* from the singularity, thus the slenderness expansion captures precisely the contributions to the Navier–Stokes equation which are relevant close to the singularity.

The prescription (25) is not yet sufficient to define a long-wavelength description uniquely, to that end a choice for the length scales ℓ_z as well as a time scale τ has to be made. Physically, each choice corresponds to a balance of terms in the Navier–Stokes equation, which will enter the description at leading order. Which balance is appropriate will depend on the character of the solution to be expected for a given set of physical parameters. The balance that will prove most useful is one in which surface tension, inertial and viscous forces all come in at leading order.

First, it is useful to introduce a reference length and a time scale which only depends on the physical parameters of the fluid, and which is thus intrinsic to the fluid motion [119]:

$$\ell_\nu = \frac{\nu^2 \rho}{\gamma}, \qquad t_\nu = \frac{\nu^3 \rho^2}{\gamma^2}. \qquad (27)$$

Parameter values for commonly used fluids are given in table 1. Naively one might think that values of ℓ_ν and t_ν, being intrinsic, might be associated with some microscopic scale of the fluid. However, this intuition is spectacularly wrong, as ℓ_ν and t_ν vary over 11 and 16 orders of magnitude, respectively! Now if, in addition to (25), one equates estimates of the Laplace pressure $\gamma/(h\rho)$, inertial force $\partial_t v_z$ and viscous force $\nu \Delta v_z$, one arrives at

$$\ell_z \sim \epsilon, \qquad \ell_r \sim \epsilon^2, \qquad \tau \sim \epsilon^2. \qquad (28)$$

If the typical scales of a solution behave according to (28), surface tension, inertial and viscous forces are of the same order.

Now the procedure to derive the leading-order equation, described in detail in [120], is fairly straightforward: all quantities are made dimensionless using the scales (28), and the expansion (26) is inserted into the Navier–Stokes equation (13), (14) for incompressible fluid motion. The kinematic boundary condition (11) gives, using the original dimensional variables,

$$\partial_t h^2 + (v h^2)' = 0, \qquad (29)$$

Table 1. The fluid parameters for water, glycerol, mercury and golden syrup. The values are quoted from [117, 118]. The internal scales ℓ_ν and t_ν are calculated from the kinematic viscosity ν and from the ratio of surface tension γ and density ρ.

	Mercury	Water	Glycerol	Golden syrup
ν (m^2 s^{-1})	1.2×10^{-7}	10^{-6}	1.18×10^{-3}	0.051
γ/ρ (m^3 s^{-2})	3.47×10^{-5}	7.29×10^{-5}	5.3×10^{-5}	5.6×10^{-5}
$\ell_\nu = \rho\nu^2/\gamma$ (m)	4.2×10^{-10}	1.38×10^{-8}	0.0279	47
$t_\nu = \nu^3\rho^2/\gamma^2$ (s)	1.4×10^{-12}	1.91×0^{-10}	0.652	4.3×10^4

where we replaced $v_0 \equiv v$ for neatness. Clearly, (29) is the conservation law for the volume $\pi h^2 \, dz$ contained in a slice of fluid, approximating the velocity field as a plug flow: $v_z(r, z, t) \approx v(z, t)$. From the z-component of (13), making use of the two equations contained in the boundary condition (15), one obtains

$$\partial_t v + vv' = -\gamma\kappa'/\rho + 3\nu \frac{(v'h^2)'}{h^2} \qquad (30)$$

to leading order in ϵ. Also to leading order, the mean curvature κ is

$$\kappa = \frac{1}{h}. \qquad (31)$$

The structure of (30) is best motivated by considering the force balance on a slice of fluid which carries momentum $m = h^2 v$ per unit length, disregarding the common factor of π. A more systematic treatment of the slice concept is found in the following subsection. Namely, the integrated form of (30) is

$$\partial_t(h^2 v) + (h^2 v^2)' = -\frac{\gamma}{\rho}\kappa'h^2 + 3\nu(h^2 v')', \qquad (32)$$

where the left-hand side is the total time derivative of m. The first term on the right comes from the capillary forcing on the slice, the second term is the viscous forcing. The prefactor comes from the fact that the viscous contribution to the axial stress σ_{zz} in an axisymmetric extensional flow is [98] $3\eta v'$, where 3η is called the Trouton viscosity [98]. In the analogous case of a plane sheet, Taylor [121][6] shows that the effective viscosity is 4η.

The set of equations (29)–(31) is a coupled system of equations for h and leading coefficient v_0 of the radial expansion (26). Apart from the fact that the spatial dimension has been reduced to one, the motion of the free surface is now given explicitly by equation (29). The system forms the basis for the similarity description of jet decay near the point of breakup, as described in detail in section 4. However, as evolution equations (29)–(31) are useless, since the second, longitudinal curvature term of (12) is not contained in (31). As a result (see section 3), the system is prone to instability at zero wavelength and is thus ill-posed.

This can be remedied [95] by replacing (31) by the full expression (12), which gives for the energy balance over a length L of the jet:

$$\partial_t(E_{\text{kin}} + E_{\text{S}}) = D + \text{boundary terms}. \qquad (33)$$

Here

$$E_{\text{kin}} = \frac{\pi}{2}\rho \int_L h^2 v^2 \, dz \qquad (34)$$

[6] A fact pointed out to us by Howard Stone.

is the kinetic energy,

$$E_{\text{S}} = 2\pi\gamma \int_L h(1 + h'^2)^{1/2} \, dz \qquad (35)$$

is the *exact* form of the surface energy and D is the (negative definite) rate of energy dissipation

$$D = -3\pi\nu\rho \int_L (hv')^2 \, dz. \qquad (36)$$

Thus in the long-time limit the system will tend to a state in which the flow ceases and which minimizes the surface area (i.e. spherical drops); these equilibrium states are reproduced correctly by (29) and (30) *iff* the full curvature (12) is taken into account.

Indeed, the system (29), (30), (12) has been used with great success to describe dripping and jetting *away* from the singularity [95–97, 122, 123]. In [96] a detailed comparison with full Navier–Stokes simulations was carried out, demonstrating excellent agreement over a wide range of parameters. A comparison with experiment is shown in figure 18 for a dripping faucet, adding the acceleration of gravity g to the rhs of (30). Indeed, a number of detailed studies of the bifurcation diagram and the chaotic states of a dripping faucet [97, 122, 124, 125] are based largely on this one-dimensional description, a full simulation being much too costly.

The method described above can be pursued to higher order in ϵ, (cf [126, 127]), continuing the radial expansion (26) to higher powers in r. The scheme of Garcia and Castellanos [127] is particularly interesting, since it leads to systems of equations in which the non-linear couplings between the variables $h, v_0, v_2, \ldots$ (cf (26)) are kept. In principle, this could lead to a systematic improvement of the description of non-linear jet dynamics, but this line of research has not been followed much, mainly because the resulting systems become very unwieldy, and contain rapidly increasing orders in the spatial derivatives.

2.4.2. Galerkin method. An alternative approach to the radial expansion method described above is the Galerkin method developed in [120], based on ideas by Dupont [128]. In this approach one represents the velocity field as a series of divergence-free basis functions $w^{(2i,\bar{z})}(r, z)$, $i = 0, \ldots, n$, each of which represents a slice of fluid at position $\bar{z}$:

$$v(r, z, t) = \sum_{i=0}^{\infty} \int_{-\infty}^{\infty} v^{(i)}(\bar{z}, t) w^{(i,\bar{z})}(r, z) \, d\bar{z}. \qquad (37)$$
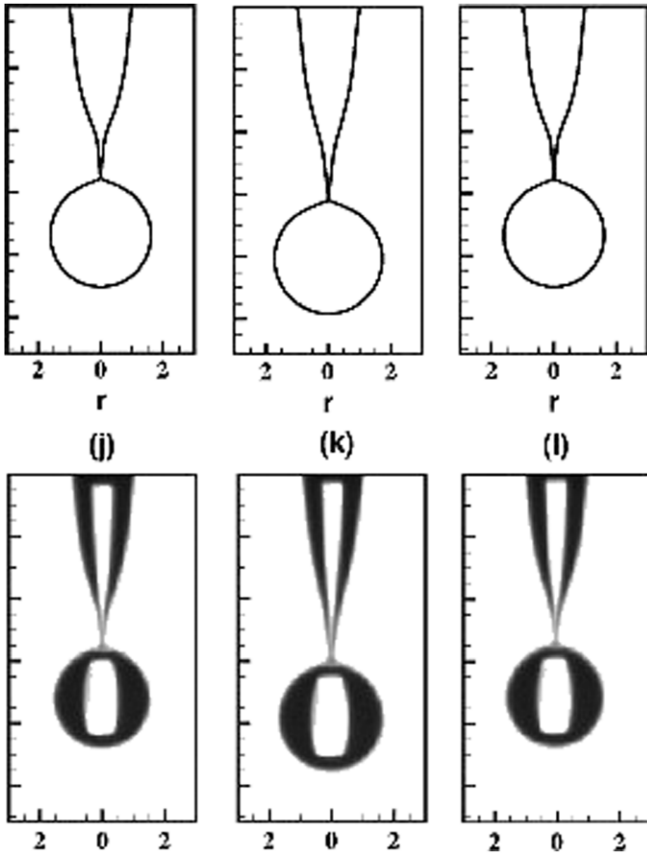
Figure 18. Period-2 dripping at $Oh = 0.13$, $Bo = 0.33$, and $We = 0.232$ [97]. (Top) simulation of (29),(30), (bottom) experiment. Reprinted with permission from [97], copyright 2006 by the American Institute of Physics.

Multiplying the Navier–Stokes equation by any of the basis functions $w(r, z)$ and averaging, one obtains

$$\rho \int_V [\partial_t v + (\nabla)v]w \, d^3x$$

$$= -\gamma \int_O \kappa(nw)d^2s - 2\eta \int_V D_{ij}(v)D_{ij}(w)d^3x \qquad (38)$$

where

$$D_{ij}(v) = \tfrac{1}{2}(\partial_j v_i + \partial_i v_0) \qquad (39)$$

is the deformation rate tensor.

In the simplest approximation, in which the velocity is represented by a plug flow, one has

$$w(r, z) := w^{(0,\bar{z})}(r, z) = \begin{pmatrix} -\frac{r}{2} \delta'(z - \bar{z}) \\ \delta(z - \bar{z}) \end{pmatrix}. \qquad (40)$$

Putting $v(z, t) := v^{(0)}(z, t)$ one obtains

$$\rho[h^2\dot{v} - \tfrac{1}{8}(h^4\dot{v})' + h^2vv' + \tfrac{1}{16}(h^4v'^2)' - \tfrac{1}{8}(h^4vv'')']$$

$$= -\gamma h^2\kappa' + \eta[3(h^2v')' - \tfrac{1}{8}(h^4v'')''], \qquad (41)$$

where the dot denotes a time derivative and primes spatial derivatives. Equation (41) replaces (30), obtained from the radial expansion method.

Equations (29), (41) are identical to the 'Cosserat' equations as given in [129], based directly on one-dimensional

fields [106–108], to which mechanical and thermodynamic principles are applied. The above approach establishes the connection to the pointwise description of hydrodynamics. The great advantage of (41) is that it builds in the full curvature term (12) in a natural fashion. Its precise structure is somewhat arbitrary since it depends on the choice of basis function $w(r, z)$. If one orders the terms in (41) according to the slenderness parameter ϵ, one recovers (30).

2.4.3. Slender-body approximation. Slender-body theory was first developed to describe the inviscid flow around bodies [130], its origins dating back to the 1920s, as reviewed in [131]. Another application is to compute the electric field around an elongated conducting body [132], as used in [133, 134] and in section 4.7.2. Namely, from the point of view of the exterior field, the surface charge can be thought to be concentrated along the centreline of the body. The strength of the distribution has to be found self-consistently, by solving an integral equation. For free-surface problems, in particular, this represents a significant advance, since the distribution has to be found in a fixed domain only, rather than on the unknown surface.

For example in the case of a fluid jet in an external electric field, described in detail in section 4.7, one needs to know the electric field E on the surface (cf (255)). The resulting equations and their approximations are described in some detail in [133]. Below we discuss the closely related case of inviscid, irrotational flow around a cavity. In the limit of highly *viscous* flow around a bubble [135, 136] or an effectively inviscid fluid [137] the slender-body approximation leads to integral equations for a charge and a dipole distribution [135]. The integrals are easily localized [138] to find a simple equation for the free surface shape $h(z, t)$ alone, first given by Taylor [139].

The inviscid, irrotational flow (17), (18) outside a cavity of length $2L$ can be written as

$$\phi = \int_{-L}^{L} \frac{C(\xi, t) \, d\xi}{\sqrt{(z - \xi)^2 + r^2}}, \qquad (42)$$

where $C(\xi, t)$ is a line distribution of sources. An equation of motion for C is furnished by Bernoulli's equation (19), but for the *exterior* flow and in a Eulerian frame of reference:

$$\partial_t\phi + v^2/2|_{r=h} = \gamma\kappa - p_0, \qquad (43)$$

where p_0 is the pressure inside the cavity. The equation of motion for $h(z, t)$ is the kinematic equation (11). The expression for the velocity field is obtained from differentiating (42) and putting $r = h(z, t)$.

So far, the description is exact, except perhaps near the ends $z = \pm L$ of the cavity [140]. To simplify the description for a slender geometry, one can use the fact that $v_r \gg v_z$ and thus neglect the axial velocity v_z. The integral giving the radial velocity is local: $|\xi - z| \lesssim h$, thus in a slender description $C(\xi, t) \approx C(z, t)$ and $L \rightarrow \infty$. With these approximations, the ξ-integration can be performed exactly, giving $v_r \approx -2C(z, t)/h(z, t)$. Thus (11) simplifies to

$\dot{a}(z, t) \approx -4C(z, t)$, where $a = h^2$ and the dot denotes the time derivative.

Finally, using the same approximations as above, (43) turns into an equation of motion for C in the slender case:

$$\int_{-L}^{L} \frac{\ddot{a}(\xi, t)\, d\xi}{\sqrt{(z - \xi)^2 + a(z, t)}} = \frac{\dot{a}^2}{2a} - \frac{4\gamma}{\rho}\kappa + \frac{4p_0}{\rho}, \qquad (44)$$

first given in [141]. Slender-body descriptions similar to (44) are common in the literature [130,142], but usually the integral is transformed further, using slenderness. In this marginal case (also encountered in the electrostatic analogue [133]) one finds a logarithmic dependence on h [138], and convergence is exceedingly slow. In fact, the usual expansion in logarithmic terms [130] does not capture the leading asymptotic of pinch-off, as we discuss in section 4.3. However, a linear stability analysis reveals that (44) is ill-posed as it stands. This can be fixed by adding a small damping to the right-hand side of (44) [141].

3. Physical mechanisms and small perturbations

Here we explain the reason why the circular jet geometry is rendered unstable by capillarity, as well as the characteristic time and length scales associated with this transition from cylinder to drops. We also discuss various phenomena influencing jet decay apart from capillarity. This is achieved using the powerful tool of linear stability analysis, pioneered by Rayleigh [17]. As we will show in the next subsection, any perturbation of sufficiently long wavelength will result in a gain in surface energy, so the perturbation grows. Rayleigh [10,17] was the first to point out the crucial significance of the *most unstable wavelength*, which is only found by studying the dynamics, as we will do throughout this section. Namely, starting from a random initial perturbation, the disturbance amplitudes on a jet will eventually be dominated by the mode with the largest growth rate. This sets the preferred wavelength of breakup, and thus the drop size, without introducing any length scale from the outside. Most experimental studies, however, consider the response to a stimulus at a given wavelength, thus avoiding the ingredient of randomness. Few studies have looked at random breakup caused by, for instance, white-noise perturbation at the nozzle, or turbulence in the liquid bulk and tried to characterize the width of the resulting drop distribution [143, 144], despite the key role played by these ingredients in the quality of sprays (see [32], section 5 and, e.g. figure 91).

3.1. Capillarity and the circular geometry: the Plateau argument

The physical meaning of surface tension is that of an energy per unit area, so if the surface area increases by δA, the surface energy changes by

$$\delta E = \gamma \delta A. \qquad (45)$$

From this statement the formula (35) for the capillary forcing can be derived [42]. One may thus ask whether some particular distortions of a liquid cylinder around its circular and straight

initial shape (at constant volume) will lower the net surface area. In any such case small perturbation or noise will drive the system towards this lower energy state.

Sinusoidal undulations of the jet centreline will not affect its net surface area if its radius remains constant. On the other hand, modulations of the jet radius may change its surface energy. The perturbation

$$h(z, \varphi) = h_0 + \epsilon \cos(kz) \cos(m\varphi), \qquad (46)$$

where k is the longitudinal wavenumber and φ the azimuthal angle, can be viewed as a Fourier mode of a given initial condition $h(z, \varphi)$. The azimuthal modulations simply correspond to a corrugation of the jet's mantle, so they always increase the surface area. Thus all azimuthal modes $m > 0$ are stable [145] and we proceed with the discussion for $m = 0$, for which the surface energy is given by (35).

The distortions of the jet radius in (46) are such that the corresponding jet portion keeps its volume

$$V = \int_L \pi h^2\, dz = V^{\text{init}} = \pi h_0^2 \int_L dz \qquad (47)$$

constant, which means the mean radius $\bar{h}$ has to adjust itself to a new value. This condition on (47) results in

$$\bar{h} = h_0 - \frac{\epsilon^2}{4h_0}, \qquad (48)$$

and thus a *smaller* mean radius $\bar{h}$ relative to the unperturbed state.

Considering now *small perturbations* $\epsilon \ll 1$, and thus $h' \ll 1$, the difference $\Delta E = E_S - E_0$ in surface energy relative to the initial state $E_0 = 2\pi h_0 \gamma \int dz$ is computed using (35)

$$\frac{\Delta E}{E_0} = \frac{\epsilon^2}{4h_0^2}[(kh_0)^2 - 1]. \qquad (49)$$

All modes whose wavelengths $\lambda = 2\pi/k$ are larger than the *perimeter* of the jet have a negative energy, and are thus potentially unstable, as concluded by Plateau [16].

3.2. Capillary instability

The above thermodynamic description does not reveal which mode is the most unstable in the range $0 < kh_0 < 1$ nor at which speed the instability develops. To this end, one has to consider the equations of motion.

3.2.1. Dynamics and mode selection. We first consider motions driven by capillarity only, the jet deforming in a passive environment. The flow in the bulk of the jet is taken as incompressible (cf (14)) and it is convenient to work in a reference frame moving at the jet velocity so that $v_0 = 0$. The pressure in the jet is initially uniform, and equal to the Laplace pressure (9), i.e. $p_0 = \gamma/h_0$. We write the velocity v and pressure p fields as their initial value plus a small perturbation:

$$v = v_0 + \delta v, \qquad p = p_0 + \delta p, \qquad (50)$$

and insert into the Navier–Stokes equations. Disregarding quadratic terms, this *linearization* procedure allows for simple quadratures and the recourse to Fourier analysis.

Combining (13) and (14) implies that

$$\nabla^2 p = 0 \tag{51}$$

in a linear approximation. In view of the discussion in section 3.1, we look for varicose, axisymmetric perturbations of the form $\delta \boldsymbol{v}(r, z)$ and $\delta p(r, z)$. We begin with the inviscid approximation $\nu = 0$. Writing the perturbed pressure as

$$\delta p = \delta \bar{p} F(r) \cos(kz), \tag{52}$$

(51) implies that $F(r)$ obeys

$$\frac{\partial^2 F}{\partial^2 r} + \frac{1}{r} \frac{\partial F}{\partial r} - k^2 F = 0. \tag{53}$$

The solution is the Kelvin function $F(r) = I_0(kr)$ [146], which has the virtue of being non-singular at $r = 0$.

At the jet surface $p_0 + \delta p$ equals the Laplace pressure (9), and thus inserting (46) into (12) one obtains to leading order in ϵ

$$\delta p(r = h_0, z) = -\frac{\gamma}{h_0^2}[1 - (kh_0)^2]I_0(kh_0)\epsilon \cos(kz). \tag{54}$$

The problem is closed by relating the amplitude of the pressure perturbation $\delta\bar{p}$ to the interface displacement ϵ Namely, the linearized form of (11) is

$$\frac{\partial h}{\partial t} = \delta v_r(r = h), \tag{55}$$

and the radial velocity and the pressure are linked by the radial component of the (linearized) Euler equation (i.e. (13) with $\nu = 0$):

$$\frac{\partial \delta v_r}{\partial t} = -\frac{1}{\rho} \frac{\partial p}{\partial r}. \tag{56}$$

Making use of $\delta p = \delta\bar{p}I_0(kr)\cos(kz)$ and looking for a time dependence of the perturbation amplitude of the form $\epsilon(t) = \epsilon_0 e^{-i\omega t}$, one finds that [147]

$$\omega^2 = -\frac{\gamma}{\rho h_0^3}(kh_0)\left[1 - (kh_0)^2\right]\frac{I_1(kh_0)}{I_0(kh_0)}. \tag{57}$$

The characteristic timescale of (57) is set by (2), representing a balance of inertia and surface tension. The instability is caused by the fact that the Laplace pressure increases in constricted regions, driving out the fluid and thus reducing the radius even more. The above dispersion relation has been successfully checked experimentally (figure 19). It is worth remarking that highly accurate measurements of linear jet stability are surprisingly difficult, even by modern standards [148–150]. First, a number of other effects govern linear growth, such as fluid viscosity and the external medium (e.g. air). Second, parameters like the jet diameter and its speed are difficult to determine reliably on account of the complicated hydrodynamics near the nozzle opening, leading to effects like jet contraction [35]. A number of optical techniques [151–153], using light beams and sheets, yield more qualitative
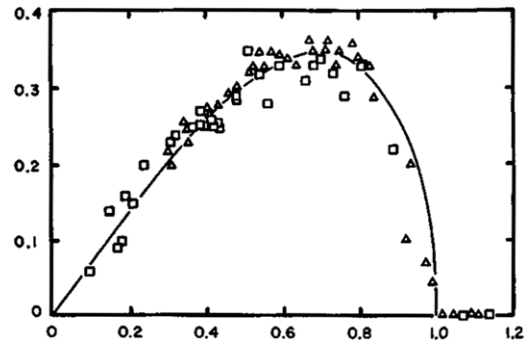

Figure 19. Dimensionless growth rate $-i\omega(k)\tau$ of sinusoidal perturbations on a cylinder as a function of the dimensionless wave number kh_0. The solid line represents Rayleigh's theory for inviscid flow [120, 159]. Reprinted with permission from [159], copyright 1975 by the American Institute of Physics.

information on the number and size of a potentially large number of drops. The above *dispersion relation* $\omega(k)$ is consistent with (49); for $kh_0 < 1$ we have $\omega(k)^2 < 0$, and thus an exponential growth of the initial disturbance. The most amplified wavenumber k_m (the Rayleigh mode) in (57) is

$$k_m h_0 \approx 0.7 \tag{58}$$

and its associated time of growth $\tau(k_m)^{-1} = Re[-i\omega(k_m)]$ is

$$\tau(k_m) \approx 3\sqrt{\frac{\rho h_0^3}{\gamma}}. \tag{59}$$

By letting a jet issue from an *elliptical* orifice, a non-axisymmetric *stable* mode with $m = 2$ is excited. By recording the wavelength of the oscillation of the jet's eccentricity (at a frequency proportional to $\sqrt{\gamma/\rho h_0^3}$), one can measure the surface tension [154–156].

3.2.2. Long-wave description. Since the most unstable wavelength is about $9h_0$, the long-wavelength model (29), (30) should describe the linear instability well, provided the full curvature (12) is kept. The latter is necessary to describe the cut-off at short wavelengths, so for $\nu = 0$ one obtains from (30)

$$\frac{\partial v}{\partial t} = -\frac{\gamma}{\rho}\left(\frac{1}{h} - h''\right)'. \tag{60}$$

Linear stability analysis, using the ansatz

$$h(z, t) = h_0 + \epsilon(t)\cos(kz) \quad \text{with } \epsilon(t) = \epsilon_0 e^{-i\omega t} \tag{61}$$

gives [38]

$$\omega^2 = -\frac{1}{2}\frac{\gamma}{\rho h_0^3}[(kh_0)^2 - (kh_0)^4], \tag{62}$$

which coincides with an expansion of (57) for small k. As seen in figure 20, (62) not only retains all the relevant facets of the problem, such as the cut-off at $kh_0 = 1$, but also fits the exact relationship (57) quantitatively, as seen in figure 20. The great advantage of the long-wave description is that it is simple and transparent, so additional ingredients can be incorporated into the picture in a straightforward way, as we shall see below.
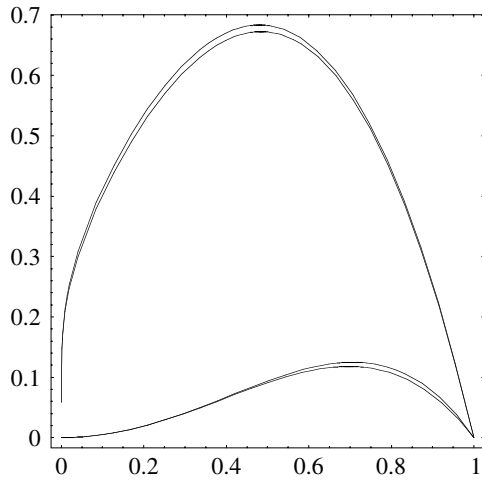
Figure 20. A comparison between dispersion relations $-\omega^2(k)\tau^2$ for inviscid flow, as function of kh_0. There is excellent agreement between the exact formula (57) for a fluid jet and the long-wavelength form (62) (top curves), as well as the analogous formulae for a hollow jet (equations (69) and (77), bottom curves).

3.3. Weakly non-linear theories

To obtain a glimpse of non-linear jet behaviour such as the formation of satellite drops, one can attempt to carry the perturbation theory to higher order, by including terms of second and third order in ϵ. As reviewed in detail in [120], this program has so far only been worked out in the inviscid case. The ansatz for the surface perturbations is [157–160]

$$h(z, t) = h + \epsilon_0 e^{-i\omega t} \cos(kz) + \epsilon_0^2 h_2(z, t)$$
$$+ \epsilon_0^3 h_3(z, t) + O(\epsilon_0^4), \qquad (63)$$

and a corresponding expression for the velocity potential (17).

Successive approximations are obtained in a perturbative fashion, leading to higher harmonics at each order. However at third order another contribution to the fundamental is produced,

$$h_3(z, t) = A_{33}(t) \cos(3kz) + A_{31}(t) \cos(kz), \qquad (64)$$

leading to secular terms as a result of resonance between the first and the third order. This complication has to be dealt with by introducing new length and time scales into the problem, either by the method of strained coordinates [157, 161] or the method of multiple time scales [158, 162].

The appearance of A_{31} also implies that a perturbation of finite amplitude introduces a small correction in the cut-off wavenumber k_c below which perturbations grow. A further complication arises in the calculation of k_c, since the characteristic timescale near cut-off diverges, leading to additional secular terms. The cut-off wavenumber was first calculated correctly in [158], with the result

$$k_c h_0 = 1 + \tfrac{3}{4}\epsilon_0^2. \qquad (65)$$

Thus at finite amplitude shorter wavelengths lead to instability, which would be stable according to (49). The theoretical prediction (65) has been confirmed in [120], but in practice the correction is too small to be seen experimentally. These

subtleties aside, [159] reports some success estimating the size of main and satellite drops using third-order perturbation theory.

3.4. A quiescent external medium

The effect of an inertial surrounding medium on the instability development can be estimated along lines very similar to those of section 3.2. Let ρ_a be the density of an incompressible and inviscid medium surrounding the jet, initially at rest. For the instability to grow, surface tension has not only to move fluid particles of the central jet along its axis to empty the constricted sections and fill the troughs, but now also to push the outer fluid away from the growing crests and bring it to fill the gap in the thinning regions.

There are now two pressure fields, p for the central jet and p_a for the ambient fluid which are both harmonic as in (51), their difference at the jet interface $r = h$ being equal to the Laplace pressure jump (9): $[p - p_a]_{r=h} = \Delta p$. In the inviscid limit ($\nu = \nu_a = 0$), the perturbed pressure fields are

$$\delta p = \delta \bar{p} \cos(kz) I_0(kr) \qquad (66)$$

$$\delta p_a = \delta \bar{p}_a \cos(kz) K_0(kr), \qquad (67)$$

with I_0 and K_0 being modified Bessel functions, non-singular in $r = 0$ and decaying at large r, respectively. Continuity of the displacements at the interface in $r = h$ leads to the dispersion relation

$$\left[1 + \frac{\rho_a}{\rho} \frac{K_0(kh_0) I_1(kh_0)}{K_1(kh_0) I_0(kh_0)}\right] \omega^2$$
$$= -\frac{\gamma}{\rho h_0^3} (kh_0) \left[1 - (kh_0)^2\right] \frac{I_1(kh_0)}{I_0(kh_0)}. \qquad (68)$$

As shown in figure 20, the presence of an external medium slows down the instability and shifts the most amplified wavenumber towards a somewhat smaller k compared with the jet without an external medium. However, the cut-off wavenumber at $kh_0 = 1$ is not altered by an outer fluid, whose presence only shows up in the kinematics of the process. The original dispersion equation (57) is recovered when $\rho_a/\rho \to 0$, and the case of a *hollow jet*, obtained for $\rho_a/\rho \to \infty$ is characterized by

$$\omega^2 = -\frac{\gamma}{\rho_a h_0^3} (kh_0) \left[1 - (kh_0)^2\right] \frac{K_1(kh_0)}{K_0(kh_0)}, \qquad (69)$$

a result also known from Rayleigh [163]. The breakup of a hollow circular soap film is a beautiful illustration of the case $\rho = \rho_a$ (figure 21), a limit also relevant to the formation of spherical shells [164], and microfluidic encapsulation [165].

3.4.1. Long-wave description and ansatz.
The above dispersion relations can, once more, be approached by a long-wave approximation leading to transparent and tractable results. The idea is to couple the response of the jet and of the ambient medium, each being described by a one-dimensional
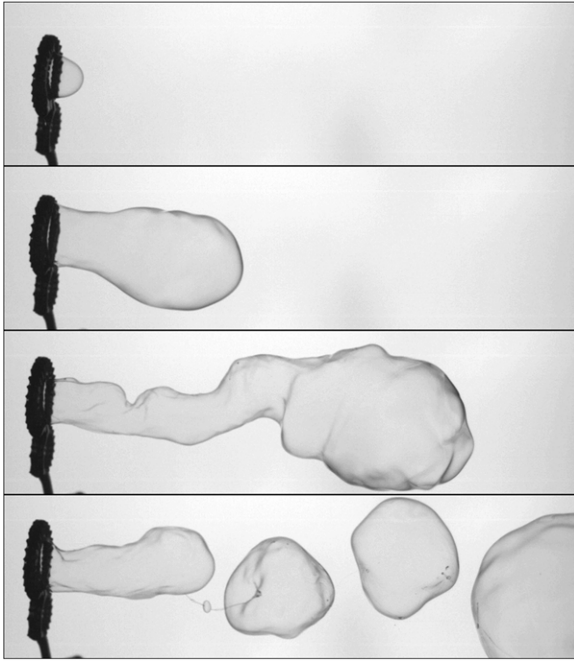
Figure 21. Blowing on a soap film inflates it in the form of a hollow tube which destabilizes into a train of soap bubbles. The wavelength is consistently given by the tube radius.

dynamics along z and along r, respectively. For the jet, one has to add the contribution from the outer pressure to (60):

$$\frac{\partial v_r}{\partial t} = -\frac{1}{\rho}\frac{\partial p}{\partial z}, \quad \text{with } p = p_a(r = h) + \gamma\left(\frac{1}{h} - h''\right). \tag{70}$$

The outer fluid is expanding and contracting radially in response to the interface deformation:

$$\frac{\partial v_r}{\partial t} = -\frac{1}{\rho_a}\frac{\partial p_a}{\partial r}, \tag{71}$$

$$\frac{1}{r}\frac{\partial(r v_r)}{\partial r} = 0. \tag{72}$$

From (72), using $u(r = h) = \dot{h}$, one finds

$$v_r = \frac{h\dot{h}}{r} \tag{73}$$

which, inserted into (71), gives

$$\frac{h\ddot{h}}{r} = -\frac{1}{\rho_a}\frac{\partial p_a}{\partial r}, \tag{74}$$

only keeping terms linear in the perturbation.

This axisymmetric description is valid for z distances along the jet where the radial velocity can be considered as constant with respect to z, that is for distances short compared with $1/k$ when the interface is distorted by a wavenumber k. The harmonicity of the pressure field also guarantees that axial and radial length scales are comparable, i.e. the pressure is essentially constant (taken equal to 0) at $r_\infty = h + 1/k$. Integration of (74) and using (70) gives

$$p = \rho_a h\ddot{h}\ln\left(1 + \frac{1}{kh}\right) + \gamma\left(\frac{1}{h} - h''\right) \tag{75}$$

and thus the dispersion relation

$$\left[1 + \frac{1}{2}\frac{\rho_a}{\rho}\ln\left(1 + \frac{1}{kh_0}\right)(kh_0)^2\right]\omega^2$$
$$= -\frac{1}{2}\frac{\gamma}{\rho h_0^3}\left[(kh_0)^2 - (kh_0)^4\right]. \tag{76}$$

The dispersion relation for the fluid jet (62) is recovered for $\rho_a/\rho \to 0$, and that of the hollow jet ($\rho_a/\rho \to \infty$) reads, within the same approximation

$$\omega^2 = -\frac{\gamma}{\rho_a h_0^3}\frac{1 - (kh_0)^2}{\ln\left(1 + \frac{1}{kh_0}\right)}. \tag{77}$$

Note the very slow *logarithmic* fall-off of the amplification rate around $k = 0$, suggesting the existence of nearly uniformly collapsing modes of a hollow cavity, cf section 4.4.2. Note finally, as seen in figure 20, that the maximal growth rate for a hollow jet in a fluid is more than five times larger than that of a jet of the same fluid without exterior fluid.

3.5. Viscous slowing

Viscous stresses affect the dynamics of jet instabilities, and their dynamics only. Indeed, the influence of viscosity η shows up solely in the presence of motion since they are proportional to *rates* of deformation, as seen in (16). Viscosity therefore does not affect the marginal stability conditions $\omega(k) = 0$, which do not involve motion.

In addition to the jet radius h_0, a new length scale comes into play, namely the 'penetration depth'

$$\delta = \sqrt{\frac{\nu}{\omega}}, \tag{78}$$

set by the Ohnesorge number (6). This length is analogous to the persistency length of vorticity $\omega = \nabla \times \boldsymbol{u}$ in a viscous fluid sheared at a rate ω. The dispersion relation for a viscous jet thus involves the additional dimensionless group $k\delta$, and (57) turns into the general form

$$\omega^2 = \frac{\gamma}{\rho h_0^3}f(kh_0, k\delta). \tag{79}$$

The first calculation of f is often attributed to Chandrasekhar [145], but is in fact contained (in a more general form including azimuthal perturbation) in Rayleigh's paper of 1892 [18]. The exponential growth of disturbances on jets of different viscosities was measured in [41, 166]. The resulting growth rates agree well with the theoretical dispersion relation over the entire range of unstable wavenumbers.

Since δ depends on ω, the expression (79) is only implicit, and thus not very useful unless solved numerically. More tractable expressions are found in the limit of very large viscosity ($Oh \gg 1$), using the Stokes equations as done by Rayleigh [18] without an external fluid:

$$-i\omega = \frac{\gamma}{2h_0\eta}\frac{1 - (kh_0)^2}{1 + (kh_0)^2[1 - (I_0(kh_0)/I_1(kh_0))^2]}. \tag{80}$$

Tomotika [167] generalized (80) to arbitrary viscosity ratios $\lambda = \eta/\eta_a$. In the limit of $\lambda = 0$ (hollow jet) the result is

$$-i\omega = \frac{\gamma}{2h_0\eta_a} \frac{1 - (kh_0)^2}{1 + (kh_0)^2[1 - (K_0(kh_0)/K_1(kh_0))^2]}. \quad (81)$$

Stone and Brenner [168] gave an elegant and direct derivation for the case $\lambda = 1$ and find

$$-i\omega = \frac{\gamma}{\eta h_0}\Bigg(I_1(kh_0)K_1(kh_0) + \frac{kh_0}{2}[I_1(kh_0)K_0(kh_0)$$
$$-I_0(kh_0)K_1(kh_0)]\Bigg). \quad (82)$$

Note that these dispersion equations involve ω and not ω^2, since in the inertia-less limit accelerations $\partial_t v$ drop out of the description. Modes are linearly damped or amplified, but the jet does not sustain waves in this limit.

Finally, [169, 170] considered the case of an array of parallel viscous thread inside a matrix of viscous fluid (the number of threads varying between 2 and infinity). The most unstable modes are either in-phase or out-of-phase between two adjacent threads, depending on the viscosity ratio and the distance between the threads. In the case of many threads, complicated combinations between in-phase and out-of-phase situations are possible.

3.5.1. Long-wave description and ansatz. The linearized version of (30) around $v = 0$ and $h = h_0$ is

$$\frac{\partial v}{\partial t} = -\frac{1}{\rho}\frac{\partial p}{\partial z} + 3\nu\frac{\partial^2 v}{\partial z^2}, \quad \text{with } p = \gamma\left(\frac{1}{h} - h''\right). \quad (83)$$

The ansatz (61) yields a dispersion relation analogous to (62), which accounts for viscosity:

$$\omega^2 = -\frac{1}{2}\frac{\gamma}{\rho h_0^3}[(kh_0)^2 - (kh_0)^4] + (-i\omega)\frac{3\nu}{h_0^2}(kh_0)^2. \quad (84)$$

As expected, the unstable range of k is unaffected by viscosity, and (62) is recovered for $\nu = 0$. In the opposite limit $Oh \to \infty$, one has (see also [145])

$$-i\omega = \frac{1}{6\tau_v}[1 - (kh_0)^2] \quad \text{with } \tau_v = \frac{\eta h_0}{\gamma}. \quad (85)$$

The ratio of the viscous timescale τ_v to its inertial counterpart $\tau = \sqrt{\rho h_0^3/\gamma}$ is precisely the Ohnesorge number (6), illustrating the *slowing down* of the instability by viscosity when Oh is large.

The strongly viscous limit (85) correctly predicts that the instability selects longer wavelengths at larger Oh, but its form is somewhat misleading since it predicts that the most amplified wavenumber is $k = 0$. The correct form, obtained by solving (84) is

$$(-i\omega)\tau = \sqrt{\frac{1}{2}(x^2 - x^4) + \frac{9}{4}Oh^2x^4} - \frac{3}{2}Ohx^2$$
$$\text{with } x = kh_0. \quad (86)$$

Translational invariance is no longer broken ($\omega(k = 0) = 0$), and the most amplified wavenumber is

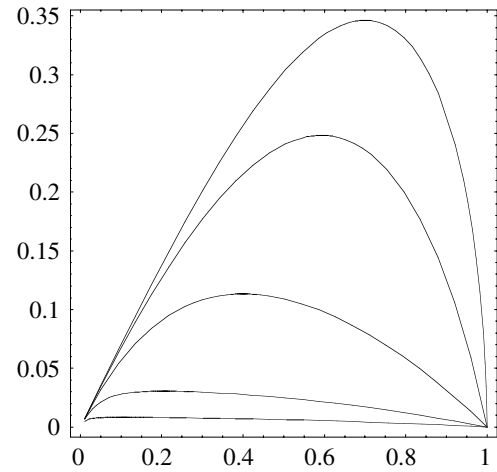$$k_m h_0 = \frac{1}{\sqrt{2 + 3\sqrt{2}Oh}}, \quad (87)$$

Figure 22. Dispersion curve $-i\omega(k)\tau$ of equation (86) for increasing Ohnesorge number $Oh^{-1} = \tau_v/\tau = 100, 5, 1, 0.2, 0.05$.
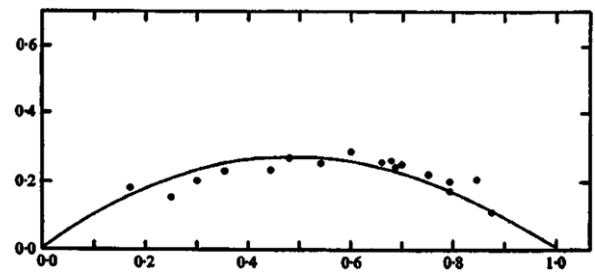

Figure 23. Dimensionless growth rate $-i\omega(k)\tau_v$ of sinusoidal perturbations on a viscous cylinder for $Oh = 0.58$ as a function of the dimensionless wave number kh_0. The solid line represents Rayleigh's and Chandrasekhar's theory [18, 145, 166]. Reprinted with permission from Cambridge University Press.

going to zero as $1/\sqrt{Oh}$ with the associated growth rate

$$-i\omega(k_m)\tau = \frac{1}{2\sqrt{2} + 6Oh}. \quad (88)$$

Figure 22 shows the deformation of the dispersion curve as the Ohnesorge number is varied, and figure 23 presents a comparison with experiments.

The case of an inviscid jet immersed in another viscous fluid can be treated along the same lines as in section 3.4, still assuming that the inner and outer media are connected to each other through the pressure field only (if the inner jet is viscous, shear is generated, a case considered below). To compute the pressure p in the jet, a contribution from the viscous stress has to be added to (70):

$$p = p_a(r = h) + \gamma\left(\frac{1}{h} - h''\right) - 2\eta_a\frac{\partial v_r}{\partial r}. \quad (89)$$

For a purely radial and incompressible velocity field $v_r(r, t)$ the viscous term cancels exactly (which is also true in the spherical case), so the pressure is given by (75), and the dispersion relation is similar to the one found before:

$$\left[1 + \frac{1}{2}\frac{\rho_a}{\rho}\ln\left(1 + \frac{1}{kh_0}\right)(kh_0)^2\right]\omega^2$$
$$= -\frac{1}{2}\frac{\gamma}{\rho h_0^3}[(kh_0)^2 - (kh_0)^4] + (-i\omega)\frac{\eta_a}{\rho h_0^2}(kh_0)^2, \quad (90)$$

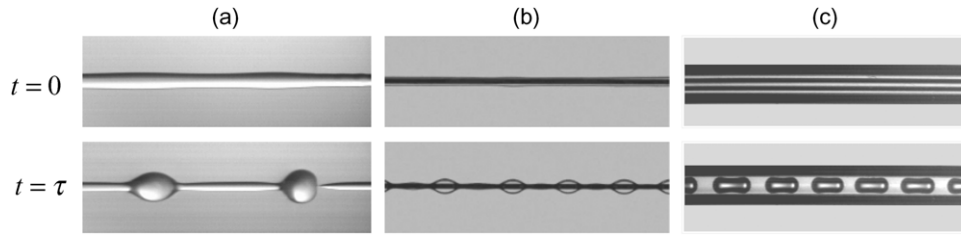incorporating all the limits and behaviours discussed above.

Figure 24. Capillary instability of cylindrical interfaces: (*a*) liquid jet, (*b*) liquid film on a fibre, (*c*) liquid film in a tube (adapted from [171]). The instability time τ equals $\sqrt{\rho h_0^3/\gamma}$ for a solid inviscid jet of radius h_0, and $\eta h_0^4/(\gamma e_0^3)$ for a thin film of thickness e_0 deposited on a fibre of radius h_0.

Figure 25. Spider web featuring condensed morning dew droplets.

3.5.2. Viscous films covering cylindrical solid bodies.
The instability of a viscous liquid film coating a fibre is a particularly straightforward application of the long-wave description, illustrated by droplets of dew forming on spider webs on humid mornings (see figure 25). If the film coating the fibre is very thin, the longitudinal motion of the liquid driven by the Laplace pressure is likely to be affected by viscosity because of the no-slip condition at the fibre surface. For a fibre of radius h_0 and a film of thickness e, the corresponding *lubrication approximation* in the film becomes [94, 172]

$$\eta \frac{\partial^2 v}{\partial r^2} = \frac{\partial p}{\partial z}, \tag{91}$$

for $h_0 < r < h_0 + e$ and assuming $e/h_0 \ll 1$. Inertia has been neglected in (91), as appropriate for a very thin film. The pressure is the usual Laplace pressure, and the motion at the film surface is stress free ($[\partial v/\partial r]_{r=h_0+e} = 0$). Taking $e(z,t) = e_0 + \epsilon_0 e^{-i\omega t} \cos(kz)$, the mass balance reads

$$-2\pi h_0 \frac{\partial e(z,t)}{\partial t} = \frac{\partial q(z,t)}{\partial z}, \tag{92}$$

where $q(z,t) = 2\pi \int_{h_0}^{h_0+e} r v(z,r)\, dr$ is the net flow rate in the film. Now elementary quadratures lead to

$$-i\omega = \frac{\gamma}{\eta} \frac{e_0^3}{3h_0^4} (kh_0)^2 [1 - (kh_0)^2], \tag{93}$$

hence providing the dispersion relation. The most amplified wavenumber is related to the fibre radius through $k_m h_0 = 1/\sqrt{2}$. The growth of the instability is all the more slow when the film is thin, and fast when the fibre radius is

small. The same physics holds for a thin film coating a hollow solid tube [171], the rigorous treatment [173] featuring all the necessary Bessel functions, and accounting for inertia as well. The three different cases described above are summarized in figure 24.

3.6. Absolute, convective and temporal instability

So far we have been analysing situations where a perturbation is imprinted on the system in a spatially uniform way, as described for example by (61); our *temporal* analysis applies to perturbations growing uniformly in space. In the case of jets, a more common situation is one in which the perturbation is applied at the nozzle only, and perturbations grow in a frame of reference convected with the jet speed v_0, see figure 13. One thus says that the jet is 'convectively unstable'. In the case of dripping, i.e. in a situation where gravity is important, a periodic train of disturbances is generated at the nozzle, which propagates away from it. As v_0 is increased, a transition to 'jetting' occurs, in which perturbations only grow convectively, cf figure 26. The dripping regime is an example of an 'absolute' instability.

3.6.1. Spatial growth. The first problem is to calculate the growth rate of perturbations along the jet, which amounts to passing to a frame of reference $z = v_0 t$ that is convected with the jet [174]. In the temporal problem, we considered perturbations of the form

$$h(z,t) = h_0 + \epsilon_0 e^{i(kz - \omega t)}, \tag{94}$$

which is now to be interpreted in the convected frame of reference. If one transforms back to a stationary frame of reference, replacing z by $z + v_0 t$, one recovers (94) if one replaces ω by $\omega - k v_0$. By making the corresponding replacement in the above dispersion relations and keeping ω real and equal to the excitation frequency, one is looking for solutions that do not grow at a fixed point in space. Instead, solutions are now expected to correspond to complex k-values. In the context of shear flows, this idea is also known as the Gaster transformation [175].

This analysis was performed in [174] for the dispersion relation (57) of an inviscid jet and in [177] for the general dispersion relation (79). By solving the resulting equation numerically for a given $\omega = 2\pi f$, where f is the excitation frequency at the nozzle (cf (3)), one finds Im(k_{conv}). This gives the rate at which perturbations grow in space, which depend on
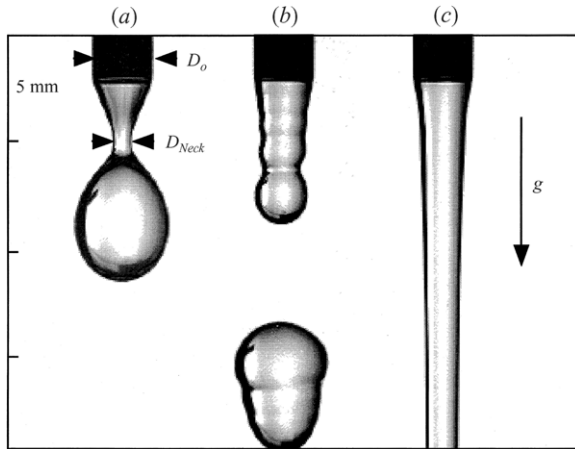
Figure 26. The transition from dripping to jetting for water issuing from a tube of radius $h_0 = 1.08$ mm. (*a*) $We = 0.031$ (dripping), (*b*) $We = 0.86$ (chaotic dripping), (*c*) $We = 1.15$ (jetting). (Adapted from [176], with permission from Cambridge University Press.)

the jet speed, and thus on We. The temporal stability theory, on the other hand, is employed by computing the growth rate $\mathrm{Im}(\omega_{\mathrm{temp}})$ for a given $k = 2\pi v_0/f$. The results agree only for large jet speeds, i.e. $\mathrm{Im}(\omega_{\mathrm{temp}}) = v_0\mathrm{Im}(k_{\mathrm{conv}}) + O(We^{-1})$ [174]. This is to be expected, since for large We the spatial structure of disturbances growing along the jet is almost uniform, and thus well described by a temporal theory. Indeed, for most experimental values of We the corrections due to a finite jet speed are small, so it is justified to use the much simpler temporal theory.

3.6.2. Bubbling and dripping. The second problem is to investigate the existence of absolutely unstable states, for which perturbations grow at a fixed point in space. For a substantial continuous portion of the jet to form near the nozzle, the transit time λ/v_0 over a distance given by an unstable wavelength λ (such that $2\pi h_0/\lambda < 1$) should be shorter than the breakup time τ (cf (2)). Since λ itself is proportional to the jet radius h_0, this condition gives a critical Weber number We_{c} (below which the jet is absolutely unstable) which is of order 1. A more formal calculation can also be performed by analysing the spatial dispersion relations as described above [177]. Namely, for a localized perturbation to be stationary, the group velocity must vanish, and $\mathrm{Im}(\omega)$ must verify the condition for temporal growth [178]:

$$\frac{\partial\omega}{\partial k} = 0 \qquad \text{and} \qquad \mathrm{Im}(\omega) > 0. \qquad (95)$$

The calculation shows that absolute instability occurs for $We < 3.15$ [180, 181], a value that decreases further if viscosity is added [177], in agreement with the above heuristic argument. This result is thus of little relevance in practice, since gravity will be important relative to inertial effects, and the absolutely unstable state will rather take the form of 'dripping', see below. A more interesting case is that of a two-fluid system [179, 182–188], for example a drop of small viscosity liquid being dragged out by a more viscous liquid, as shown in figure 27(*a*). Another example is selective
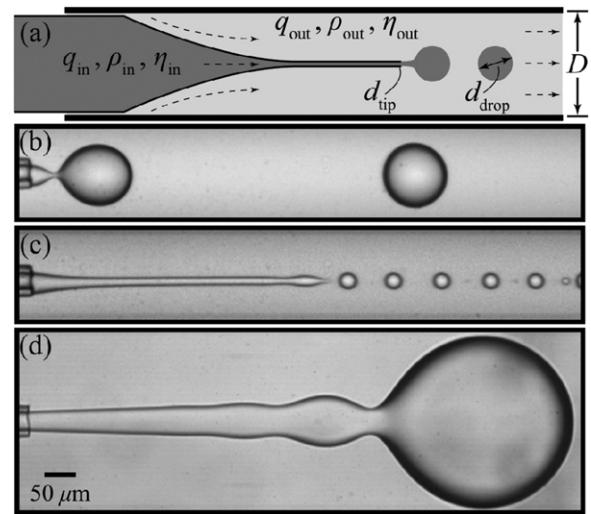

Figure 27. A coflowing liquid stream, driven by the outer fluid [179]. (*a*) device geometry, (*b*) dripping regime, (*c*) jetting, kepping the inner flow rate q_{in} constant, but increasing q_{out}; $\eta_{\mathrm{in}}/\eta_{\mathrm{out}} = 0.1$. (*d*) widening jet, obtained by increasing q_{in}. Reprinted with permission from [179]. Copyright 2007 by the American Physical Society.

withdrawal [189–192], discussed in section 4.7.3. The inner fluid is supplied slowly through a capillary. At low flow rates, bubbling occurs (cf figure 27(*b*)), corresponding to an absolute instability. As the flow rate increases, there is a transition from bubbling to jetting (cf figure 27(*c*)), the jet being convectively unstable. At higher flow rates of the *inner* fluid, another kind of dripping is observed (cf figure 27(*d*)).

In a recent series of papers [185–187], the transition shown in figure 27 was investigated using (95), on the basis of the dispersion relations for two-fluid systems derived in the previous sections. For a finite viscosity and density of the inner fluid (or gas), a transition occurs at a finite velocity of the outer fluid. The limit of a 'hollow' jet inside a liquid is however quite singular [187]: in the limit of vanishing viscosity and density, the system is always absolutely unstable.

If gravity is taken into account, the transition to jetting takes place at a Weber number that depends on two parameters: $We_{\mathrm{c}}(Bo, Oh)$. As illustrated in figure 26, the calculation is complicated by the fact that there is more than a single absolutely unstable state, for example a chaotic regime that lies between periodic dripping and jetting [122]. Recently, yet another 'global' mode has been discovered, which consists of elongated bulges growing at the nozzle, but which do not lead to breakup as the bulges are convected downstream [193].

Clanet and Lasheras [176] use a phenomenological description to calculate We_{c} in the limit $Oh \to 0$. For the long-wavelength case, in which azimuthal curvature is negligible, it is cleverly observed in [193] that the three-dimensional parameter space (We, Oh, Bo) is described by just two dimensionless parameters

$$u_0 = \left(\frac{1}{3\nu g}\right)^{1/3} v_0 \qquad \text{and} \qquad a_0 = \left(\frac{9\nu^2 g^2 \rho^3}{\gamma^3}\right)^{2/3} h_0^2. \qquad (96)$$
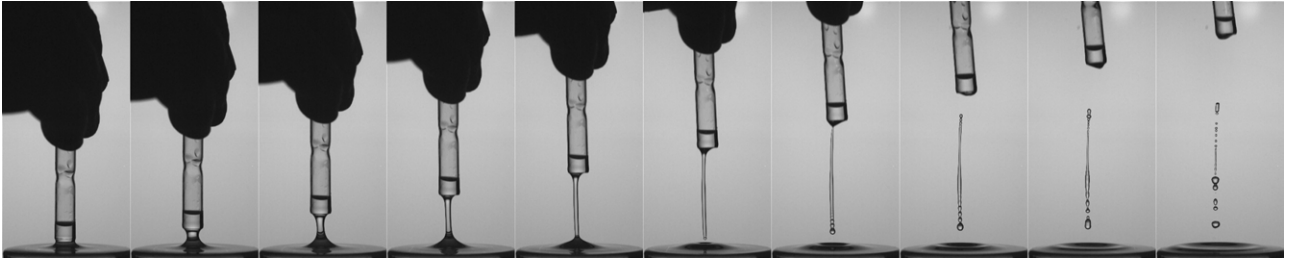
Figure 28. A pipette dipping into still water is rapidly removed vertically, producing a liquid ligament from the elongation of the bridge between the liquid and the pipette end. When the motion is fast enough, the ligament stretches while remaining smooth. As soon as the stretching stops, because the ligament is no longer connected to the liquid bath, it breaks into drops.

A numerical search for a global instability yields the empirical formula $a_0 = 1/(40 u_0^{5/2})$ for the boundary between stable and unstable regions. In terms of the usual parameters, this yields

$$We_c = 0.034(BoOh)^{-6/15}, \qquad (97)$$

a result which agrees well with experiments in [176, 193].

3.7. Longitudinal stretch

Stretching alters the development of capillary instabilities dramatically. For the rarer case of compression, see section 3.7.4. By stretching we mean an extensional motion in, for instance, the longitudinal direction of a jet. The phenomenon was recognized early by Taylor, who was able to produce appreciably elongated drops by immersing them into an extensional flow at the stagnation point of a 'four roll mill' [194]. Instability, however, sets in as soon as the stretch is turned off, demonstrating the interplay between substrate deformation and the development of instability (see [195] for a review). Tomotika (1936) [196] first demonstrated the damping role of stretching for a viscous elongating cylinder. For example, it is a common experience that a thread of honey is elongated by gravity to a very small radius before breaking (if it ever does, a question to which we shall come back below). Even inviscid fluids can be elongated to long ligaments provided the stretch is strong enough, as shown in figure 28.

3.7.1. Core thinning and wavenumber stretching.
We first consider a rate of stretch σ which is constant in time and uniform along the jet. The distance between two material points $\delta z(t)$ in the z direction thus increases exponentially as $\delta z(t) = \delta z(0) e^{\sigma t}$ since their axial velocity $v_0(z)$ differs by an amount $\sigma \delta z$. Thus by mass conservation, the radius of the jet $h_0(t)$ decays in time. Therefore, the basic state describing the stretched jet about an arbitrary origin in $z = 0$ is

$$v_0(z) = \sigma z, \qquad (98)$$

$$h_0(t) = h_0(0) e^{-\sigma t/2}. \qquad (99)$$

The stability of this solution is investigated by considering the (inviscid) dynamics of small velocity and radius perturbations v and r, which reads

$$\partial_t r + \frac{\sigma}{2} r + \frac{h_0}{2} \partial_z v = 0, \qquad (100)$$

$$\partial_t v + \sigma v = -\frac{\gamma}{\rho} \left(-\frac{1}{h_0^2} \partial_z r - \partial_z^3 r \right). \qquad (101)$$

Combining (100) and (101) leads to an evolution equation for the perturbation of the radius $r(z, t)$ along the jet

$$\partial_t^2 r + 2\sigma \partial_t r + \frac{3}{4}\sigma^2 r - \frac{\gamma}{2\rho h_0^3} \left(-h_0^2 \partial_z^2 r - h_0^4 \partial_z^4 r \right) = 0, \quad (102)$$

thereby generalizing the result of section 3.2.2 to the stretched case. Equation (102) is the characteristic equation of an over-damped oscillator because of the stretching term, with a source term depending on the shape of the radius undulations via its spatial derivatives, through the Laplace pressure. Since the radius of the basic state is itself time dependent, we rescale time by $\sqrt{2\rho h_0(0)^3/\gamma}$, wavenumbers by $x = k h_0(0)$, and look for solutions of the form $r(z, t) = \epsilon(t) e^{ikz}$ to get

$$\partial_t^2 \epsilon + 2\sigma \partial_t \epsilon + \frac{3}{4}\sigma^2 \epsilon - (x^2 - x^4 e^{-3\sigma t}) e^{-\frac{3}{2}\sigma t} \epsilon = 0, \qquad (103)$$

which is a modified form of (62), with stretch. The exponential factors proportional to $e^{\sigma t}$ in (103) signal a fundamental ingredient, first noticed by Tomotika (1936) in the same context [196], and later used in other areas with the same meaning (see, e.g. Saffman (1974) [197], Zeldovich *et al* (1980) [198]): if fluid elements are stretched by the base flow, so are the radius modulations. Equation (103) incorporates this effect through the stretching of the wavenumbers where an initial wavenumber k becomes

$$k \to k e^{-\sigma t} \qquad (104)$$

in the course of time.

It is interesting to follow the fate of one mode's amplitude in the course of time, as illustrated by figure 29: for a mode lying in the initially unstable range ($x = kh_0 < 1$) the early time ($\sigma t \ll 1$) unstable branch of ϵ is proportional to $e^{(-\sigma + \sqrt{\sigma^2/4 + x^2 - x^4})t}$ and actually leads to an amplification provided the stretching rate is not too strong, that is, for the initially most amplified mode $k_m = 1/\sqrt{2}$ when $\sigma < 1/\sqrt{3}$. The long-time ($\gamma t \gg 1$) form of $\epsilon(t)/\epsilon(0)$ is always dominated by the stretching, decaying as $e^{-\sigma t/2}$, thereby following the stretching induced rate of approach of the marginal stability condition at $k = 0$, which itself follows the thinning rate of the base jet radius $h_0 \sim e^{-\sigma t/2}$.

To add viscosity, as well as other effects like a time-dependent stretching rate to this analysis, we make the simplifying assumption that the perturbation grows on a quasi-stationary base solution, so previously calculated growth rates can be taken from earlier sections. The effect of stretching is in the increasing wavelength of a given perturbation, and a
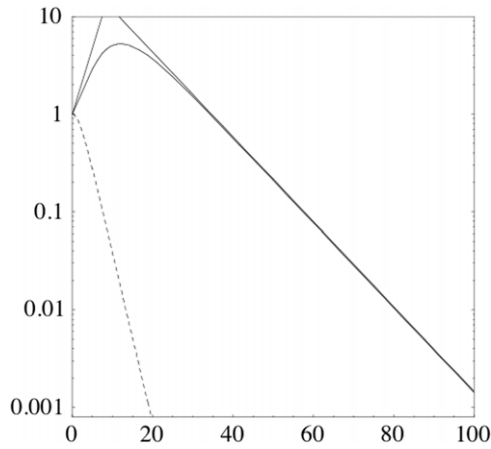
Figure 29. Temporal evolution of the amplitude $\epsilon(t)/\epsilon(0)$ according to equation (103) for $\sigma = 0.2$ (weak stretching, continuous line) and $\sigma = 0.8$ (strong stretching, dashed line), with $kh_0 = 1/\sqrt{2}$. The straight lines are the short time growth, and long-time relaxation limit behaviours for $\sigma = 0.2$. Time t is in units of σ^{-1}.

contraction of the perturbation amplitude resulting from mass conservation. Namely, the radius modulation $r(z, t)$ on the base state $h_0(t)$ follows from

$$r(t + \delta t) = [h_0 + r(t)]e^{-\sigma \delta t/2} - h_0 e^{-\sigma \delta t/2} + [-i\omega(k)]r(t)\delta t, \tag{105}$$

where $-i\omega(k)$ is the growth rate as calculated from any of the dispersion relations (e.g. (85) or (86)) described in the previous sections. Of course, k has to be calculated according to (104) to account for wavenumber stretching. By taking the limit $\delta t \to 0$, (105) turns into

$$\frac{d \ln(r)}{dt} = -\frac{1}{2}\sigma + [-i\omega(k)], \tag{106}$$

illustrating the competing role of stretching and capillary destabilization. Since $d \ln(h_0)/dt = -\sigma/2$, the *relative* growth takes the even simpler form [196]

$$\frac{d}{dt} \ln \left(\frac{r}{h_0} \right) = -i\omega(k). \tag{107}$$

The above analysis is readily generalized to a time-dependent stretching rate $\sigma(t)$, which occurs when longitudinal distances along the jet only grow as a power law of time. This is encountered in some impact and entrainment problems (see section 5.1), or when the jet accelerates by free fall. Equation (99) for the stretching jet then has to be replaced by

$$h_0(t) = h_0(0) \exp \left(-\frac{1}{2} \int_0^t \sigma(t') \, dt' \right). \tag{108}$$

3.7.2. Integrated gain. To answer the question which of the initial Fourier modes k_0 of the jet radius will be the most amplified after a given time t, we insert the current rate $-i\omega(k_0, t)$ into (107). The *net gain* of the amplitude growth $s(k_0, t)$ for wavenumber k_0 is thus

$$s(k_0, t) = \ln \left(\frac{r(k_0, t)}{h_0(t)} \right) \bigg|_0^t = \int_0^t \{-i\omega(k_0, t')\} \, dt'. \tag{109}$$
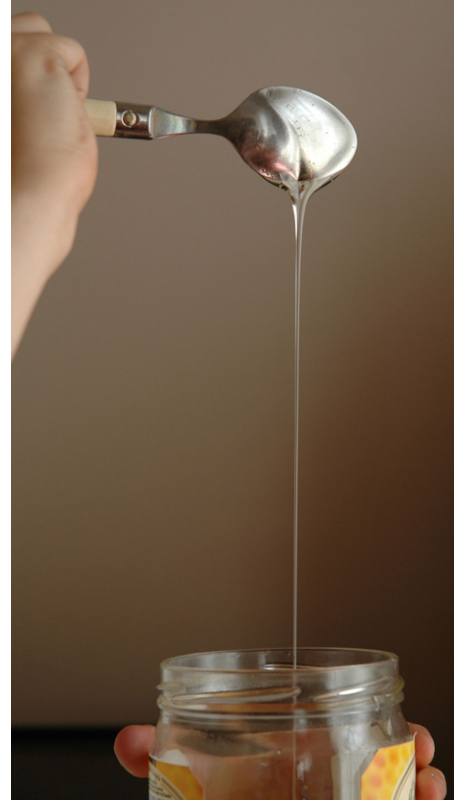

Figure 30. A viscous thread (honey) is falling downwards by its own weight. Will the thread remain intact? (Courtesy of Céleste Villermaux.)

The most amplified wavenumber $k_{opt}(t)$ at time t is thus the one for which

$$\frac{\partial s(k_0, t)}{\partial k_0} = 0, \tag{110}$$

giving maximal gain $s(k_{opt}(t))$. The approach implicitly assumes that the initial disturbance spectrum is broad, and flat in k_0, and that the only relevant effect is that of transient amplification, regardless of initial conditions. This strategy was adopted in [199] for an inviscid jet with $v_0 = Kz/(1+Kt)$ and $h_0(t) = h_0(0)/\sqrt{1+Kt}$, corresponding to a *linear* axial velocity field. Using the full inviscid dispersion equation (57), [199] found an optimal wavenumber *increasing* in time, with an associated gain increasing algebraically: stretching damps growth. An alternative approach, where the initial roughness sets the future of the jet disturbances, and thus the drop size distribution, is given in section 5.

3.7.3. Honey, why are you so thin? The aim is to understand a simple and practical problem: why is it that a (very) viscous thread falling under its own weight (cf figure 30) seems to thin forever as it falls, with no sign of destabilization? The case of gravitational stretching at small to moderate viscosities was considered in [200, 201], with reasonable agreement between experiment and numerical simulations. However, how viscous does the fluid need to be for a long thread to form? In particular, their surprising stability allows liquid threads to behave like a piece of rope: once it hits a solid surface, it buckles and performs a coiling motion [202, 203]. The resulting motion can

be remarkably complex and exhibits multiple coexisting states [204, 205]. If the substrate is moving, even more transitions between different states are possible [206].

Even at high viscosities, inertia will quickly be dominant as the fluid falls [193], so the thread is well described by Mariotte's free fall solution (1), thus defining a constant *elongation rate*

$$\sigma = \frac{g}{u_0}. \tag{111}$$

Using mass conservation, one finds for the shape of a steady stream of fluid (in units of the nozzle radius h_0):

$$h(z) = \left[\frac{z_0}{z + z_0}\right]^{1/4}, \qquad z_0 = \frac{v_0^2}{2h_0}. \tag{112}$$

An element of volume $\delta V = h_0(0)^2 \delta z(0) = h_0(t)^2 \delta z(t)$ elongates in the course of time and space, so that an initial disturbance wavelength behaves as $\lambda(z) = \lambda_0 / h^2(z)$.

Thus, using the long-wave end of the dispersion relation (62), one finds from (109)

$$s(\lambda_0, z) = \int_0^z \frac{-\mathrm{i}\omega(k_0, z')}{h^2} \, \mathrm{d}z' \propto \exp\left\{8\pi\sqrt{2}\frac{z_0}{\lambda_0}\left(\frac{z}{z_0}\right)^{1/8}\right\}, \tag{113}$$

in agreement with [207]. Thus although growth of perturbations is slowed as compared with the usual exponential behaviour, (113) evidently is not enough to explain observations, since it contains no viscosity dependence. In reality, the complete amplification history of a given mode k_0 of the thread has to be taken into account, including its early stages, where the dispersion curve still has significant dependence on the viscosity parameter Oh. Once this is accomplished, the total growth has to be *optimized* over all possible initial wavelengths λ_0 assuming a white-noise spectrum [208].

Let us only note that the ability to form very thin structures by means of stretch is encountered in some other natural processes: in particular, thin strands of volcanic glass drawn out from molten lava have long been called Pele's hair, named after Pele, the Hawaiian goddess of volcanoes (figure 31). A single strand, with a diameter of less than 0.5 mm, may be as long as 2 m. The strands are formed by the stretching or blowing-out of molten basaltic glass from lava (a highly viscous fluid), usually from lava fountains, lava cascades and vigorous lava flows. Pele's hair is often carried high into the air during fountaining, and wind can blow the glass threads several tens of kilometres from a vent. The phenomenon lacks a quantitative description [209].

3.7.4. Kinematic gathering. In addition to stretching, jets may also be subjected to axial compression. Let the exit velocity at a nozzle be modulated according to

$$v(z = 0, \tau) = v_0(1 + \epsilon \sin(\omega\tau)), \tag{114}$$

where ϵ is now a number of order unity (in contrast to the case where the goal is to excite a particular capillary mode to measure its growth rate, and where ϵ is small). For simplicity

Figure 31. Images of 'Pele's hair', named after Pele, the Hawaiian goddess of fire. These thin filaments of stretched basaltic glass form during times of high fire-fountaining, often in the presence of strong winds. (Top) The example shown here erupted from Kilauea on the Big Island of Hawaii. Courtesy of D W Peterson, USGS. (Bottom) A view showing how thin these hairs can become.

we neglect viscous or surface tension forcing as well as body forces, i.e.

$$\frac{\partial v}{\partial t} + v\frac{\partial v}{\partial z} = 0. \tag{115}$$

An element of volume $\pi/4 h_0^2 \ell_0$ with $\ell_0 = v(z = 0, \tau)\Delta t$ released at time τ will thus be kinematically stretched or compressed depending on the sign of $(\partial v/\partial t)_\tau$. Its length $\ell(t)$ is given by

$$\ell(t) = \ell_0 + (v(0, \tau) - v(0, \tau + \Delta t))[t - \tau]$$
$$= \left(v(0, \tau) - \left.\frac{\partial v}{\partial t}\right|_\tau [t - \tau]\right)\Delta t, \tag{116}$$

so that, by volume conservation, its radius evolves according to

$$\left(\frac{h_0}{h(t)}\right)^2 = 1 - \frac{1}{v}\left.\frac{\partial v}{\partial t}\right|_\tau [t - \tau]. \tag{117}$$

There are, depending on the phase of $v(0, \tau)$, two distinct behaviours:

- If $(\partial v/\partial t)_\tau < 0$, then, for $t \to \infty$,

$$\left(\frac{h_0}{h(t)}\right)^2 \sim -\frac{1}{v}\left.\frac{\partial v}{\partial t}\right|_\tau t \tag{118}$$

  and therefore the radius decays as $h(t) \sim t^{-1/2}$ while it is advected to the downstream position $z(t) = v(0, \tau)[t - \tau]$.
- If $(\partial v/\partial t)_\tau > 0$, then the jet radius blows up in finite time $t^\star$ such that

$$t^\star - \tau = \left.\frac{v}{\partial v/\partial t}\right|_\tau, \tag{119}$$
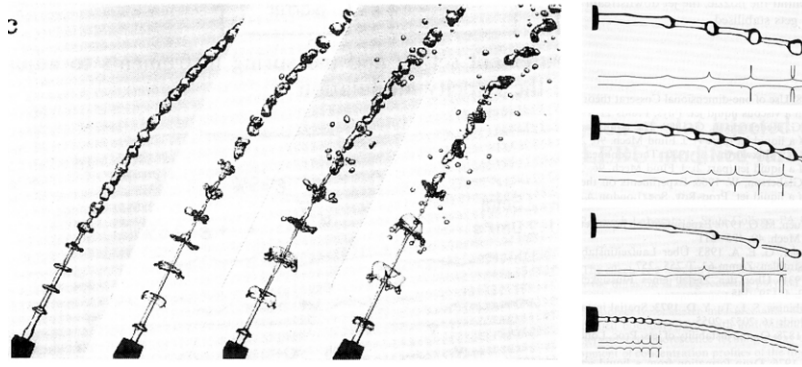
Figure 32. Kinematic gatherings (shocks) formed by a pulsatile axial velocity at the jet exit $v(z = 0, \tau) = v_0(1 + \epsilon \sin(\omega \tau))$. Pure kinematics anticipates that the jet's cross-section blows up in finite time, i.e. at a finite distance from the exit. Surface tension bounds the blow-up forming a finite extent radial sheet. (Adapted from [210].)

corresponding to a downstream position $z^\star = v(0, \tau)$ $[t^\star - \tau]$. Thus the spatial radius profile $h(z)$ is

$$\frac{h(z)}{h_0} = \frac{1}{\sqrt{1 - z/z^\star}}. \tag{120}$$

as seen in figure 32.

Experiments and analysis by Meier *et al* (1992) [210] (see figure 32) fit nicely and the singularity (120) leads to the formation of a liquid sheet. However, surface tension bounds the blow-up so that crowns are formed, strongly reminiscent of crowns formed by the impact of drops onto a thin liquid layer [211–213].

3.8. Shear at the interface

We now turn to the effect of what in practice is an important ingredient of jet instability, namely a velocity difference between the jet and its surroundings, producing shear at the jet interface. Indeed, the disintegration and dispersion of a liquid volume by a gas stream is a phenomenon which encompasses many natural and industrial processes. The entrainment of spume droplets by the wind over the ocean, the generation of pharmaceutical sprays or the atomization of liquid propellants in combustion engines are among the obvious examples [215, 216].

The interface separating two initially parallel streams having different velocities v_1 and v_2 is naturally unstable: this is the Kelvin–Helmholtz paradigm. The mode selection involves properties of the interface between the streams like its surface tension or the details of the velocity profiles. Both of these ingredients are important in practice, as demonstrated in this section.

A way to produce a shear between the jet and the surrounding air is to blow through an injector built around the jet nozzle. The method implies the formation of *boundary layers* at the wall of the conveying channels resulting in thickened velocity profiles at their merging location. In addition to the two boundary layer thicknesses δ_2 and δ_1 of each stream (see figure 33), another length scale is set by the ratio of surface tension to inertia

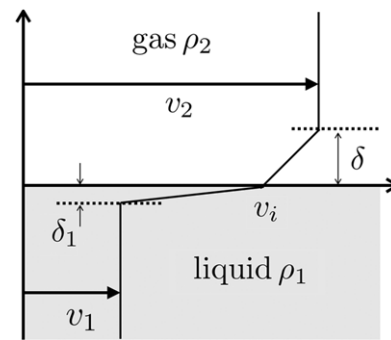$$\frac{\gamma}{\rho_2 (\Delta v)^2}. \tag{121}$$

Figure 33. Following Rayleigh (1880) [214], the piecewise linear velocity profile as a paradigm for inflectional instabilities.

Here $\Delta v = v_2 - v_1$ is the relative velocity and ρ_2 is the density of, say, the light stream.

3.8.1. Sharp discontinuity: the Kelvin–Helmholtz limit. Let us consider first a velocity discontinuity, corresponding to vanishingly small vorticity thickness ($\delta_1 = \delta_2 = 0$). The two potential flows of the jet and its surrounding have constant velocities v_1 and v_2, and densities ρ_1 and ρ_2, respectively, in a *planar geometry*. Taking the displacement of the interface proportional to $e^{ikx - i\omega t}$, the dispersion relation, in the absence of gravity is [145, 217–219]

$$-i\omega = -ik \frac{\rho_1 v_1 + \rho_2 v_2}{\rho_1 + \rho_2}$$
$$\pm \frac{k}{\rho_1 + \rho_2} \sqrt{\rho_1 \rho_2 (v_2 - v_1)^2 - (\rho_1 + \rho_2) \gamma k}, \tag{122}$$

where the real part of ω corresponds to the advection of a plane wave by the mean flow. Note that the effect of shear is always destabilizing. Assuming a spatially uniform perturbation (k real), the temporal growth rate Re$[-i\omega]$ is proportional to k for small wavenumbers, and surface tension is stabilizing at large k i.e. for

$$k > k_c = \frac{\rho_1 \rho_2}{\rho_1 + \rho_2} \frac{(v_2 - v_1)^2}{\gamma}. \tag{123}$$

For, say, a liquid–gas interface ($\rho_1 \gg \rho_2$), with a large velocity difference ($v_2 \gg v_1$), the most amplified mode and group

velocity are

$$k_m = \frac{2}{3} \frac{\rho_2 v_2^2}{\gamma} \qquad \text{and} \qquad \frac{\partial}{\partial k}(\text{Im}[-i\omega]) = v_1 + \frac{\rho_2}{\rho_1} v_2.$$

$$(124)$$

In the case of jets, the analysis has to be performed in a *cylindrical* geometry, including the destabilizing capillary term coming from the radial curvature. Setting $\rho \equiv \rho_1$, $\rho_a \equiv \rho_2$ and $v_2 = 0$, $v_1 \equiv v_0$, one has

$$(\omega - k v_0)^2 + \frac{\rho_a}{\rho} \omega^2 \frac{I_1(kh_0)K_0(kh_0)}{I_0(kh_0)K_1(kh_0)}$$

$$= -\frac{\gamma}{\rho h_0^3}(kh_0)[1 - (kh_0)^2]\frac{I_1(kh_0)}{I_0(kh_0)}, \qquad (125)$$

where viscous corrections can also be incorporated [220].

The long-wavelength version of (125) follows easily along the lines of section 3.4, but accounting for the additional drift term $v_0 \partial_z v$:

$$\frac{\partial v}{\partial t} + v_0 \frac{\partial v}{\partial z} = -\frac{1}{\rho} \frac{\partial p}{\partial z}. \qquad (126)$$

This leads to a dispersion relation similar to (76), but with a Doppler shift which makes the velocity difference v_0 always destabilizing for non-zero ρ_a:

$$(\omega - k v_0)^2 + \frac{1}{2} \frac{\rho_a}{\rho} \ln\left(1 + \frac{1}{kh_0}\right)(kh_0)^2 \omega^2$$

$$= -\frac{1}{2} \frac{\gamma}{\rho h_0^3}[(kh_0)^2 - (kh_0)^4]. \qquad (127)$$

The dispersion relation (127) describes plane waves $\omega = k v_0$ advected by the flow. In the absence of an external medium, they are subject to capillary destabilization only, but are now unstable for

$$k < \frac{\rho_a v_0 2}{\gamma}. \qquad (128)$$

Thus in the limit $kh_0 \gg 1$, so that $\ln(1 + 1/kh_0) \approx 1/kh_0$, perturbations are unstable for

$$We = \frac{\rho_a v_0^2 h_0}{\gamma} \gg 1. \qquad (129)$$

This means that the capillary instability is overpowered in the high Weber number limit. In the opposite limit of $We_a \ll 1$, the usual cut-off at $kh_0 = 1$ holds, and the external shear is only a small correction.

However, the above results apply only in the rare situations where a sharp velocity discontinuity is a good description. It may be relevant to the initial destabilization of high-speed jets issuing into a quiescent environment from a nozzle at very high Reynolds number (see figures 34 and 35 as well as [221]). It is also found to be a good model for the *flapping instability* of liquid *sheets* formed by the impact of a jet on a solid surface, or from a fan spray nozzle [222–226], for which the boundary layers have no time to form. However, for a large class of other systems, the boundary layer thickness has to be taken into account.
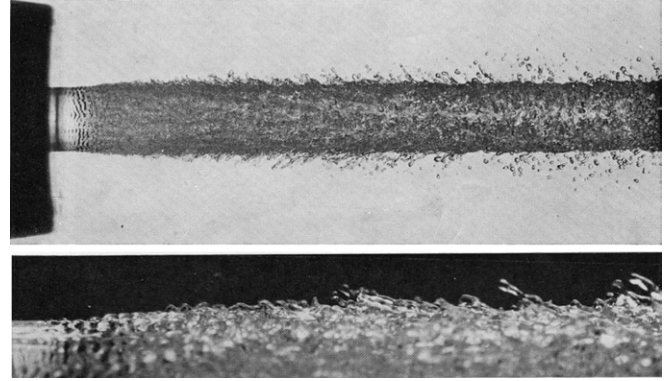

Figure 34. A fast water jet issuing into air. Photographs by Hoyt and Taylor [221]. Reprinted with permission from Cambridge University Press.
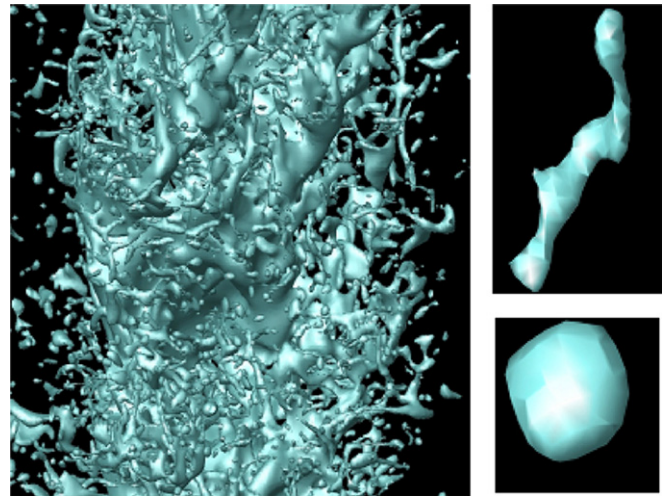

Figure 35. The intricate forest of liquid ligaments and drops in a flow similar to that of figure 34 revealed by numerical simulations [78]. Courtesy of A Berlemont.

3.8.2. Smooth crossover: the Rayleigh limit. Rayleigh (1880) [214,219] first showed that a uniform layer of vorticity of finite thickness δ selects a mode of maximum growth $k_m \sim 1/\delta$. He also showed that the instability of an inflectional profile, relevant to jet stability (cf figure 33) is of purely inviscid origin. It was quantified later (see, e.g. [227]), how viscosity weakens the growth rate at very low Reynolds number.

One of the subtleties of the present problem is that it incorporates two phases, with different densities and viscosities and thus, *a priori*, different vorticity thicknesses. Let us consider the limit of a fast gas phase shearing, through a thick layer of vorticity δ, a nearly quiescent liquid ($v_2 \gg v_1$ and $\rho_2/\rho_1 = O(10^{-3})$. This is the limit in which 'air blast sprays' are formed. A very short time after the streams have met, the overall velocity profile can be approximated as sketched in figure 33. From the continuity of viscous stress across the interface [228] we obtain

$$\eta_2 \frac{v_2 - v_i}{\delta} = \eta_1 \frac{v_i - v_1}{\delta_1}, \qquad (130)$$

with η_1 and η_2 the viscosities of each phase and v_i the velocity at the interface. In this parallel stream approximation, the liquid

layer can only grow by viscous diffusion so that $\delta_1 \sim \sqrt{\nu_1 t}$. Let the Reynolds number based on the gas shear layer thickness

$$Re_\delta = \frac{u_2 \delta}{\nu_2} \qquad (131)$$

be larger than the value of ≈ 100 below which the damping role of viscosity becomes effective [227, 229].

For the liquid shear layer, on the other hand, it takes some time to reach this condition. The growth rate of the inflectional profile neglecting the contribution of the liquid layer (i.e. setting $\delta_1 = 0$) is $(\rho_2/\rho_1)(v_2/\delta)$ (see below). Hence the instability based on the gas profile alone has, by the time the liquid layer has grown appreciably, developed within

$$10 \frac{\delta^2}{\nu_2} \frac{\rho_2}{\rho_1} \frac{u_2}{\delta} \approx 5 \text{ turnover times.} \qquad (132)$$

This safely justifies the approximation $\delta_1 = 0$. The piecewise linear profile shown in figure 33 is but a caricature of an actual velocity profile, but is known, in single phase flows, to capture all the essential physics (wavenumber cut-off, growth rate) of the instability [230]. The obvious advantage of the simplified profile is that it yields transparent analytical expressions.

Using dimensionless variables $\kappa = k\delta$ and $\Omega = \omega\delta/(v_2 - v_1)$, the dispersion relation becomes [231]

$$e^{-2\kappa} = \left[1 - 2\left(\Omega + \kappa \frac{v_2/v_1}{v_2/v_1 - 1}\right)\right]$$

$$\times \frac{1 + \left(\frac{\rho_1}{\rho_2} + 1\right)\left(\Omega + \frac{\kappa}{v_2/v_1 - 1}\right) - \frac{\kappa^3}{We_\delta}\left(\Omega + \frac{\kappa}{v_2/v_1 - 1}\right)^{-1}}{1 + \left(\frac{\rho_1}{\rho_2} - 1\right)\left(\Omega + \frac{\kappa}{v_2/v_1 - 1}\right) - \frac{\kappa^3}{We_\delta}\left(\Omega + \frac{\kappa}{v_2/v_1 - 1}\right)^{-1}},$$
$$(133)$$

where

$$We_\delta = \frac{\rho_2 (v_2 - v_1)^2 \delta}{\gamma} \qquad (134)$$

is the Weber number based on the gas shear layer thickness δ.

The dispersion relation (133) contains the effect of both a finite size of the boundary layer and of surface tension. In the large Weber number limit, factors containing $1/We_\delta$ are negligible and the stability properties of the layer amount to an extension of Rayleigh's theory, but incorporating density differences [231, 232]. Thus in the reference frame moving at the average velocity $(v_1 + v_2)/2$ (133) becomes

$$e^{-2\kappa} = [1 - (2\Omega^* + \kappa)] \frac{1 + \dfrac{\dfrac{\rho_1}{\rho_2} + 1}{2}(2\Omega^* - \kappa)}{1 + \dfrac{\dfrac{\rho_1}{\rho_2} - 1}{2}(2\Omega^* - \kappa)} \qquad (135)$$

with

$$\Omega^* = \Omega - \kappa \frac{(v_2 + v_1)/2}{v_2 - v_1}. \qquad (136)$$

Setting $\omega = \omega_r + i\omega_i$, the temporal stability analysis of (136) displays a growth rate $\omega_i(k)$ tangent to the
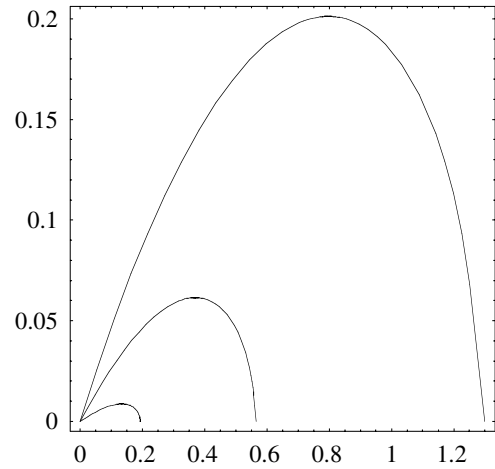

Figure 36. Dispersion relation $\text{Re}[-i\omega_i(k)]$ as given by (136), shown as a function of $k\delta$ for three different density ratios $\rho_a/\rho = 1, 0.1, 0.01$.

velocity discontinuity dependence at small k (i.e. $\omega_i(k) \sim k(\rho_2/\rho_1)^{1/2}(v_2 - v_1)$, see (122)) and an overall bell-shape with a cut-off at $k_c = 2(\rho_2/\rho_1)^{1/2}/\delta$, as seen in figure 36. The most amplified wavenumber and the associated growth rate now depend on δ and read (for $v_2 \gg v_1$)

$$k_m \simeq 1.5 \left(\frac{\rho_2}{\rho_1}\right)^{1/2} \frac{1}{\delta}, \qquad \omega_i(k_m) \simeq \frac{\rho_2}{\rho_1} \frac{v_2}{\delta}. \qquad (137)$$

The group velocity at k_m is very well represented by the convection velocity as estimated from the stress continuity at the interface [233, 234]

$$\left.\frac{\partial \omega_r}{\partial k}\right|_{k_m} \simeq \frac{\sqrt{\rho_1}\, v_1 + \sqrt{\rho_2}\, v_2}{\sqrt{\rho_1} + \sqrt{\rho_2}}. \qquad (138)$$

Using the method of section 3.6.1, the above *temporal analysis* can be transformed to the case of *spatial growth*, which is legitimate if the *momentum ratio* between the streams

$$M = \frac{\rho_2 v_2^2}{\rho_1 v_1^2} \qquad (139)$$

is large enough (see [231, 232] for a discussion). At a fixed spatial location, the passage frequency f of unstable disturbance waves at the interface is thus

$$f \sim k_m (\partial \omega_r/\partial k)_{k_m} \sim u_2/\delta, \qquad (140)$$

as seen clearly in the measurements in [232, 235], reported in figure 39. This effectively demonstrates the relevance of the above description for the destabilization of jets by a fast gas stream.

3.8.3. Transition between the two limit cases. The numerical solution of the complete dispersion equation (133) shows, as expected, a transition from the results for a thin vorticity layer ($We_\delta \ll 1$) to a thick vorticity layer ($We_\delta \gg 1$). As predicted, the selected wavenumber is $k_m = 2/3\, \rho_2 v_2^2/\sigma$ for small We_δ, and tends to $k_m = 1.5(\rho_1/\rho_2)^{1/2}/\delta$ at large We_δ. The group
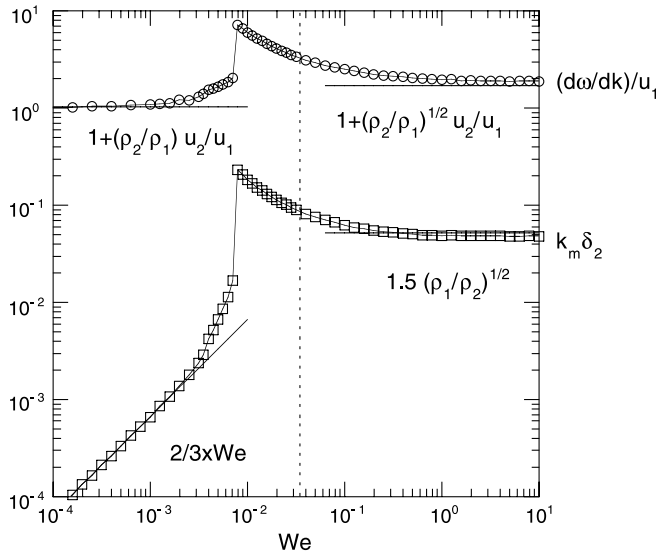
Figure 37. Transition from a thin shear layer to a thick shear layer as a function of the Weber number We_δ for $v_2/v_1 = 20$, using the parameters of an air/water interface; $\bigcirc$, group velocity; $\square$, most unstable wavenumber; - - - -, transition value of $(\rho_2/\rho_1)^{1/2}$.

velocity $\partial\omega_r/\partial k$ jumps from nearly v_1 to the value given in (138) when the Weber number increases, after a discontinuous transition (see figure 37); this transition occurs for

$$We_\delta \sim \left(\frac{\rho_2}{\rho_1}\right)^{1/2}. \tag{141}$$

Even in the presence of surface tension, the shear does not affect the layer for wavelengths shorter than $\delta(\rho_1/\rho_2)^{1/2}$. The Rayleigh mode selection thus *overcomes* the selection of the Kelvin–Helmholtz mode as long as $\gamma/\rho_2 v_2^2 < \delta(\rho_1/\rho_2)^{1/2}$, resulting in (141) above [231].

Note finally that, if the liquid phase is a jet of radius h_0, the shear instability overcomes the capillary instability of the jet itself as soon as its growth rate $(v_2/\delta)(\rho_2/\rho_1)$ is larger than the capillary growth rate $\sqrt{\sigma/\rho_1 h_0^3}$. This is equivalent to

$$We_\delta \gg \frac{\rho_1}{\rho_2}\left(\frac{\delta}{h_0}\right)^3, \tag{142}$$

a condition fulfilled for example in the experiment shown in figure 38.

The above scenario, based on the instability of an inflectional profile, was first suggested in [231]. Viscous corrections were considered in [237] and used in [236] to compute the breakup of a liquid jet in air. Even for moderate jet speeds, significant deviations from Rayleigh's analysis are found [148, 238], since the shear generated by the surrounding air enhances destabilization. Such an analysis was first carried out by Weber [38], using the Kelvin–Helmholtz approximation, which is irrelevant in this context (cf section 3.8.1). Later, Sterling and Sleicher [238] included the effect of viscosity on the shear profile, whose finite thickness reduces the aerodynamic effects. However, to achieve quantitative agreement with theory, an empirical

Figure 38. Destabilization of a slow water jet ($h_0 \approx 4$ mm) by a fast coaxial air stream [232] ($v_1 = 0.6$ m s^{-1}, $v_2 = 35$ m s^{-1}). The wavelength of the primary axisymmetric undulation is governed by (137).

correction factor had to be introduced. The origin of this correction has finally been explained in [236], by including a full self-consistent account of the air boundary layer (see figure 39 and also section 3.12).

These studies have led to a fully quantitative explanation of the observed growth rates and mode selection of a liquid jet in relative motion to a gas phase. They have been a crucial step in understanding the subsequent *atomization* of the liquid discussed in section 5.

3.9. Charged jets

New phenomena arise when the jet contains electric charges, which can be achieved by letting the jet fall into a bucket maintained at a given potential, while an electrode upstream of the jet orifice is set at a different potential. This was demonstrated in the 18th century by Abbé Nollet (1749) [33], cf figure 10. If the liquid is not too conductive, the charges have time to migrate, by electrostatic repulsion, to the jet's surface before reaching the counter-electrode at the bucket, inducing new instabilities of the interface.

3.9.1. Electrostatic repulsion. Let a jet be superficially charged at potential V_0 with a charge (positive or negative) per unit area $\sigma_0 = V_0 \varepsilon_0/h_0$. The repulsion between the charges tends to push the interface outwards, therefore counteracting the cohesive action of capillarity. If the charges are confined to the jet surface, a direct application of Gauss' theorem ($\nabla \cdot E = \rho_e/\varepsilon_0$, where ρ_e is the charge volume density) shows that the field E is zero inside the jet, since there are no charges in the liquid bulk. Outside of the (unperturbed) jet (i.e. for $r > h_0$), the field is radial:

$$E = \frac{\sigma_0}{\varepsilon_0}\frac{h_0}{r}e_r, \tag{143}$$

corresponding to a potential V ($E = -\nabla V$)

$$V = V_0 - \frac{\sigma_0 h_0}{\varepsilon_0}\ln\left(\frac{r}{h_0}\right), \tag{144}$$

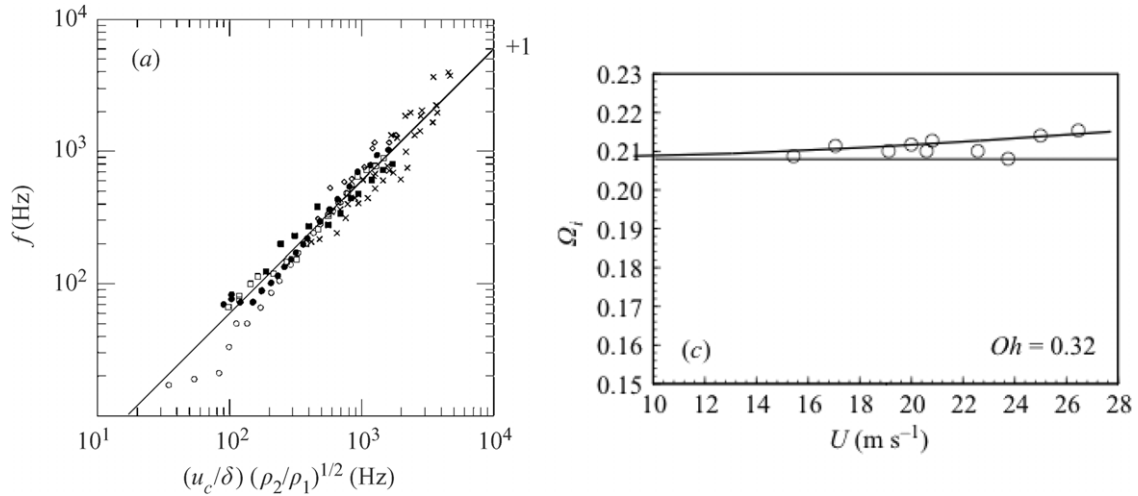where ε_0 is the permittivity of free space.

Figure 39. (Left) Passage frequency f of the optimal disturbance of the interface as a function of frequency, compared with the prediction of (140). Here u_c stands for the group velocity in (138). Measurements are from [232,235]. (Right) Dimensionless growth rates $\Omega_i = \omega\tau$ of perturbations growing on a liquid jet issuing into air as a function of the jet speed U. The wavelength is close to the optimum value. Experimental data are from [148], theory according to [236].

To investigate stability, we consider the general (not necessarily axisymmetric) perturbation (46), ensuring mass conservation by requiring (48). Since charges are confined to the surface, Laplace's equation $\nabla^2 V = 0$ holds inside and outside the jet. Assuming, in addition, that the charges are sufficiently *mobile* along the surface to make the interface an *equipotential*, one finds that

$$V(r < h) = V_0, \tag{145}$$

$$V(r > h) = V_0 - \frac{\sigma_0 h_0}{\varepsilon_0} \ln\left(\frac{r}{h_0}\right)$$
$$+ \frac{\sigma_0 \epsilon}{\varepsilon_0} \frac{K_m(kr)}{K_m(kh_0)} \cos(m\varphi)\cos(kz). \tag{146}$$

To this perturbed potential corresponds a perturbed surface density such that

$$\sigma_1 = -\varepsilon_0 \frac{\partial V}{\partial r}\bigg|_{R=h}$$
$$= \frac{\varepsilon_0 V_0}{h_0}\left(1 - \frac{\epsilon}{h_0}\left[1 + kh_0 \frac{K'_m(kh_0)}{K_m(kh_0)}\right]\cos(m\varphi)\cos(kz)\right). \tag{147}$$

The corresponding electrostatic contribution E_e to the potential energy of the jet is (with a sign opposite that of the surface energy (35), since electrostatic forces are repulsive)

$$E_e = -\frac{1}{2}V_0 \int \sigma_1[h_0 + \epsilon\cos(m\varphi)\cos(kz)]\,\mathrm{d}\varphi\,\mathrm{d}z. \tag{148}$$

The electric potential energy reckoned from equilibrium is [241,242]

$$\Delta E_e = \frac{\pi}{4}\varepsilon_0 V_0^2 \left(\frac{\epsilon}{h_0}\right)^2 \left[1 + kh_0 \frac{K'_m(kh_0)}{K_m(kh_0)}\right], \tag{149}$$

which is negative, indicating the possible existence of an instability, for all values of $m > 0$. For $m = 0$, a range of stable wavenumbers exists for $0 < kh_0 \lesssim 0.6$. This *stabilizing* role of surface charges on the varicose mode at long wavelength was first noticed by Rayleigh [242].

3.9.2. Dispersion equations. The full dispersion equation, incorporating the effect of surface tension, is obtained along the same lines as in section 3.2 (see, e.g. [241,243–245], and the review [246]):

$$\omega^2 = -\frac{\gamma}{\rho h_0^3}(kh_0)\frac{I'_m(kh_0)}{I_m(kh_0)}$$
$$\times\left[1 - m^2 - (kh_0)^2 - \Gamma\left(1 + kh_0\frac{K'_m(kh_0)}{K_m(kh_0)}\right)\right]. \tag{150}$$

The parameter

$$\Gamma = \frac{\varepsilon_0 V_0^2}{\gamma h_0} = \frac{\sigma_0^2/\varepsilon_0}{\gamma/h_0} \tag{151}$$

represents the relative importance of electric to surface tension energy, or, equivalently, the ratio of the electrostatic pressure σ_0^2/ε_0 to the capillary pressure γ/h_0. A corresponding long-wavelength description is found in [247,248], while Huebner and Chou [241] give an elegant energetic derivation.

In the spherical geometry relevant to isolated drops, Rayleigh [242] has shown by the same energetic arguments as above that there is a critical value of this ratio above which a cohesive drop cannot sustain its charge anymore and has to destabilise. The drop undergoes an oblate transformation (shown in figure 40) and the formation of thin, elongated jets ('Rayleigh jets'), which are discussed in detail in section 4.7. A much more detailed bifurcation analysis of charged drops was performed in [249].

The dispersion relation (150) of the varicose mode $m = 0$ is shown in figure 41. It displays, as soon as $\Gamma > 1$, an enhanced rate of instability compared with that of the pure capillary destabilization, and a range of unstable wavenumbers extended to values of kh_0 larger than 1. Also of interest by contrast to the pure capillary destabilization, for which all non-axisymmetric modes are stable, is the case $m = 1$. The initial destabilization of the jet in figure 40 is more of the $m = 2$ type, squeezing the jet into a dumbbell shape, clearly demonstrating the destabilizing character of electric repulsion,
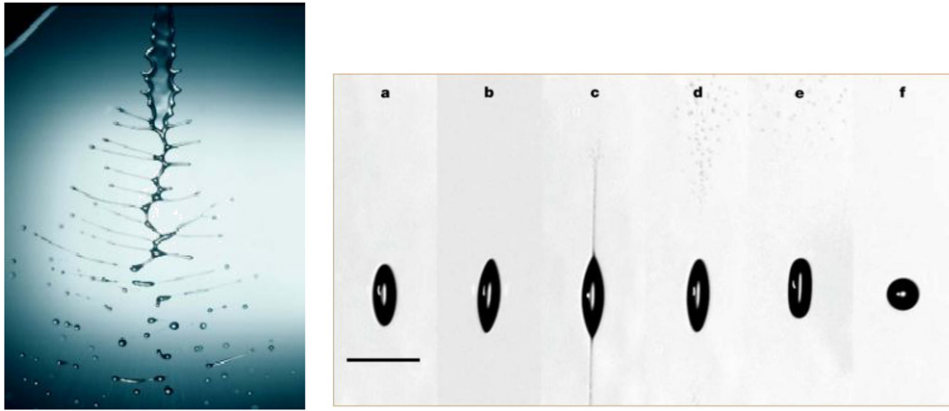
Figure 40. (Left) Instantaneous realization of the electrostatic disruption of room-temperature paraffinic white oil. The oil is issuing at $5\,\mathrm{ml\,s^{-1}}$ from a circular orifice ($h_0 = 0.5$ mm) after having been negatively charged to a mean charge density of $0.15\,\mathrm{Cb\,m^{-3}}$. The liquid is charged by a submerged electrode, which is positioned immediately upstream of the grounded orifice through which the fluid issues. In the absence of charge injection the liquid would exit as a glassy smooth cylindrical stream. The elegant filamentary structure and subsequent droplet development is purely electrostatic. No mechanical or aerodynamic forces are involved. Reprinted with permission from [239], copyright 2000 by the American Institute of Physics. (Right) High-speed imaging of the disintegration of a levitated droplet charged to the Rayleigh limit. The droplet (radius, $24\,\mu$m) is imaged at Δt values (in μs) of: a, 140; b, 150; c, 155; d, 160; e, 180 and f, 210. The droplet changes from a sphere to an ellipsoid (a), tips appear at the poles (b) and a fine jet of liquid is ejected from each tip (c); the jets disintegrate (d) and the elliptical droplet re-assumes a spherical shape (e), (f). Scale bar, $100\,\mu$m. Reprinted from [240], copyright 2003, with permission from Nature Publishing Group.
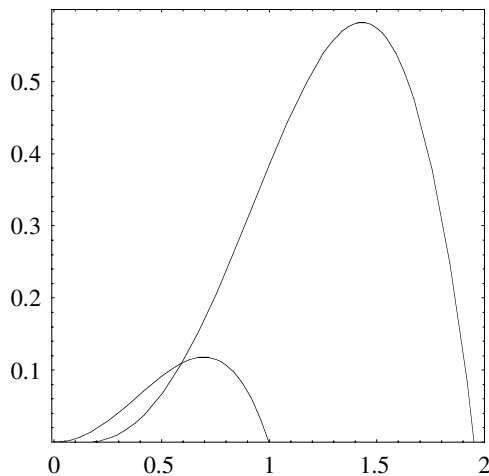

Figure 41. Stability curve $-\mathrm{i}\omega\tau$ versus kh_0. Destabilizing effect of surface charges with $\Gamma = 2$ on the varicose mode $m = 0$ in equation (150). The neutral jet dispersion curve is shown for comparison.

which may even lead to 'jet splitting' in some cases (see [250] and references therein).

The stability of a charged jet in an external electric field is of the utmost importance for applications. If the jet breaks up into droplets, one speaks of 'electrospraying'. Another possibility is the whipping mode shown in figure 42, on which the 'electrospinning' technique of producing polymer fibres is based [251–253], for example to make fabrics. The stability of a cylindrical jet, reviewed in [247, 254], now depends not only on the fluid parameters ϵ_i and K but also on external parameters such as the applied electric field and the surface charge, to be determined from the cone-jet solution. The problem becomes manageable in a long-wavelength description [247], which is self-consistent in most cases.

Apart from a modified Rayleigh mode, which is gradually suppressed as the electric field is increased, another varicose

'conducting' mode becomes increasingly unstable, which comes from the redistribution of surface charges. A third 'whipping' mode is most significant for large surface charges: namely, imagine three like charges on a line. A lower energy state is achieved if the middle charge breaks out of line, so the jet is no longer straight. For a quantitative analysis, the axial variations of $h(z)$ and $\sigma(z)$ must be taken into account [248], so the stability depends significantly on the downstream distance. With this in mind, the onset of whipping can be predicted quantitatively [248].

Charges also play an important role for the stability of nuclei [255], which may be modelled as charged liquid drops [256] or, in a more extended state, jets [257]. The stability of *uniformly* charged jets was investigated in [258], and its relevance to the stability and the breakup of nuclei is discussed at length in [257].

3.10. Ferrofluids in a magnetic field

Ferrofluids are colloidal dispersions of small (typically micrometre-sized) magnetized dipolar particles which are spread out in a continuous, liquid phase. Application of an external magnetic field $\boldsymbol{H}$ induces a magnetization of the dispersion $\boldsymbol{M} = \chi\boldsymbol{H}$, where χ is the magnetic susceptibility of the medium, such that the net induction field is $\boldsymbol{B} = \mu\boldsymbol{H} = \mu_0(1 + \chi)\boldsymbol{H}$, with μ the permeability of the medium and μ_0 that of vacuum. The resulting stresses lead to an additional body force in the Navier–Stokes equation, which adds a term $\mu_0 M\boldsymbol{\nabla}H$ to the internal pressure gradient. Rosensweig [259] gives a comprehensive exposition of these notions, illustrated by many examples including the two discussed below.

3.10.1. Parallel field. A magnetic field H_0 applied perpendicular to a free plane magnetic fluid interface leads to an instability very similar to a Rayleigh–Taylor instability [219, 259], because of the magnetic susceptibility jump,
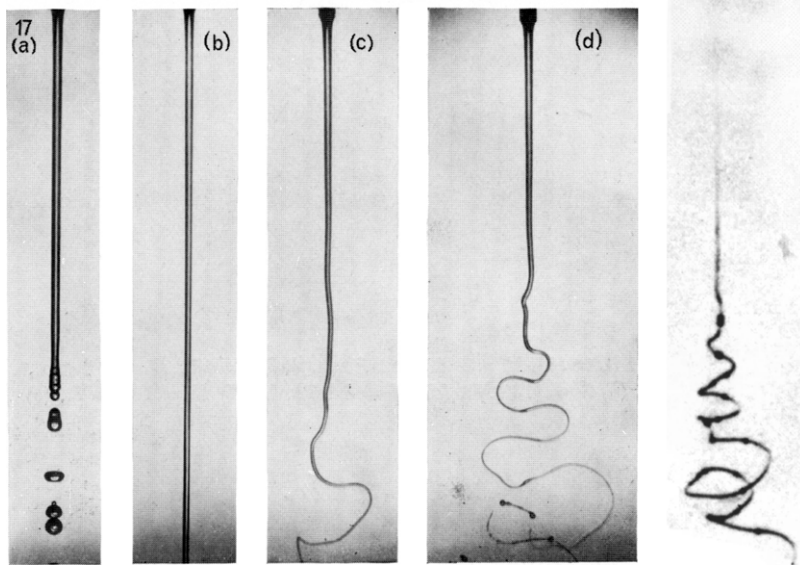
Figure 42. (Left) Whipping instability. Water jet exposed to an increasing longitudinal potential difference from left to right [244]. (Right) Strobe photograph of the overall picture of an unstable jet. Reprinted with permission from [247], copyright 2001 by the American Institute of Physics.

inducing a normal stress at the interface. But when the field H_0 is applied *parallel* to the surface of a jet, as for instance when a ferrofluid jet is immersed at the centre of a coaxially positioned solenoid, the effect of the field is stabilizing. The dispersion relation reads [259]

$$\frac{\rho h_0^3}{\gamma}\omega^2 = -(kh_0)\frac{I_1(kh_0)}{I_0(kh_0)}[1-(kh_0)^2] \tag{152}$$

$$+\Gamma_m\,(kh_0)^2\frac{I_0(kh_0)K_0(kh_0)(\mu/\mu_0-1)^2}{(\mu/\mu_0)I_1(kh_0)+I_0(kh_0)K_1(kh_0)}, \tag{153}$$

where μ_0 and μ stand for the permeabilities of the vacuum and of the fluid, respectively. The parameter

$$\Gamma_m = \frac{\mu_0 H_0^2}{\gamma/h_0} \tag{154}$$

is the ratio of the magnetic pressure to the Laplace pressure, analogous to (151). The magnetic term in this equation is always positive.

3.10.2. Azimuthal decaying field. A thin layer of fluid of thickness e_0 coating a cylindrical fibre, or a wire of radius h_0, suffers a capillary instability, as described in section 3.5.2. If the wire is conductive and carries a current I, the magnetic field is azimuthal and decays with the distance r from the wire according to Biot and Savart's law

$$H = \frac{I}{2\pi r}, \qquad \text{giving } G = \left.\frac{\mathrm{d}H}{\mathrm{d}r}\right|_{r=h_0} = \frac{H}{h_0}. \tag{155}$$

When the liquid layer coating the wire is thin compared with the wire radius (i.e. when $e_0/h_0 \ll 1$), the dispersion relation reads [259]

$$\frac{\rho h_0^3}{\gamma}\omega^2 = \frac{e_0}{h_0}(kh_0)^2[N+(kh_0)^2-1], \tag{156}$$
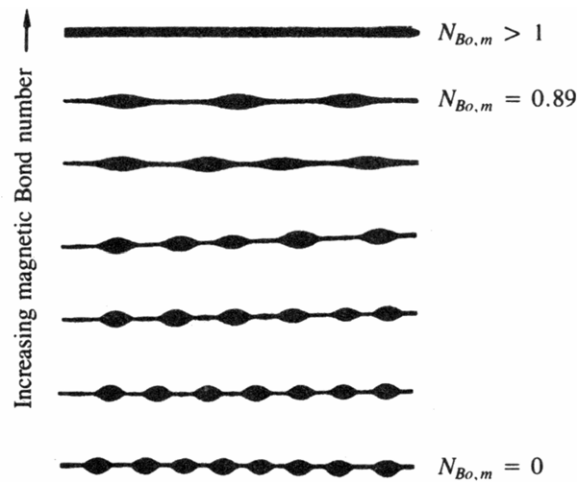

Figure 43. Suppression of the capillary instability by a radially decaying azimuthal magnetic field generated by a current in the wire coated by the magnetic fluid [259].

where the so-called 'magnetic Bond number' N is

$$N = \frac{\mu_0 MGh_0}{\gamma/h_0} = \frac{\mu_0\chi I^2}{4\pi^2 h_0\gamma}. \tag{157}$$

The dispersion relation (156) shows that the usual Rayleigh–Plateau instability is weakened as N increases from zero, and completely disappears for $N > 1$, as shown in figure 43. Note that (156) applies to the inviscid limit, as opposed to (93), which applies for highly viscous fluids.

3.11. Other body forces

The effect of body forces on the dynamics of liquid jets has already been alluded to in section 3.5, where we described the gravitational stretch of a viscous thread, and in section 3.10 above. Here we mention a few more examples which are important in practice.
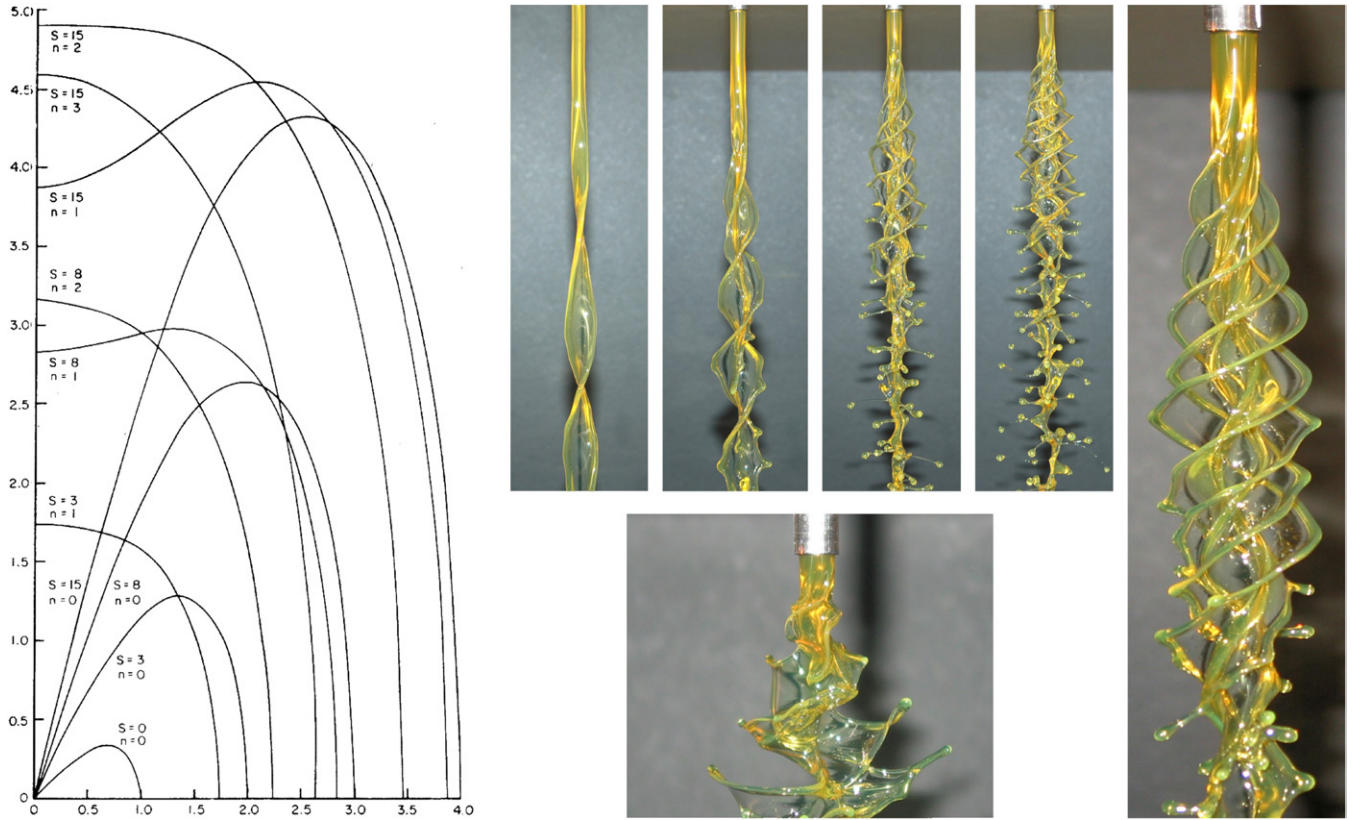
Figure 44. (Left) Dispersion curve of a *swirling* jet representing the growth rate (in units of $\sqrt{\gamma/\rho h_0^3}$) versus dimensionless longitudinal wavenumber kh_0 for various azimuthal wavenumbers m. Adapted from Ponstein (1959) [260]. (Right) Still images of helical instabilities on a *rotating* jet, showing how the most amplified azimuthal wavenumber increases as the rotation increases, subsequent ligament and drop formation. Courtesy of Kubitschek and Weidman [261]. Reprinted with permission, copyright 2007 by the American Institute of Physics.

3.11.1. Swirling jets. A convenient way to communicate a body force to a the jet is to impose a rotation of the jet, sometimes called *swirl*. This can be achieved using a so-called 'cyclone spray chamber', which is a rotating pressurized chamber, from which the jet is expelled tangentially. In [262, 263], the trajectory of such a swirling jet was calculated. The effect of the swirl on the base flow is usually modelled as one around a line vortex along the jet's axis, with a radially decaying azimuthal velocity

$$v_\phi = \frac{\Gamma}{r} \qquad \text{and} \qquad v_r = 0. \tag{158}$$

Here $2\pi\Gamma$ is the circulation, with a negligible viscous core. This imparts a centrifugal acceleration $g \equiv \Gamma^2/h_0^3$ on the jet. The entire jet is being translated at the issuing velocity $v_z = v_0$. The alternative case of a *solid body rotation*, or when the viscous core is as thick as the injector diameter, is considered below.

Ponstein (1959) [260] has considered the stability of a jet flow with base flow (158) by considering perturbations of the form (46). When the influence of the external medium, as well as of the viscosity, is neglected the dispersion relation becomes

$$\left(\omega - \frac{m\Gamma}{h_0^2} - kv_0\right)^2$$

$$= \frac{\gamma}{\rho h_0^3}[m^2 - 1 + (kh_0)^2 - S](kh_0)\frac{I_m'(kh_0)}{I_m(kh_0)}, \tag{159}$$

where S is the 'Swirl number' given by

$$S = \frac{\rho\Gamma^2}{\gamma h_0}. \tag{160}$$

Not surprisingly, centrifugal forces enhance instability because the acceleration is directed outwards, pointing towards the light phase. A hollow jet is correspondingly stabilized by rotation. Azimuthal modes are now unstable too; in the limit of very large rotation ($S \gg 1$), the jet interface is unstable to all modes m and is quasi-planar for large m. From (159), the marginal azimuthal wavenumber $k_\perp$ such that $m_c = k_\perp h_0$ is, for $k = 0$ (azimuthal modulation uniform in the z direction),

$$k_\perp = \sqrt{\frac{\rho g}{\gamma}} \qquad \text{with } g = \frac{\Gamma^2}{h_0^3}. \tag{161}$$

This is to be expected by analogy to the associated Rayleigh–Taylor instability [219] with acceleration g. This instability hinders the capillary instability of the jet when its time of growth $(\gamma/\rho g^3)^{1/4}$ is smaller than the capillary timescale $\tau = \sqrt{\rho h_0^3/\gamma}$, that is for

$$S > 1. \tag{162}$$

Figure 44 summarizes these trends.

Note finally that this technique of rapid rotation is used as an atomization process employing 'spinning cups'. The
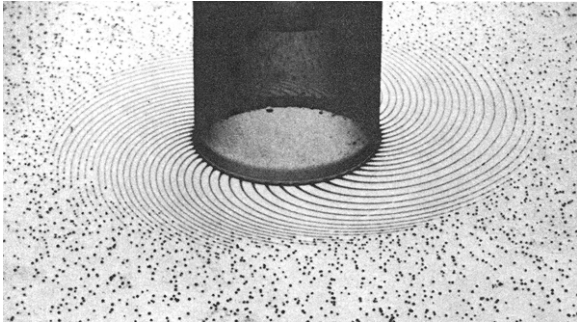
Figure 45. Formation of liquid threads from a rotating hollow tube [264].

liquid is deposited as a film on a rapidly rotating disc or hollow tube, and ejects liquid threads spaced by the above length scale $2\pi/k_\perp$ (see figure 45 and [264–266]). In another context, the process is known as 'prilling', and used to produce fertilizer and magnesium pellets [262, 263, 267].

3.11.2. Rotating jets. The study of jets in solid body rotation was pioneered by Beer [15]. Here, the base flow (158) is replaced by

$$v_\phi = \Omega r \qquad \text{and} \qquad v_r = 0. \qquad (163)$$

This is produced very easily by rotating the entire nozzle from which the jet is emerging [268], or by rotating one fluid inside another, as already done by Plateau [269] (see also [261] and figure 44). The latter is the geometry of the 'spinning drop tensiometer' [270], which is used to measure very small values of the surface tension between two liquids. The result of an axisymmetric stability analysis in the absence of an outer liquid [268, 271] is that angular rotation, as quantified by the parameter

$$L = \frac{\gamma}{\rho \Omega h_0^3}, \qquad (164)$$

always destabilizes the jet. In particular, the jet is unstable for

$$0 < kh_0 < \sqrt{1 + L^{-1}}, \qquad (165)$$

independent of viscosity [272].

The full axisymmetric stability analysis (again without outer fluid), as well as experimental tests, was performed by [268]. The limiting case of an inviscid fluid [271] shows an increase in the growth rate with the speed of rotation relative to (57), and consistent with (165). The opposite case of very large viscosity leads to a simple extension of (80)

$$-i\omega = \frac{\gamma}{2h_0\eta} \frac{1 - (kh_0)^2 + L^{-1}}{1 + (kh_0)^2[1 - (I_0(kh_0)/I_1(kh_0))^2]}, \qquad (166)$$

which is of course once more consistent with (165). In a rather extensive recent study [273], the transition towards non-axisymmetric 'swirling' modes was considered as well.

It is interesting to note that a naive long-wavelength description of a rotating jet [274] is in general not consistent with (165). The reason for this is the formation of a very thin boundary layer near the free surface of the jet for small ω, i.e. near the stability boundary [275]. Namely, Rayleigh's

stability criterion for a rotating fluid implies that the interior of the fluid be stabilized, while the Rayleigh–Taylor mechanism destabilizes the free surface, squeezing disturbances to within a very thin layer. For very large viscosities, however, the long-wavelength description becomes consistent, and the analogue of (85) becomes

$$-i\omega = \frac{1}{6\tau_v}[1 - (kh_0)^2 + L^{-1}]. \qquad (167)$$

Finally, the two-fluid case, relevant to the measurement of surface tension, was investigated in the viscous limit in [276]. In the spinning drop tensiometer the lighter fluid moves to the centre, where it is stabilized by the rotation. The stability is controlled by the 'rotational Bond number' [276]

$$Bo_\Omega = \frac{(\rho_2 - \rho_1)\Omega^2 h_0^3}{\gamma}, \qquad (168)$$

which without an outer fluid ($\rho_1 = 0$) is $Bo_\Omega = -L^{-1}$. When $0 < Bo_\Omega < 1$, the thread is unstable in the wavenumber region $0 < kh_0 < \sqrt{1 - Bo_\Omega}$, while it becomes completely stable for $Bo_\Omega > 1$. Thus as Ω is reduced, the liquid cylinder breaks up, and from a measurement of the growth rates the surface tension can be deduced [270, 276].

3.11.3. Jet in a cross flow. Consider a jet of radius h_0 and density ρ issuing at velocity v_0 into a gaseous environment (density ρ_a) flowing at a translational velocity u perpendicular to the ejection direction of the jet (figure 46). The drag force exerted by the velocity contrast bends the jet. A simple force balance on a length element $d\ell$ of the jet between the air drag and the centrifugal inertia of the liquid reads

$$C_D \rho_a u^2 h_0 \, d\ell \sim \rho h_0^2 \frac{v_0^2}{R} \, d\ell, \qquad (169)$$

where R is the radius of curvature of the jet's trajectory in the fixed frame, and C_D a drag coefficient of order unity. The balance can thus be simplified to

$$\frac{R}{h_0} \sim \frac{\rho}{\rho_a}\left(\frac{v_0}{u}\right)^2. \qquad (170)$$

Now, the jet fluid is subjected to an acceleration $g \equiv v_0^2/R$ in the plane of the jet's trajectory, so the outer surface of the jet suffers a Rayleigh–Taylor instability, whose wavelength is controlled by the capillary length $\lambda \sim \sqrt{\gamma/(\rho - \rho_a)g}$. Thus for $\rho \gg \rho_a$ one obtains

$$\frac{\lambda}{h_0} \sim We^{-1/2} \qquad \text{with} \qquad We = \frac{\rho_a u^2 h_0}{\gamma}. \qquad (171)$$

The wavelength (171) is independent of the liquid velocity and its density. This instability hinders the capillary instability when its time of growth $\sqrt{\lambda/g} = (\gamma/\rho g^3)^{1/4}$ is shorter than the capillary time $\tau = \sqrt{\rho h_0^3/\gamma}$, that is, as soon as

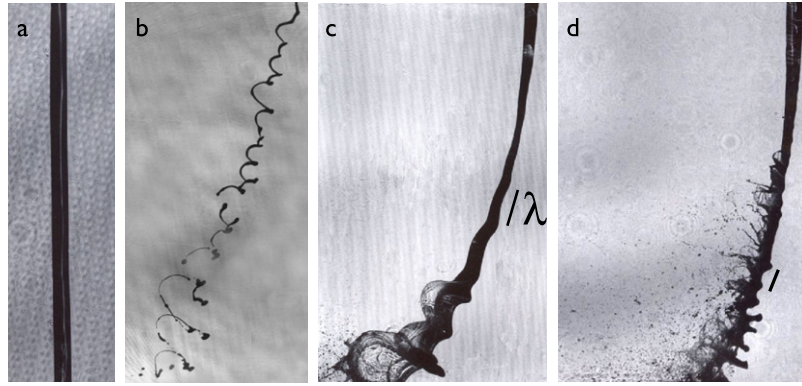$$We = \frac{\rho_a u^2 h_0}{\gamma} > 1. \qquad (172)$$

Figure 46. Liquid jet in a transverse cross flow of air. (*a*) Reference jet with no air, (*b*) $We = 3$, (*c*) $We = 8$, (*d*) $We = 30$ with $We = \rho_a u^2 d/\gamma$ as defined in (171). The jet diameter is millimetric and the liquid velocity v_0 is of the order of a few $10\,\mathrm{m\,s^{-1}}$. The bar indicates the length of the Rayleigh–Taylor wavelength λ. Courtesy of K A Sallam [277].

The scaling law (171) has been checked by [277] over more than two orders of magnitude in *We*, for different liquids and issuing velocities.

The above mechanism by which the liquid follows a curved base flow and thus sustains a centrifugal instability is reminiscent of the 'wavy corridor' mechanism, responsible for the destabilization of undulated liquid sheets [278].

3.12. Liquid intact length

The minimum distance from the nozzle over which the liquid jet is still connected is usually called 'liquid intact length' *L* [215,216,279]. This distance can fluctuate by several wavelengths, but is defined in the mean. Scaling theories for *L* are readily derived from the discussion in sections 3.2 through 3.8. Namely, the intact length is

$$L = v_0 \tau, \tag{173}$$

where τ is the characteristic time of the instability, needed to break the jet. Let us describe two simple extreme cases:

- For a pure capillary instability at negligible viscosity τ is given by (2), and thus

$$\frac{L}{h_0} \sim We^{1/2}, \tag{174}$$

  as is indeed observed for jets beyond the jetting transition and entering a gaseous environment [119,280,281].

- For larger Weber number, the shear instability overcomes the capillary destabilization (see section 3.8). Consider for instance that the jet is 'peeled off' by an instability of the type sketched in figure 33, the injection velocity v_0 also being the velocity contrast setting the shear intensity. This instability turnover time has been shown to be $\mathrm{Re}[-i\omega_i(k_m)]^{-1} \sim (\delta/v_0)(\rho/\rho_a)$, and the associated wavelength $k_m^{-1} \sim \delta(\rho/\rho_a)^{1/2}$. If these conditions are maintained for several turnover times of the instability, the breakup time is

$$\tau \sim h_0 k_m \frac{\rho}{\rho_a} \frac{\delta}{v_0} = \frac{h_0}{v_0}\left(\frac{\rho}{\rho_a}\right)^{1/2}, \tag{175}$$

leading to an intact length

$$\frac{L}{h_0} \sim \left(\frac{\rho}{\rho_a}\right)^{1/2}, \tag{176}$$

independent of the jet velocity. This intact length can reach several hundred jet radii if $\rho_a/\rho \ll 1$ [228,231]. Note that (176) is scale invariant and holds whatever δ may be. In other words, whatever the physical process which fixes δ (which may be a boundary layer thickness imposed externally, or an intrinsic wavelength $\gamma/\rho_a v_0^2$ as in section 3.8), *L* will always have the form (176), as soon as the jet destabilization is due to shear [231].

The overall dependence of *L* on the ejection velocity v_0 for simple jets usually displays a linear increase at small v_0, consistent with (174), and then a saturation whose level is higher for a lighter environment, cf (176), and as seen in figure 47. Both dependences can be incorporated by saying that v_0/L is the sum of the characteristic growth rates of each of the competing instabilities, i.e.

$$\frac{v_0}{L} = \frac{1}{\sqrt{\rho v_0^2/\gamma}} + \frac{\delta\sqrt{\rho/\rho_a}/h_0}{\rho/\rho_a(\delta/v_0)}. \tag{177}$$

Thus, disregarding prefactors, we have

$$\frac{h_0}{L} = \frac{1}{\sqrt{We}} + \frac{1}{\sqrt{\rho_a/\rho}}, \tag{178}$$

so the transition between the two limits occurs for a Weber number of order

$$We \sim \frac{\rho}{\rho_a}. \tag{179}$$

In particular, at large Weber number L/h_0 saturates at a value proportional to $\sqrt{\rho/\rho_a}$, which is inversely proportional to ambient gas pressure P_a. Data to support this conclusion are shown in figure 47. Contrary to a common belief since [238], this saturation is *not* an effect of viscosity on the capillary instability development, but relates to the appropriate shear instability responsible for the jet peeling-off (see also section 3.8 and the point made in [236]).
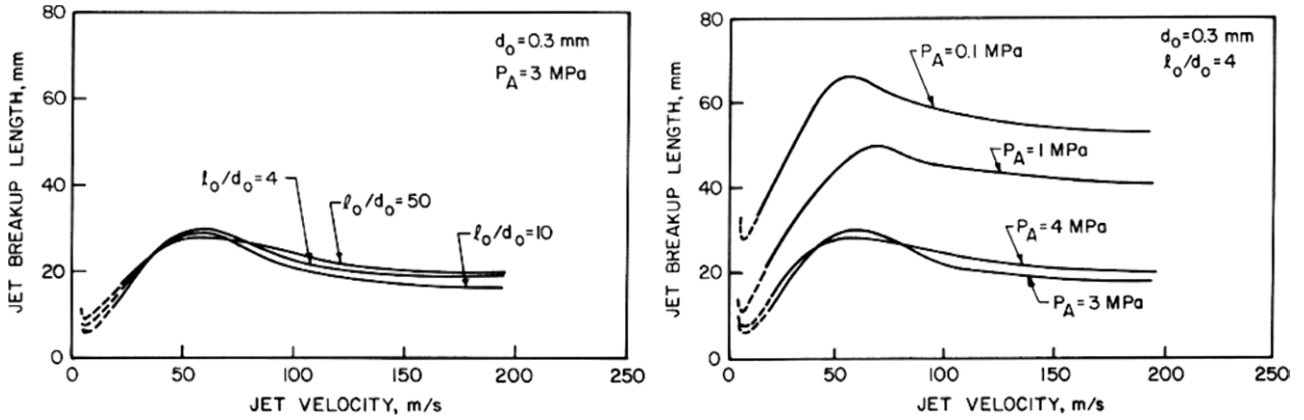
Figure 47. Liquid intact lengths (or jet breakup length) measured for increasing jet velocity v_0 for various injection conditions (d_0 is the injector diameter and ℓ_0 denotes the orifice length, setting the boundary layer thickness at the exit) as well as different ambient gas pressures. (Adapted from Hiroyasu *et al* (1982) [282]).

When the injection velocity v_0 is very different from the one setting the shear $v_a - v_0 \approx v_a$, as is the case for coaxial jets with a strong momentum ratio contrast $M = \rho_a v_a^2 / \rho v_0^2 \gg 1$ between the streams, one has $L = v_0 \tau$ and $\tau \sim h_0 / v_a (\rho_a / \rho)^{1/2}$, and thus

$$\frac{L}{h_0} \sim \frac{v_0}{v_a} \left(\frac{\rho}{\rho_a} \right)^{1/2} \tag{180}$$

sometimes written $L/h_0 \sim M^{-1/2}$ [231, 283, 284].

The effect of *initial turbulence* in the jet as it issues from the nozzle is to hasten the capillary instability (when the turbulence level is a few per cent of the injection velocity v_0, as for pipe flow turbulence). In the capillary dominated regime, this will lead to a moderate shortening of the intact length [285]. In the shear dominated regime, the influence of background turbulence is immaterial, the primary shear instability being essentially unchanged by initial surface roughness and liquid velocity fluctuations as soon as the momentum ratio is large enough (i.e. $M \gg 1$) (see e.g. [232] and figure 48).

The way in which viscous slowing and longitudinal stretch can modify the scaling dependence for L (sometimes drastically!) has been explained in section 3.7.3. But the construction underlying L is always the same and given by (173); this standard procedure is also useful to predict the extent of unstable liquid sheets [226].

3.13. Gravitational collapse

The phenomena we have described up to now were all on a human scale or below, for which gravity is either sub-dominant (when the Bond number is small) or of order one (see section 3.7.3). At larger scales, the gravitational interaction may be felt, and if one considers objects sufficiently remote from massive sources of gravity, suspended in the interstellar medium, their shape and evolution is now determined by their own gravity. This problem was first described for a self-gravitating compressible medium in thermal equilibrium, motivated by the understanding of the formation of galaxies, nebulae and the known spottiness of the interstellar medium [286] and fractality of its mass distribution support [287].

We will once more consider an incompressible fluid of density ρ, having initially the shape of an infinitely long jet of radius h_0, remaining cohesive due to its own gravitational field $g = (g_r, g_\psi, g_z)$ alone. That field obeys a Poisson-Gauss law

$$\nabla \cdot g = 4\pi \rho \, \mathcal{G} \tag{181}$$

inside the jet (with $\mathcal{G} = 6.67 \times 10^{-11}$ kg^{-1} m^{-3} s^{-2} the constant of gravity), and a Laplace law

$$\nabla \cdot g = 0 \tag{182}$$

outside the jet, neglecting an external medium. For an infinitely long straight cylinder, the field is purely radial, equal to $g_r = 2\pi \rho \, \mathcal{G} r$ in the jet, and the pressure in the jet is $p = \pi \rho^2 \mathcal{G}(h_0^2 - r^2)$, obeying

$$g = -\frac{1}{\rho} \nabla p. \tag{183}$$

Note that for a dense fluid, the radius h_0 need not be very large for gravitational forces to be dominant compared with surface energy. Indeed, at equilibrium, the gravitational pressure scale $\rho^2 \mathcal{G} \ell^2$ balances the capillary pressure scale γ / ℓ for

$$\ell_\star = \left(\frac{\gamma}{\rho^2 \mathcal{G}} \right)^{1/3}. \tag{184}$$

For a fluid such as water, $\ell_\star \approx 1$ m, which is not an astronomically large distance.

As before, we investigate the stability of a cylinder. Varicose undulation of the jet radius will again be unstable, as can be guessed from the following argument: as known since Kepler and Newton [288], distant masses attract mutually with an intensity F proportional to their masses (say m and M) and inversely proportional to their distance (say z) squared, i.e. $F = \mathcal{G} m M / z^2$. Thus from Newton's second law $\ddot{z}_m = F/m$, and for $M > m$ we can conclude that $\ddot{z}_m > \ddot{z}_M$. This suggests that a constriction of the jet's cross-section (of smaller mass m) will move in the direction of a bulge with a larger mass M, thus thinning even more while feeding the bulge. If the masses are
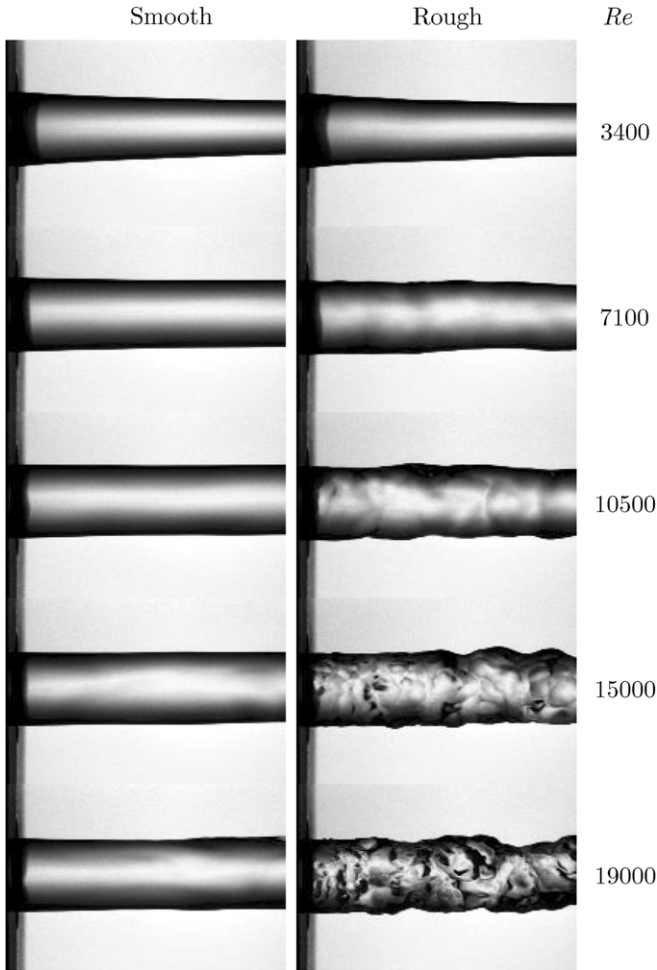
Smooth   Rough Re

Figure 48. Surface profiles of a jet issuing from a smooth pipe (left), and one whose surface is rough (right), as a function of the Reynolds number $Re = 2v_0 h_0/\nu$ (adapted from [232]). At high Reynolds numbers, the jet on the right is much more corrugated. However, the initial destabilization of the jet by a coaxial stream is insensitive to the surface roughness and associated liquid velocity fluctuations as soon as the momentum ratio M between the streams is large enough (i.e. $M \gg 1$).

such that $m \ll M$ and are initially at a distance, say, R apart, they collapse according to

$$\ddot{z} = -\mathcal{G}\frac{M}{z^2},\tag{185}$$

in the finite Kepler time T

$$T^2 \sim \frac{R^3}{\mathcal{G}M}.\tag{186}$$

If furthermore the masses are compact in space so that $M \sim \rho R^3$, one has

$$T^2 \sim \frac{1}{\rho\mathcal{G}}.\tag{187}$$

This is the instability mechanism which, however, has to be examined more closely since the pressure gradient along the jet counteracts the motion, the pressure in the bulge being larger (because it is thicker) than in the constricted region (which is thinner), this effect representing a potential stabilizing

mechanism. We thus refine the above qualitative discussion by a somewhat more elaborate argument, using a long-wavelength description of the longitudinal rearrangements along the jet. The dynamics of small corrugations $h = h_0 + \epsilon(z,t)$ is described by

$$\frac{\partial v}{\partial t} = -\frac{1}{\rho}\frac{\partial p}{\partial z} + g_z,\tag{188}$$

$$\frac{\partial \epsilon}{\partial t} + \frac{h_0}{2}\frac{\partial v}{\partial z} = 0,\tag{189}$$

$$\nabla \cdot \boldsymbol{g} = \frac{\partial g_z}{\partial z} + \frac{1}{r}\frac{\partial}{\partial r}(r g_r) = 4\pi\rho\,\mathcal{G},\tag{190}$$

where v is the velocity component in the jet along z, and g_r and g_z stand for the radial and longitudinal components of the gravity. According to the above system, the dynamics of ϵ is given by

$$\frac{\partial^2 \epsilon}{\partial t^2} + \frac{h_0}{2}\left(-\frac{1}{\rho}\frac{\partial^2 p}{\partial z^2} + \frac{\partial g_z}{\partial z}\right) = 0.\tag{191}$$

The pressure of the base state is $p = \pi\rho^2\mathcal{G}(h^2 - r^2)$, and thus, at first order,

$$-\frac{1}{\rho}\frac{\partial^2 p}{\partial z^2} = -2\pi\rho\mathcal{G}h_0\frac{\partial^2 \epsilon}{\partial z^2}.\tag{192}$$

The radial gravity g_r is altered by the radius corrugations $\epsilon(z,t) \sim \mathrm{e}^{\mathrm{i}kz - \mathrm{i}\omega t}$ and the associated modulations of the local mass as

$$g_r = 2\pi\rho\mathcal{G}r\left(1 + \frac{2}{\pi}|k|\epsilon\right).\tag{193}$$

Namely, crests and troughs, where $g_z = 0$, are separated by a longitudinal distance $\lambda/2 = k/\pi$. The longitudinal gravity g_z, which is zero in the straight cylinder configuration, is thus given by the Poisson equation as

$$\frac{\partial g_z}{\partial z} = 4\pi\rho\mathcal{G} - \frac{1}{r}\frac{\partial}{\partial r}(r g_r),\tag{194}$$

$$= -4\pi\rho\mathcal{G}\frac{2}{\pi}|k|\epsilon.\tag{195}$$

Thus, from (191), the dispersion relation reads

$$\omega^2 = \frac{1}{T^2}\left(-\frac{4}{\pi}|k|h_0 + (kh_0)^2\right),\tag{196}$$

$$T^2 = \frac{1}{\pi\rho\mathcal{G}}.\tag{197}$$

The gravitational collapse occurs for a wavenumber given by the inverse of the jet radius, at a rate $1/\sqrt{\pi\rho\mathcal{G}}$, independent of the radius, as expected from (187). These features are correctly reproduced (unlike the numerical value of the cut-off wavenumber and the detailed dependence of $\omega(k)$ at $k = 0$) compared with the true dispersion relation, given in Chandrasekhar [145]:

$$\omega^2 = -4\pi\rho\mathcal{G}kh_0\frac{I_1(kh_0)}{I_0(kh_0)}\left(K_0(kh_0)I_0(kh_0) - \frac{1}{2}\right).\tag{198}$$

In [145] it is also noted that all purely non-axisymmetric perturbations are stable, consistent with our qualitative argument above.

4. Breakup

4.1. Overview

The initial stages of breakup are governed by linear theory. Since growth is exponential, this gives a good estimate of the total time to breakup, and thus of the breakup length of a jet, as discussed in section 3.12 above. Yet the growth of sinusoidal modes cannot even explain basic features such as satellite drops, so the inclusion of nonlinear effects is essential. The aim of this section is to explain what actually takes place as the radius of the fluid neck goes to zero, to produce a theory of drop formation from the continuum perspective.

Near breakup, the typical size of the solution goes to zero, and thus does not possess a characteristic scale. It is therefore natural to look for solutions that are *invariant* under an appropriate scale transformation, i.e. to look for similarity solutions. We choose the intrinsic scales (27) as units of length and time, and the point z_0, t_0 where the singularity occurs as the origin of our coordinate system. The dimensionless coordinates are thus $z' = (z - z_0)/\ell_\nu$ and $t' = (t_0 - t)/t_\nu$. In the simplest case that a one-dimensional description (29), (30) is appropriate, we expect a similarity description

$$h(z,t) = \ell_\nu |t'|^{\alpha_1}\phi(\xi), \qquad v(z,t) = (\ell_\nu/t_\nu)|t'|^{\alpha_2}\psi(\xi),$$

$$\xi = z'/|t'|^\beta, \tag{199}$$

as first postulated in [29].

To calculate the values of the exponents, one must know the balance of terms in the original equation, or its one-dimensional counterpart. We will see below that in the absence of an outer fluid, asymptotically breakup always proceeds according to a solution first described in [21], which balances surface tension, viscous and inertial forces. However, for extreme values of the Ohnesorge number (6), other *transient* regimes are possible. For example if the viscosity is small ($Oh \ll 1$), it must initially drop out of the description. Assuming that the solution is governed by a single length scale, determined by the minimum radius $h_{\min}$, it follows from dimensional analysis that $h_{\min} \propto (\gamma((t_0 - t)^2/\rho)^{1/3}$, and thus $\alpha = \beta = 2/3$ [22, 289].

In the opposite limit still another scaling solution is found [290], characterized by a set of *irrational* scaling exponents, an example of self-similarity of the second kind [291, 292]. Both viscous and inviscid similarity solutions eventually *cross over* to the asymptotic solution [21]. If an outer fluid is present, it will exert a shear force which leads to a crossover to still another solution [293, 294] in which the simple self-similar form (199) is broken by the presence of *logarithmic terms*.

Once microscopic scales are reached, it was predicted [295, 298] that thermal noise drives the pinching and changes the qualitative behaviour of the solution. This was confirmed by recent experiments for very small surface tension [299]. The different scaling regimes to be described in this section are summarized in table 2, demonstrating the remarkable richness of the phenomenon, even in the context of Newtonian fluids.

Table 2. Balances of inertia (I), surface tension (ST), viscosity (V), noise (N) and gravity (G) that may appear during pinching of Newtonian fluids. The absence of an outer fluid is marked (NO), of an inner fluid (NI), and the general case is (GEN). The typical size of the profile in the radial direction is Δt^α, in the axial direction Δt^β.

Balance	α	β	Logs	Reference
ST-I-V, NO	1	1/2	No	[21]
ST-V, NO	1	0.175...	No	[290]
N-I-V, NO	0.418...	1/2	No	[295]
G-V, NO	1/2	$-1/2$	No	[296]
I-ST, GEN	2/3	2/3	No	[22, 289]
ST-V, GEN	1	1	Yes	[22, 289]
ST-V, NI	1	0	No	[137]
I, NI	1/2	1/2	Yes	[141]
I, GEN	1/3	1/3	No	[297]

4.2. Asymptotics of viscous breakup

It is easy to confirm that with the choice $\alpha_1 = 1$, $\alpha_2 = -1/2$, $\beta = 1/2$, the self-similar profile (199) solves the slender-jet equations (29)–(31), in which all terms are balanced as $t' \to 0$. The scaling implies that ϵ is proportional to $|t'|^{1/2}$, thus higher-order terms in the expansion in ϵ go to zero as the singularity is approached. In addition, (29)–(31) is now transformed into a similarity equation for the scaling functions ϕ, ψ:

$$\pm(-\phi + \xi\phi'/2) + \psi\phi' = -\psi'\phi/2, \tag{200}$$

$$\pm(\psi/2 + \xi\psi'/2) + \psi\psi' = \phi'/\phi^2 + 3(\psi'\phi^2)'/\phi^2. \tag{201}$$

The plus sign refers to the time before breakup ($t < t_0$), for ($t > t_0$) all terms involving time derivatives change sign. Equations (200) and (201) were rederived in [300] starting directly from a similarity solution of the Navier–Stokes equation, choosing the similarity exponents appropriately.

Let us focus first on the time before breakup. As it stands, the system (200) and (201) has many solutions; which is selected depends on matching conditions [138] to the flow away from the singularity. At a finite value of the *outer variable* z', $h(z,t)$ remains finite as $t' \to 0$; this corresponds to the physical condition that the outer solution cannot follow the singular motion near the singularity. As the *inner variable* ξ goes to infinity, (199) then implies that

$$\phi(\xi)/\xi^{\alpha_1/\beta} = \phi(\xi)/\xi^2 \to a_0^\pm \qquad \text{for } \xi \to \pm\infty. \tag{202}$$

A WKB analysis [301] of (200), (201) reveals that solutions that grow quadratically at plus or minus infinity form a two-dimensional submanifold of the three-dimensional space of solutions. Thus each of the two conditions (202) corresponds to one real condition on the solution. In addition, it is readily seen that (201) has a movable singularity at the 'sonic point' ξ_0 [302] with $\psi(\xi_0) + \xi_0/2 = 0$. Avoiding this singularity corresponds to another condition, so that only one unique physical solution remains [21].

More precisely, there is a discrete sequence of solutions, corresponding to increasingly thin threads [303], but numerical evidence [120] suggests that only the first solution in the sequence is linearly stable and thus physically realizable. We return to question of stability in section 4.2.1 below.
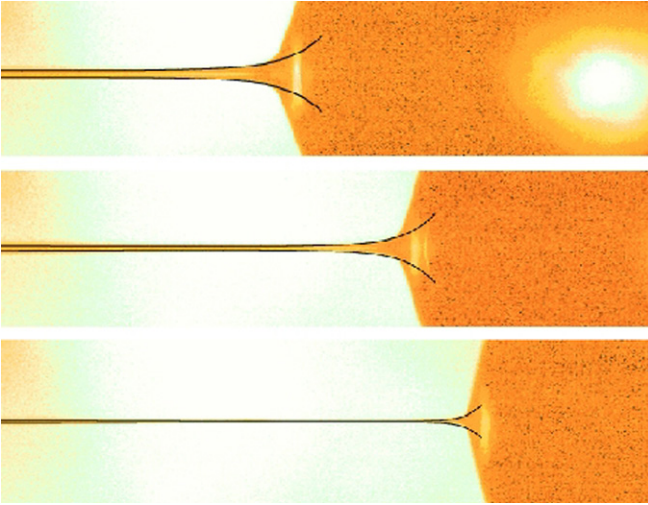
Figure 49. A sequence of interface profiles of a jet of glycerol close to the point of breakup [304] (the centre of the drop being formed is seen as a bright spot in the top picture). The experimental images correspond to $t_0 - t = 350$, 298 and 46 μs (from top to bottom). Corresponding analytical solutions based on (200), (201) are superimposed [120]. There is no adjustable parameter in the comparison.

The minimum of the only stable similarity solution is $\phi_{\min} = 0.030\,426\ldots$ [120]. In figure 49, this solution is compared with an experimental sequence of photographs of a viscous jet near breakup. Owing to the scaling $\ell_r = |t'|^{1/2}\ell_z$ the similarity solution appears increasingly elongated, leading to a thin thread connecting two drops (of which only one is shown). In summary, asymptotically pinch-off is described by the 'Navier–Stokes solution', which has the form

$$h(z, t) = \ell_\nu |t'| \phi_{\mathrm{NS}}(z'/|t'|^{1/2}),$$
$$v_0(z, t) = (\ell_\nu/t_\nu)|t'|^{-1/2}\psi_{\mathrm{NS}}(z'/|t'|^{1/2}). \tag{203}$$

The universality of pinching solutions has remarkable consequences: at a time Δt away from the singularity the minimum radius of a fluid thread is $h_{\min} = 0.0304\gamma\,\Delta t/\eta$, independent of the initial jet radius [304]. The values of the constants $a_0^+ = 4.6$ and $a_0^- = 6 \times 10^{-4}$ are also universal properties of the similarity solution, indicating the extreme asymmetry of the solution. On its steep side, it merges onto the drop, on the other it forces the shape into a thin thread. Thus the universal properties of the local solution impose a certain structure onto the *global* form of the pinch-off. This is remarkable, since in most matching problems, such as the prototypical Prandtl boundary layer [42], the inner solution depends on constants provided by the outer solution. Some universal properties of the Navier–Stokes solution, as well as other similarity solutions, introduced below, are summarized in table 3.

4.2.1. Approach to the singularity. The comparison with experiment in figure 49, as well as a host of more recent experiments (for example, figure 61 below), indicate that the convergence onto the similarity solution is rather quick. This explains why the basic nonlinear features of breakup,

Table 3. Universal properties of similarity solutions corresponding to the three possible balances in the absence of an outer fluid. The fourth row applies to the breakup of one fluid inside another fluid of equal viscosity. The second column refers to symmetry with respect to the pinch point, the third column to the three scaling exponents α_1, α_2, and β defined by (199). The + sign in the third column refers to a logarithmic correction. The fourth column is the prefactor of the minimum radius, defined by $\phi_{\min} = h_{\min}/t'^{\alpha_1}(t_\nu^{\alpha_1}/\ell_\nu)$.

Balance	Symmetry	Exponents	$\phi_{\min}$
Navier–Stokes	No	$1, -1/2, 1/2$	0.0304
Stokes	Yes	$1, -0.825, 0.175$	0.0709
Euler	No	$2/3, -1/3, 2/3$	0.7
Outer	No	$1, -1, 0+$	0.0328

such as satellite drops (see section 4.7.1 below) are explained by considering the self-similar asymptotics of breakup. To understand the convergence to the similarity solution, it is useful to linearize the slender-jet equations (29)–(31) around this *time-dependent* solution. To do this, a very useful trick is to keep the full time dependence in the similarity transformation (203), but to pass to the *logarithmic* time $\tau = -\ln|t'|$ [305]:

$$h(z, t) = \ell_\nu |t'|\phi(\xi, \tau), \quad v(z, t) = (\ell_\nu/t_\nu)|t'|^{-1/2}\psi(\xi, \tau). \tag{204}$$

Inserting this into (29), (30), one obtains for the dynamics leading up to breakup:

$$\left.\begin{aligned}
\partial_\tau\phi &= \phi - \xi\phi'/2 - \psi\phi' - \psi'\phi/2, \\
\partial_\tau\psi &= -\psi/2 - \xi\psi'/2) - \psi\psi' + \phi'/\phi^2 + 3(\psi'\phi^2)'/\phi^2.
\end{aligned}\right\} \tag{205}$$

The important point to note is that the similarity solution (203) is a *fixed point* of the system (205), greatly simplifying a linear analysis.

Namely, denoting the similarity solution by ϕ_{NS}, the general evolution can now be written as

$$\phi(\xi, \tau) = \phi_{\mathrm{NS}}(\xi) + \sum_i a_i(\tau)\Phi_i(\xi), \tag{206}$$

where $\{\Phi_i\}$ is a suitable set of basis functions. For simplicity, we will only consider the similarity solution corresponding to $h(z, t)$; the velocity field is treated analogously. Inserting (206) into (205), and neglecting terms quadratic in a_i, one arrives at a linear set of equations

$$\partial_\tau a_i(\tau) = M_{ij}a_j. \tag{207}$$

If the largest eigenvalue ν_1 of M_{ij} is negative, the corresponding similarity solution is stable and will be approached exponentially. In terms of the minimum radius, for example, this means that

$$h_{\min} = \ell_\nu t'(\phi_{\min} + \Phi_1(0)t'^{-\nu_1} + \ldots), \tag{208}$$

if $\Phi_1(\xi)$ is the eigenfunction corresponding to ν_1. Thus one finds a correction familiar from the theory of critical phenomena [306]. As shown in [307], the eigenfunction Φ_1 has the asymptotic behaviour

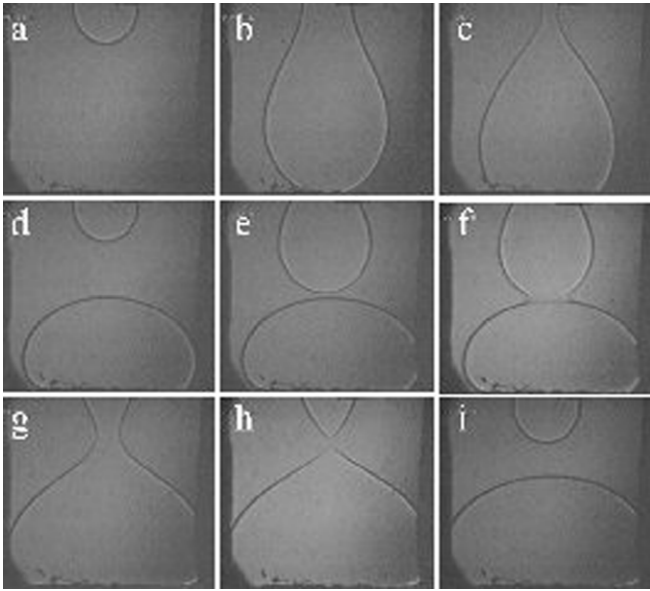$$\Phi_1(\xi) \propto \xi^{2-2\nu_1}. \tag{209}$$

Figure 50. Nine images (of width 3.5 mm) showing how a ^{3}He crystal 'flows' down from the upper part of a cryogenic cell into its lower part [308]. The recording takes a few minutes, the temperature is approximately 0.32 K. The crystal first 'drips' down, so that a crystalline 'drop' forms at the bottom (a)–(c); then a second drop appears (d) and comes into contact with the first one (e); coalescence is observed (f) and subsequently breakup occurs (h).

In terms of the spatial structure, analysing (206) for large ξ, this implies that convergence occurs in a fixed region *in space*. In terms of the similarity variable ξ the region of convergence *expands* as $t'^{-1/2}$ [21].

The program of calculating ν_1 has unfortunately not yet been carried out for the Navier–Stokes solution, although numerical evidence [21] unequivocally shows that ν_1 is indeed negative. As for the infinite sequence of additional solutions found in [303], it was reported that they are extremely unstable numerically, indicating that the corresponding exponent ν_1 is positive. However, the calculation has been performed for the related problem of the capillary breakup of a cylinder by surface diffusion [307]. The situation parallels the fluid problem exactly: there is an infinite sequence of similarity solutions, which can be ordered according to their decreasing minimum radius. Only the solution with the largest radius is found to be stable, all others are unstable. The same observation holds true in the pinch-off of a very viscous fluid, discussed in section 4.3.2 below.

There are however examples of pinch-off problems for which a different type of behaviour is observed: the exponent ν_1 vanishes, a situation called 'type II singularity' [309]. In that case convergence towards the similarity solution is much slower, and logarithmic factors arise. One such example, known as 'mean curvature flow', is illustrated in figure 50: the 'dripping' of a ^{3}He crystal, surrounded by its melt [310]. The surface shape may change only by melting and freezing, driven by gravity and surface tension forces. Close to pinch-off, where surface tension dominates, this leads to the equation

$$\frac{dh}{dt} = -K\sqrt{1 + h'^2}\,\kappa, \qquad (210)$$

where K is a constant and κ the mean curvature. A detailed analysis of (210) was performed in [311], using an expansion of the type (206). The result for the minimum radius is

$$h_{\min} = \sqrt{2K\Delta t}\left[1 - \frac{1}{\tau} + O(\tau^{-2})\right], \qquad (211)$$

where $\tau = -\ln(K\Delta t/h_0^2)$, implying only logarithmic convergence onto the similarity solution. In space, convergence only occurs in a finite region of order one *in similarity variables* [310], and thus only describes a region of size $|t'|^{1/2}$ in space.

4.3. Other scalings and crossover

The universality of the solution described by (200), (201) of course implies that it holds equally well for the water jet shown in figure 12, as it does for the glycerol jet of figure 13. The reason this common feature is not immediately apparent is that viscosity only becomes important on a scale of $\ell_\nu \approx 10$ nm for water (cf table 1). To measure the Navier–Stokes solution one would need to observe the neighbourhood of the point of breakup under extreme magnification. For the more relevant part of the evolution where the minimum radius $h_{\min}$ is much larger than ℓ_ν, one can neglect viscosity, so that figures 12 or 14 are effectively described by inviscid dynamics.

Thus to understand the scaling properties of pinch-off on a given scale of observation r_0 (such as the nozzle radius), one has to take into account the phenomenon of crossover: if initially $r_0 \gg \ell_\nu$, the dynamics is characterized by a balance of inertial and surface tension forces. As $h_{\min}$ reaches ℓ_ν, the dynamics changes towards an inertial-surface tension-viscous balance. If on the other hand $r_0 \ll \ell_\nu$ initially, inertia cannot play a significant role: the dynamics is dominated by viscosity and surface tension. In the course of this evolution, however, inertia becomes increasingly important and finally catches up with the other two. As a result, the same universal solution as before is finally observed.

4.3.1. Inviscid pinch-off. Unfortunately, inviscid pinch-off is not described by slender-jet equations: the profile *overturns* and the parametrization $h(z, t)$ fails. Instead, one needs to solve the full inviscid equations (17)–(19), which is done conveniently using the boundary integral description (19)–(21). Inviscid similarity solutions were first found by Chen and Steen [289] for the case that the jet is surrounded by another fluid of the same density; this includes the pinch-off of a soap bubble, the air assuming the role of the fluid. The case that the outer fluid is negligible was treated in [22], the most general case of arbitrary density ratios $D = \rho_{\text{out}}/\rho$ in [52].

The inviscid equations for the free surface $\boldsymbol{x} = (z, r)$ can be recast in similarity variables using the length $\ell_{\text{in}} = (\gamma\Delta t^2/\rho)^{1/3}$ [52]:

$$R = r/\ell_{\text{in}}, \qquad Z = (z - z_0)/\ell_{\text{in}},$$
$$\Phi = (\phi - \phi_0)\Delta t/\ell_{\text{in}}^2. \qquad (212)$$

We will call the solution $(Z(\xi), R(\xi))$ of the corresponding *time independent* equation the 'Euler solution'. Like the
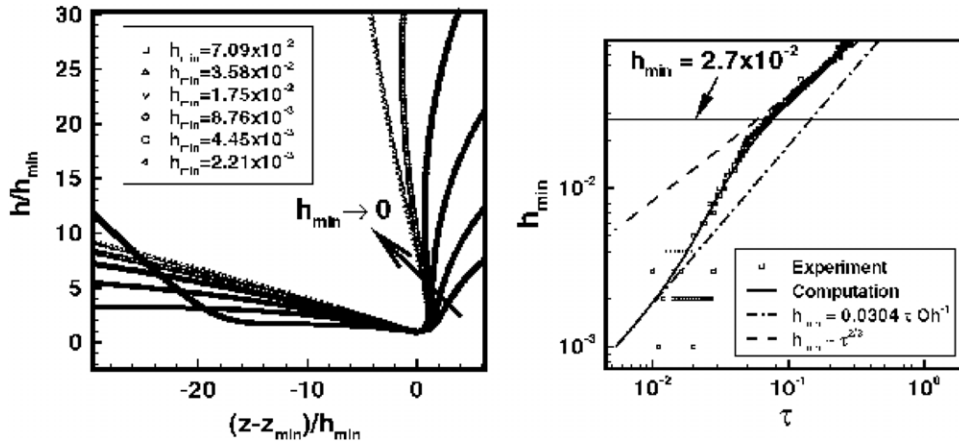
Figure 51. (Left) Profiles from a Navier–Stokes simulation of the pinch-off of a water drop ($Oh = 1.81 \times 10^{-3}$), the axes are rescaled by $h_{\min}$. (Right) $h_{\min}/r_0$ for a 83% glycerol–water mixture ($Oh = 1.63 \times 10^{-1}$), showing crossover from the Euler to the Navier–Stokes solution. Reprinted with permission from [74]. Copyright 2002 by the American Physical Society.
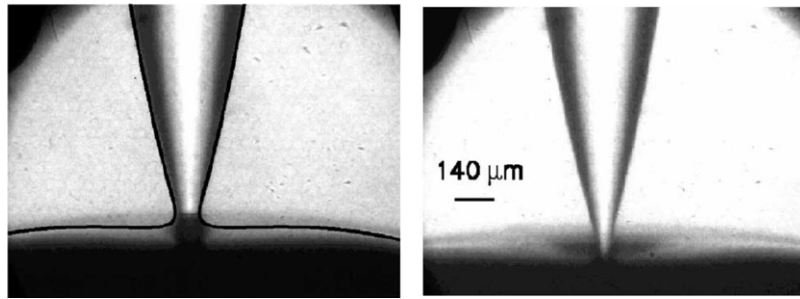

Figure 52. Closeup of the pinching of a water drop [74]. The left picture is a comparison with a full Navier–Stokes simulation, the right picture is taken at an angle to show overturning. Reprinted with permission from [74]. Copyright 2002 by the American Physical Society.

Navier–Stokes solution, it is completely universal. For all density ratios D, similarity solutions are found to have a double-cone shape, (cf figure 51), with one shallow angle, the other *larger than* 90°, so the profile is always predicted to overturn. This was found theoretically by Schulkes [53], cf figure 14, but overturning had long before been seen experimentally [20]. For $D = 0$ the minimum radius is given by $h_{\min} = 0.7(\gamma \Delta t^2/\rho)^{1/3}$, the two angles are 18.1° and 112.8°; these are all universal properties of the Euler solution, independent of initial conditions, see table 3. Experimentally, photographs thus have to be taken at an angle to show the overturning, cf figure 52 (right).

The left panel of figure 51 shows a numerical simulation of the pinch-off of a water drop. The profiles are rescaled using the minimum thread radius, so they approach the inviscid similarity solution as $\Delta t \rightarrow 0$. However, the inviscid scaling does not remain valid, since the viscous term becomes increasingly important. This is easily confirmed by inserting the Euler solution into (13) and comparing magnitudes [293]. A crossover is expected to occur when the minimum radius reaches the viscous scale ℓ_ν [292], or

$$\frac{h_{\min}^{\text{Eu} \rightarrow \text{NS}}}{R} \approx Oh^2. \tag{213}$$

Such a crossover is seen in figure 51, where the minimum radius first follows the Euler solution, and then starts to cross over at about $h_{\min}/r_0 = 2.5 \times 10^{-2}$, until the Navier–Stokes

solution is finally reached at $h_{\min}/r_0 = 3 \times 10^{-3}$. The above prediction (213) amounts to $h_{\min}^{\text{Eu} \rightarrow \text{NS}}/R \approx 2.6 \times 10^{-2}$, in very good agreement with numerical simulations.

For $D \geqslant 6.2$ pre-breakup solutions are found to be subject to an oscillatory instability, and for $D \geqslant 11.8$ they disappear altogether when the original branch of similarity solutions bifurcates. It is an open question how pinch-off is reached for $D > 6.2$; an intriguing possibility is that pinch-off becomes inherently unsteady. Some earlier work [312, 313], reinforced by more recent studies [141, 297, 314], has shown that the limiting case $D \rightarrow \infty$ (breakup of a gas bubble in water) is special, and leads to new scaling behaviour studied in section 4.4.2 below.

4.3.2. Very viscous pinch-off. We now turn to the case of large viscosity, $Oh \gg 1$, such that inertia will initially be subdominant, first studied in [290]. As an aside, a freely suspended drop will *never* break up in this limit, regardless of the initial condition [315]. We will see below that in this limit pinch-off is described by (199) with $\beta < \alpha_1$, i.e. the jet is slender and the long-wave description (29)–(31) applies with the lhs of (30) put to zero. Since the density ρ cannot figure in a description without inertia, the only scale is the capillary velocity $v_\eta = \gamma/\eta$. Thus assuming that there is only a single length scale characterizing the similarity solution, on dimensional grounds one would expect $\ell_r = \ell_z = v_\eta(t_0 - t)$.

This would imply that $\alpha_1 = \beta = 1$. However, multiplying (30) by h^2 (neglecting inertia), integrating and using (31), one finds

$$h + 3v_0'/v_\eta = T(t), \tag{214}$$

where $T(t)$ is the tensile force in the fluid thread [316]. It is easy to confirm that the inertia-less problem (29), (214) is *invariant* under the transformation $z = a\tilde{z}$. But this means that for any solution $h(z, t)$ there is another profile whose axial scale is stretched by an arbitrary factor a, so the local profile close to pinch-off *cannot* be universal. Rather, there must be an *external* length scale ℓ_{ex} such as the nozzle radius r_0 entering the local scale ℓ_z, making this a self-similar problem of the second kind [291]. One expects ℓ_z to have the general scaling form [291] $\ell_z = (v_\eta(t_0-t))^\beta \ell_{ex}^{1-\beta}$, where the exponent β is no longer fixed by any dimensional argument, but will in general assume an irrational value.

To compute β, it is useful to introduce the *Lagrangian* position $z(\alpha, t)$ of a fluid volume, labelled by α [317]. With the transformations

$$\partial_\alpha z = 1/h^2, \qquad \partial_t z = v_0 \tag{215}$$

(29) is satisfied identically, and (30) can be written as a single second-order equation for $z(\alpha, t)$ [120]. In the Stokes case (214), the equation for the Lagrangian profile $H(\alpha, t) \equiv h(z(\alpha, t), t)$ becomes

$$H - 6v_\eta\partial_t H H = T(t), \tag{216}$$

where all spatial derivatives have dropped out of the equation. The equivalent of the similarity form (199) in Lagrangian variables is

$$H(\alpha, t) = \ell_v |t'| \chi(\zeta), \qquad \zeta = ((\alpha - \alpha_0)/\ell_v^3)/|t'|^{2+\beta},$$
$$T = |t'|\bar{T}. \tag{217}$$

Note that formally other asymptotic behaviours of T are possible [318, 319], but simulations [290] and experiment [320] show that (217) is selected. Inserting (217) into (216) leads to the similarity equation

$$\bar{T} = \chi + 6\chi^2 - 6(2 + \beta)\zeta\chi'\chi, \tag{218}$$

where the constant of integration can be computed by noting that $H^{-2} = \partial_\alpha z$, and therefore $\chi^{-2} = F'$ for a suitable $F(\zeta)$. Then, dividing (218) by χ^4 it follows that $\bar{T}/\chi^4 - 1/\chi^3$ is a total derivative, and thus

$$\bar{T} = \int_{-\infty}^{\infty} \chi^{-3}(\zeta)\,d\zeta \Big/ \int_{-\infty}^{\infty} \chi^{-4}(\zeta)\,d\zeta \tag{219}$$

by integrating from $-\infty$ to ∞.

The integral constraint (219) can now be turned into an equation for β, using the *symmetric solution*

$$\zeta = \left(\frac{6(1+\beta)}{2+\beta}\right)^{(3+2\beta)/2} \left[\chi + \frac{3+2\beta}{12(1+\beta)}\right]^{(3+2\beta)/2} (\chi - \chi_{min})^{1/2} \tag{220}$$

of (218). The form of the solution (220) assumes implicitly a quadratic minimum, which is given by $\chi_{min} = 1/(12(1+\beta))$

and $\bar{T} = (3+2\beta)/(24(1+\beta)^2)$. Using these results, (219) can be converted into a non-linear eigenvalue equation for β:

$$\frac{(1-\beta)(3+2\beta)}{(1+\beta)(3-2\beta)} = \frac{F(-1/2-\beta, 1-\beta; 3/2-\beta; -3-2\beta)}{F(-1/2-\beta, 2-\beta; 5/2-\beta; -3-2\beta)}. \tag{221}$$

A numerical solution, using e.g. MAPLE, gives $\beta = 0.174\,871\,700\,652\,042\,307\,111\ldots$. Once more there is an infinite hierarchy of similarity solutions [303], of which (220), (221) is the first. The sequence of solutions is found by requiring that solutions of (218) have minima of 4th, 6th and higher order. However, arguments advanced in [321] show that all higher order solutions are unstable and converge onto the lowest order solution.

Once β is known, the 'Stokes solution'

$$h(z, t) = \ell_v |t'| \phi_{St}(z'/|t'|^\beta),$$
$$v_0(z, t) = (\ell_v/t_v)|t'|^{\beta-1}\psi_{St}(z'/|t'|^\beta), \tag{222}$$

can be computed [120] using

$$\frac{\xi}{\bar{\xi}} = \int_1^{\phi_{St}/\chi_0} \frac{(x+3+2\beta)^{(1+2\beta)/2}}{x(x-1)^{1/2}}\,dx, \tag{223}$$

where $\bar{\xi}$ depends on initial conditions; this implies that the Stokes solution is universal, up to a single parameter which sets the width of the solution. The minimum radius behaves like $h_{min} = 0.0709v_\eta\Delta t$, see table 3.

For $Oh \gg 1$ pinching is at first symmetric according to (223); however, this solution does not remain valid in the limit of $|t'| \to 0$. Namely, the inertial term in (30) can be estimated as $vv_z \propto v_\eta^2\ell_z/\ell_r^2$, whereas surface tension has the size $(\gamma/\rho)(1/h)_z \propto (\gamma/\rho)/(\ell_z\ell_r)$. Since $\beta < 1/2$ the former grows *more quickly* than the latter, and inertia eventually becomes relevant, leading to a crossover to the asymptotic, highly asymmetric solution. By equating the above estimates, the crossover is expected to occur when the minimum radius is [292]

$$\frac{h_{min}^{St \to NS}}{R} \approx Oh^{2/(2\beta-1)}. \tag{224}$$

Both the predictions of symmetric pinching and its transition to the Navier–Stokes solution is nicely confirmed in figure 53. However, a very careful study of the transition to asymmetric pinching for a drop falling under gravity [320, 322] finds that $h_{min}^{St \to NS}$ is to a good approximation *independent* of viscosity. This contradicts the strong viscosity dependence $h_{min}^{St \to NS} \propto \nu^{-3.1}$ predicted by (224). The reason for this discrepancy is at present not understood. One factor that has not been taken into account is the fact that the transition involves a symmetry breaking, which might delay the crossover. In particular, the transition might depend on the overall geometry (dripping tap or liquid bridge, for example), which may or may not break the symmetry.
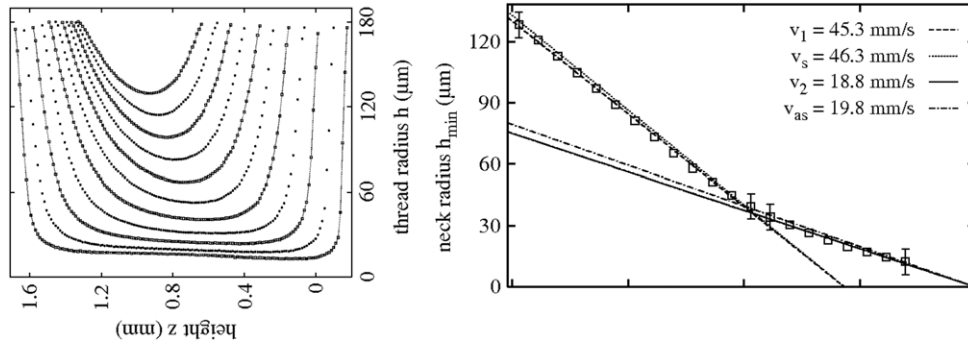
Figure 53. The neck of a falling drop of glycerol–water mixture [320], $Oh = 0.49$, $Bo = 0.047$, making a transition from symmetric (Stokes) to asymmetric (NS) pinching. Accordingly, the rate of pinching changes at the transition point (right). The theoretical predictions for the two solutions are marked by the dotted and the dotted–dashed lines, respectively. Reprinted with permission from [320]. Copyright 2001 by the American Physical Society.

4.3.3. Vanishing surface tension. Finally, the dripping of a viscous liquid in the limit of small surface tension, as may be realized in the recent experiment [299], was considered in [296]. Namely, the Lagrangian equation (216) in the absence of surface tension, but including gravity, can be integrated to give

$$H^2(T, t) = r_0^2 - C(Tt - T^2), \qquad (225)$$

where $C = \rho g Q/(3\eta)$ and Q the volume flow rate from the tap. The Lagrangian marker T is the time at which the corresponding fluid element has emerged from the nozzle, thus $T = 0$ corresponds to the lower edge of the thread, and $T = t$ is the element at the nozzle. The thread radius goes to zero as $h_{\min} \approx r_0\sqrt{2(1 - t/t_0)}$ at $t_0 = 2\sqrt{r_0^2/Q}$, cf table 2. This apparent pinch singularity at zero surface tension is however an artefact of the neglect of inertia: if inertia is added, no singularity occurs [323]. Indeed, t_0 corresponds to the total length of the fluid thread stretching to infinity! Namely, the position of a Lagrangian particle is

$$z(T, t) = \frac{Q}{r_0^2\sqrt{1 - (t/t_0)^2}}\left[\arctan\left(t/\sqrt{t_0^2 - t^2}\right)\right.$$
$$\left. - \arctan\left((2T - t)/\sqrt{t_0^2 - t^2}\right)\right], \qquad (226)$$

which completely determines the thread profile. In particular, the length of the thread diverges as $\sqrt{t - t_0}$.

4.4. Outer fluid: logarithmic scaling

4.4.1. Two viscous fluids Figure 54 shows a drop of viscous liquid pinching off in an ambient fluid of comparable viscosity. The pinch region has a highly asymmetric double-cone structure, qualitatively different from the Stokes solution in the *absence* of an outer fluid. This is not surprising since the velocity field in Stokes flow only decays as $1/r$ (cf (22), (23)), so the outer fluid leads to an effective long-ranged interaction between different parts of the liquid column.

The linear asymptotics of the profile suggests that the solution is characterized by a single length scale $\ell_{\text{out}} \propto v_\eta\Delta t$. However, this solution fails because for a linear profile the first integral on the rhs of (24) diverges as $1/r$ at infinity. As the singularity is approached, the two cones of the far-field solution
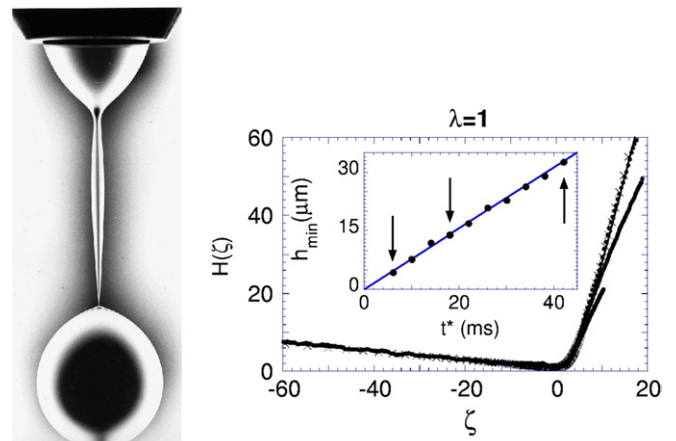

Figure 54. (Left) A drop of glycerin dripping through polydimethylsiloxane (PDMS) near snap-off [294]. The nozzle diameter is 0.48 cm, the viscosity ratio is $\lambda = 0.95$. (Right) the inset shows the minimum radius, $h_{\min}(t)$, as a function of time for the drop shown on the left. The solid line is the theoretical prediction. The main figure shows the similarity function $H(\xi)$ as defined by (227). The dots are rescaled experimental profiles corresponding to the times indicated as arrows in the inset. The solid line is the theory, and the ×'s mark the result of a numerical simulation using (22)–(24). There are no adjustable parameters in the comparisons.

generate a velocity field that diverges as $\ln(\ell_{\text{out}}/r_0)$, where r_0 is some outer length scale [293]. It is therefore natural to try a similarity form which accounts for a corresponding uniform translation [294]:

$$h(z, t) = v_\eta\Delta t\, H(\xi),$$
$$\xi = v_\eta^{-1}(\Delta z/\Delta t) + b\ln(v_\eta\Delta t/r_0) + \xi_0, \qquad (227)$$

with $\Delta z = z - z_0$ and $\Delta t = t_0 - t$. In accordance with (202), the matching condition is

$$H(\xi) \approx s^\pm\xi, \qquad \xi \to \pm\infty. \qquad (228)$$

Inserting (227) into (11) gives

$$-H + H'(V_z^s + \xi - \xi_0 - b) = V_r^s, \qquad (229)$$

where $V^s = V - b\ln(v_\eta\Delta t/r_0)e_z$ and V is the solution of (24) in similarity variables. By properly adjusting the constant
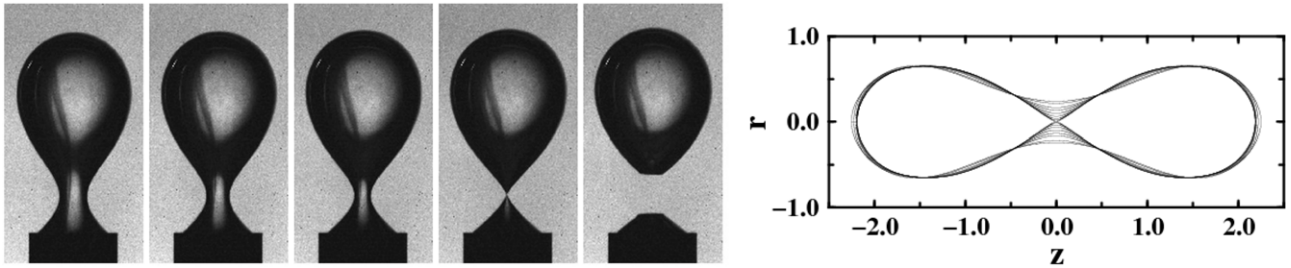
Figure 55. (Left) The pinch-off of an air bubble in water [326]. An initially smooth shape develops a localized pinch point. (Right) Numerical simulation of bubble pinch-off from initial conditions given by the shape with the largest waist; there is no gravity, so all shapes are symmetric about the pinch point. Reprinted with permission from [326], copyright 2007 by the American Physical Society.

b, the singularity can be subtracted to make V_z^s finite in the limit $\Delta t \to 0$. Performing the angular integration (which can be done in terms of elliptic integrals [136]) the integral kernels become:

$$\bar{J}(\xi, \xi') = \frac{H(\xi')}{8\pi} \int_0^{2\pi} J(r) \mathrm{d}\theta,$$

$$\bar{K}(\xi, \xi') = -\frac{3H(\xi')}{4\pi} \int_0^{2\pi} K(r) \, \mathrm{d}\theta, \qquad (230)$$

$$r = (H(\xi) - H(\xi') \cos\theta) e_x + H(\xi') \sin\theta e_y + (\xi - \xi') e_z.$$

Thus the equation for the singular velocity becomes

$$\frac{1 + \lambda^{-1}}{2} V^s(\xi) = \lim_{A \to \infty} \left[-\int_{-A}^A \kappa(\zeta) \bar{J}(\xi, \zeta) n(\zeta) \, \mathrm{d}\zeta + b \ln A e_z \right]$$

$$+ (1 - \lambda^{-1}) \int_{-\infty}^\infty V^s(\zeta) \bar{K}(\xi, \zeta) n(\zeta) \, \mathrm{d}\zeta, \qquad (231)$$

which is finite, iff

$$b = -\frac{1}{4} \left[\frac{s_+}{1 + (s_+)^2} + \frac{s_-}{1 + (s_-)^2} \right]. \qquad (232)$$

The similarity description (229)–(232) was developed in [294], and compared with experiment for the case $\lambda = 1$ (see figure 54), in which case the minimum radius $H_{\min}$ and the asymptotic slopes are

$$H_{\min} = 0.0328, \qquad s_- = -0.105, \qquad s_+ = 4.81. \qquad (233)$$

Simulations [324] and experiments [325] for general λ are reviewed, together with a detailed study of similarity solutions, in [59]. For decreasing outer viscosity (large λ), the shallow slope s^- decreases, while the steep slope increases. However, for $\lambda \geqslant 32$ solutions are subject to an oscillatory instability, and are thus well separated from the Stokes case $\lambda = \infty$ (cf 222), for which solutions are symmetric. In the opposite limit of $\lambda \to 0$ both slopes go to zero. The case $\lambda = 0$ (gas bubble surrounded by a viscous fluid) is another interesting singular limit [137]. Namely, the local cavity radius $h(z, t)$ collapses at a uniform rate $\partial_t h(z, t) = \gamma/(2\eta_{\text{out}})$. The self-similar scaling is lost, and the form of the profile depends entirely on the initial condition.

4.4.2. Bubble breakup in water. Another example in which the fluid exterior to the 'jet' modifies the dynamics in a fundamental way is that of a bubble breaking up in water [141, 297, 314, 326–328]. An example is a bubble rising from a submerged capillary (cf figure 55, left). To a very good approximation, this situation is described by an inviscid fluid surrounding a fluid which is not dynamically active, and thus corresponds to taking the limit $D \to \infty$ in section 4.3.1. Using the same computational techniques as before, simulations of bubble breakup [141] can be produced as shown in figure 55, right. Surprisingly, both experiment and theory suggest that pinch-off occurs with a scaling exponent of $\alpha \approx 0.56$, significantly smaller than the value of 2/3 suggested by scaling theory (212). In particular, this means that surface tension makes a *subdominant* contribution, even in the limit of small $h_{\min}$! Of course, at extremely small scales, both viscosity of the fluid and the presence of the internal gas will become important, see below.

Indeed, initial theories of bubble pinch-off [312, 313] treated the case of an approximately cylindrical cavity, which leads to the radial exponent $\alpha = 1/2$, with logarithmic corrections. Interestingly, in this approximation the problem is essentially equivalent to that of the shape of a cavity behind a high-speed object, treated frequently from the 1940s [130, 142, 329].

However both experiment [326] and simulation [141] show that the cylindrical solution is unstable; rather, the pinch region is rather localized, see figure 55. To describe this cavity, we use the slender-body description (44) developed in section 2.4.3. Since surface tension is subdominant, we can drop the last two terms on the right of (44).

The integral in (44) is dominated by a local contribution from the pinch region. To estimate this contribution, it is sufficient to expand the profile around the minimum at $z = 0$: $a(z, t) = a_0(t) + a_0''(t)/2 z^2 + O(z^4)$. As in previous theories, the integral depends logarithmically on a, but the axial length scale Δ is computed self-consistently from the inverse curvature $\Delta \equiv (2a_0/a_0'')^{1/2}$. Thus evaluating (44) at the minimum, one obtains [141] to leading order

$$\ddot{a}_0 \ln(4\Delta^2/a_0) = \dot{a}_0^2/(2a_0), \qquad (234)$$

which is a coupled equation for a_0 and Δ. Thus, a second equation is needed to close the system, which is obtained by
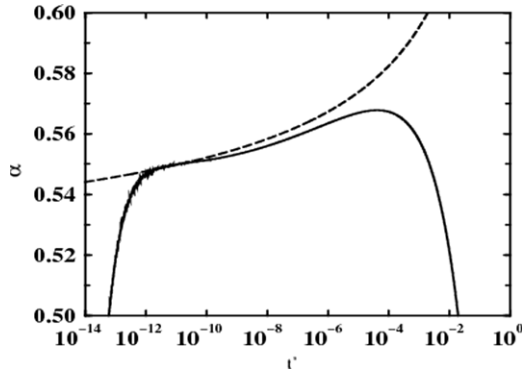
Figure 56. A comparison of the exponent α between full numerical simulations of bubble pinch-off (——) and the leading-order asymptotic theory (239) (- - - -).

evaluating the second derivative of (44) at the pinch point [141]:

$$\ddot{a}_0'' \ln\left(\frac{8}{e^3 a_0''}\right) - 2\frac{\ddot{a}_0 a_0''}{a_0} = \frac{\dot{a}_0 \dot{a}_0''}{a_0} - \frac{\dot{a}_0^2 a_0''}{2a_0^2}. \quad (235)$$

Equations (234), (235) are most easily recast in terms of the time-dependent exponents

$$2\alpha \equiv -\partial_\tau a_0/a_0, \qquad 2\delta \equiv -\partial_\tau a_0''/a_0'', \quad (236)$$

where $\tau \equiv -\ln t'$ and $\beta = \alpha - \delta$, are a generalization of the usual exponents α and β defined by (199). The exponent δ characterizes the time dependence of the aspect ratio Δ. Now we expand the values of α and δ around their expected asymptotic values 1/2 and 0:

$$\alpha = 1/2 + u(\delta)\delta = v(\delta). \quad (237)$$

To leading order in δ, the resulting equations are

$$\partial_\delta u = -8vu^2, \qquad \partial_\delta v = -8v^3, \quad (238)$$

which describe perturbations around the leading-order similarity solution, which is a collapsing cylinder. These equations are analogous to (207), but they have a degeneracy of third order, leading to zero eigenvalues. Equations (238) are easily solved to yield, in an expansion for small δ [141],

$$\alpha = 1/2 + \frac{1}{4\sqrt{\tau}} + O\tau, \qquad \delta = \frac{1}{4\sqrt{\tau}} + O(\tau^{-3/2}). \quad (239)$$

Thus the exponents converge towards their asymptotic values $\alpha = \beta = 1/2$ only very slowly, as illustrated in figure 56. This explains why typical experimental values are found in the range $\alpha \approx 0.54$–0.58 [326], and why there is a weak dependence on initial conditions [327].

4.4.3. Suction. The presence of an inner fluid will eventually become important [297, 330]. In a symmetrical situation, the inner fluid will resist pinch-off, thus leading to the formation of tiny satellite bubbles, which have also been seen experimentally [326, 328]. In an asymmetrical situation, i.e. if there is a gas flow Q across the pinch region, the inner gas can significantly enhance pinch-off [297]. To analyse this

situation, it is useful to consider a rough estimate, based on a local version of (44).

Namely, disregarding logarithmic factors, one might approximate the term on the left of (44) as $\ddot{a} \ln(h_0^2/a)$, where the jet radius h_0 provides the cut-off. According to Bernoulli's equation, the gas flow generates a *suction* $p_0 = -\rho_a v^2/2$. Thus, since the volume flow rate $Q = hv^2$ of the gas along the cavity is conserved, one obtains

$$\ddot{a} \ln(h_0^2/a) = \frac{\dot{a}^2}{2a} - \frac{4\gamma}{\rho}\kappa + \frac{2\rho_a}{\rho}\frac{Q^2}{a^2}. \quad (240)$$

This description is equivalent to that given in [312, 313] and worked out in detail in [331]. A balance of the first two terms correctly captures the leading expression $\alpha = 1/2$ of (239), but with incorrect logarithmic corrections.

However, as a goes to zero, the last Bernoulli term in (240) becomes important. Balancing it against the inertial term on the right, one finds $\alpha = 1/3$, up to logarithmic corrections. This is even more singular than the exponent of $\alpha \approx 1/2$, observed without gas flow. The new scaling exponent has been observed experimentally in a setup with external fluid flow, which provokes a breaking of the symmetry.

4.5. Noise

Thermal fluctuations become important if the jet diameter is small, to be distinguished from macroscopic noise, that is responsible for the random breakup of ligaments, and whose origin presumably lies in the non-linear character of jet dynamics. These issues will be addressed in section 5. The length scale where thermal fluctuations become important is the scale where the thermal energy becomes comparable to the surface energy, giving [332]

$$\ell_T = (k_B T/\gamma)^{1/2}. \quad (241)$$

For typical fluids at room temperature, this length is about a nanometre, corresponding to the size of the jet shown in figure 57. Thus the character of the breakup is changed qualitatively, yet the jet still has a coherent appearance. Thus it is possible to describe the fluid in a continuum picture [298], but with fluctuations taken into account, as we will do below.

Fortunately, for small system sizes, molecular dynamics (MD) simulations, which take into account the microscopic interaction potentials between particles, become feasible. Figure 58 shows such a MD simulation of a jet of propane, emanating from a gold nozzle 6 nm in diameter. The initial (linear) stages of breakup are well described by standard hydrodynamic theory, in agreement with other MD studies [333], and the jet eventually decays into droplets. Strikingly, satellite drops are almost completely absent, although they are a universal feature of macroscale breakup. The reason is seen in figure 58: the profile near the pinch point has a symmetric double-cone structure, very different from the thread-like structures expected in the absence of noise, and shown in the simulation marked 'LE'. This means that fluctuations become relevant on a scale of nanometres, thereby changing the character of the breakup qualitatively.
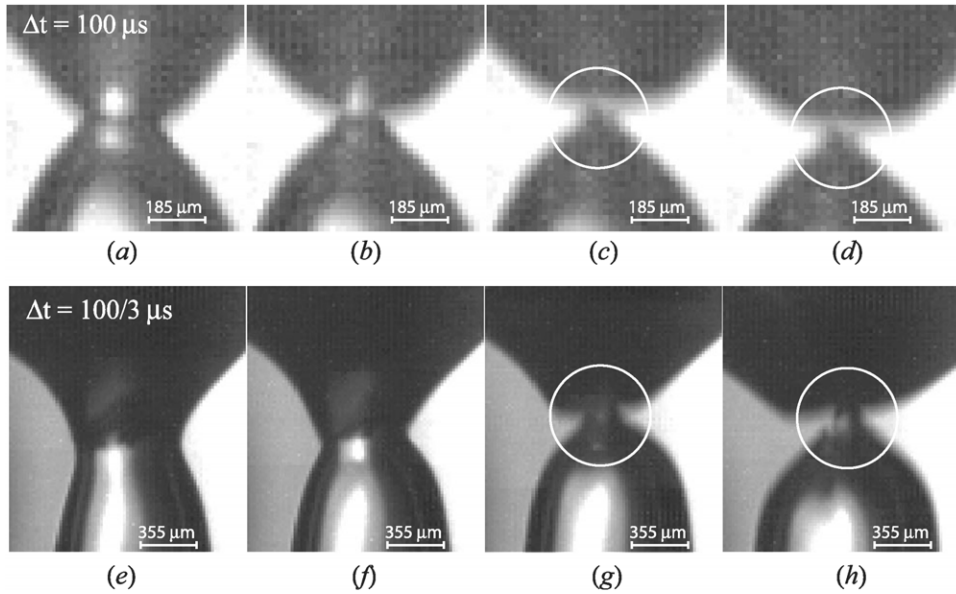
Figure 57. A fast gas jet blowing through an inertial liquid. The bubble pinches off extremely violently. Adapted from [297], with permission. Original figure copyright 2005 by the American Physical Society.
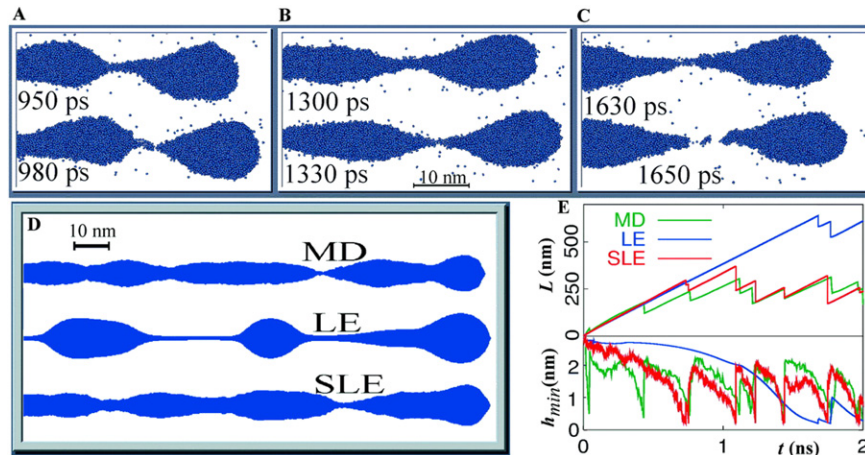

Figure 58. A comparison between MD simulations of the jet in figure 5 and simulations of (246) for $M_l = 0$ (no noise, curves and profiles marked LE) and $M_l = 0.24$ (marked SLE). From [298]. Reprinted with permission from AAAS.
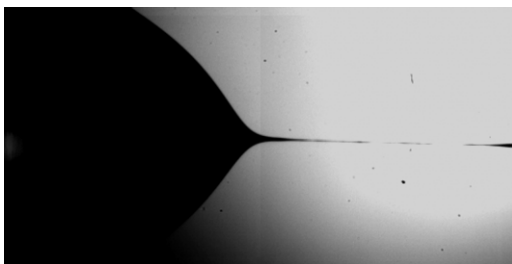

Figure 59. A drop of silicone oil, viscosity $\eta = 300$ mPa, falling from a tap [334]. The width of the frame is 2 mm. Just before breakup, the thin thread has become unstable and produced several 'bumps'. The moment of breakup shows irregular breakup at several places.

However, it was noticed [335] that thin viscous threads produced for large viscosity (cf figure 13) are very sensitive to perturbations, as illustrated in figure 59. Although the thread is still about 10 μm in radius, it has become irregular in appearance and breaks up in several places. This is related to the fact that the shape of the thread is close to a cylinder, and thus susceptible to the Rayleigh instability. Thus the effect of noise may show up on a scale much larger than (241). We return to the stability of viscous threads below.

To derive a consistent description of these phenomena, the effect of thermal noise has to be added to equation (30) for the velocity field. The noise is added to the stress tensor, making sure that *local* thermal equilibrium is preserved [42], thus in addition to the viscous contribution to the slice equation (32) one has

$$3\nu h^2 v' + s/(\pi\rho), \tag{242}$$

with white noise

$$\langle s(z_1, t_1)s(z_2, t_2)\rangle = 6\pi k_B T \eta h^2(z_1)\delta(z_1 - z_2)\delta(t_1 - t_2). \tag{243}$$

The noise amplitude is proportional to the volume of a slice of fluid, as expected. The slice equation (32) with added

45

noise thus becomes

$$\partial_t(h^2 v) + (h^2 v^2)' = -\frac{\gamma}{\rho} G' + 3\nu(h^2 v')' + \frac{6}{\pi}\frac{k_B T}{\rho}\nu(h\xi)'. \tag{244}$$

Here we have used the fact that G, as defined by

$$G = -\frac{h}{\sqrt{1 + h'^2}} - \frac{h^2 h''}{\sqrt{1 + h'^2}^3}, \tag{245}$$

obeys the relation $G' = h^2\kappa'$.

The form (244) of the equation of motion is still awkward to treat numerically, since it contains derivatives of the singular process ξ. This can be overcome by introducing the integral $P(z) = \int_0^z m(x)\,dx$ of the momentum, so (244) can be integrated. Non-dimensionalizing the equations using the intrinsic scales (27), there remains a single quantity [298] $M_l = \ell_T/\ell_\nu$ characterising the strength of the noise. Thus we finally arrive at the conserved form of the equations

$$\partial_t h^2 = -P'', \tag{246}$$

$$\partial_t P = -(P'^2/h^2) - G + 3h^2(P'/h^2)' + M_l\frac{6}{\pi}h\xi.$$

4.5.1. Nanojets. In figure 58, MD simulations are compared with stochastic simulations of (246). The dimensionless noise strength M_l is of order unity, thus pinch-off is expected to change qualitatively. Most notably, the pinch profile becomes symmetric, and the minimum radius precipitates to zero, faster than surface tension could drive it. The reason thermal fluctuations drive breakup can be understood by modelling the liquid bridge as a single particle, whose mass goes to zero with h_{min} [336]. A fluctuation which increases h_{min} will be slowed down as the effective mass increases, while in the opposite case the dynamics is sped up. On average this leads to a force driving the bridge toward breakup.

Although fluctuations are strong, the basic characteristics of each event remain the same. It thus makes sense to look for a 'typical' event, or the most probable sequence of profiles, which connects an initial profile to one whose neck radius has gone to zero. This means one has to maximize the probability [337]

$$W\{h(z, t), P(z, t)\} \sim \exp\left\{-\int_0^{t_0} dt\, L\right\}, \tag{247}$$

where the 'Lagrangian' (in units of ℓ_ν, t_ν) is

$$L = \frac{1}{2D^2}\int dz\,\frac{(\dot{P} + (P'^2/h^2) + G - 3h^2(P'/h^2)')^2}{h^2}. \tag{248}$$

In [295], the most probable solution is found by by solving the Euler–Lagrange equations corresponding to (248) [338]. Unfortunately, the resulting set of 'instanton' equations is ill-posed [339], reflecting the divergence of paths owing to noise. This problem is addressed by looking for *self-similar* solutions

$$h(z, t) = |t'|^\alpha \phi_{noise}(z'/|t'|^{1/2}),$$
$$P(z, t) = |t'|^{2\alpha}\psi_{noise}(z'/|t'|^{1/2}), \tag{249}$$

of the instanton equations, which in the spirit of the previous sections are expected to correspond to jet pinch-off. This leads to a system of ordinary differential equations for ϕ_{noise}, ψ_{noise}, and the corresponding 'response' fields [340]. In particular, this overcomes the problem of ill-posedness. For the case $\alpha < 1$, suggested by numerical simulations [298], surface tension becomes subdominant and pinch-off is driven by noise. Remarkably, the physical solution to this system, obeying the matching conditions (202), can be found analytically:

$$\phi^2 = \psi/3, \qquad \psi = 3F(-2\alpha, 1/2, -\xi^2/12), \tag{250}$$

where F is the confluent hypergeometric function [341]. In particular, this pinching solution is symmetric, in agreement with figure 58 and the experiment reported in figure 60 below.

The scaling exponent α is found by inserting the solution (249), (250) back into the Lagrangian, and optimizing the probability as a function of α. The result is $\alpha = 0.418$ [295], which is indeed smaller than 1. An experimental test (cf figure 60) of these ideas was performed recently using a polymer–colloid mixture, which phase separates into a gas (polymer-rich) and fluid (colloid-rich) phase, with a very small surface tension in between [299]. As a result, ℓ_T becomes macroscopic, and interface fluctuations are easily observable under a microscope (see figure 60, top, and digitized version of interface, bottom left). Experimental measurements of the minimum radius as a function of time indeed show scaling exponents of about 0.45, which is much smaller than expected from surface-tension-driven breakup. Thus although the presence of an outer phase might slightly alter the dynamics, the crucial effect of fluctuations in speeding up breakup is demonstrated, in agreement with theory [295].

4.5.2. Iterated instabilities. As shown by [335], thin viscous threads are extremely sensitive to noise. Using the linear stability analysis of section 3.5.1, i.e. *neglecting the flow in the thread*, the most unstable wavelength in the viscous limit gives $\lambda_{bump} \propto h(\ell_\nu/h)^{1/4}$. Hence using the scaling $\ell_r \propto |t'|^{1/2}\ell_z$ for the Navier–Stokes solution (203), perturbations are highly localized 'bumps' on the scale over which the thread radius is varying. However, since there is flow in the thread, bumps become stretched as they grow, making them more benign. At the same time they are convected out of the similarity region, where eventually they no longer grow. As a result, perturbations of *finite amplitude* are needed to destroy the similarity solution, as follows from the weakly non-linear stability theory of threads developed in [335].

To solve the problem analytically, a two-scale approach has been developed [120, 335], in which the perturbations move on a much shorter wavelength than the underlying similarity solution. To leading order in ϵ, which measures the scale separation, equations for the amplitude and the wavelength of the bump are found. Bumps are convected with the interfacial velocity $\psi_i = \psi + \xi/2$, hence perturbations that start near the stagnation point $\psi_i = 0$ have the longest time to grow. From the growth rate, on the other hand, one finds that the minimum wavelength for growth is $\propto |t'|^{1/2}$, which sets the effective initial distance from the stagnation point the 'most dangerous' perturbation can have.
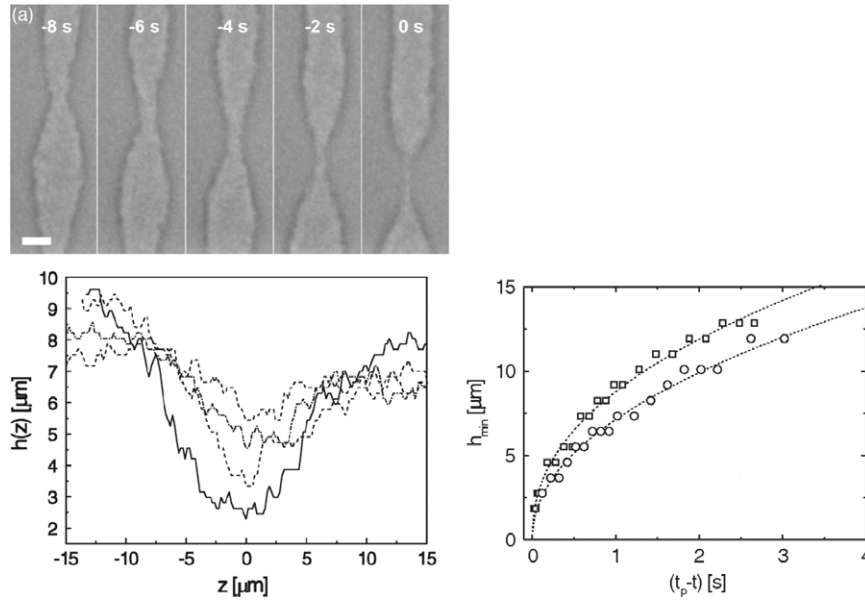
Figure 60. The breakup of a colloid-rich 'fluid' phase inside a polymer-rich 'gas' phase. Shown are typical 'secondary' breakup events, for which gravitational stretching plays a minor role. On the left, a typical experimental breakup sequence (top) is shown together with its digitized version (bottom). For system S1, shown on the left, $\ell_T = 0.45\,\mu$m. On the right, the minimum neck radius is plotted as a function of time (system S2, $\ell_T = 0.09\,\mu$m) for two different events. Best fits give $\alpha = 0.43 \pm 0.01$ ($\square$) and $\alpha = 0.47 \pm 0.02$ ($\circ$).
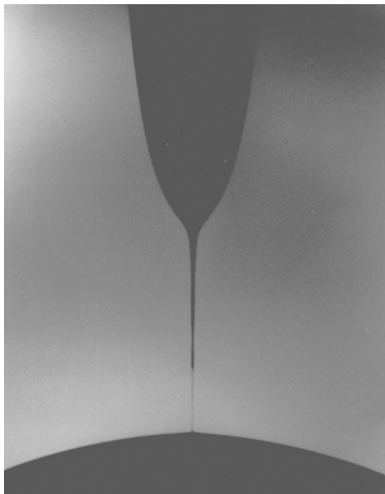

Figure 61. A drop of glycerol in water (85%) pinching off. Out of the main neck grow two more generations 'micro-threads' [304], which have the form of similarity solutions. From [332]. Reprinted with permission from AAAS.

Integrating the equations for the amplitude and wavelength of a bump, one finds that surface perturbations of size

$$h_c = 4 \times 10^{-3} h_{min}(h_{min}/\ell_\nu t)^{1.5} \tag{251}$$

suffice to destabilize the thread. Thus in the later stages of pinch-off, and for more viscous fluids, the thread becomes more and more vulnerable to small, random perturbations. A curious phenomenon [332] that results from this increasing sensitivity is shown in figure 61. Once a fluid neck has destabilized, another similarity solution is growing on it. Thus the pinching of a viscous thread becomes a noise-driven superposition of nested singularities. In other circumstances, breakup merely becomes irregular, as shown in figure 59. A

proper framework to use (251) in the context of *thermal noise* would be equation (246). Simple estimates for h_c based on thermal noise have led to the conclusion that thermal effects are not sufficient to explain the destabilization seen in figures 59 and 61 [335]. We have recently performed a numerical solution of (246) for a drop of viscous liquid falling from a tap, using the same parameters as in figure 59 [342]. In the simulation, no irregularities were visible on the scale of figure 59, confirming the need to search for other possible sources of noise.

4.6. Continuation through the singularity

The Navier–Stokes description on which the similarity solution is based does of course break down when the minimum thread radius approaches the size of molecules. Even before this happens, thermal fluctuations may modify, as seen in the preceding section. After the singularity, the Navier–Stokes equation (13) becomes once more the appropriate mathematical description for a *different* moving boundary problem, which consists of two separate pieces of fluid, and thus needs a different set of initial conditions. We now show how similarity solutions can be utilized to continue the Navier–Stokes equation across the singularity [301], using a method introduced in [343].

By the same logic as before, solutions after the singularity are described by (200), (201), but with a minus sign instead of a plus sign. As a result, the stability properties for $\xi \to \pm\infty$ are reversed: *all* solutions behave like (202), i.e. $\phi \approx a_0^\pm \xi^2$ and $\psi \approx b_0^\pm/\xi$, and possible solutions (for either part) are parametrized by a_0 and b_0. A short time t' after the singularity, only a region of size $|t'|^{1/2}$ will have moved appreciably, while the outer solution remains unaffected. Thus the values of a_0, b_0 for the post-breakup solution have to be the ones selected by the pre-breakup solution, ensuring unique continuation.
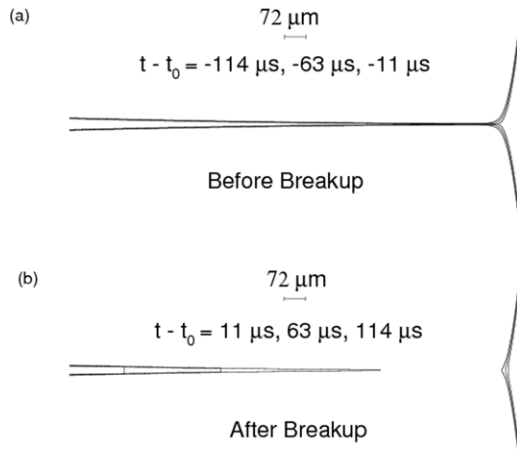
Figure 62. The breakup of a mixture of glycerol in four parts of ethanol, as calculated from similarity solutions before and after breakup. (*a*) shows three profiles before breakup, in time distances of 46 μs, corresponding to $|t'| = 1$, 0.55 and 0.1. In part (*b*) the same is shown after breakup.

The process is illustrated by an example shown in figure 62. After breakup, either side of the solution has a receding tip whose position is given by $z_{tip} - z_0 = \ell_\nu \xi_{tip} |t'|^{1/2}$. The asymmetry of the solution before breakup translates into two very different post-breakup solutions, with $\xi_{tip} = -17.452$ for the rapidly receding thread, and $\xi_{drop} = 0.4476$ for the opposite part of the drop. A technical problem which has to be overcome is that at the tip the solution cannot be slender, since axial and radial scales become comparable. However, the size of this region is only $\propto |t'|$ compared with the typical axial scale $|t'|^{1/2}$, hence its total contribution becomes negligible asymptotically. In [301], the slender-jet equations were amended to include the tip region; when rescaled according to the slender-jet scalings, all solutions converge onto the universal solution shown in figure 62.

Unfortunately, little experimental confirmation for the breakup scenario of figure 62 exists today. The reasons are threefold: first, the recoil of the thread is extremely fast, even by the standards of modern high-speed cameras. For example, if one continues the sequence shown in figure 49 to only $10 \mu s$ after breakup, the tip has receded by 0.6 mm, which is more than half the width of the frame. Second, at elevated viscosities the thread becomes very unstable, and breaks at several places, as shown in the preceding section. Third, the air drag on the thread can be estimated to become significant [120], slowing down the recoil. For a more detailed discussion, see [120]; more detailed experimental studies remain a challenge for the future.

Just as in the viscous case [301], inviscid similarity solutions can be used to continue the equations across the singularity, but on scales $h(z, t) \ll \ell_{min}$ [344]. Namely, the pre-breakup solution effectively provides an initial condition in the form of a cone and an inverted cone, respectively. The cone opening angles together with the leading-order decay of the velocity field away from the pinch point completely determine the similarity solution for the post-pinch-off problem [344]. Namely, the tip of the fluid neck recoils as $z_{tip} - z_0 = \xi_{tip}^{in} \ell_{in}$,

where the coefficient ξ_{tip}^{in} is completely determined by the density ratio D. In addition, similarity theory predicts the wavelength and amplitude of the capillary waves which are excited on the fluid neck by the recoiling motion, characteristic for pinch-off at low viscosities, as is evident from figure 12. Images of recoil in liquid–liquid systems are found in [345]. However, the corresponding analytical analysis of continuation still remains to be done.

4.7. Controlling breakup

In the preceding sections we have focused on surface-tension-driven breakup of jets. While for myriads of applications drops are desired, the results show that the breakup process is difficult to tailor to a specific application. On one hand, satellite formation leads to a bimodal drop size distribution. On the other hand, the size of the main drop is set by the jet radius and thus the size of the orifice. In particular, small drops are inefficient to produce since the fluid needs to be pressed through a small orifice at high pressure. This also causes very high shear gradients, which are likely to damage sensitive biological molecules by pulling them apart [346]. Below, we briefly discuss satellite drops, and then demonstrate the power of electric fields, as well as hydrodynamic forces to produce very small drops.

4.7.1. Satellites. Universality means that breakup is difficult to control, since its characteristics are *independent* of initial conditions. In particular, the asymmetry of the pinch-off profile implies that satellite drops are forming at each breakup event, and thus there is a bimodal distribution of drops, as was painfully rediscovered in the 1970s [103, 120, 347], when ink-jet printing technology was widely introduced. This applies in particular if drops are produced by jet decay ('continuous' ink-jet printing).

In recent years, ink-jet printing technology has moved far beyond its original application in printing [73, 348, 349], for example to print integrated circuits, make optical elements and for so-called microarrays in biotechnology, see figure 63. Ink-jet printers work by first charging a drop and then using an electric field to deflect the drop towards the desired position. For all these applications, a bimodal drop size distribution is a problem, since drops of different sizes are deflected differently in the electric field. Bimodal drop size distributions can be avoided if the velocity of main drops and satellites are sufficiently different [347], so both merge before they reach the target. However, the breakup mode depends very sensitively on the amplitude of the initial perturbation [347, 350], as well as on the presence of higher harmonics [120, 351–353]. Thus a small detuning can lead to an undesirable bimodal distribution of drop sizes.

Better means of control are available if individual drops are squeezed out of the nozzle ('drop-on-demand' ink-jet printing), by either piezoelectric actuation or by local heating [349]. In the latter case a bubble is nucleated, which pushes out the ink. While this does not avoid satellite drops, the mode of breakup can be engineered to impart a strong additional impulse on the satellite drop. Thus the satellite drop merges
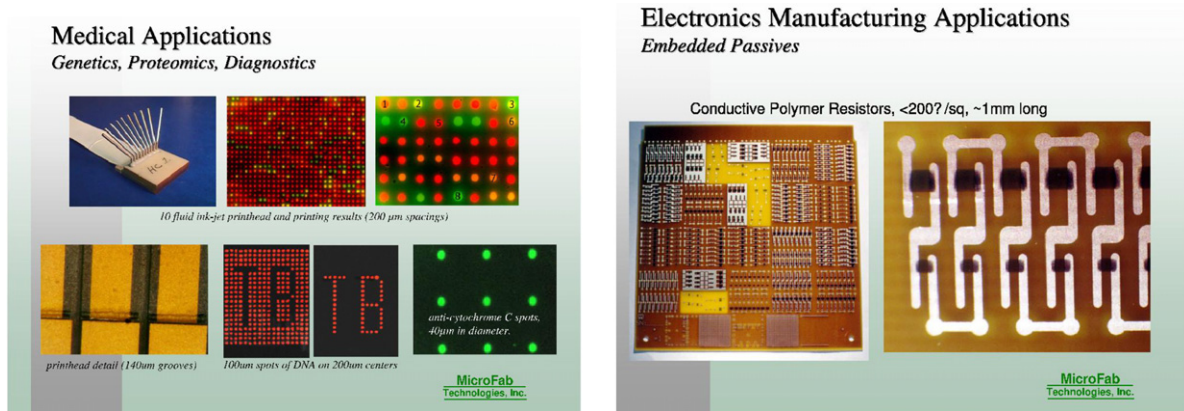
Figure 63. Commercial applications of ink-jet printing. The left panel shows so-called microarrays of drops laden with different biological samples. This permits one to test a large number of samples, using a small amount of space. The right panel shows integrated circuits, which can be printed 'on-the-fly' using ink jets.

with the main drop before it is deflected in the electric field. Detailed experimental [354] and computational [355] studies of different printing regimes were performed recently. Similarly a clever protocol of pressure and suction is used in [96] to eliminate the main drop altogether, making sure that only the small satellite drop is ejected.

4.7.2. Electric jets and Taylor cones. The most versatile methods of controlling breakup, though, are achieved by applying external forcing, either using an external flow or by applying an external electric field or even combinations thereof [356, 357]. Either type of forcing can be used to mould the fluid into an extremely fine jet, thus beating constraints imposed by the nozzle size. In addition, the rapidly developing microfluidic technology [358–360] has developed many ways of controlling the formation of drops and bubbles in confined geometries.

The technique of using electric fields to make extremely fine sprays has a long history [361] and many important applications [362], for example in biotechnology [346]. The tendency of electric fields to 'focus' a fluid into very pointy objects is epitomized by the static 'Taylor cone' solution, for which both surface tension and electric forces become infinite as the inverse distance r from the tip [363]. This means the electric field has to diverge as $r^{-1/2}$. Almost all fluids in question have some, if small, conductivity [246], so the appropriate boundary condition for an equilibrium situation is that of a conductor, i.e. the tangential component of the electric field vanishes. Using the solution for the electric field of a cone with the proper divergence $r^{-1/2}$ [364], this leads directly to the condition

$$P_{1/2}(\cos(\pi - \theta)) = 0. \qquad (252)$$

From the first zero of the Legendre function of degree 1/2 one finds the famous result $\theta = 49.29°$ for the Taylor cone angle in the case of a conducting fluid.

Figure 64 shows such a Taylor cone on a drop at the end of a capillary, held in a strong electric field. Note the very fine jet emerging from the apex of the cone (the so-called 'cone-jet' mode [246, 366]), which is not part of Taylor's analysis, but which is our main interest below. A similar phenomenon
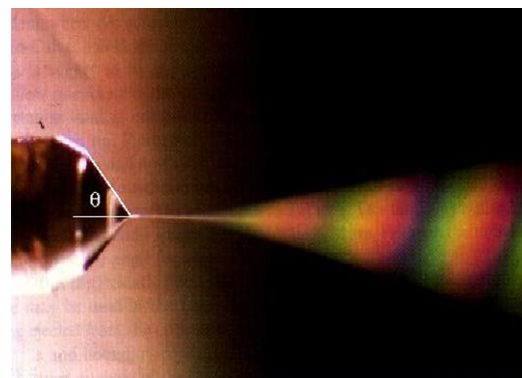

Figure 64. A Taylor cone in the cone-jet mode (reprinted from [365], copyright 1994, with permission from Elsevier). The opening half-angle shown is $\theta = 52°$. A large voltage difference is maintained between the capillary on the left, and an electrode on the right. The cone-like structure on the right is produced by a cloud of little droplets.

is observed for an isolated, charged drop in a strong electric field [240]. To produce a Taylor cone, the applied electric field has to be raised above a critical value, which is calculated by matching the Taylor cone to an appropriate far-field solution, such as a drop [133, 134, 365]. However, a simple argument reveals that the static Taylor cone solution is in fact *unstable* [134]: namely, the electric field becomes stronger if the angle is perturbed to a smaller value, as the tip becomes sharper. Thus the tip is pulled out, making the angle yet smaller. This is consistent with the cone either spouting irregularly [363, 367], or exhibiting a stationary flow out of the tip (cf figure 64). Since the size of the jet is now controlled by electric fields, drops of micrometre [368] or even nanometre radius [369] (in the case of liquid metals) can be produced.

In a pioneering paper, Gañán-Calvo [370] has described the cone-jet mode as a combination of a thin jet and a static Taylor cone near the nozzle, using a slender-jet description. The most useful limiting case for the study of this problem is one in which the fluid is modelled as a dielectric, yet having some conductivity (the 'leaky' dielectric) [246, 372]. This means that the local time scale of electric relaxation $t_e = \epsilon_i/K$ is much smaller than any time associated with the

flow [247, 373], where ϵ_i is the dielectric constant of the fluid and K is the conductivity. As a result, the field inside the fluid is very weak, and the surface charge density is simply given by $\sigma = \epsilon_0 E_n$, where E_n is the normal component of the electric field. The surface charges, however, take much longer to reach their equilibrium than they would in a good conductor. On the other hand, they move much faster than the carrier liquid inside the jet.

In a slender-jet approximation, electric forces have to be added to the rhs of (30) [247, 373, 374],

$$\partial_t v_0 + v_0 v_0' = -p_{\text{tot}}'/\rho + \frac{2\sigma E}{h} + 3\nu \frac{(v_0' h^2)'}{h^2}, \qquad (253)$$

with $E \approx E_t$ the z-component of the electric field. The most important new contribution is the second term on the right, which describes the electrostatic pull of the field on the surface charges. The effective pressure

$$p_{\text{tot}} = \gamma \kappa - \epsilon_0 E^2/2 - \sigma^2/(2\epsilon_0) \qquad (254)$$

has the usual capillary contribution, as well as a contribution from polarization forces, induced by the deformation of the jet. Conservation of charge [247]

$$\partial_t(\sigma h) + \left(\sigma h v_0 + \frac{K}{2} h^2 E\right)' = 0 \qquad (255)$$

yields an equation of motion for σ, which contains, apart from convection, a contribution from bulk conduction in the fluid.

To find the electric field E along the jet, one needs to solve the electrostatic equations in the exterior of the jet, with an imposed electric field E_∞ as a boundary condition. The equation for E is usually given as an integral equation, using for example the slender-body description given in section 2.4.3. In the case of a uniformly slender problem the electric field can be computed from a local equation [247]. In general, however, an accurate modelling of the jet requires a more detailed description of the electrostatic problem, including the nozzle and the far-field electrode [248, 371].

Under conditions of small flow rate [365], such as shown in figure 64, the problem reduces to matching a jet to a static Taylor cone. The most commonly observed force balance in (253) is the one between inertia and the electrostatic pull, resulting in a jet thinning as $h \propto z^{-1/4}$. So far, the joining of the Taylor cone with the jet has only been achieved by patching [370, 373, 375, 376]. Remarkably, the analysis predicts [374] that the total current I through the jet is *independent* of the applied voltage, and

$$I = 2.6(\gamma K Q)^{1/2}, \qquad (256)$$

with Q the mass flow rate. Originally, a logarithmic dependence on Q/Q_0 (with $Q_0 = \rho K/(\epsilon_0\gamma)$) was predicted in [370], but so far has not been found experimentally. As discussed in [248], the idealized conditions for a Taylor cone solution at the nozzle are not always met (and not perfectly known), so often the prefactor in (256) is less universal. In particular, it may depend on the voltage [248, 371]. However, once sufficient care is taken to model the electric field correctly, remarkable agreement with theory can be achieved, as seen in figure 65.
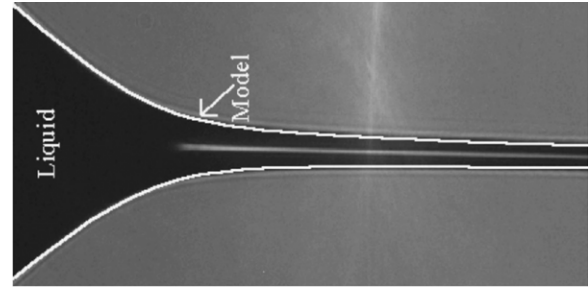

Figure 65. Comparison between theory, based on the slender-jet description (253), (255) and experiment with an ethylene glycol jet at $Q = 2.78 \times 10^{-9}$ m^3 s^{-1}. Reprinted from [371], copyright 1999, with permission from Elsevier.

Figure 64 shows an essentially stationary situation. A problem that has been addressed only very recently is how the cone-jet state is approached *dynamically*, for example as seen in the experiments of [367] or [240]. In particular, how does the Taylor cone give way to the new jet, a question that has recently arisen in similar form in air entrainment [377, 378], hydrodynamically forced jets [379, 380] (to be discussed below), or contact line instability [381]. A recent study [382] (see also [383]) looks at the dynamical process by which a charged drop, with or without an electric field, develops pointed ends as the drop turns unstable. The drop is treated as a perfect conductor, and the dynamics is assumed to be described by the Stokes approximation.

A new similarity solution is found [382], in which the drop shape is of the form

$$h(z,t) = t'^{1/2} H(z/t'^{1/2}), \qquad (257)$$

where for $t' \to \infty$ a cone is formed. The solution (257) (with corresponding equations for electric field and the charge) represents a balance of electrostatic repulsion and viscosity, so surface tension drops out of the description! Namely, the cone angle is found to be *smaller* than the static angle expected on the basis of Taylor's solution (252). Indeed, recent experiments of bursting drops, both with and without external field, turn out to be described by this dynamical cone formation, see figures 40 and 66. The thickness of the jet, which eventually emanates from the tip of the cone, is presumably set by the finite conductivity, and is thus beyond the present description [382].

4.7.3. Outer flow. Instead of electric fields, an outer flow is also a very versatile tool to control the thickness of jets and their breakup behaviour [182, 186, 379, 380, 385]. Both inertial and viscous forces can be harnessed to focus jets; an example of the former case is shown in figure 67. The jet shape is molded by the external air stream, for which a pressure difference Δp is maintained across the hole shown in (a). When Q is the mass flux, the jet radius is determined by the inertial balance

$$r_0 \sim (Q^2 \rho/\Delta p)^{1/4}, \qquad (258)$$

hence by making Δp large the jet radius becomes small.

Electric jets can be employed to produce more complex structures by having one liquid inside another one [386], and
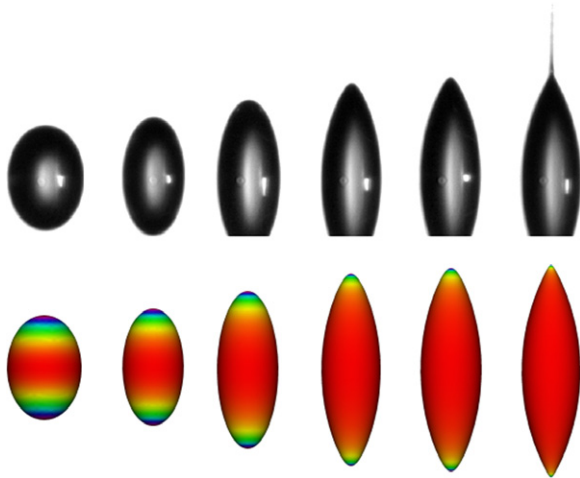
Figure 66. Comparison between experimental profiles [240] and numerical 3D simulation based on a boundary integral code for Stokes fluids [382, 384]. The ratio of viscosities considered in the numerical simulation is $\lambda = 0.3$ and Rayleigh's fissibility parameter is $X = 1.01$, just slightly over the critical limit $X = 1$. The parameter X, defined as the ratio of Coulomb energy to surface energy, is the analogue of (151) in section 3.9. Numerical simulations indicate very little dependence of the shapes during the evolution and the final angle of the singular cones developing for $\lambda < 1$ and $X > 1$.
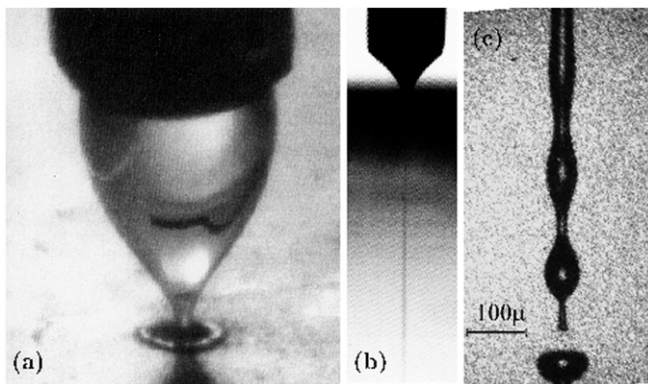

Figure 67. A view of the experimental apparatus. Fluid is sucked through a hole opposite a capillary tube (*a*). This leads to a much thinner micro-jet (*b*). This micro-jet decays into droplets by surface tension forces (*c*). Reprinted with permission from [379]. Copyright 1998 by the American Physical Society.

driving one to produce a Taylor cone. Using this method compound jets and, after breakup, near monodisperse capsules are produced. The same geometry can be used in the reverse case of gas being driven by an external stream of liquid [182]. The crucial difference is that the jet is now absolutely unstable [178], so that instead of a gas jet, a series of monodisperse bubbles emanate from the orifice. The transition from convective to absolute instability is investigated in [186], under much more general circumstances, including viscous fluids. Again, more complex structures can be produced using compound jets, such as bubbles inside a viscous jet, driven by an external air stream.

The mechanism by which viscous forces lead to focusing is much less understood. A classical realization is the selective withdrawal experiment [189–192, 380], shown in figure 68. Before the jet becomes entrained, the interface forms a hump,

which becomes unstable at a tip size of about 0.1 mm, for a viscosity ratio between $\lambda = 1$ and 10^{-3} [189, 190]. This result appears to be at odds with results for drops and bubbles in an extensional flow, a subject pioneered once more by Taylor [194, 363]. Namely, if the drop viscosity is small, their pointed ends seem to become sharp without limit [194, 195, 387]. Using the same geometry as that of selective withdrawal, but air as the inner 'liquid', it was shown in [191] that the size of the tip could be made small without apparent limit. No evidence for air entrainment was found, unless the tip had entered the nozzle. At present it is not known what constitutes the crucial difference between the two systems [189, 191] and under what conditions a steady stream is entrained. In [192] it is shown experimentally that the transition towards a spout is hysteretic: a thin thread (cf figure 68(*b*)) persists to flow rates *Q below* the critical flow rate for the disappearance of a hump as *Q* is lowered. The thread radius saturates at values of around 22 μm.

A theoretical study [388] of a drop attached to a capillary in an external flow, a geometry closer to that of figure 27, analysed the existence of thin spouts (jets) using slender-body theory [139]. The viscosity ratio between the inner and the outer fluid was small but finite. A solution corresponding to a vanishing jet thickness as the outer flow strength is tuned towards a critical value can be realized, but only on a lower-dimensional subspace: another experimental parameter needs to be tuned along with the flow strength. Recent experimental results [183, 389] and simulations [188] indicate that the thread radius can indeed be made small in a coflowing geometry, but no quantitative test of theory has been performed as yet. For an appropriate choice of parameters, the jet can be made stable [187] according to the analysis discussed in section 3.6.2.

Finally, in highly confined geometries, such as those arising in microfluidic applications, the possibilities for direct control of flows is even greater [358]. Flow focusing can be replicated on a smaller scale to form jets of different stability characteristics [390]. In addition, drop breakup is modified by the confinement. For example, drops can be forced to break up at T-junctions of small channels. If the T-junctions are arranged sequentially, the drop size decreases continuously. If breakup takes place in long and narrow channels [391], breakup can be halted so as to yield a sequence of stationary equilibrium shapes, making the process of breakup highly controllable.

5. Sprays

The fragmentation of compact macroscopic objects is a phenomenon linking complicated microscopic phenomena, such as fracture in solid fragmentation and drop pinch-off in liquid atomization, with the statistics of the fragment sizes. The resulting statistical distributions are typically broad, as seen qualitatively in figure 69, and non-Gaussian. Early in history, in fact from the time when the need was felt to rationalize empirical practices in ore processing [393], questions about the principles of matter division have been recurrent in science, up to modern developments in nuclear fission [257, 394]. For instance, Lavoisier (1789) [395] devotes chapter IV of his *Elementary Treatise of Chemistry* to the
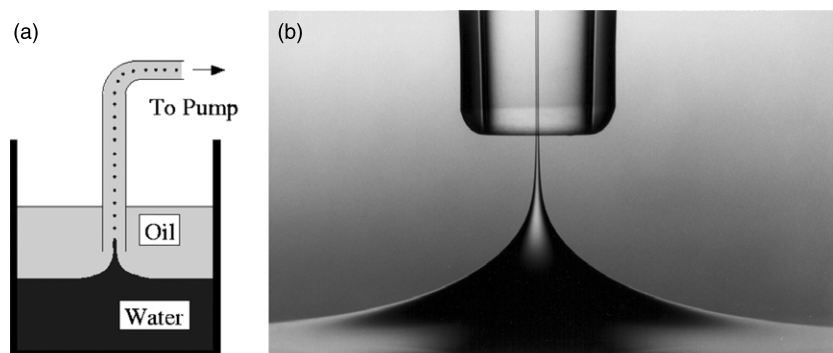
Figure 68. In the selective withdrawal experiment, two viscous liquids are layered atop of one another. The upper, more viscous liquid is withdrawn through a capillary and entrains a thin stream of the lower liquid. From [380]. Reprinted with permission from AAAS.
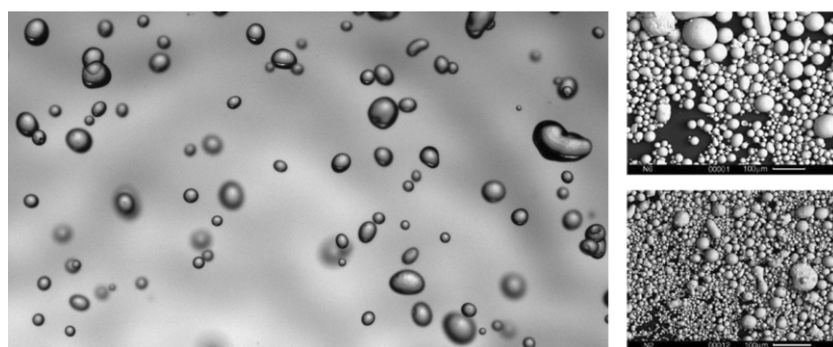

Figure 69. (Left) Drops in a liquid spray formed in an uncontrolled way are naturally distributed in size. (Right) Solid tin powder formed from the atomization of a liquid tin stream for two operating conditions [392]. Obviously the resulting powder is far from uniform in size.

different techniques for dividing matter, and the monumental treatise of Coulson and Richardson (1968) [396] has several sections dealing with the many 'unit operations' of the chemical industry to fragment, atomize, blend and mix. The timeless character of the subject is certainly not a sign of a lack of progress, but rather reflects its growing number of applications.

As for liquid atomization (literally 'subdivide down to the size of an atom'), examples abound ranging from distribution of agricultural sewage, diesel engines and liquid propellant combustion in the aerospace industry [215, 216, 397], geophysical balances and ocean–atmosphere exchanges [398–400], volcanic eruptions and tephra formation [401], sprayed paint and cosmetics, ink-jet printers, microfluidic and novel devices [358, 359], medical diagnostics [402], to quote but a few among the many applications where it is desirable to have an *a priori* knowledge of the spraying mechanism. Of particular interest is the distribution of droplets sizes as a function of the control parameters, the optimal design of injector size and shape and other external parameters such as wind speed and liquid surface tension.

5.1. Jets everywhere: ligaments production and dynamics

Drops come from the rupture of objects having the form of threads or ligaments, whose instability and breakup into drops has been the major subject of the previous sections. This has been speculated on by Lord Rayleigh in 'Some Applications of Photography' (1891) [23]. Later time-resolved still images,

Figure 70. A bubble bursting from a lava tube at Kilauea's shoreline illustrates the simultaneous cooling and breakup of magma during turbulent mixing with water and steam. Visible lava has been hurled upwards in a fraction of a second, stretching the outer surface to several times its original length, bursting through the formation of ligaments (*a*), and exposing a new, hot, incandescent surface. Width of the photo is about 3 m. USGS photo by Takahashi, 10 February 1988 (adapted from [403]).

and more recently high-speed movies have substantiated this claim [32, 264, 266, 404–411]. The thread and ligaments can come from many different sources, which can itself be jets (cf figure 38), violent eruptions (cf figure 70), impact of drops with other drops or liquid pools (cf figure 72), converging

flows (cf figure 73), and sheets (cf figure 79). The observed polydispersity of drop sizes results mainly from the dynamics peculiar to ligaments, as suggested by the examples given below.

5.1.1. Wind over wave crests: spume. The disintegration and dispersion of a liquid volume by a gas stream is a phenomenon which embraces many natural and industrial operations. The spray droplets torn off by the wind at the crest of waves in the ocean are obvious examples [412, 413], see also [414] in another context. As suggested by figure 38, at the root of the disintegration process is the shear between the light, fast stream and the slow, dense liquid. The change of the liquid topology proceeds from a two-stage instability mechanism: the first instability is of a shear type described in section 3.8 forming axisymmetric waves. It is controlled by the boundary layer thickness δ of the gas at the interface, and produces interfacial undulations whose selected wavelength is proportional to $\delta\sqrt{\rho/\rho_a}$, where ρ and ρ_a stand for the densities of the liquid and gas, respectively.

For large enough amplitudes, these undulations undergo a transverse destabilization of the Rayleigh–Taylor type [415–417], caused by the accelerations imposed on the liquid–gas interface by the passage of the primary undulations. These transverse corrugations have a wavelength given by

$$\frac{\lambda_\perp}{\delta} \simeq 3 \, We_\delta{}^{-1/3} \left(\frac{\rho}{\rho_a} \right)^{1/3} \qquad \text{with } We_\delta = \frac{\rho_a v_a^2 \delta}{\gamma}, \tag{259}$$

where v_a is the relative gas velocity. This last instability sets the volume of liquid eventually atomized: the modulation of the crests is further amplified by the air stream, forming ligaments of total volume

$$\Omega = d_0^3 \sim \lambda_\perp^3. \tag{260}$$

The axial momentum of a cylindrical volume $\Omega = d_0^3$ in uniform extension is $\frac{1}{2}\rho\Omega\frac{dL}{dt}$ and the force balance on a ligament entrained in the wind gives

$$\frac{1}{2}\rho\Omega\frac{d^2 L}{dt^2} = \frac{1}{2}\rho_a v_a^2 C_D \frac{\Omega}{L} - \gamma \left(\frac{\Omega}{L} \right)^{1/2}, \tag{261}$$

where C_D is a drag coefficient of order unity [418]. The ratio of aerodynamic to capillary forces

$$C_D \frac{\rho_a v_a^2}{\gamma} \left(\frac{\Omega}{L} \right)^{1/2} \tag{262}$$

indicates that capillary retraction gets weaker as the ligament elongates and one has approximately

$$\frac{L}{\Omega^{1/3}} \simeq 1 + \left(\frac{t}{\tau_a} \right)^2, \tag{263}$$

with a characteristic time of acceleration

$$\tau_a = \frac{\Omega^{1/3}}{v_a} \sqrt{\frac{\rho}{\rho_a}}. \tag{264}$$

The ligaments detach from the liquid bulk by a pinching of their base. The time τ it takes for the pinch-off to be completed is close to the capillary time based on the ligament volume Ω, independent of its rate of elongation because the ligament's foot is weakly stretched:

$$\tau = \sqrt{\frac{\rho\Omega}{\gamma}}. \tag{265}$$

The length L_b and thickness ξ_b at the breakup time thus follow from (263), and thus (remembering that $\Omega = d_0^3 = L\xi^2$),

$$L_b/d_0 \sim (\tau/\tau_a)^2 \sim We, \tag{266}$$

$$\xi_b/d_0 \sim (\tau/\tau_a)^{-1} \sim We^{-1/2}, \tag{267}$$

with $We = \rho_a v_a^2 d_0/\gamma$ (see [232]).

Once detached from the bulk, ligaments break by capillarity. Although stretched by the gas stream, the final drop size is larger than the ligaments thickness ξ_b just after they have been released from the liquid bulk. This is due to coalescence between the blobs making up a ligament, an aggregation process which also determines the drop size distribution $p(d)$ in the resulting spray. This distribution is the convolution of the relatively narrow distributions of the ligament sizes $p_L(d_0)$ and of the distribution of drops sizes coming from the ligaments. It is found to be very well represented by a *Gamma* distribution, as shown in figure 71:

$$p_B(x = d/d_0) = \frac{n^n}{\Gamma(n)} x^{n-1} e^{-nx}, \tag{268}$$

and first emphasized in [32, 232]. The problem only depends on relative velocities, and the same 'stripping' phenomenology occurs when a liquid jet is moving in a still atmosphere, as can be seen from the early instantaneous pictures of Hoyt and Taylor (1977) [221] (see figure 34). The size of the droplets peeled off from the liquid surface is also found to decrease with the velocity contrast, in that case given by the liquid velocity [285, 419].

5.1.2. Impacts. Ligaments often form upon various types of impact (cf figure 72), see figure 81 for an unconventional example. Particular attention has been paid to drop impact on thin layers of fluid, which leads to the celebrated Worthington–Edgerton crown [212, 421], which eventually produces drops. However, data on fragmentation following drop collision, a phenomenon potentially crucial to understanding the structure of the Solar system [422], are scarce. Various authors [420, 423] have quantified the conditions for coalescence or satellite formation in binary collisions of drops, and measured [424] the number of fragments of a water drop colliding with a solid surface and qualitative hints for their distribution. A systematic study exploring the dependences of the fragments size on initial drop sizes, impact Weber and Reynolds numbers, roughness of the solid substrate, ambient conditions, etc is certainly desirable (see however [425]).

Violently accelerated and *initially corrugated* density interfaces are unstable in the sense of Richtmeyer and Meshkov [429, 430]. A version of this instability for an order one corrugation amplitude is shown in figure 73: a cavity at a
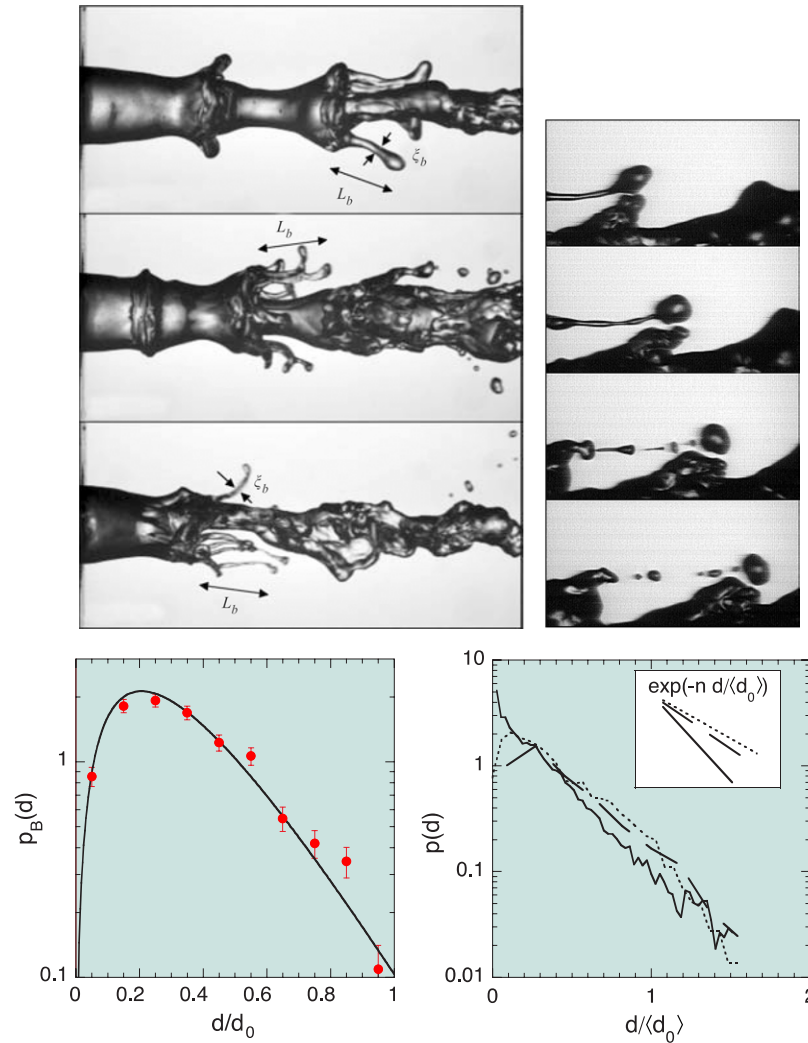
Figure 71. (Left) Formation of ligaments peeled off from a liquid jet at fixed velocity by an increasingly fast coaxial gas stream, showing the aspect ratio of the resulting ligament [232]. (Right) Time resolved series of the elongation and breakup of a ligament in the wind showing the coalescence between the blobs constitutive of the ligament as it breaks. Time interval between pictures is 1.34 ms. (Bottom) Droplet sizes distribution after ligament break-up $p_B(d)$ for air velocity 29 m s^{-1}. Here d_0 is the volume-equivalent ligament size, the line is a fit by a *Gamma* distribution. Distribution of droplet sizes in the spray $p(d)$. The slight increase of the exponential slopes with air velocity (inset) reflects the variation of the Gamma orders n on $\langle d \rangle / \xi$ (see section 5.3.3 and [32]).
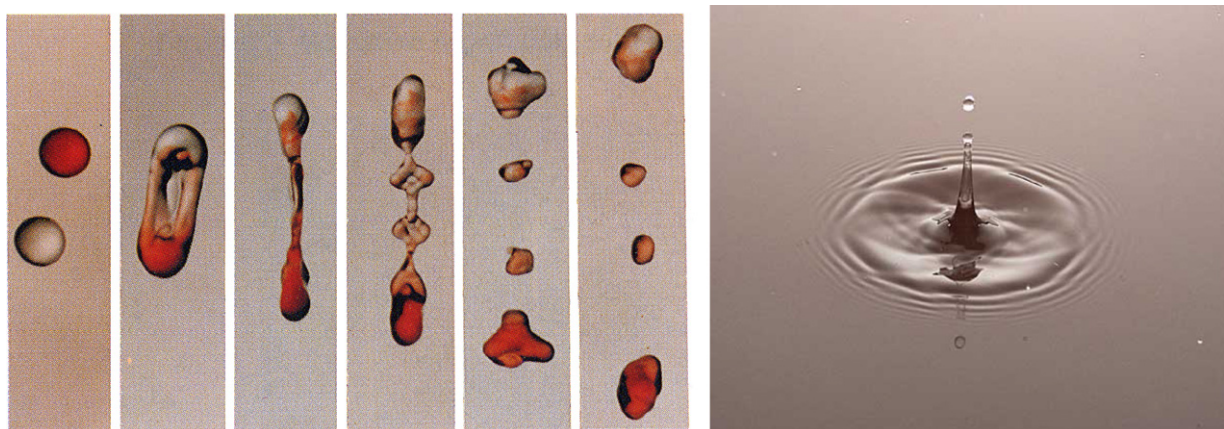

Figure 72. (Left) Binary collision of drops, stretching and fragmentation. $We = 83$ based on the relative velocity between the drops [420]. Reprinted with permission from Cambridge University Press. (Right) A jet emerging from the closing cavity left after the impact of a drop on a layer of the same liquid.

Figure 73. Axial impact of a cylindrical tube falling under gravity and filled with a liquid wetting the tube wall. Following the impact on a rigid floor, the curvature of the spherical meniscus initially fixed by the tube radius reverses violently, a prelude to the birth of a rapidly ascending jet [426].
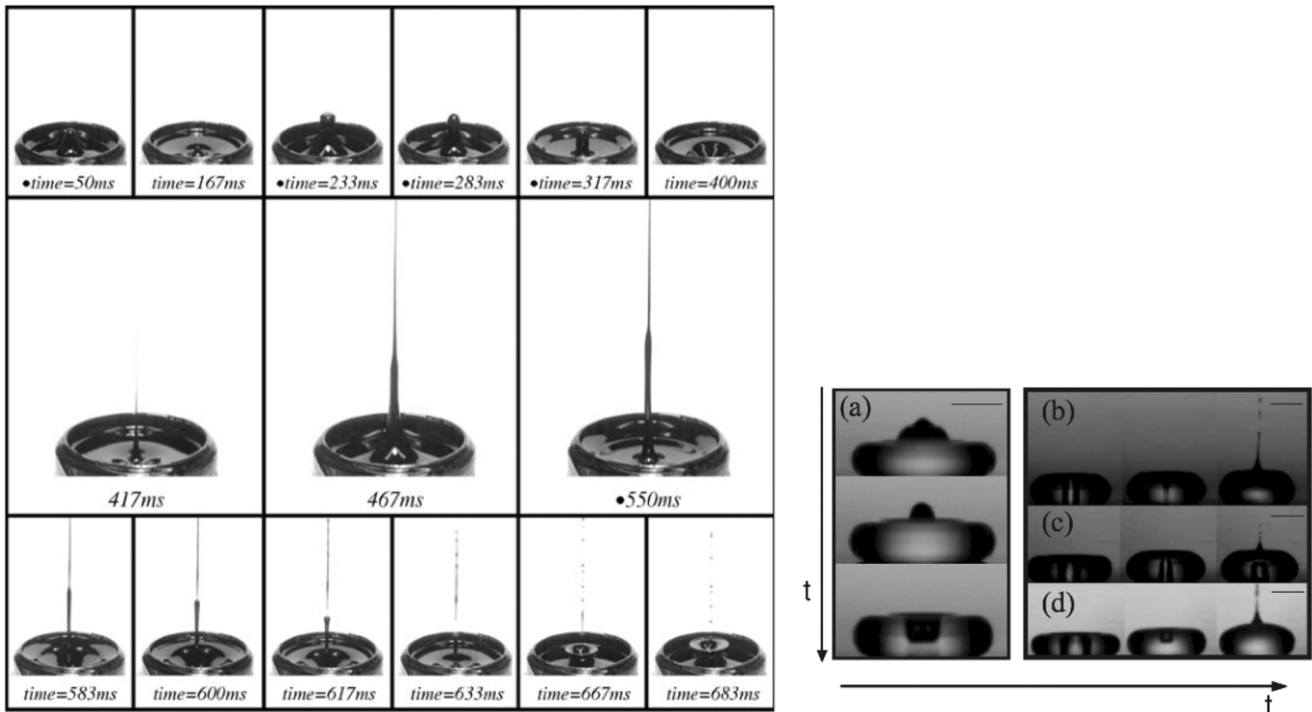

Figure 74. (Left) Sequence of frames showing a rapidly moving jet evolving from an over-forced standing wave in a ferrofluid [427]. (Right) Impact of a (millimetric) water drop on a super-hydrophobic surface, formation of a cavity and ejection of a highly focused jet. Reprinted with permission from [428]. Copyright 2006 by the American Physical Society.

free liquid/gas interface collapsing due to an impulsive body force forms an intense focused jet [426]. This is the paradigm for bubbles bursting at a liquid surface [85], the collapse of cavitation bubbles near a rigid boundary [84], collapsing voids following an impact [47], shaped charges, gravity waves colliding with a dam and high amplitude Faraday waves [431], to quote just a few examples among many [432]. The collapse produces a jet, as seen in bursting bubbles at the surface of

the ocean, a mechanism responsible for most atmospheric aerosol generation [398, 433]. The shape, dynamics and resulting drops of the corresponding jet are a problem still under debate [426] (figure 74).

5.1.3. Rain. The phenomenon of rain is documented in much more detail. Bentley (1904) [30], an autodidactic farmer from Vermont, was the first to capture the broad distribution of
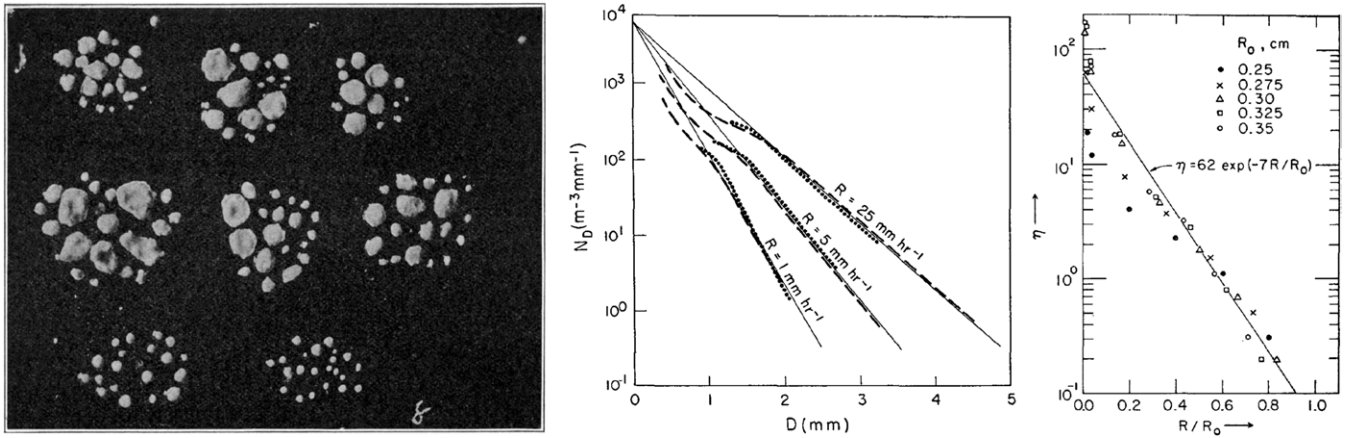
Figure 75. (Left) Raindrop specimens [30] captured by allowing drops to fall into a 1 in. deep layer of fine un-compacted flour. (Middle) drop size distributions for three different rainfall rates [436]. (Right) Cumulative drop size distribution $\eta = \int_R^\infty p(R, R_0)\, \mathrm{d}R$ resulting from the breakup of a drop with initial radius R_0 falling in air [439].
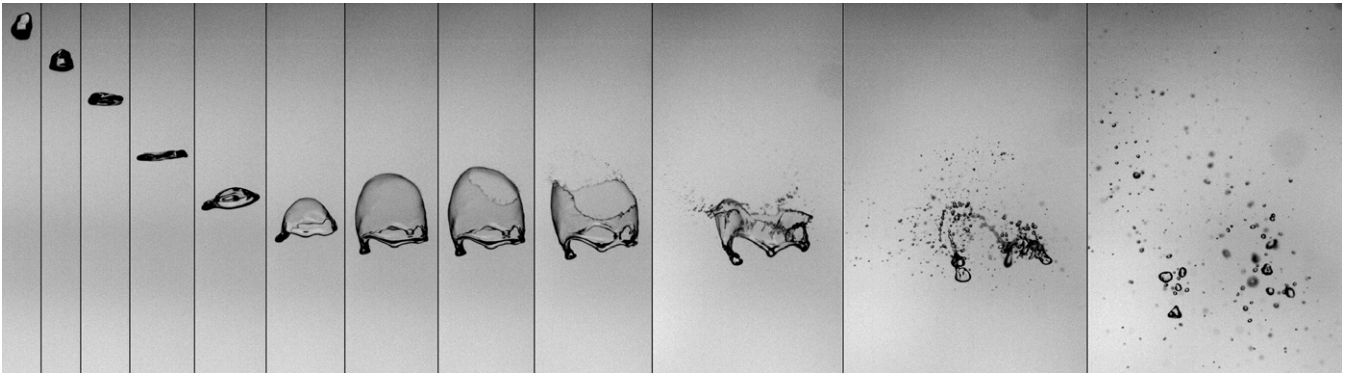

Figure 76. Fragmentation of a water drop (diameter 5 mm) falling in an ascending stream of air [404]. Images are taken at $(t = 0, 4, 9, 17, 24, 30, 33, 34, 35, 37, 43$ and $60\,\mathrm{ms.})$

drop sizes. His ingenious experiments (figure 75) allowed him to conclude: '*Perhaps the most remarkable fact, early brought to our notice, was the astonishing difference in the dimensions of the individual drops, both in the same and different rainfalls*', thus singling out the most salient feature of rain. At the same time, Lenard [434], a professor in Heidelberg and a future Nobel Prize winner (see also figure 8), was mainly contemplating drop shapes and terminal velocities. Subsequent measurements [435, 436] established the exponential shape of the distribution, and related its steepness to the intensity of rainfall: drop sizes are more broadly distributed in heavy storms than in fine mists, a trend already visible from Bentley's records (figure 75).

Existing interpretations of these facts essentially pertain to the aggregation scenario summarized in section 5.2.2 below, plus condensation of ambient water vapour and possibly evaporation of the drops [399,400,437,438]. This emphasizes the (presumed) role of coalescence in the falling rain. However, Srivastava (1971) [439] mentions that spontaneous drop breakup could also be incorporated in the global balance describing the evolution of the drop size population and, using earlier measurements [440], devises arguments to interpret the Marshall–Palmer law [436] on this basis.

A very different, but tempting idea is that the polydispersity of raindrops results from the breakup of isolated, large drops (compare figures 76 and 75). Indeed, figure 76 shows how a liquid drop, falling in a counter-ascending air current first deforms, then destabilizes and finally breaks into stable fragments. The process, usually called 'bag breakup' [404], exemplifies the three stages shared by all atomization processes:

- *A change of topology of the initial object*: the big drop flattens into a pancake shape as it decelerates downwards.
- *The formation of ligaments*: the toroidal rim of the bag collects most of the initial drop volume.
- *A broad distribution of fragment sizes*: the rim is highly corrugated and breaks into many small, and a few larger drops.

If Δu is the velocity difference between the drop and the air stream in a Galilean frame, the drop will break as soon as the stagnation pressure of order $\rho_a(\Delta u)^2$ overcomes the capillary restoring pressure γ/d_0. This condition indicates that the Weber number

$$We = \frac{\rho_a(\Delta u)^2 d_0}{\gamma} \tag{269}$$

should be larger than some critical value [441,442], with some corrections accounting for possible viscous effects [404,443]. In this as in many atomization processes, there is no *typical* size of fragment. There is an average size, and an obvious upper bound, namely the size of the initial drop; it is even unclear if there should be a lower bound. However, the hierarchy of fragment sizes d follows a *regular distribution* $p(d)$, giving the probability to find a drop size between d and $d + \mathrm{d}d$. The tail of the distribution is described by an exponential law

$$p(d) \sim \mathrm{e}^{-d/d_0}, \qquad (270)$$

up to some cut-off parametrized by the drop's initial size d_0 [440,444]. The exponential tail is also shared by the *Gamma* distribution (268).

5.1.4. Sheets. The transition from a compact macroscopic liquid volume to a set of dispersed smaller drops often involves as a transient stage the change of the liquid topology into a sheet shape. This transition is sometimes enforced by specific man-made devices, and also occurs spontaneously as a result of various impacts and blow-ups. An easy way, widely used in the technological context, to produce a spray is to form a liquid sheet by letting a jet impact on a solid surface, or by two jets impacting each other. The sheet disintegrates into drops by the destabilization of its edges. Pioneering works of Savart (1833) [445–447], and later Taylor (1959) [448,449] and Huang (1970) [450] focused on the resulting sheet shape and its spatial extension. Depending on the Weber number (5) the sheet is either smooth with a radial extension increasing as

$$\frac{R}{h_0} = \frac{We}{4} \qquad (271)$$

or, for higher impact Weber number, decreases as

$$\frac{R}{h_0} \sim \alpha^{-2/3} We^{-1/3}. \qquad (272)$$

Here α is the ratio of the liquid to ambient medium densities ρ_a/ρ; the transition occurs for [226]

$$We \gtrsim \frac{20}{\sqrt{\alpha}}. \qquad (273)$$

Above this limit, the sheet sustains a flag-like instability generated by shear [222–224, 451, 452]. The undulations may also be enforced artificially by vibrating the impact point [278]. Leaving aside some qualitative early work [223, 453, 454], the quantitative study of the drop formation process itself was addressed only recently [226, 278, 455, 456]. While drops of the order of the jet diameter are formed from the destabilization of the thick rim bordering the sheet in the smooth regime, the average drop size is a strongly decreasing function of the Weber number in the flapping regime (figure 77). In all cases, the sheet fragments by the destabilization of its rim, forming cusps at the tip of which ligaments are ejected, a prelude to the formation of drops (figure 78). These ligaments were already visible on the early drawings of Savart [446], and have been observed more recently with air blasted liquid sheets [457, 458]. They are
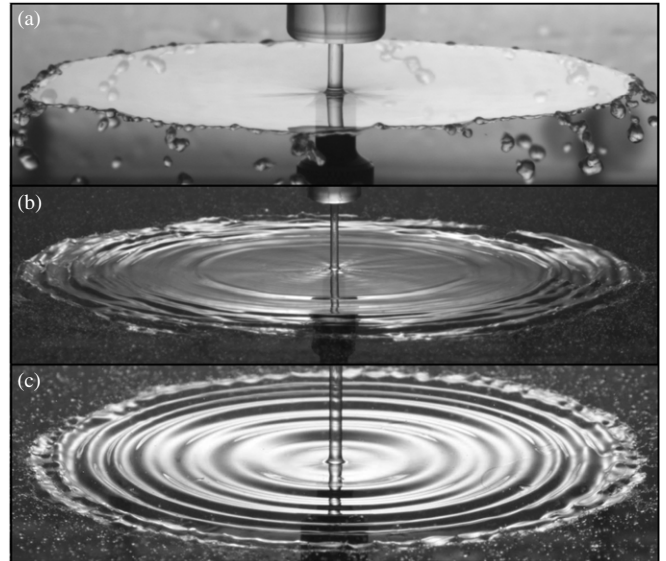

Figure 77. Axisymmetric liquid sheet states: (*a*) Smooth regime. (*b*) Flapping regime for larger Weber number (higher than 1000). (*c*) Perturbation of the smooth regime by imposing vertical oscillations of the impact rod. Adapted from [278].
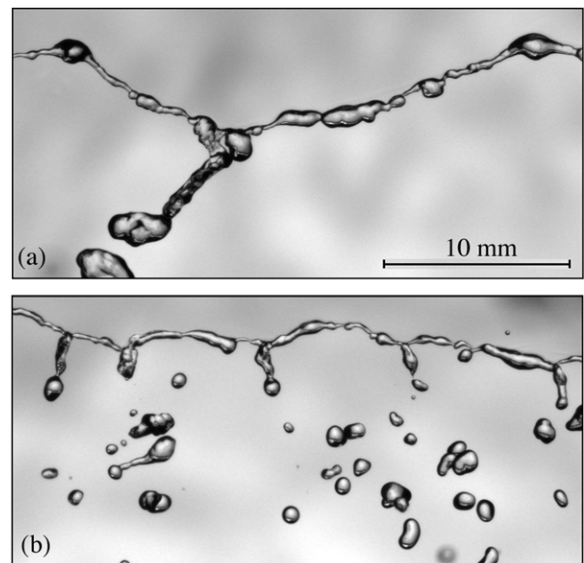

Figure 78. Close-up views of the free rim of a smooth liquid sheet, taken from the top (*a*). In (*b*), a periodic vibration of the impact point at 120 Hz has been added. The scale indicated in (*a*) is the same for both images, and $h_0 = 3$ mm. Adapted from [278].

also seen in numerical simulations [459, 460], if a span-wise perturbation is added to the flow initially.

In the *oblique* collision of two identical jets (figure 79), the liquid expands radially, forming a sheet in the form of a bay leaf bounded by a thicker rim; the ligament production phenomenology persists [456, 461–467]. This is a particularly interesting configuration because the distribution of the drop sizes can be manipulated at will by varying the impact angle and the Weber number. The volume d_0^3 of massive regions centrifuged along the rim (where d_0 is here the diameter of the rim [456]) is both insensitive to the external parameters and narrowly distributed (figure 80). It elongates and stretches in
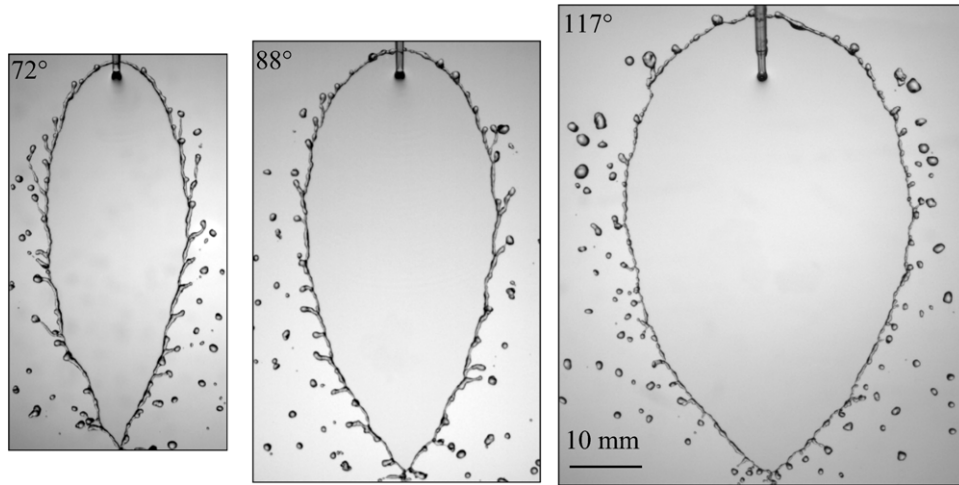
Figure 79. Water sheet fragmentation for three collision angles, the jet velocity is equal to $4\,\mathrm{m\,s^{-1}}$ and the jet diameter is 1.05 mm. Elongation of ligaments is clearly enhanced when the collision angle is decreased [456].
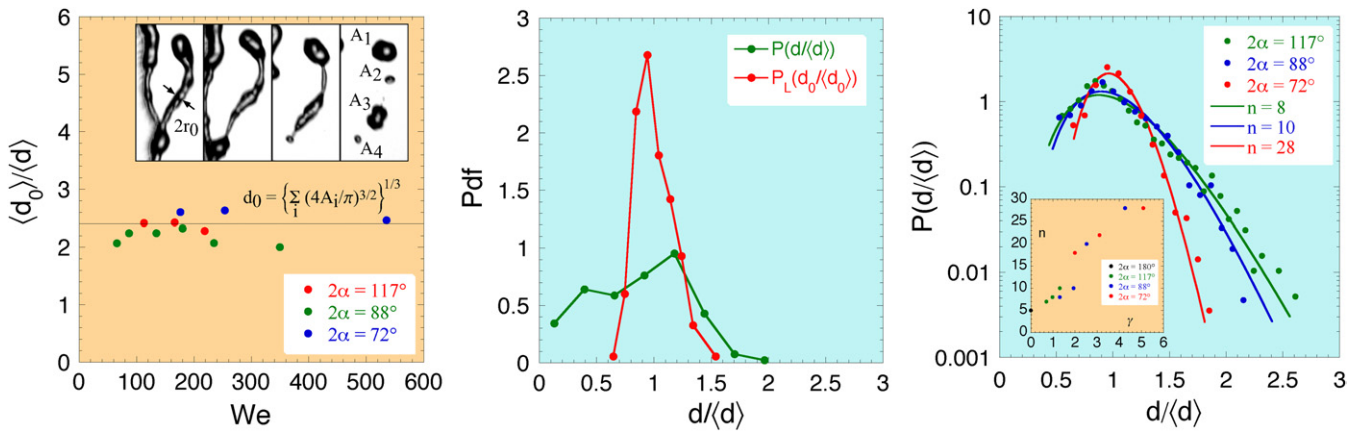

Figure 80. (Left) Definition of the equivalent sphere diameter d_0 of a ligament, as well as its value normalized by the average drop size for several injection conditions. Typically, $\langle d_0 \rangle / \langle d \rangle \approx 2.5$. (Centre) Distributions $p_L(d_0)$ and $p_B(d)$; the distribution of d_0 is narrower than that of d. (Right) Probability density functions of the drop size normalized by the mean drops size $d/\langle d \rangle$ for a fixed impact velocity $u_j = 3.5\,\mathrm{m\,s^{-1}}$ and three collision angles. The fitted curves are Gamma distributions with parameters n as indicated in each case and reported in the inset versus dimensionless stretch γ for all conditions [456].

the form of ligaments, with their foot attached to the rim. The transient development of the capillary instability at the early stages of ligament elongation determines the local radius along the centre-line at the moment it detaches. Corrugations are more pronounced when stretching is weak, giving broader size distributions. Drop sizes are distributed according to (268), and are parametrized by the single quantity

$$\dot{\gamma}\sqrt{\frac{\rho d_0^3}{\gamma}}, \tag{274}$$

which is the rate of stretch in the rim normalized by the capillary timescale. The size d_0 of the rim is a function of both the Weber number and the collision angle (see figure 80 and [456]).

5.1.5. Blow-ups. A fascinating problem, and a very efficient atomizing process [468], is the 'explosion' of cavities in a liquid volume (expanding micro-bubbles injected *in situ*, dissolved gases, etc). Its two-dimensional version, i.e. a film

bursting by hole nucleation (figures 83 and 84), suggests that interesting geometrical ingredients probably influence final drop size distributions.

Rayleigh [415] first analysed the stability of an interface between two media (with density difference ρ), subjected to a constant acceleration a normal to the interface. Taylor (1950) [416] subsequently studied the stability of a layer sandwiched between two phases of a different density. In the absence of surface tension, these situations are always unstable, with no mode selection. The growth rate depends solely on the density contrast, acceleration and wavenumber. In the case studied by Taylor, it is independent of the layer thickness h. However, surface tension does induce mode selection on the capillary wavenumber $k_c = \sqrt{\rho a/\gamma}$ [145]. Soon after the works of Taylor and Lewis (1950) [416,417], Keller and Kolodner (1954) [470] extended Taylor's analysis incorporating surface tension. A new phenomenon arises in that case from the coupling between the two interfaces of the layer which, when it is much thinner than the capillary length (i.e. when $k_c h \ll 1$), induces a considerable slowing down of
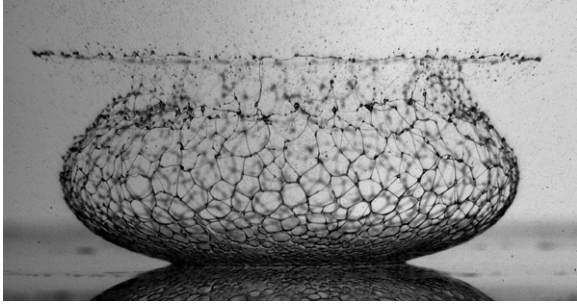
Figure 81. The 'crystal crown' formed by the impact of a 5 mm viscous drop (89% glycerin/water solution) onto a 35 μm thick layer of ethanol ($We = 5720$). Marangoni forces thin the sheet locally, leading to a myriad of holes, ligaments and then drops [469]. Reprinted with permission from Cambridge University Press.
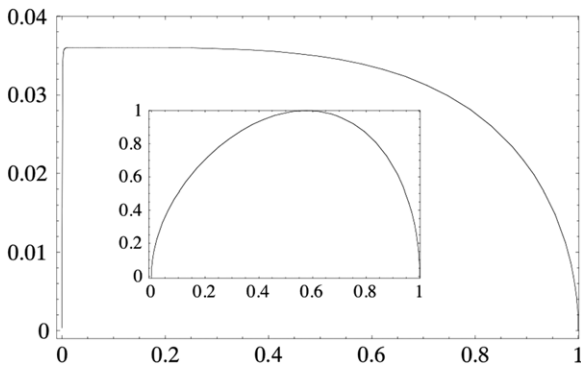

Figure 82. Growth rate $-i\omega$ of the instability of a thin liquid sheet accelerated perpendicular to its plane, according to [470, 471]. The growth rate has been made dimensionless by $\sqrt{2/3\sqrt{3}}\sqrt{\rho a^3/\gamma}$, the maximal growth rate of the infinite thickness limit obtained when $k_c h \gg 1$. It is plotted as a function of k/k_c with $k_c = \sqrt{\rho a/\gamma}$ the capillary wavenumber. The curve has been drawn for $k_c h = 0.001$ and the inset shows the same relation for $k_c h \gg 1$ in the same units [278]. Note the invariance of k_c with h, the strong dependence of both the shape and amplitude of ω as h decreases and, in particular, the presence of a plateau of wavenumbers with uniform amplification at low $k_c h$.

the amplification rate and a shift of the selected mode towards larger length scales [471]. The most amplified wavenumber k_m lies between 0 and k_c on a *broad plateau of wavenumbers*, all having growth rates ω_m close to the maximal one, which goes to zero as $k_c h \rightarrow 0$ (see figure 82):

$$k_m = \frac{1}{6^{1/6}} k_c^{4/3} h^{1/3} \qquad \text{and} \qquad \omega_m = \left(\frac{\rho h a^2}{2\gamma}\right)^{1/2}.$$
(275)

A sudden acceleration imparted to the film also causes its destabilization [429, 430, 472]. In practice, this is achieved by imposing a pressure difference between both sides of a soap film, stretched on a frame positioned at the exit of a shock tube [471]. The film accelerates impulsively as the shock passes through it (with $k_c h \gg 1$). The resulting thickness modulations amplify and eventually form holes, which subsequently grow in radius and connect to each other (figures 83 and 84). The patterns thus formed resemble that obtained from the spinodal decomposition of thin liquid films

on solid substrates [473, 474], or 'punctuated' liquid films (figure 81 and [469]). The hole density and their rate of nucleation increase with shock strength, as measured by the incoming wave Mach number. Thin films, although rigidified by capillarity, can disintegrate too. Not much is known, however, about the resulting drop size distribution.

5.1.6. Bubbles. The examples discussed so far all concerned liquid drops forming in a gaseous environment. There is no reason to think that the same phenomenology and ideas should not apply to the opposite situation of bubbles forming in a continuous liquid phase: the fundamental instability, that of a hollow ligament in a liquid is of the same nature as that of a liquid ligament in vacuum, although developing with a stronger growth rate (see, e.g. section 3.4 and [145]). Large cavities entrained at the sea surface by breaking waves form elongated void structures with an eccentricity up to 8 [476]. Those formed by the impact of a solid object at a free surface can be even longer (see figure 85 and [477]). The resulting bubble size distributions are very likely Gamma distributions [478, 479].

5.2. Fragmentation scenarios

The ubiquity of fragmentation phenomena has prompted a number of interpretations and paradigms, which can be grouped into roughly three distinct classes. If none of them is satisfactory, all of them warrant further exploration.

5.2.1. Sequential cascades of breakups. A first class of models was introduced by Kolmogorov (1941) [480], motivated by ore grinding, a process where repeated size reductions are imparted on brittle solid particles. Kolmogorov later applied the same model to turbulence [481, 482], and it was later extended to liquid atomization. Spray formation is visualized as a sequential process where mother drops give rise to daughter drops which themselves break into smaller drops, producing ever smaller sizes. In this cascade process and many of its variants (see e.g. [483–486]), a drop of initial volume v_0 breaks, after n steps of the cascade, into a family of drops of volume $v_n = v_0 \prod_{i=0}^{n-1} \alpha_i$ where the α_i are random multipliers smaller than unity.

The distribution of the α_i (assumed to be identical in each generation), depends on the atomization mechanism, but they are constrained to guarantee volume conservation. The distribution of volumes $\mathcal{P}(v)$ is governed by large deviation theory [487, 488] and depends on the distribution of multipliers. In particular, the moments of v depend exponentially on n. Defining the size of a drop d by $d_n^3 = v_n$, the drop size distribution is recovered from $p(d) = 3d^2 \mathcal{P}(v = d^3)$. Defining

$$M = \frac{1}{n} \sum_{i=0}^{n-1} \ln \alpha_i \qquad \text{and} \qquad S^2 = \frac{1}{n} \sum_{i=0}^{n-1} (\ln \alpha_i)^2 - M^2,$$
(276)

the variance of the drop size distribution is given *approximately* by

$$\frac{\langle d^2 \rangle - \langle d \rangle^2}{\langle d \rangle^2} = e^{nS^2/9} - 1,$$
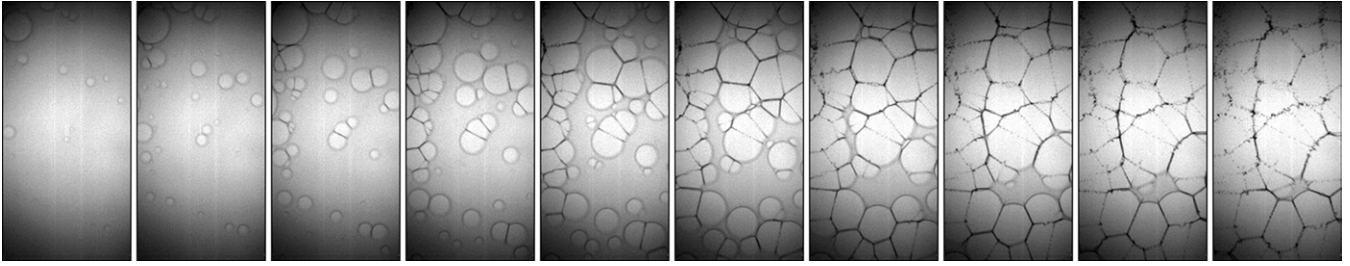(277)

Figure 83. Bursting of a soap film accelerated by the parallel impact of a shock wave. Time goes from left to right with time step $\Delta t = 0.05$ ms. Incoming wave Mach number is $M = 1.21$ [471].
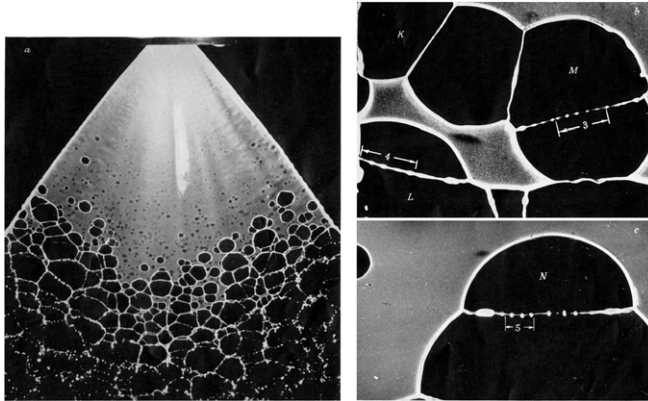

Figure 84. Sheet formed from a water/oil emulsion showing hole nucleation and ligaments formation. Adapted from [475].
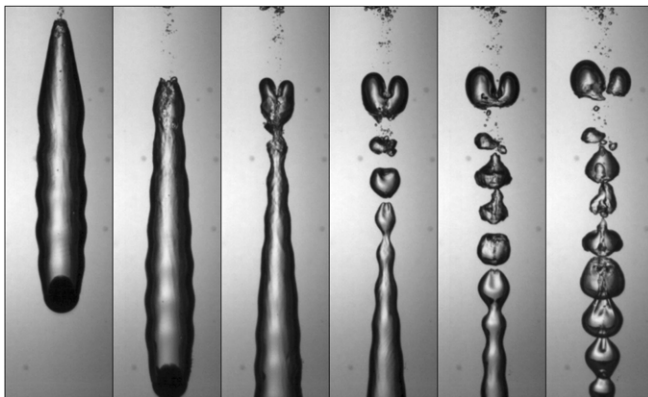

Figure 85. Ripple-induced breakup of the entrained bubble behind a 1/2 in. diameter steel sphere impacting at 4.1 m s^{-1} in water. Courtesy of A Belmonte [477]. Reprinted with permission, copyright 2007 by the American Physical Society.

and increases exponentially with the cascade step n. If one anticipates that the cascade will end at some generation $n = m$, when the Weber number (269) based on d_m is of order unity, the shape of the distribution will depend on the initial Weber number $We = d_0/d_m$. The size of the *largest* drops in stirred suspensions is indeed found to obey this rule, see e.g. [441, 489–492].

5.2.2. Aggregation. The process of aggregation is inverse to the above idea of size reduction: an ensemble of initially small elementary particles form clusters of increasing average size as they collide and merge, and the evolution is towards ever larger

sizes. The paradigm of this process is Smoluchowski's kinetic aggregation, initially imagined to represent the coagulation of colloidal particles moving by Brownian motion in a closed vessel [493]. For instance, this idea has been popular in representing growth of aerosols in clouds [400]. In other applications, mechanical agitation first forms small pieces, which then grow by mutual collision.

If $n(v, t)$ is the number of clusters whose volume is between v and $v+dv$ and $K(v, v')$ is the aggregation frequency per cluster between clusters of volumes v and v', then

$$\partial_t n(v, t) = -n(v, t) \int_0^\infty K(v, v') n(v', t) dv'$$

$$+ \frac{1}{2} \int_0^v K(v', v - v') n(v', t) \, n(v - v', t) dv'. \quad (278)$$

This is an evolution equation for $n(v, t)$, to which additional effects like liquid evaporation can be added in the form of a Liouville term—$\partial_v \{q(v)n(v, t)\}$, where $q(v)$ is the rate of evaporation [400]. The volume distribution of the drops $\mathcal{P}(v, t)$ is equal to $n(v, t)/N(t)$ with $N(t) = \int_0^\infty n(v, t) \, dv$ the total number of clusters. This framework has been popular in modelling the breakup and coalescence of drops in emulsions [494], turbulent clouds of drops [495], gas–liquid dispersions in stirred media [496], and breath figures [497]. In each case, a suitable frequency factor $K(v, v')$ has to be found. Similarity solutions have been found for various forms of the interaction kernel $K(v, v')$, which all display an exponential tail [498, 499]

$$\mathcal{P}(v, t \to \infty) \sim e^{-v/\langle v \rangle} \qquad \text{for } v \gtrsim \langle v \rangle, \quad (279)$$

similar to (270). Here $\langle v \rangle = \int_0^\infty v n(v, t) dv / N(t)$ is the average volume, which is a function of time.

The exponential law (279) is easily found for the case that $K \equiv K(v, v')$ is constant, using the Laplace transform $\tilde{n}(s, t) = \int_0^\infty e^{-sv} n(v, t) dv$. Namely, in the long-time limit in which the distribution becomes stationary, one finds that the solution of (278) becomes

$$n(v, t) = \frac{N}{\langle v \rangle} e^{-v/\langle v \rangle} \qquad \text{with } N = \frac{1}{1 + t/2}, \quad (280)$$

where $N = \int_0^\infty n(v, t) dv$ is the total number of clusters at time t. Thus one finds (279) for the asymptotic cluster volume distribution $\mathcal{P}(v) = n(v, t)/Ne$ with $N\langle v \rangle = V$, the (conserved) total volume of the aggregates. For example, this solution applies to the coarsening of an assembly of droplets exchanging solute by diffusion through the continuous phase [500].
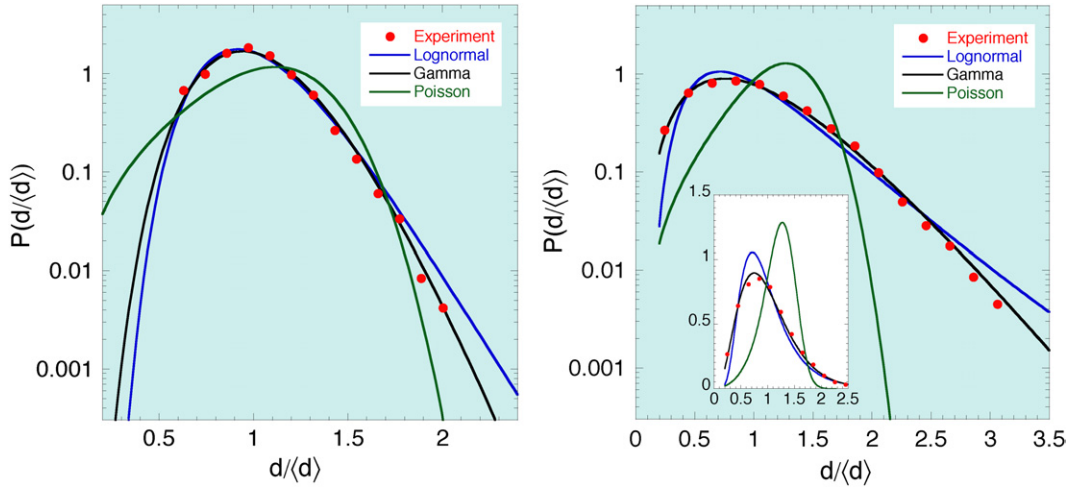
Figure 86. Comparison between experimental records of drop size distributions in liquid sheet fragmentation (data from [456]) and various models. The distributions are normalized by their mean and have the same variance $\langle d^2 \rangle$ (lognormal) and skewness $\langle d^3 \rangle$ (Poisson) as the experimental ones. (Left) Narrow size distribution showing how the lognormal (section 5.2.1) and an experimental distribution can be easily confused for a single data set. (Right) A broader distribution showing how the lognormal fit over-estimates both the distribution around its maximum (inset) and its tail. The maximum entropy distributions (Poisson and similarly exponential, see sections 5.2.3 and 5.2.2) have a much too sharp fall-off (i.e. $\sim \exp\{-(d/\langle d \rangle)^3\}$) at large sizes. The Gamma fit discussed in section 5.3 has $n = 17$ (left) and $n = 4$ (right).

5.2.3. Maximum entropy principle and random breakups. Another approach considers the random splitting of an initial volume into various disjointed elements, all in one step. This is an ensemble theory as commonly used in statistical physics, with no explicit reference to dynamics. Similar ideas were developed for the kinetic theory of gases [501] and the physics of polymers ([502], see also [503,504] for a review). The idea is to visualize a given volume $v_0 = d_0^3$ as a set of

$$K = (d_0/d_m)^3 \qquad (281)$$

elementary bricks of volume $v_m = d_m^3$, whose linear sizes are for instance linked by the requirement $We = d_0/d_m$ as in section 5.2.1. The distribution is found by computing the *most probable* distribution of the disjointed clusters incorporating all the bricks [505,506].

Let us thus consider a drop consisting of N clusters which make up the K elementary bricks. We call n_k the number of clusters consisting of k bricks, the average number of bricks per cluster is $\langle k \rangle = K/N$. Then the number of microscopic states leading to a given cluster partition $\{n_k\}$ is

$$w(\{n_k\}) = \frac{N!}{\prod_{k=0}^{K} n_k!} \cdot \frac{K!}{\prod_{k=0}^{K} (k!)^{n_k}}, \qquad (282)$$

together with the conservation laws

$$\sum_{k=0}^{K} n_k = N, \qquad \text{and} \qquad \sum_{k=0}^{K} k n_k = K. \qquad (283)$$

Looking for the maximum number of microscopic states (282), subject to the constraints (283), one finds the optimal distribution $\mathcal{P}(k) = n_k/N$ to be a Poisson distribution

$$\mathcal{P}(k) = \frac{n_k}{N} = \frac{\langle k \rangle^k}{k!} e^{-\langle k \rangle}, \qquad (284)$$

of parameter $\langle k \rangle$, the average number of bricks per cluster. This is also the distribution of the number of objects in a regular partition of space, when the objects are spread at random as sometimes encountered with low inertia particles in turbulent flows [507,508]. The drop size distribution then follows from $p(d) = 3 d^2/d_m^3 \mathcal{P}(k = (d/d_m)^3)$.

Following the same line of thought, Longuet–Higgins [509] considered the fragment distribution produced when a volume is cut at random into exactly m pieces. The answer is

$$\mathcal{P}(x) = m(1-x)^{m-1}, \qquad (285)$$

for a linear segment of length unity where x is the fragment length, with average $\langle x \rangle = 1/(1+m)$. This distribution tends towards a pure exponential characteristic of shot noise $\mathcal{P}(x) \simeq m e^{-mx}$ (Poisson intervals) for $m \gg 1$. Longuet–Higgins [509] also provides the corresponding distribution for random breakup of surfaces and volumes. These purely combinatory descriptions do not account for any interaction between the clusters as they separate. They lead to fragment size distributions determined entirely by their mean, as does the aggregation scenario in section 5.2.2 above.

The above three classes of models are compared with figure 86 to experimentally measured and statistically converged drop size distributions (cf section 5.1). Maximum entropy or aggregation scenarios are far from the truth: nature does not aggregate nor split *liquid volumes* at random. Small but significant differences exist between the lognormal fit and real data; more evidence that liquid atomization does not proceed from a sequential cascade of breakups is given in section 5.3.3.

5.3. Drop size distributions

5.3.1. A toy model to understand timescales. We have already discussed ligaments in section 5.1.4, and pursue
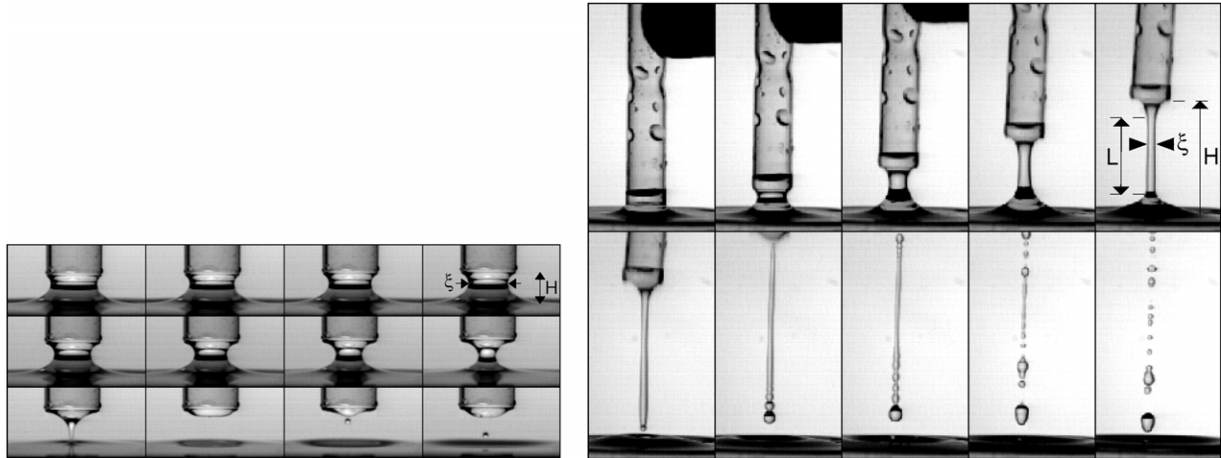
Figure 87. Condition for ligament formation from the withdrawal of a capillary tube (diameter $D = 7$ mm) whose end dips into water [510]. (Left) Ligament contraction with a slow tube elevation velocity (time intervals $\Delta t = 10.7$ ms). (Right) Fast elongation and ligament formation ($\Delta t = 4.5$ ms).

the discussion here to point out the hierarchy of timescales associated with substrate deformation, inertial rearrangements and breakup.

A ligament is a more or less columnar object (a jet), attached by its foot to the liquid bulk from which it has been stripped. To produce a model ligament, one can withdraw a capillary tube (diameter D) rapidly from a free surface (figure 87). The conditions for the entrainment of a ligament are easily understood by the following argument: suppose the tube elevation H above the surface increases at a constant rate $\dot{\gamma}$ and that the column length L in between the end menisci is proportional to H, so that $L = D \exp(\dot{\gamma} t)$ if D is the initial elevation. The liquid can flow out of the column through the attached end, whose surface area is $S \simeq \pi \xi^2/4$. The flow velocity is $u = 2\sqrt{\gamma/\rho\xi}$, as determined by Bernoulli's equation, using the capillary pressure $2\gamma/\xi$ in the middle of the column of diameter ξ. With $V = \pi L \xi^2/4$ being the total volume, continuity $dV/dt = -uS$ leads to

$$\frac{d(\xi^2 L)}{dt} = -2\sqrt{\frac{\gamma \xi^3}{\rho}}. \tag{286}$$

The solution of this equation is

$$\frac{\xi}{D} = e^{-\sigma t/2} \left\{ 1 - \frac{2}{3\sigma\tau}(1 - e^{-3\sigma t/4}) \right\}^2$$

$$\text{with } \tau = \sqrt{\frac{\rho D^3}{\gamma}}. \tag{287}$$

For weak stretching ($\sigma\tau \ll 1$), the ligament empties completely in a finite time t, set by the capillary time τ, and dependent on its initial size:

$$\xi/D = (1 - t/2\tau)^2. \tag{288}$$

The (unphysical) exponent 2 is a geometrical artefact originating from the assumption of a fixed external length L. The exponent could be 1/3, 2/5, 1/2, 2/3 or 1 depending on other choices dictated by other constraints, see table 2. Large

stretching ($\sigma\tau \gg 1$) prevents capillary contraction, and the ligament thins at constant volume

$$\xi/D \sim \exp(-\sigma t/2). \tag{289}$$

Note that this caricature cannot be completely realistic, since the ligament shape is itself a solution of the elongation function $H(t)$; a cylindrical shape (with uniform σ along the ligament) is only compatible with an elongation linear in time [199]. Indeed, the column eventually pinches off from its ends and, if no longer stretched, fragments into drops (figure 87).

Stretching prevents a ligament from emptying, and also hinders its destabilization, as explained in section 3.7. The initial fluid motion along a ligament is well described, as shown in sections 3.2.2, 3.5 and 3.7, within the long-wavelength approximation, thereby giving the dynamics of the capillary waves along the ligament. Note that a localized pinching event only takes of the order of 10^{-3} of the total time t_ξ for the ligament to disintegrate (figure 88 and [120,289]). Most of the time is thus spent moving the fluid around the initial ligament shape. This demonstrates that a random superposition of capillary waves can lead to the ligament's corrugations, and the distribution of the resulting drop sizes.

5.3.2. Construction mechanism. The statistics $P(h)$ of heights h of a large number of overlapping waves with random amplitude and phase but with the 'same pitch' was first examined by Rayleigh (1880) [511]. It leads to the celebrated 'Rayleigh distribution'

$$P(h) = \frac{h}{\sigma_h^2} \exp\left(-\frac{h^2}{2\sigma_h^2}\right), \tag{290}$$

popular in optics, acoustics and oceanography [512, 513]. Another idealization has been proposed in [32]: when two liquid blobs of different sizes d_1 and d_2 (with, say, $d_1 < d_2$) are connected to each other, they aggregate due to the Laplace pressures difference $\propto \gamma(1/d_1 - 1/d_2)$. The time it takes for coalescence to be completed is of order $\sqrt{\rho d_1^3/\gamma}$, the same time
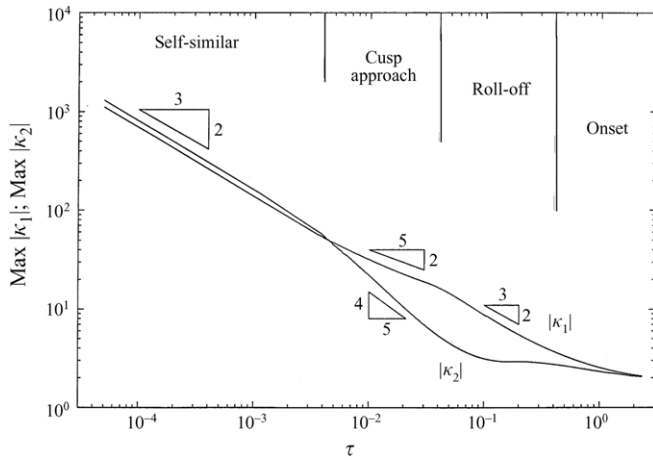
Figure 88. Time sequence of the maximum principal curvatures of a liquid bridge as it pinches-off under mild stretching (see also figure 87). Time $\tau = t_p - t$ is the time from pinch-off. The onset of the instability, as well the boundary conditions influence the evolutions down to 10^{-2}–10^{-3} of the overall time t_p, after which the dynamics is universal. Adapted from [289].
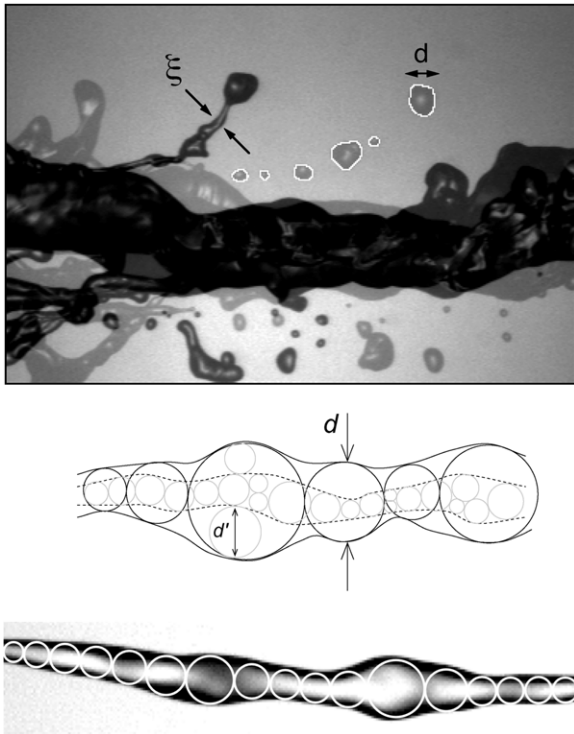

Figure 89. Double flash exposure of a ligament torn off by the wind (section 5.1) just before and after breakup. (Middle) A sketch of the layer interaction scheme. (Bottom) An isolated ligament covered with blobs of various sizes d corresponding to the local thickness.

it takes for the neck connecting the two blobs to destabilize and break (section 5.3.1). A particular consequence of this equality is the 'coalescence cascade' described in [514]. For the same reason, the blobs which make up a ligament tend, as they detach, to coalesce, thereby forming bigger and bigger blobs (see also [515]).

If $n(d, t)\mathrm{d}d$ is the number of blobs constituting a ligament whose size is within d and $d + \mathrm{d}d$ at time t (figure 89), the total

number of blobs is

$$N(t) = \int n(d, t)\mathrm{d}d. \tag{291}$$

Conjecturing that blob sizes result from a *random* overlap of *independent* layers, whose width is set by the 'mean free path' of fluid particle motions across the ligament, the evolution equation for $n(d, t)$ can be computed along lines similar to those in section 5.2.2. A layer of given size d_1 overlaps with another one of size d_2 with a probability proportional to $n(d_1, t)n(d_2, t)$. This gives rise, at a time δt after merging, to a size d with probability $n(d, t+\delta t) = \int n(d_1, t)n(d_2, t)\mathrm{d}d_2$ with $d = d_1 + d_2$, corresponding to self-convolution of the size distribution. In addition, the net ligament volume

$$V = \int d^3 n(d, t)\mathrm{d}d \equiv d_0^3, \tag{292}$$

must be conserved. The continuous version of this evolution for $n(d, t)$ can thus be written, in its most general form, as

$$\partial_t n(d, t) = -n(d, t)N(t)^{\zeta-1} + \frac{1}{3\zeta - 2}n(d, t)^{\otimes\zeta},$$

$$\text{with } \zeta = 1 + \frac{1}{n}. \tag{293}$$

Here $\otimes$ denotes the convolution operation on the *linear sizes d*. Time t is counted from the moment the ligament detaches from the liquid bulk. Time is nondimensionalized by the capillary time $t_\xi = \sqrt{\rho\xi^3/\gamma}$, based on the initial average blob size

$$\xi = \int \mathrm{d}n(d, 0)\,\mathrm{d}d/N(0). \tag{294}$$

The interaction parameter ζ is determined from the initial blob distribution along the ligament requiring that

$$\zeta = \frac{\langle d^2 \rangle_0}{\xi^2} \qquad \text{with} \qquad \langle d^2 \rangle_0 = \int d^2 n(d, 0)\mathrm{d}d/N(0). \tag{295}$$

A uniform thread of constant thickness (made of many thin layers) is characterized by $\zeta = 1$, while a corrugated ligament (made up from a few independent layers) has $\zeta > 1$. The asymptotic solution of equation (293) for $p_B = n(d, t)/N(t)$ is the *Gamma* distribution (268) of order

$$n = \frac{1}{\zeta - 1}. \tag{296}$$

The Gamma shapes fit the experimental distributions of the blob sizes *before* breakup (figure 90), and that of the drop sizes *after* ligament breakup, as substantiated in this review. For an initially corrugated ligament, coalescence between the blobs tends to restore the average diameter $\langle d \rangle$ from ξ to d_0. This is at the expense of the number of blobs, decreasing in time as

$$\frac{N(t)}{N(0)} = \left(1 + \frac{N(0)^{1/n}t}{n(1 + n/3)}\right)^{-n}. \tag{297}$$

Concomitantly, the average diameter increases as $\langle d \rangle/\xi \sim N(t)^{-1/3}$, and the net projected ligament surface $S(t) = N(t)\int d^2 p(d, t)\mathrm{d}d$ behaves like $N^{1/3}$ (figure 90).
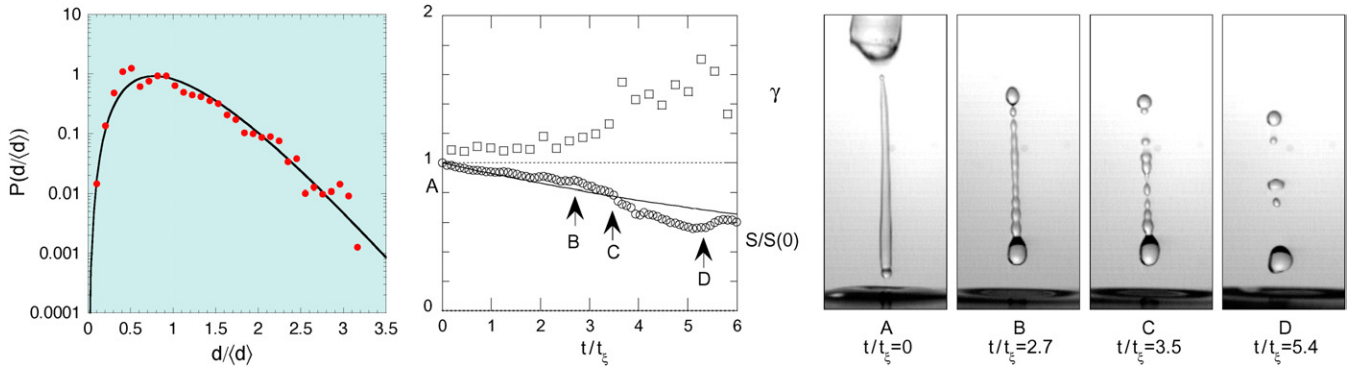
Figure 90. Blob size distribution of the ligament in figure 89 just prior to its breakup, fitted by a *Gamma* distribution of order $n = 4.5$. (Left) Evolution of the roughness ζ of the ligament ($\square$) and of the surface $S/S(t = 0)$ ($\bullet$) as a function of the time in units of the capillary time t_ξ. The continuous line is the prediction for $S(t)$ based on equation (293). (Right) Corresponding ligament.
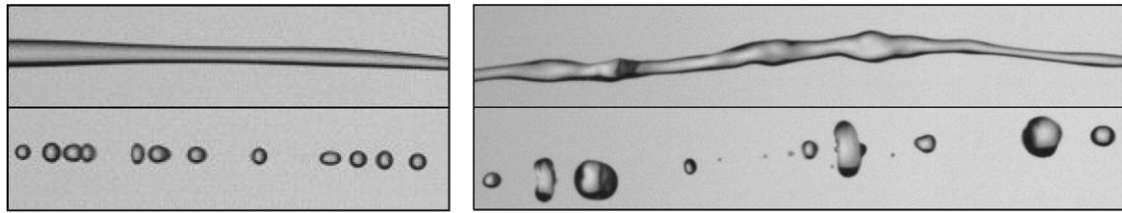

Figure 91. An initially smooth ligament produces a set of close to mono-disperse drops, while a rough ligament breaks into drops with a broad collection of sizes. The parameter n is large on the left and small on the right.

5.3.3. Average drop size versus variance. The dependence of the resulting average droplet sizes $\langle d \rangle$ on n contains two distinguished limits: for large n (i.e. for smooth and uniform ligaments) one finds a narrow distribution (width $\sim 1/\sqrt{n}$) centred around ξ:

$$\ln \frac{\langle d \rangle}{\xi} \simeq \frac{1}{n}. \qquad (298)$$

This means drop sizes are proportional to the initial thread diameter, cf [147]. For small n (strongly corrugated ligaments) one has

$$\ln \frac{\langle d \rangle}{\xi} \simeq \ln(N(0)^{1/3}) - \frac{1}{3} n \ln(n), \qquad (299)$$

giving an average drop size $\langle d \rangle \approx \xi N(0)^{1/3} = V^{1/3} = d_0$, of the order of the equivalent diameter (in terms of volume) of the entire ligament. Ligaments which break into one big drop, plus a few smaller ones, produce the *broadest* possible size distribution. These distributions resemble those encountered in section 5.1.1. Interestingly, (299) predicts that thinner, but nevertheless corrugated ligaments produce not only finer drops, but also narrower distributions (figures 71 and 80). Ligaments of this type are formed by fast winds, or when capillary breakup is slowed down by an increased liquid viscosity [516, 517] so that the ligament is stretched longer [456].

This trend is the opposite of the sequential cascade mechanism, for which the width of the distribution is increasing with the cascade step, while drop sizes are decreasing as the steps are accumulated (section 5.2.1 and (277)). On the contrary, breakup of corrugated ligaments involves an *inverse cascade*, going from the smallest towards the larger sizes, the coarsening process being interrupted earlier

for smooth ligaments, and going on up to d_0 for rough ligaments (figure 91).

When the diameter d_0 is itself distributed among the ligaments population as $p_L(d_0)$, the size distribution in the spray is

$$p(d) = \int p_L(d_0) p_B(d/d_0) \mathrm{d}d_0. \qquad (300)$$

Generically (see figure 80), $p_B(d/d_0)$ is narrower than $p_L(d_0)$. The composition operation stretches the large excursion wing of $p_B(d/d_0)$ over nearly the whole range of sizes d; as a result, the distribution in the spray (figure 71) once more has an exponential tail

$$p(d) \sim \exp(-n\, d/\langle d_0 \rangle). \qquad (301)$$

The steepness of the fall-off depends on the average ligament volume through $\langle d_0 \rangle$, which also sets the average drop size in the spray, independent of Weber number [518, 519]. This fact is once more in disagreement with the direct cascade scenario (section 5.2.1). Instead, the exponential shape of spray size distributions originates from the large excursion tail of the Gamma distribution, which in turn arises from ligament dynamics, the crucial step of atomization.

The examples discussed so far all concerned liquid drops forming in a gaseous environment. There is no reason to think that the same phenomenology and ideas should not apply to the opposite situation of bubbles forming in a continuous liquid phase: the fundamental instability, that of a hollow ligament in a liquid, is of the same nature as that of a liquid ligament in vacuum (see e.g. section 3.4 and [145]). Bubbles entrained at the sea surface by breaking waves have size distributions very likely to be Gamma distributions [478, 479].

5.3.4. Minimum value of the Gamma order. The relative roughness of the ligament $\zeta = \langle d^2 \rangle_0 / \xi^2$ sets the width of the resulting drop size distribution, since the order n is

$$n = \frac{\xi^2}{\langle d^2 \rangle_0 - \xi^2}. \tag{302}$$

The strongest corrugations of the initial ligament are bounded by the ligament diameter. Thus estimating the maximum roughness by $\sqrt{\langle d^2 \rangle_0 - \xi^2} \approx \xi/2$, one finds the minimum value of n to be

$$n_{\min} \approx 4 \tag{303}$$

or slightly above. This is close to the value found for liquid sheets (for which $n \approx 5$) as seen in figure 93. This reflects the strong corrugation of the sheet's rim, which have reached their saturation level, independent of the injection parameters (see figure 78 and [278, 450]).

5.4. Origin of roughness: the case study of merging jets.

The roughness of jets and ligaments sets the width of the resulting drop size distribution. This roughness has multiple origins in various practical situations and it is difficult to anticipate *a priori*. However, in the model problem of the merging of two identical jets, parameters can be controlled more carefully.

Consider the inelastic collision of two identical jets with diameter d_1 and velocity u_1, merging at an angle 2θ, and thus forming another free ligament. Let the jets Weber number *We* be moderate, between 5 to 10 (figure 94); it must in fact be smaller than $4(1 + \cos\theta)/(\sin\theta)^2$, the value above which the jets form a sheet [456]. We show that an energy balance explains the corrugations amplitude of the resulting jet, and consequently the width of the drop size distribution.

We take the jets as initially smooth, and call u and p the resulting ligament velocity and internal pressure, and d its diameter (figure 92). Momentum and mass conservation give

$$\rho u_1 \cos\theta \cdot 2u_1 d_1^2 - \rho u \cdot u d^2 = (p - p_1)d^2, \tag{304}$$

$$2u_1 d_1^2 = u d^2. \tag{305}$$

Surface tension enters through the internal pressures $p_1 = 2d_1/\gamma$ and $p = 2d/\gamma$. The pressure difference before and after merging is, according to (304), (305), given by

$$p_1 - p = \rho u(u - u_\parallel) \qquad \text{with } u_\parallel = u_1 \cos\theta. \tag{306}$$

On a pressure scale given by the incident kinetic pressure ρu_1^2, the pressure difference $p_1 - p = 2/\gamma(1/d_1 - 1/d)$ is of order We^{-1}. The velocity of the resulting jet u is thus

$$u \approx u_\parallel = u_1 \cos\theta, \tag{307}$$

up to terms of order $We_1^{-1} = O(1/10)$, so that typically $d/d_1 \approx \sqrt{2/\cos\theta}$. However, the loss of energy q during the collision

$$q = \frac{1}{2}\rho u_1^2 (1 - \cos^2\theta) + \frac{2\gamma}{d_1}\left(1 - \frac{d_1}{d}\right) \tag{308}$$
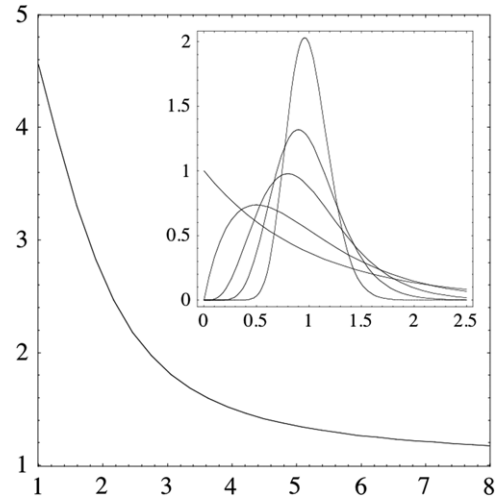

Figure 92. Average diameter of the drop's dispersion normalized by the ligament initial average radius $\langle d \rangle / \xi$, as a function of n according to (297) for $N(0) = 125$. An initially strongly corrugated ligament gives rise to an average droplet size appreciably larger than its average initial diameter. Inset: corresponding distributions $p(d/\langle d \rangle)$ as a function of $d/\langle d \rangle$ for $n = 1, 2, 5, 10, 25$.

is of order one, and dominated by the surface energy term. Namely, the destruction of surface area in the collision is

$$q = \frac{2\gamma}{d_1}\left(1 - \frac{1}{\sqrt{2}}\right) + O(\theta^2), \tag{309}$$

as illustrated in figure 95.

We know of no *ab initio* principle that determines how this energy will be dissipated. Irregular motions in the bulk of the resulting jet will excite capillary waves at its surface, which ultimately decay by viscous friction. We proceed by invoking an equipartition between bulk agitation and surface energy [520], although we are not describing an equilibrium situation. The change of surface energy ΔE of a cylinder of radius $h = d/2$, perturbed at wavenumber k with amplitude ϵ_k, is given by (49). We attribute the amount of energy ultimately dissipated to the (transient) excess of surface energy (implying de facto that $k > 2/d$):

$$\Delta E \sim q \frac{\pi d^2}{4} \ell, \tag{310}$$

with an unknown prefactor, presumably of order unity. This gives the relative amplitude of the corrugations thus formed as

$$\frac{\epsilon_k^2}{d^2} = \frac{1}{2} \frac{\sqrt{2} - 1}{\left(\frac{kd}{2}\right)^2 - 1}, \tag{311}$$

independent of surface tension. In the confluence region, the resulting jet is excited essentially at a scale given by the size of the incoming jets d_1. Putting therefore $k = 2\pi/d_1$, and remembering that the width of the drop size distribution is set by the order $n = d^2/\epsilon_k^2$, one finds that

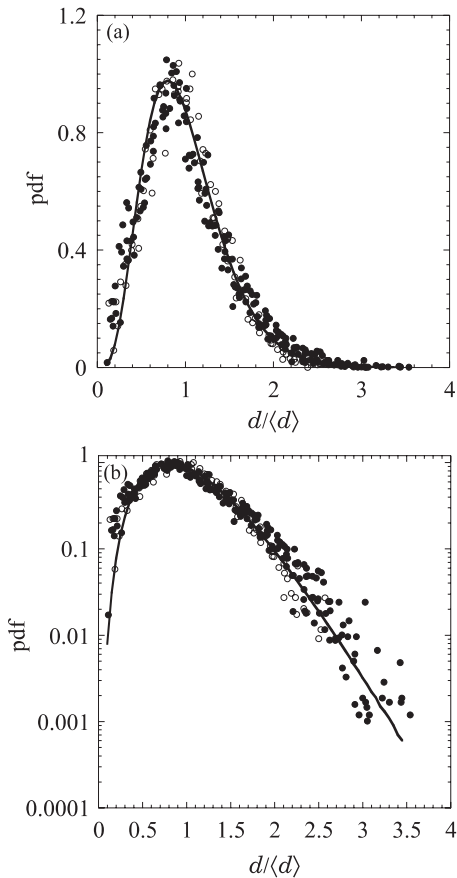$$n = \frac{4\pi^2 - 2}{\sqrt{2} - 1} \approx 90. \tag{312}$$

Figure 93. (*a*) Probability density functions of the drop size d, normalized by the arithmetic mean $\langle d \rangle$ for a number of jet velocities u_j and for several conditions of forcing ● as well as without forcing ○. The solid curve represents the Gamma distribution with $n = 5$. (*b*) Semi-logarithmic representation of the size distributions shown in (*a*); for details see [278].
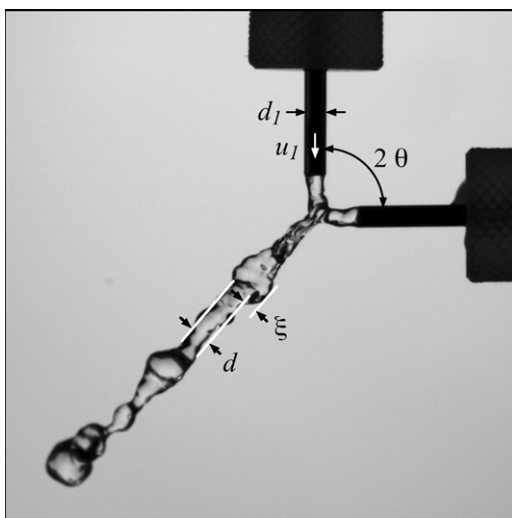

Figure 94. Two liquid jets, impacting at an angle 2θ, at small Weber number ($We = 5$).

Figure 96 indeed shows that when two nearly (but not strictly) smooth jets merge, they give rise to drop distributions essentially independent of the merging angle, and well fitted by Gamma distributions with an order ($n = 70$), a large figure
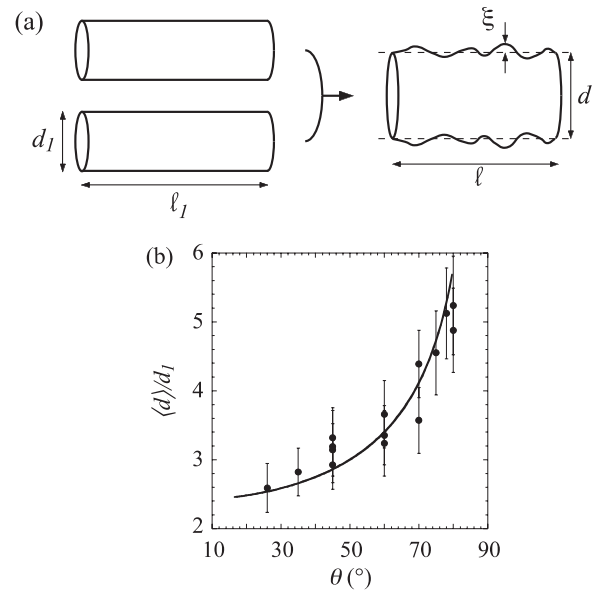

Figure 95. (*a*) Schematic of jet merging, and surface roughness generation. Corrugations expanded in Fourier modes: $\xi = \sum_k \epsilon_k \cos(kx)$. (*b*) Dependence of the average drop size from the destabilization of the resulting jet on the impact angle. Solid line is $\langle d \rangle / d_1 = \sqrt{2/\cos\theta}$.

characteristic of 'nearly smooth jets', but somewhat smaller than the expected one. This latter difference is an indication of the residual fluctuations in the incoming jets (see figure 96(*a*) and (*b*)). According to this mechanism, the stronger the noise, the broader the distribution. Note, however, a recent observation that reports an opposite trend [299].

6. Non-Newtonian effects

The universal structure of pinch-off solutions owes everything to the fact that the Navier–Stokes equations retain the same structure, independent of the fluid. An important assumption underlying this statement is that the time scale of all relaxation processes is short compared with the time scale of the flow. Near pinch-off, in particular, this assumption is bound to be violated, since the time scale of the flow goes to zero.

The most common case is that the fluid contains molecules of high molecular weight, whose relaxation time towards their equilibrium state is no longer negligible. In addition, if the polymers are flexible, they are able to store energy, resulting in elastic behaviour. Indeed, flexible polymers have the most dramatic effects, as concentrations as low as 10 ppm can completely alter the character of jet breakup [521]. Other examples of non-Newtonian behaviour whose effect on jet breakup has been studied are shear-thinning liquids [522], yield-stress fluids [523], liquid crystals [524], superfluid helium [525] and sand [526]. Surfactants, on the other hand, alter the surface tension, which is driving much of jet dynamics [527].

6.1. Flexible polymers

Many liquids of biological and industrial importance contain very long, flexible polymers. Figure 97 shows a jet of
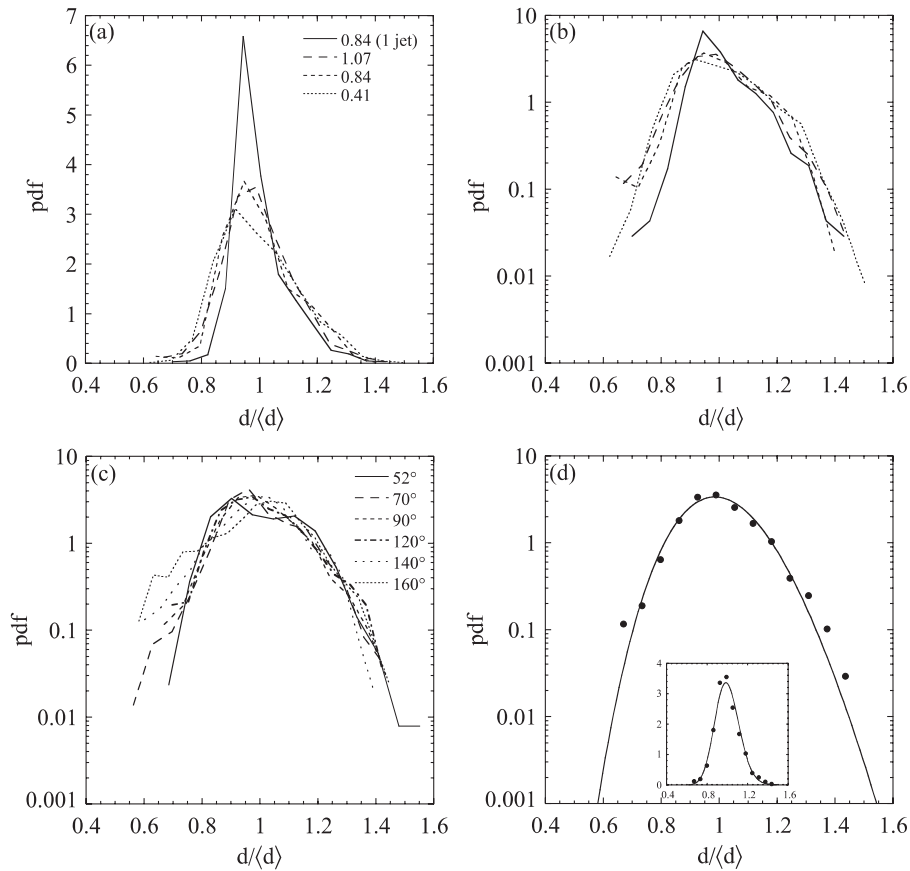
Figure 96. Probability density functions (pdf) of the drop size d normalized by the arithmetic mean $\langle d \rangle$ for (a) two jets at an angle of $90°$ and three different diameters d_j. For comparison, the pdf for a single jet is also shown. (b) Same as (a) in log–lin units. (c) Pdf for an impact angle 2θ varying from $52°$ to $160°$ with two identical jets of 1.07 mm. (d) Pdf for two jets with $d_j = 1.07$ mm, $\alpha = 90°$ superimposed with a Gamma fit with $n = 70$.
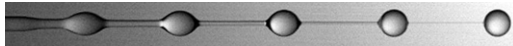

Figure 97. Photograph of a jet of dilute (0.01 wt%) aqueous polyacryamide solution (surface tension $\gamma = 62$ mN m^{-1}) undergoing capillary thinning [316]. The polymeric contribution to the viscosity is $\eta_p = 0.0119$ Pa s, and the polymer timescale is found to be $\lambda = 0.012$ s. This corresponds to a Deborah number of $De = 18.2$.

water, into which a small amount of flexible polymer has been dissolved. Instead of breaking up like a jet of water (cf figure 12), adjacent drops remain joined by threads, which grow increasingly thinner, delaying breakup significantly [528]. The reason for this 'beads-on-a-string' structure is that polymers become stretched in the extensional flow inside the thread, and thus depart from their ideal coiled state [529]. The polymers' tendency to return to their equilibrium configuration results in a buildup of extensional stresses, which resists pinching.

The initial stages of jet instability, as shown in figure 97, are of course governed by a linear instability, as analysed in [528, 530, 531] for, among others, the general 'Oldroyd 8-constant model' [529]. The most outstanding conclusion from these studies is that the non-Newtonian liquid breaks up *faster* than a corresponding Newtonian liquid. Namely, in the limit of very low shear rates Newtonian behaviour is

recovered, which defines a 'zero-shear rate viscosity'. The quantitative consequences of this observation seem to be small, however, as we are sadly unaware of any experimental test of the theory. What is more important is that threads *under tension* are stable [530]. Below we will see that threads in the late stages of pinching, as seen towards the right of figure 97, are indeed under tension.

Polymeric threads have been observed in liquid jets [528, 532], drops falling from a capillary [521] or in filament breakup devices [533, 534]. The latter consist of two rigid plates which are rapidly pulled apart, to form an unstable liquid bridge, which then pinches owing to surface tension. The thickness of a thread is very nearly uniform in thickness [316], since any reduction in radius increases extensional stresses, as argued above. Thus from a simple measurement of the thread radius, information on the polymeric stresses at very large deformations can be deduced, which is virtually unobtainable by any other measurement. The only alternative is much more elaborate 'filament stretching devices' [535–537], in which plates are separated *exponentially*, to keep the extension rate constant. Eventually external forcing leads to de-cohesion from the endplate [538], and thus breakdown of the method. Capillary thinning thus plays an important role in polymer rheology, and filament breakup devices are being marketed under the name CABER [539].
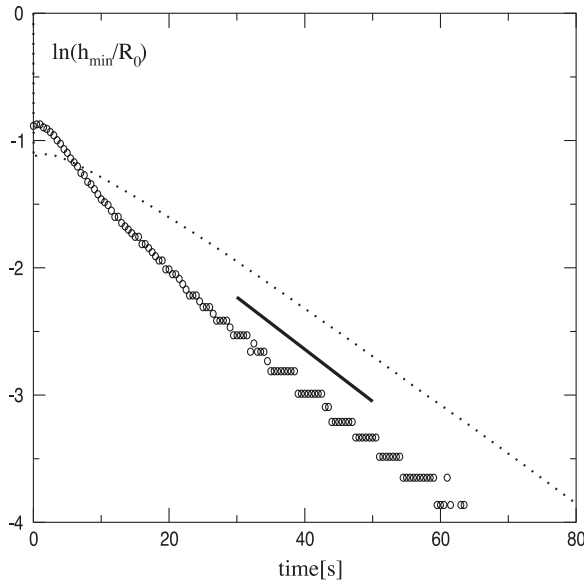
Figure 98. The logarithm of the normalized minimum radius of a liquid bridge, which was produced by a very rapid initial stretch [316]. The circles correspond to experiment, theory to the dotted line. The thick line is the theoretical prediction for the slope $-1/(3\lambda)$.

Figure 98 shows some typical data obtained for the case of a highly dilute polymer in a *viscous* solvent [533, 540]. A simple interpretation of thinning data is aided by the fact that the threads are very generally observed to thin exponentially [540]:

$$h = h_0 \exp(-\beta t), \qquad (313)$$

thus defining a single characteristic timescale β^{-1} of the system. In a simple extensional flow (29), (313) produces a constant extension rate $\dot{\epsilon} = v' = 2\beta$, to which polymers are subjected. The straight line in figure 98 is the theoretical prediction $\beta = 1/(3\lambda)$, to be explained below, where λ is the *longest* relaxation time of the polymer, obtained from a near-equilibrium measurement alone [533, 541]. Unfortunately, this simple interpretation of the thinning rate fails for small viscosities [521, 541, 542], as we will see below.

Two different approaches have been used to describe the motion of polymeric liquids [529]. In the spirit of continuum modelling, the first aims at identifying proper 'slow' variables to describe the additional degrees of freedom. There is much debate as to what these slow variables are, and how the right conservation laws and symmetry principles are built into the theory [543–545]. Worse still, even when properly accounting for symmetry constraints, there is a virtually infinite freedom in proposing 'constitutive' equations, which relate the average state of the polymers to the flow they are experiencing.

An alternative is to start from 'microscopic' models of polymers in a flow. Much progress has been made by modelling their equilibrium behaviour as long chains of beads, tied together by elastic springs [546]. Far from equilibrium, the state of the art remains much more rudimentary [547]: just *two* beads, connected by a spring. Moreover, the polymer solution is assumed to be 'dilute', so there is no interaction

between polymers. As a 'polymer' is stretched, additional stress is supported by the tension in the spring, leading to a strong increase in the effective 'extensional' viscosity. The simplest, exactly solvable model is the Hookean spring, which quite unrealistically allows the polymer to become infinitely stretched, once it is subjected to a sufficiently strong extensional flow. An attempt to improve this is the so-called FENE model [529], for which the restoring force diverges once a critical extension is reached. This model is no longer exactly solvable, but requires moment closures, the simplest of which is called FENE-P.

It goes without saying that these models can in no way do justice to real polymer–fluid interactions. The best one can hope for is to build in some simple physical ideas in a consistent fashion. In a one-dimensional description, the polymers lead to an additional contribution from the axial components $\sigma_z(z, t)$, $\sigma_r(z, t)$ of the stress to the force balance (30) [126, 542, 548]:

$$\partial_t v + v v' = -\gamma \kappa'/\rho + [(\sigma_z - \sigma_r + 3\nu_s v')h^2]'/h^2. \qquad (314)$$

In a FENE-P description, the stresses are related to the corresponding components of the conformation tensor **L** of the polymer via $\sigma_z = \nu_p L_z/(\lambda_p N) - \nu_p/\lambda_p$ and $\sigma_r = \nu_p L_r/(\lambda_p N) - \nu_p/\lambda_p$, where $N = 1 - (L_z + 2L_r)/b$. The extensibility parameter b limits the maximal extension a polymer can have, ν_s is the viscosity of the solvent, while ν_p is the zero-shear contribution of the polymer.

Finally the stretching of the polymer is described by

$$\partial_t L_z + v L_z' = 1/\lambda_p + (2v' - 1/(\lambda_p N))L_z \qquad (315)$$

$$\partial_t L_r + v L_r' = 1/\lambda_p - (v' + 1/(\lambda_p N))L_r. \qquad (316)$$

If the flow is such that $2v' > 1/\lambda_p$ and constant, corresponding to a strong elongation, L_z will grow exponentially, while L_r remains inconsequential for most slender-jet problems. If the polymer is infinitely extensible ($b = \infty$), one obtains the classical Oldroyd-B model [529], and exponential growth continues forever. The zero-shear rate viscosity ν_p can be determined by rheological measurements [549].

If polymers are still far from full extension, (314)–(316) predicts exponential thinning of the thread at a rate $1/(3\lambda_p)$, as we are going to see now. When the polymers have reached their maximum extension, breakup proceeds more rapidly, since the stress supported by the polymers no longer increases [548]. Thus to understand (313) we consider the limit $b \to \infty$, in which case the longitudinal stress σ_z is proportional to L_z. Assuming a spatially constant stress, from (315) we then find exponential growth of σ_z, at a rate $4\beta - 1/\lambda_p$.

Now we use the force balance (314), which in the late stages of pinching is dominated by surface tension and polymeric stress. In particular, since inertia can be neglected, one can integrate (314) spatially to give the balance

$$(\gamma/\rho)h + h^2\sigma_z = T(t), \qquad (317)$$

where $T(t)$ is the tension in the string. Since pinching is driven by surface tension and resisted by polymer stretching, it is reasonable to expect that the two terms on the left are of the

same order, $\sigma_z \propto 1/h$. Thus $\beta = 1/(3\lambda_p)$ and the stress increases at the same rate as the radius decreases:

$$h = h_0 \exp(-t/(3\lambda_p)), \qquad \sigma_z = \sigma_0 \exp(t/(3\lambda_p)). \quad (318)$$

As shown in figure 98, (318) works reasonably well. The polymer relaxation time was determined by fitting small amplitude oscillatory shear data to a Zimm spectrum [546], and identifying λ_p with the longest time scale [550].

However to determine the so-called extensional viscosity $\nu_e = \sigma_z/\dot\epsilon$, the prefactor σ_0 in (318) is needed, which according to (317) is determined by the tension $T(t)$ in the thread. To this end one has to understand how a thread, as seen in figure 97, is matched to the drops between which it is strung. As is evident from figure 97, the transition region where the thinning thread is attached to a drop develops into an increasingly sharp corner. Recently [316] it has been shown experimentally and theoretically that the profile in the corner region is self-similar, with a typical size that is set by the thread radius. Using this self-similar structure, and within the confines of the one-dimensional model equations (314)–(316), the tension was found to be $T = 3\gamma h/\rho$. The extensional viscosity

$$\nu_e = 3\lambda_p \gamma/(\rho h) \qquad (319)$$

can thus be determined from a measurement of the thread thickness alone. However, the slenderness assumptions underlying the one-dimensional description is no longer valid inside the drop, so the precise value of the prefactor in (319) is expected to be different if the full axisymmetric flow profile is used. Thus, a fully quantitative calculation of the extensional viscosity of a thinning polymeric thread remains an unsolved problem.

A particularly simple description of a polymeric thread is achieved for observation over a time short compared with λ_p, formally derived from (315), (316) in the limit $\lambda_p \to \infty$. In particular, one finds [551, 552] that for negligible initial deformation $\sigma_z - \sigma_r = G(1/h^2 - h^4)$, where $G = \nu_p/\lambda_p$ is the 'elasto-capillary' number [533]. In this limit in which there is no polymer relaxation, the fluid behaves like an elastic solid. As a result, a stationary thread thickness is reached, corresponding to a balance of surface tension and elastic stresses [551]. A linear analysis of this stationary state shows that it is stable, with non-dispersive elastic waves running on it.

Figure 99 illustrates the effect of flexible polymers on the dripping of a low-viscosity solvent (water), (a) showing the case of pure water for reference. The images in (b) and (c) are split to demonstrate the considerable power of the one-dimensional model (314)–(316) in reproducing experimental data. In this comparison, only the polymer timescale λ_p was used as an adjustable parameter [542]. If polymers are added to the water, a thin thread forms between the main drop and the nozzle, analogous to figure 97. However, if the nozzle diameter is sufficiently large, a smaller 'satellite' bead is trapped in the middle of the thread. In particular, if the polymer timescale λ_p is greater than the Rayleigh time (2), polymer stretching sets in right after the initial linear disturbance growth on the fluid neck, resulting in a symmetric profile, cf figure 99(c). In this case, a uniform thread is formed. In the opposite case, polymer stretching is negligible at first,
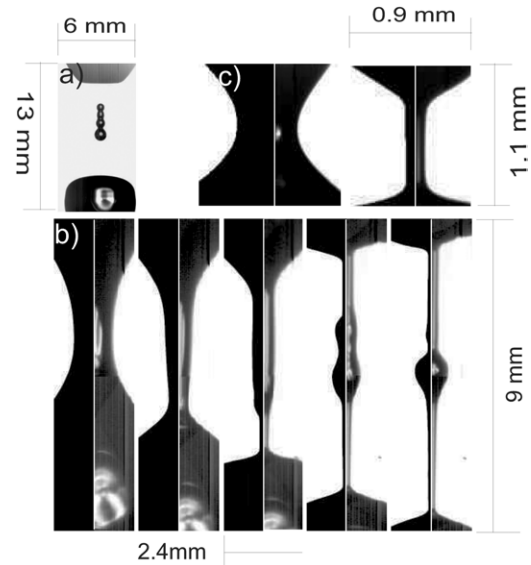

Figure 99. (a) A drop of water falling from a faucet, $h_0 = 3$ mm. (b), (c): closeup of the pinch region, with 100 ppm of PEO solution added. (left: numerical simulations, right: experiment) (b): $h_0 = 3$ mm, $t_c - t = 6, 2, 0, -3, -5$ ms; (c): $h_0 = 0.4$ mm $t_c - t = 1, 0$ ms. Model parameters: $\eta_p = 3.7 \times 10^{-4}$ Pa s, $\lambda_p = 1.2 \times 10^{-2}$ s, $b = 2.5 \times 10^4$, $\eta_s = 1 \times 10^{-3}$ Pa s, $\gamma = 6 \times 10^{-2}$ N m^{-1}.

and a highly asymmetric Euler solution (212) develops [521], see also figure 14. This normally leads to the formation of a satellite drop, but since polymer stretching eventually becomes important, this satellite drop is connected by thin threads cf figure 99(b). In [521], the thinning rate at the abrupt transition between the Euler solution and a thread was proposed as a measure for the polymer time scale. This rate was found to be similar to, yet significantly different from the subsequent thinning rate of the thread.

Indeed, while the FENE-P model (314)–(316) is successful in describing the early stages of pinching shown in figure 99, it fails to satisfactorily describe the subsequent thinning of the thread. In [541] a strong dependence of β on the polymer concentration c was found, which persists to concentrations far below overlap concentration c^*, and which is attributed to interactions between polymers. Namely, polymers become highly deformed in the early stages of pinching, which greatly increases their interaction radius. However, two observations made in [542] point to even more fundamental problems of classical descriptions like FENE-P. Firstly, in [542] λ_p was fitted to match the transition from the Euler solution to a polymeric thread, but the same value does not predict the correct thinning rate of the thread. Thus more than one time scale seems to be necessary. Even more worryingly, the value of β was also found to depend on the radius of the capillary, so β cannot be an intrinsic property of the model. In [542] it is argued that for small solvent viscosities, polymer deformation is already large at the onset of thread formation, so finite size effects may play a significant role.

Still another phenomenon occurs for somewhat more concentrated (above c^*) aqueous solutions, as first described
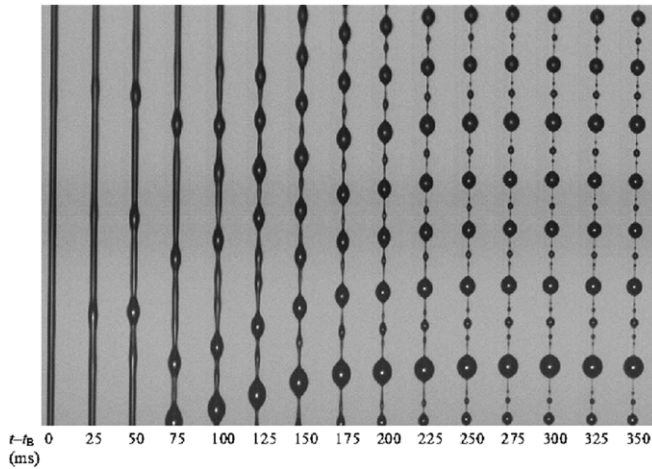
$t-t_B$　0　25　50　75　100　125　150　175　200　225　250　275　300　325　350
(ms)

Figure 100. Blistering of an aqueous solution of $M_w = 3.8 \times 10^6\,\mathrm{g\,cm^{-3}}$ PEO solution at a concentration of $c = 2000\,\mathrm{ppm}$. Reprinted with permission from [515], copyright 2005 by the American Institute of Physics.

by [515]. The first image shown in figure 100 is a closeup of a single, highly stretched polymer thread such as the one seen suspended between the two rightmost drops in figure 97. At first, the thread is subject to what appears to be a linear instability with a well-defined wavelength [553]. Interestingly, the process goes through several stages, leading to up to 4 generations of droplets of decreasing size (cf figure 100). The phenomenon appears not to be described by the FENE-P model (314)–(316), as shown in [548]. Namely, according to (314)–(316), when polymers become fully stretched, the thread breaks in a localized fashion, once more described by a similarity solution, whose exact form depends on the polymer model used [554, 555].

A similar phenomenon of 'iterated stretching' had been observed earlier in [556]. However, the theoretical analysis is based on dilute, infinitely extensible polymers, and occurs only in the corner region, where the thread meets the drop. This is contradicted both by experiment (since the instability grows in the interior of the thread, cf figure 100 [515]), and subsequent slender-body analyses of the Oldroyd-B equations [316, 548, 557]. Finally, in his classical monograph Boys [558] shows a picture of a thread taken from a spider web, showing droplets of various sizes on the thread, whose appearance is strikingly similar to figure 100. The 'sticky' droplets have an important biological function in capturing insects [559]. It remains to be seen whether they are produced by the same blistering instability seen in figure 100, or whether they come from a coat of sticky liquid applied to an existing thread, as is usually supposed in the literature [559].

6.2. Shear-thinning fluids

If the polymer molecules in solution become stiffer, ideally like rods, memory effects diminish. A particularly simple case is the 'generalized Newtonian liquid' [529], for which the stress tensor is proportional to the deformation rate tensor $\boldsymbol{D}$ (cf (39)), but with a viscosity that depends on the invariants of $\boldsymbol{D}$. Very often it is observed that the viscosity diminishes like a power

law as a function of the second invariant $\dot{\gamma} = \sqrt{D_{ij}D_{ij}}$, if $\dot{\gamma}$ is greater than a critical value $\dot{\gamma}_0$ (Carreau fluid):

$$\eta/\eta_0 = (1-\beta)[1+(\dot{\gamma}/\dot{\gamma}_0)^2]^{(n-1)/2} + \beta. \qquad (320)$$

For low shear, the viscosity tends towards a constant value. If $n < 1$, as is observed for xanthan gum solutions [560], the behaviour is shear thinning.

Note that (320) implies the same shear-thinning behaviour under extension; namely, in a thin filament $\dot{\gamma} = |\partial v_z/\partial z| = |v'|$ to leading order. This determines the slender-jet equations (30), with the viscosity replaced by (320). The problem is that there is not much evidence so far that (320) is a faithful description for extensional flows, as most rheological measurements are under shear. In fact, there is evidence that xanthan gum solutions (like suspensions of rigid rods), *thicken* under extension [561–563]. By contrast, there is some evidence that concentrated suspensions of *spherical particles* show not only shear thinning [564] but also extensional thinning [565]. The latter has also been found in polymer melts [566].

It is simplest to analyse pinching in the limit $\dot{\gamma} \gg \dot{\gamma}_0$, for which there is pure power-law behaviour, and a similarity solution of the form (199) can be found [567–569]. Namely, from (29) one estimates that $v' \propto t'^{-1}$, and a capillary-viscous balance gives $1/h \propto \eta v' \propto v^n$. From this we deduce immediately that $\alpha_1 = n$: not surprisingly, pinching is speeded up, because the viscosity decreases as pinching progresses. As in the previous section, pinching experiments have the potential of conveying useful information on the extensional rheology of the liquid, which is difficult to obtain by other means. This statement is not tied to power-law behaviour, although this of course simplifies the analysis.

The axial extension of the solution is determined from including inertia in the balance [567, 568], leading to

$$\alpha_1 = n, \qquad \alpha_2 = -n/2, \qquad \beta = 1 - n/2. \qquad (321)$$

Thus as n decreases, the solution becomes more localized, and for $n = 2/3$ axial and radial length scales become the same, so that a long-wavelength description is no longer justified. This makes intuitive sense, since the dynamics accelerates rapidly as one gets close to the pinch point. In addition, as solutions of the similarity equations demonstrate [568], profiles become increasingly symmetrical. The net result is that even if the base viscosity is high, thread-like features close to breakup disappear, as seen in the one- and two-dimensional simulations shown in [522]. Instead, breakup is localized and less likely to produce satellite drops. From an engineering point of view, this is a desired effect for many foods, for example yoghurt, for which a 'stringy' appearance is not considered attractive [570]. In fact, preliminary experiments show that some brands of yoghurt are indeed shear thinning. Breakup experiments then demonstrate that the pinching exponent α_1 is indeed smaller than 1, showing that the thinning effect extends to extensional flow [570].

If the base viscosity is high, one expects inertia to be irrelevant initially; of course, as viscosity decreases, a crossover to an inertial–viscous balance will occur even sooner [567, 568]. For $n \neq 1$ new branches of *symmetric* solutions are
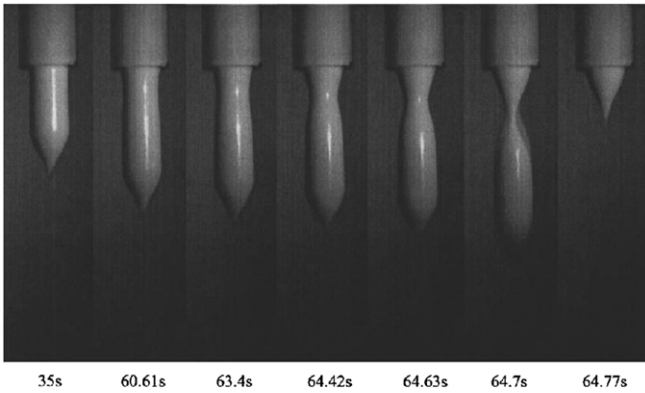
35s   60.61s   63.4s   64.42s   64.63s   64.7s   64.77s

Figure 101. Successive views of a mayonnaise sample at different times, pushed out of a nozzle of radius $h_0 = 3$ mm. The initial time (0 s) corresponds to the separation of the previous extrudate. Reprinted with permission from [523]. Copyright 2005 by the American Physical Society.

found, which connect between the symmetric Stokes solution branch and the asymmetric Navier–Stokes solution branch far away from $n = 1$. In the Newtonian case $n = 1$ itself, no symmetric solutions are known to exist if inertia is present. Just as in the purely Newtonian case, the axial exponent β is no longer determined by dimensional analysis if inertia is absent, but has to be obtained from solving the similarity problem explicitly, as done in detail in [569]. As expected, β increases with decreasing n, making the profile less slender.

6.3. Other non-Newtonian behaviour

Another interesting type of rheological behaviour is displayed by materials like toothpaste, bread dough or mayonnaise (cf figures 101 and 4), which are so-called 'yield-stress' fluids [529]. This means they do not flow if the viscous shear stress they are subjected to is below a threshold value σ_0: $\sigma_{ij}\sigma_{ij} < 2\sigma_0^2$. In this regime the viscosity is effectively infinite. Above the yield stress σ_0, the viscosity is given by

$$\eta = \eta_0 + \frac{\sigma_0}{\sqrt{2}\dot{\gamma}} \qquad (322)$$

in the so-called Bingham model [529]. Mayonnaise is more realistically described by the Herschel–Buckley model, for which the divergence of the viscosity for $\dot{\gamma} \to 0$ is weaker than by the power of -1 in (322) [523].

Using the Lagrangian methods developed in [296, 571] analyses dripping using a generalized form of (322) (the two-fluid model), neglecting both inertia and surface tension. In the lower part of the drop the material does not move, but once gravitational stresses have become large enough the material starts to yield and pinch-off eventually occurs. The form of pinch-off is very similar to that of a purely Newtonian fluid with the same approximations, i.e. the liquid bridge has to extend to infinity before pinch-off occurs (cf (226)). Experiments, on the other hand, exhibit breakup profiles close to conical (see figure 101) [523], indicating that a description which predicts very long threads is not realistic. Clearly, it will be crucial to include surface tension into the description.

Jets of superfluid liquid helium are also a potentially interesting subject, because of the unique hydrodynamic

properties of the superfluid phase. Rayleigh breakup has been demonstrated as a useful source of superfluid helium droplets [525], and pinch-off of both normal and superfluid helium has been studied in [572]. Unfortunately, no qualitative difference between the two cases has been detected. An even more exotic 'fluid' that has recently attracted interest is formed by granular materials or sand [573]. Curiously, a jet of sand has been one of the earliest subjects investigated by photographic means [34], and one observes a decay into drops or clusters of sand, which is superficially similar to Rayleigh breakup [34, 526, 574]. A recent study suggests this to be a purely *kinematic* effect, based on the free fall of particles [526], pouring out of a container. Khamontoff [34] already investigated the effect of gravity, projecting the jet horizontally using compressed air. According to his preliminary investigation, the tendency to form clusters remained the same, which appears to contradict the simple kinematic theory [526]. Hence the true mechanism for cluster formation in a granular jet remains an open problem.

6.4. Surfactants

The value of the surface tension, in particular for aqueous solutions, depends strongly on the concentration of surface-active molecules or 'surfactants' [575]. Either surfactant molecules are inherently present, as in inks and DNA arrays [73], or they are added to control the drop sizes in sprays [576]. In general the surfactant distribution is non-uniform, hence non-trivial effects are to be expected, apart from renormalizing the surface tension.

Most existing studies consider the insoluble case ([527] is an exception), for which the surfactant remains on the surface. Then, the surfactant concentration $\Gamma(s, t)$ is described by [577]

$$\frac{\partial \Gamma}{\partial t} + \nabla_s(\Gamma \boldsymbol{v}) = D_s \nabla_s^2 \Gamma, \qquad (323)$$

where $\nabla_s = (\boldsymbol{I} - \boldsymbol{nn}) \cdot \nabla$ is the surface gradient operator. A non-dimensional measure of the diffusion constant D_s is the surface Peclet number $Pe = \sqrt{R\gamma_0/\rho}/D_s$, where γ_0 is the surface tension in the absence of surfactant. The Peclet number is usually large ($\approx 10^6$ for mm-sized jets [578]), so diffusion can be neglected [579]. The equation most commonly used to describe the dependence of surface tension on concentration is the non-linear Frumkin equation [578]

$$\gamma = \gamma_0 + \Gamma_m RT \ln(1 - \Gamma/\Gamma_m). \qquad (324)$$

At the maximum packing density Γ_m the surface tension reaches a plateau, an effect which is not captured by (324). Apart from changing the value of surface tension, the most important effect of (324) is that it introduces surface tension gradients: this results in Marangoni forces [42], which act to restore a uniform distribution of surfactant.

The most important parameter is thus the surface activity number $\beta = \Gamma_m RT/\gamma_0$, which measures the 'effectiveness' of the surfactant. For $\beta = 0$ the surfactant has no effect; in the extreme case of $\beta \to \infty$ the surface becomes rigid in the sense that any tangential flow must be balanced by radial contraction [579]. Typically, β is of order one ($\beta \approx 0.3$ in the experiments [578]).

The linear stability of a jet, uniformly covered by surfactant, has been studied for a long time [580, 581] in the absence of a surrounding liquid [579, 582, 583] and when an external fluid is present [584–586]. The most remarkable general feature is that in the inviscid limit surfactants leave the linear behaviour *unchanged* [581, 585]. In all cases, the surfactant slows down the instability. In the absence of an outer fluid, the surfactant tends to increase the most unstable wavelength [579, 585], which for vanishing Ohnesorge number becomes finite if $\beta > 1/2$ [579] (namely, it is *infinite* without surfactant according to (85)).

As for the non-linear behaviour, the most significant result is that the asymptotics of breakup, as described for Newtonian jets above, remains unchanged by the presence of surfactant [578, 579, 583]. The reason is that the strong extensional flow near the pinch point sweeps all the surfactant out of the pinch region. Most of the non-linear analyses of surfactant-laden jets are based on a slender-jet description analogous to (29), (30). However, comparison with fully three-dimensional, axisymmetric calculations shows that a slender-jet description is only quantitative for $\beta \lesssim 0.5$, when radial variations in the velocity field are not too great. It is found that satellite formation is suppressed by the presence of surfactant [576, 578, 583], since concomitant surface rigidification reduces axial velocities, and thus the role of inertia. More recently, it was shown that surfactants can promote the growth of several secondary necks during the small-scale evolution of a fluid jet [587], thus mimicking phenomena observed in the presence of noise [335].

Finally, we mention the so-called 'dynamic surface tension' [575], usually associated with soluble surfactants. Namely, if the surface and bulk concentrations are not in equilibrium, it will take a certain time for surfactants to diffuse to the surface and to establish equilibrium. Such effects were first discovered by [588], and measured by Rayleigh [155] using oscillations of a jet around a circular profile. Close to the nozzle, where the interface is still fresh, surface tension is found to be higher than away from it [155, 589]. Such measurements are notoriously difficult, among others since close to the nozzle the jet has not yet relaxed to a plug profile [590]. Dynamic surface tension also has dramatic consequences for the radial extent of Savart's sheets, an elegant configuration to study the transient diffusion of bulk surfactant towards the interface [591]. As a historical aside, phenomena which are most likely explained by the presence of surfactants have let to a spirited controversy between Phillip Lenard [20, 592] and the young Niels Bohr [156, 593], the former having erroneously claimed evidence for a dynamic surface tension of *pure* water [594, 595].

The issue of dynamic surface tension of a *pure liquid* has resurfaced recently [596], based on a surface tension measurement of water, using Rayleigh's and Bohr's method [597]. Introducing a phenomenological correction factor for the relaxation of the jet's velocity profile near the nozzle opening [590], a relaxation time of 3 ms was found for water, but not for any other pure fluid. As far as we are aware, this measurement has not been confirmed by any other group. A more recent review of dynamic surface tension measurements

[37] concludes that the fluid mechanics at the jet entry may not be sufficiently well understood for the oscillating jet method to be reliable. Instead, a recent study [589] found no evidence of relaxation behaviour of pure liquids. More importantly, the description used in [596] to model dynamic surface tension is physically flawed, and leads to predictions which are unrealistic [598]. Therefore, we do not believe that any meaningful conclusions can be drawn from an application of such models to jet breakup [599].

7. Perspectives

Given the breadth of the subject we have treated, a simple 'conclusion' would not be appropriate. Rather, we would like to indicate possible future directions of research.

- Armed with a good understanding of jet dynamics, one could tackle more ambitious questions of optimization and control: designing a nozzle 'on purpose' to get rid of satellites, or to minimize/maximize drop size under dripping, in the spirit of the 'optimal faucet' [600]. Also, what is the minimum energy needed to transform a certain amount of fluid into a spray with a given mean droplet size, and is the concept of energy useful in these instances [278]?
- A proper treatment of the capillary instability for the frequent case of a time-varying base solution, as epitomized by the stability problem of a falling thread (section 3.7.3), is still lacking.
- A few issues remain in the context of section 4 on breakup. Most notably, the destabilization of threads by noise (section 4.5.2), the transition from symmetric to non-symmetric pinch-off (figure 53), an experimental confirmation of post-breakup solutions such as that shown in figure 62 and cases where 'simple' breakup solutions can no longer be found, for example in inviscid pinch-off for large D (cf section 4.3.1).
- Jets produced from the collapse of a cavity and/or impulsive acceleration (see figures 73 and 74) are very important, for example to understand droplet production and its effect on the albedo of the ocean. The shape, dynamics and fragmentation of these jets remain an issue. For example, is there a 'generic' jet/ligament shape other than a uniform one, that would explain the observed drop size distributions?
- The self-convolution model conjectured in section 5.3.2 works well, but lacks a fundamental justification. A justification based on the equation of motion is needed.
- The intelligent use of polymers, for example to produce very thin yet persistent strands (cf section 6.1), with possible applications as synthetic textiles, or in understanding spider webs.
- Free-surface flows lead to highly non-linear fluid motion, in particular strong stretching. Non-Newtonian constitutive laws are usually not well tested in this regime, and few quantitative experiments are available. Even the much-studied case of flexible polymers (cf section 6.1), usually only leads to qualitative agreement between theory and experiment.

- The *extensional* rheology of dense suspensions [601], in particular, is not understood. Jet dynamics would furnish an ideal testing ground.

References

[1] da Vinci L 1980 *Codex Leicester* (London: Christie's)
[2] da Vinci L 1508 *The Notebooks of Leonardo da Vinci* ed and Transl. E MacCurdy (New York: George Brazillier) p 756
[3] Mariotte E 1686 *Traité du Mouvement des Eaux et Des Autres Corps Fluides* (Paris: E Michallet)
[4] de Laplace P S 1805 *Mechanique Celeste Supplement au X Libre* (Paris: Courier)
[5] Young T 1805 *Phil. Trans. R. Soc. Lond.* **95** 65–87
[6] Rowlinson J S 2002 *Cohesion* (Cambridge: Cambridge University Press)
[7] Navier C L 1827 *Mem. Acad. R. Sci. France* **6** 389–440
[8] Stokes G G 1845 *Trans. Camb. Phil. Soc.* **8** 287
[9] Savart F 1833 *Ann. Chim.* **53** 337–98
[10] Rayleigh Lord 1878 *The Theory of Sound* vol 2 (London: Macmillan) (reprinted 1945 New York: Dover)
[11] Plateau J A F 1843 *Acad. Sci. Brux. Mem.* **16** 3
[12] Plateau J A F 1849 *Acad. Sci. Brux. Mem.* **23** 5
[13] Hagen G 1849 *Verhandlungen Preuss. Akad. Wissenschaften* p 281
[14] Plateau J A F 1850 *Ann. Phys. Chem.* **80** 566
[15] Beer A 1855 *Ann. Phys. Chem.* **96** 1
[16] Plateau J A F 1873 *Statique Expérimentale et Theorique des Liquides Soumis aux Seules Forces Moléculaires* vol 2 (Paris: Gauthier Villars)
[17] Rayleigh Lord 1879 *Proc. R. Soc. Lond.* **10** 4
[18] Rayleigh Lord 1892 *Phil. Mag.* **34** 145–54
[19] Magnus G 1859 *Ann. Phys. Chem.* **106** 1
[20] Lenard P 1887 *Ann. Phys. Chem.* **30** 209
[21] Eggers J 1993 *Phys. Rev. Lett.* **71** 3458
[22] Day R F, Hinch E J and Lister J R 1998 *Phys. Rev. Lett.* **80** 704
[23] Rayleigh Lord 1891 *Nature* **44** 249–54
[24] Boys C V 1890 *Phil. Mag.* **30** 248
[25] Eggers J 2006 *Nonsmooth Mechanics and Analysis* ed P Alart *et al* (Berlin: Springer) p 163
[26] Edgerton H E, Hauser E A and Tucker W B 1937 *J. Phys. Chem.* **41** 1029
[27] Hauser E A, Edgerton H E, Holt B M and Cox J T Jr 1936 *J. Phys. Chem.* **40** 973
[28] Peregrine D H, Shoker G and Symon A 1990 *J. Fluid Mech.* **212** 25
[29] Ting L and Keller J B 1990 *SIAM J. Appl. Math.* **50** 1533
[30] Bentley W A 1904 *Mon. Weather Rev.* **10** 450–6
[31] Thoroddsen S T, Etoh T G and Takehara K 2008 *Annu. Rev. Fluid Mech.* **40** 257
[32] Villermaux E, Marmottant P and Duplat J 2004 *Phys. Rev. Lett.* **92** 074501
[33] Nollet A 1749 *Recherches Sur les Causes Particulières des Phénomènes Électriques* (Paris: les Frères Guerin)
[34] Khamontoff N 1890 *J. Russ. Physico-Chem. Soc. Saint Petersburg* **22** 281
[35] Gavis J and Modan M 1967 *Phys. Fluids* **10** 487
[36] Aiello G 1977 *Phys. Fluids* **20** 165
[37] Franses E I, Basaran O A and Chang C H 1996 *Curr. Opin. Colloid Interface Sci.* **1** 296
[38] Weber C 1931 *Z. Angew. Math. Mech.* **2** 136
[39] v Ohnesorge W 1936 *Z. Angew. Math. Mech.* **16** 355
[40] Rutland D F and Jameson G J 1971 *J. Fluid Mech.* **46** 267
[41] Donnelly R J and Glaberson W 1966 *Proc. R. Soc. Lond.* A **290** 547
[42] Landau L D and Lifshitz E M 1984 *Fluid Mechanics* (Oxford: Pergamon)
[43] Batchelor G K 1967 *An Introduction to Fluid Dynamics* (Cambridge: Cambridge University Press)
[44] Longuet-Higgins M S and Cokelet E D 1976 *Proc. R. Soc. Lond.* A **350** 1
[45] Mansour N N and Lundgren T S 1990 *Phys. Fluids* A **2** 1141
[46] Baker G R D, Meiron I and Orszag S A 1980 *Phys. Fluids* **23** 1485
[47] Oğuz H N and Prosperetti A 1990 *J. Fluid Mech.* **219** 143
[48] Moore D W 1983 *IMA J. Appl. Math.* **31** 1
[49] Dold J W 1992 *J. Comput. Phys.* **103** 90
[50] Tsai W T and Yue D K P 1996 *Annu. Rev. Fluid Mech.* **28** 249
[51] Lindblad H 2005 *Ann. Math.* **162** 109
[52] Leppinen D and Lister J 2003 *Phys. Fluids* **15** 568
[53] Schulkes R M S M 1994 *J. Fluid Mech.* **278** 83
[54] Ladyzhenskaya O 1969 *The Mathematical Theory of Viscous Incompressible Flow* (London: Gordon and Breach)
[55] Youngren G K and Acrivos A 1975 *J. Fluid Mech.* **69** 377
[56] Rallison J M and Acrivos A 1978 *J. Fluid Mech.* **89** 191
[57] Tjahjadi M, Stone H A and Ottino J M 1992 *J. Fluid Mech.* **243** 297
[58] Zhang D F and Stone H A 1997 *Phys. Fluids* **9** 2234
[59] Sierou A and Lister J R 2003 *J. Fluid Mech.* **497** 381
[60] Eggers J, Lister J R and Stone H A 1999 *J. Fluid Mech.* **401** 293–310
[61] Sussman M and Pucket E G 2000 *J. Comput. Phys.* **162** 301
[62] Scardiovelli A and Zaleski S 1999 *Annu. Rev. Fluid Mech.* **31** 567
[63] Tryggvason G, Bunner B, Esmaeeli A, Juric D, Al-Rawahi N, Tauber W, Han J and Jan Y J 2001 *J. Comput. Phys.* **169** 708
[64] Wilkes E D, Phillips S D and Basaran O A 1999 *Phys. Fluids* **11** 3577
[65] Li J, Renardy Y Y and Renardy M 2000 *Phys. Fluids* **12** 269
[66] Lowengrub J S and Truskinovsky L 1998 *Proc. R. Soc. Lond.* A **454** 2617
[67] Léopoldès J, Dupuis A, Bucknall D G and Yeomans J M 2003 *Langmuir* **19** 9818
[68] Magnaudet J, Rivero M and Fabre J 1995 *J. Fluid Mech.* **284** 97
[69] Shokoohi F and Elrod H G 1987 *J. Comput. Phys.* **71** 324
[70] Shokoohi F and Elrod H G 1990 *J. Comput. Phys.* **89** 483
[71] Notz P K, Chen A U and Basaran O A 2001 *Phys. Fluids* **13** 549
[72] Chen A U and Basaran O A 2002 *Phys. Fluids* **14** L1
[73] Basaran O A 2002 *AIChE J.* **48** 1842
[74] Chen A U, Notz P K and Basaran O A 2002 *Phys. Rev. Lett.* **88** 174501
[75] Ambravaneswaran B, Subramani H J, Phillips S D and Basaran O A 2004 *Phys. Rev. Lett.* **93** 034501
[76] Lapidus L and Pinder G F 1982 *Numerical Solution of Partial Differential Equations in Engineering* (New York: Wiley)
[77] Schulkes R M S M 1996 *J. Fluid Mech.* **309** 277
[78] Menard T, Tanguy S and Berlemont A 2007 *Int. J. Multiphase Flows* **33** 510–24
[79] Townsend A A 1976 *The Structure of Turbulent Shear Flow* (Cambridge: Cambridge University Press)
[80] Hirt C W and Nichols B D 1981 *J. Comput. Phys.* p 201
[81] Osher S and Fedkiw R P 2001 *J. Comput. Phys.* **169** 463

[82] Sethian J A 2001 *J. Comput. Phys.* **169** 503

[83] Josserand C and Zaleski S 2003 *Phys. Fluids* **15** 1650

[84] Popinet S and Zaleski S 1999 *Int. J. Numer. Methods Fluids* **30** 775

[85] Duchemin L, Popinet S, Josserand C and Zaleski S 2002 *Phys. Fluids* **14** 3000

[86] Lafaurie B, Nardone C, Scardovelli R, Zaleski S and Zanetti G 1994 *J. Comput. Phys.* **113** 134

[87] Popinet S 2006 *GERRIS* Available from http://gfs.sourceforge.net/wiki/index.php/Main_Page

[88] Biben T, Misbah C, Leyrat A and Verdier C 2003 *Europhys. Lett.* **63** 623

[89] Lee H G, Lowengrub J S and Goodman J 2002 *Phys. Fluids* **14** 492

[90] Rowlinson J S and Widom B 1982 *Molecular Theory of Capillarity* (Oxford: Clarendon)

[91] Rothman D H and Zaleski S 1994 *Rev. Mod. Phys.* **66** 1417

[92] Succi S 2001 *The Lattice Boltzmann Equation, for Fluid Dynamics and Beyond* (Oxford: Oxford University Press)

[93] Kitakawa A 2005 *Chem. Eng. Sci.* **60** 5612

[94] Reynolds O 1886 *Phil. Trans. R. Soc.* **177** 157

[95] Eggers J and Dupont T F 1994 *J. Fluid Mech.* **262** 205

[96] Ambravaneswaran B, Wilkes E D and Basaran O A 2002 *Phys. Fluids* **14** 2606

[97] Subramani H J, Yeoh H K, Suryo R, Xu Q, Ambravaneswaran B and Basaran O A 2006 *Phys. Fluids* **18** 032106

[98] Trouton F T 1906 *Proc. R. Soc. Lond.* **77** 426–40

[99] Matovitch M A and Pearson J R A 1969 *Ind. Eng. Chem. Fundam.* **8** 512

[100] Pearson J R A and Matovitch M A 1969 *Ind. Eng. Chem. Fundam.* **8** 605

[101] Schultz W W and Davis S H 1982 *J. Rheol.* **26** 331

[102] Markova M P and Shkadov V Y 1972 *Izv. Akad. Nauk SSSR Mekh. Zhidk. Gaza* **3** 30

[103] Lee H C 1974 *IBM J. Res. Dev.* **18** 364

[104] Keller J B and Weitz M L 1956 *J. Fluid Mech.* **2** 201

[105] Eggers J 2000 *SIAM J. Appl. Math.* **60** 1997

[106] Green A E 1976 *Int. J. Eng. Sci.* **14** 49

[107] Cosserat E and Cosserat F 1909 *Théorie des Corps Déformables* (Paris: Hermann)

[108] Green A E and Laws N 1966 *Proc. R. Soc. Lond.* A **293** 145

[109] Entov V M, Kordonskii W E, Shul'man V A K Z P and Yarin A L 1980 *Zh. Prikl. Mekh. Tekh. Fiz.* **3** 90

[110] Renardy M 1982 *SIAM J. Math. Anal.* **13** 226

[111] Markovich P and Renardy M 1985 *J. Non-Newtonian Fluid Mech.* **17** 13

[112] Entov V M and Yarin A L 1980 *Fluid Dyn.* **15** 644

[113] Entov V M and Yarin A L 1984 *J. Fluid Mech.* **140** 91

[114] Yarin A L 1993 *Free Liquid Jets and Films: Hydrodynamics and Rheology* (New York: Wiley)

[115] Dewynne J N, Ockenden J R and Wilmott P 1992 *J. Fluid Mech.* **244** 323

[116] Dewynne J N, Howell P D and Wilmott P 1994 *Q. J. Mech. Appl. Math.* **47** 541

[117] Weast R C (ed) 1978 *Handbook of Chemistry and Physics* (Boca Raton, FL: CRC Press)

[118] Llewellin E W, Marder H M and Wilson S D R 2002 *Proc. R. Soc. Lond.* A **458** 987

[119] Haenlein A 1934 *Forsch. Gebiete Ing.* **2** 139

[120] Eggers J 1997 *Rev. Mod. Phys.* **69** 865–929

[121] Taylor G I in an Appendix to Brown D 1961 *J. Fluid Mech.* **10** 305

[122] Ambravaneswaran B, Phillips S D and Basaran O A 2000 *Phys. Rev. Lett.* **85** 5332

[123] Yildrim O E, Xu Q and Basaran O A 2005 *Phys. Fluids* **17** 062107

[124] Fuchikami N, Ishioka S and Kiyono K 1999 *J. Phys. Soc. Japan* **68** 1185

[125] Coullet P, Mahadevan L and Riera C S 2005 *J. Fluid Mech.* **526** 1

[126] Bechtel S E, Bolinger K, Cao G and Forest M G 1995 *SIAM J. Appl. Math.* **55** 58

[127] Garcia F J and Castellanos A 1994 *Phys. Fluids* **6** 276

[128] Dupont T F 1993 private communication

[129] Bogy D B 1979b *Annu. Rev. Fluid Mech.* **11** 207

[130] Ashley H and Landahl M 1965 *Aerodynamics of Wings and Bodies* (Reading, MA: Addison-Wesley)

[131] Moran J P 1963 *J. Fluid Mech.* **17** 285

[132] Handelsman R A and Keller J B 1967 *SIAM J. Appl. Math.* **15** 824

[133] Stone H A, Lister J R and Brenner M P 1999 *Proc. R. Soc. Lond.* A **455** 329

[134] Li H, Halsey T C and Lobkovsky A 1994 *Europhys. Lett.* **27** 575

[135] Buckmaster J D 1972 *J. Fluid Mech.* **55** 385

[136] Acrivos A and Lo T S 1978 *J. Fluid Mech.* **86** 641

[137] Doshi P, Cohen I, Zhang W W, Siegel M, Howell P, Basaran O A and Nagel S R 2003 *Science* **302** 1185

[138] Hinch E J 1991 *Perturbation Methods* (Cambridge: Cambridge University Press)

[139] Taylor G I 1966 *Proc. 11th Int. Congress of Applied Mathematics* ed G Batchelor (Heidelberg: Springer) pp 770–96

[140] Fontelos M A, Eggers J and Snoeijer J H 2007 unpublished

[141] Eggers J, Fontelos M A, Leppinen D and Snoeijer J H 2007 *Phys. Rev. Lett.* **98** 094502

[142] Serebryakov V V 1973 *Dokl. Akad. Nauk Ukr. SSR.* A **12** 1119

[143] Lafrance P, Aiello G, Ritter R C and Trefil J S 1974 *Phys. Fluids* **17** 1469

[144] Lafrance P and Ritter R C 1977 *ASME J. Appl. Mech.* **44** 385

[145] Chandrasekhar S 1961 *Hydrodynamic and Hydromagnetic Stability* (New York: Dover)

[146] Abramowitz M and Stegun I A 1968 *Handbook of Mathematical Functions* (New York: Dover)

[147] Rayleigh Lord 1879 *Proc. Lond. Math. Soc.* **4** 4–13

[148] Kalaaji A, Lopez B, Attané P and Soucemarianadin A 2003 *Phys. Fluids* **15** 2469

[149] González H and Garcia F J 2006 *Phys. Fluids* **18** 019101

[150] Attané P 2006 *Phys. Fluids* **18** 019102

[151] Ritter R C, Zinner N R and Sterling A M 1974 *Phys. Med. Biol.* **19** 161

[152] Quian S X, Snow J B, Tzeng H M and Chang R K 1986 *Science* **2341** 486

[153] Vaago N, Spiegel A, Couty P, Wagner F R and Richerzhagen B 2003 *Exp. Fluids* **35** 303

[154] Rayleigh Lord 1879 *Proc. R. Soc. Lond.* **29** 71–97

[155] Rayleigh Lord 1890 *Proc. R. Soc. Lond.* **47** 281

[156] Bohr N 1909 *Phil. Trans. R. Soc.* A **209** 281

[157] Yuen M C 1968 *J. Fluid Mech.* **33** 151

[158] Nayfeh A H 1970 *Phys. Fluids* **14** 841

[159] Lafrance P 1975 *Phys. Fluids* **18** 428

[160] Chaudhary K C and Redekopp L G 1980 *J. Fluid Mech.* **96** 257

[161] Van Dyke M 1975 *Perturbation Methods in Fluid Mechanics* 2nd edn (Stanford, CA: Parabolic)

[162] Bender C M and Orszag S A 1978 *Advanced Mathematical Methods for Scientists and Engineers* (New York: McGraw-Hill)

[163] Rayleigh Lord 1892 *Phil. Mag.* **34** 177–80

[164] Kendall J M 1986 *Phys. Fluids* **29** 2086–94

[165] Utada A S, Lorenceau E, Link D R, Kaplan P D, Stone H A and Weitz D A 2005 *Science* **308** 537–41

[166] Goedde E F and Yuen M C 1970 *J. Fluid Mech.* **40** 495

[167] Tomotika S 1935 *Proc. R. Soc. Lond.* A **150** 322–37

[168] Stone H A and Brenner M P 1996 *J. Fluid Mech.* **318** 373–4

[169] Gunawan A Y, Molenaar J and van de Ven A A F 2002 *Eur. J. Mech.* B **21** 399

[170] Gunawan A Y, Molenaar J and van de Ven A A F 2004 *J. Eng. Math.* **50** 25

[171] Duclaux V, Clanet C and D Q 2006 *J. Fluid Mech.* **556** 217–26

[172] de Gennes P G, Brochart-Wyart F and Quéré D 2003 *Capillarity and Wetting Phenomena: Drops, Bubbles, Pearls, Waves* (Berlin: Springer)

[173] Goren S L 1962 *J. Fluid Mech.* **12** 309–19

[174] Keller J B, Rubinov S I and Tu Y O 1973 *Phys. Fluids* **16** 2052

[175] Gaster M 1962 *J. Fluid Mech.* **14** 222–4

[176] Clanet C and Lasheras J 1999 *J. Fluid Mech.* **383** 307

[177] Leib S J and Goldstein M E 1986 *Phys. Fluids* **29** 952

[178] Huerre P and Monkewitz P A 1990 *Annu. Rev. Fluid Mech.* **22** 473

[179] Utada A S, Fernandez-Nieves A, Stone H A and Weitz D 2007 *Phys. Rev. Lett.* **99** 094502

[180] Leib S J and Goldstein M E 1986 *J. Fluid Mech.* **168** 479

[181] Le Dizes S 1997 *Eur. J. Mech.* B **16** 761

[182] Gañán-Calvo A M and Gordillo J M 2001 *Phys. Rev. Lett.* **87** 274501

[183] Gañán-Calvo A M, González-Prieto R, Riesco-Chueca P, Herrada M A and Flores-Mosquera M 2007 *Nat. Phys.* **3** 737

[184] Basaran O A and Suryo R 2007 *Nat. Phys.* **3** 679

[185] Sevilla A, Gordillo J M and Martinez-Bazan C 2005 *Phys. Fluids* **17** 018105

[186] Gañán-Calvo A M, Herrada M A and Garstecki P 2006 *Phys. Rev. Lett.* **96** 124504

[187] Gañán-Calvo A M 2007 *Phys. Rev.* E **75** 027301

[188] Suryo R and Basaran O A 2006 *Phys. Fluids* **18** 082102

[189] Cohen I and Nagel S R 2002 *Phys. Rev. Lett.* **88** 074501

[190] Cohen I 2004 *Phys. Rev.* E **70** 026302

[191] Courrech du Pont S and Eggers J 2006 *Phys. Rev. Lett.* **96** 034501

[192] Case S C and Nagel S R 2007 *Phys. Rev. Lett.* **98** 114501

[193] Sauter U S and Buggisch H W 2005 *J. Fluid Mech.* **533** 237

[194] Taylor G I 1934 *Proc. R. Soc. Lond.* A **146** 501

[195] Stone H A 1994 *Annu. Rev. Fluid Mech.* **26** 65

[196] Tomotika S 1936 *Proc. R. Soc. Lond.* A **153** 302–18

[197] Saffman P G 1974 *Arch. Mech.* **26** 423–39

[198] Istratov A G, Kidin N I, Librovich V B and Zeldovich Y B 1980 *Combust. Sci. Technol.* **24** 1–13

[199] Frankel I and Weihs D 1985 *J. Fluid Mech.* **155** 289–307

[200] Cheong B S and Howes T 2004 *Chem. Eng. Sci.* **59** 2145

[201] Cheong B S and Howes T 2005 *Chem. Eng. Sci.* **60** 3715

[202] Barnes G and Woodcock R 1958 *Am. J. Phys.* **26** 205

[203] Mahadevan L and Keller J B 1996 *Proc. R. Soc. Lond.* A **452** 1679

[204] Maleki M, Habibi M, Golestanian R, Ribe N M and Bonn D 2004 *Phys. Rev. Lett.* **93** 214502

[205] Ribe N M, Huppert H E, Hallworth M A, Habibi M and Bonn D 2006 *J. Fluid Mech.* **555** 275

[206] Chiu-Webster S and Lister J R 2006 *J. Fluid Mech.* **569** 89

[207] Senchenko S and Bohr T 2005 *Phys. Rev.* E **71** 056301

[208] Villermaux E and Eggers J 2007 In preparation

[209] Shimozuru D 1994 *Bull. Volcanol.* **56** 217–19

[210] Meier G E A, Klopper A and Grabitz G 1992 *Exp. Fluids* **12** 173–80

[211] Yarin A L 2006 *Annu. Rev. Fluid Mech.* **38** 159–92

[212] Worthington A M 1908 *A Study of Splashes* (London: Longmans)

[213] Vander Wal R L, Berger G M and Mozes S D 2006 *Exp. Fluids* **40** 33

[214] Rayleigh Lord 1880 *Proc. Lond. Math. Soc.* **11** 57

[215] Bayvel L and Orzechowski Z 1993 *Liquid Atomization* (London: Taylor and Francis)

[216] Lefebvre A H 1989 *Atomization and Sprays* (New York: Hemisphere)

[217] von Helmholtz H 1868 *Phil. Mag.* **36** 337–46

[218] Kelvin L 1871 *Phil. Mag.* **42** 362–77

[219] Drazin P G and Reid W H 1981 *Hydrodynamic Stability* (Cambridge: Cambridge University Press)

[220] Reitz R D and Bracco F V 1982 *Phys. Fluids* **25** 1730–42

[221] Hoyt J W and Taylor J 1977 *J. Fluid Mech.* **83** 119–27

[222] Squire H B 1953 *Br. J. Appl. Phys.* **4** 167–9

[223] York J L, Stubbs H E and Tek M R 1953 *Trans. ASME* **10** 1279–86

[224] Hagerty W W and Shea J F 1955 *J. Appl. Mech.* **22** 509–14

[225] Asare H R, Takahashi R K and Hoffman M A 1981 *Trans. ASME: J. Fluids Eng.* **103** 395–604

[226] Villermaux E and Clanet C 2002 *J. Fluid Mech.* **462** 341–63

[227] Betchov R and Szewczyk A 1963 *Phys. Fluids* **6** 1391–6

[228] Taylor G I 1940 *G I Taylor Scientific Papers* ed G Batchelor vol III (Cambridge: Cambridge University Press) pp 244–54

[229] Villermaux E 1998 *Phys. Fluids* **10** 368–73

[230] Huerre P and Rossi M 1998 *Hydrodynamics and Nonlinear Instabilities* ed C Godrèche and P Manneville (Cambridge: Cambridge University Press) pp 81–386

[231] Villermaux E 1998 *J. Propulsion Power* **14** 807–17

[232] Marmottant P and Villermaux E 2004 *J. Fluid Mech.* **498** 73–112

[233] Bernal L P and Roshko A 1986 *J. Fluid Mech.* **170** 499–525

[234] Dimotakis P E 1986 *AIAA J.* **24** 1791–6

[235] Eroglu H and Chigier N 1991 *Atom. Sprays* **1** 349–66

[236] Gordillo J M and Pérez-Saborid M 2005 *J. Fluid Mech.* **541** 1–20

[237] Gordillo J M, Pérez-Saborid M and Gañán-Calvo A M 2001 *J. Fluid Mech.* **541** 23–51

[238] Sterling A and Sleicher C 1975 *J. Fluid Mech.* **68** 477

[239] Nikitopoulos E and Kelly A J 2000 *Phys. Fluids* **12** S7

[240] Duft D, Achtzehn T, Müller R, Huber B A and Leisner T 2003 *Nature* **421** 128

[241] Huebner A L and Chu H N 1971 *J. Fluid Mech.* **49** 361–72

[242] Rayleigh Lord 1882 *Phil. Mag.* **14** 184–6

[243] Basset A 1894 *Am. J. Math.* **16** 93–110

[244] Taylor G I 1969 *Proc. R. Soc. Lond.* A **313** 453–75

[245] Saville D A 1971 *Phys. Fluids.* **14** 1095–9

[246] Saville D A 1997 *Annu. Rev. Fluid Mech.* **29** 27

[247] Hohman M M, Shin M, Rutledge G C and Brenner M P 2001 *Phys. Fluids* **13** 2201

[248] Hohman M M, Shin M, Rutledge G C and Brenner M P 2001 *Phys. Fluids* **13** 2221

[249] Fontelos M A and Friedman A 2004 *Arch. Ration. Mech. Anal.* **172** 267

[250] Paruchuri S and Brenner M P 2007 *Phys. Rev. Lett.* **98** 134502

[251] Baumgarten P K 1971 *J. Colloid Interface Sci.* **36** 71

[252] Shin Y M, Hohman M M, Brenner M P and Rutledge G C 2001 *Appl. Phys. Lett.* **78** 1149

[253] Fridrikh S V, Yu J H, Brenner M P and Rutledge G C 2003 *Phys. Rev. Lett.* **90** 144502

[254] López-Herrera J M, Riesco-Chueca P and Gañán-Calvo A M 2005 *Phys. Fluids* **17** 034106

[255] Bohr N and Wheeler J A 1939 *Phys. Rev.* **56** 426

[256] Bohr N 1939 *Nature* **143** 330

[257] Brosa U, Grossmann S and Müller A 1990 *Phys. Rep.* **197** 167

[258] Grossmann S and Müller A 1984 *Z. Phys.* B **57** 161

[259] Rosensweig R E 1985 *Ferrohydrodynamics* (Cambridge: Cambridge University Press)

[260] Ponstein J 1959 *Appl. Sci. Res.* A **8** 425–56

[261] Kubitschek J P and Weidman P D 2007 *Phys. Fluids* **19** 114108

[262] Wallwork I M, Decent S P, King A C and Schulkes R M S M 2002 *J. Fluid Mech.* **459** 43

[263] Parau E I, Decent S P, Simmons M J H, Wong D C Y and King A C 2007 *J. Eng. Math.* **57** 159

[264] Fraser R P, Dombrowski N and Routley J H 1963 *Chem. Eng. Sci.* **18** 323–37

[265] Walton W H and Prewett W C 1949 *Proc. Phys. Soc.* B **62** 341–50

[266] Einsenklam P 1964 *Chem. Eng. Sci.* **19** 693–4

[267] Wong D, Simmons M, Decent S, Parau E and King A 2004 *Int. J. Multiphase Flow* **30** 499–520

[268] Rutland D F and Jameson G J 1970 *Chem. Eng. Sci.* **25** 1689

[269] Plateau J A F 1859 *Acad. Sci. Brux. Mem.* **31** 3

[270] de Hoog E H A and Lekkerkerker H N W 2001 *J. Phys. Chem.* B **105** 11636

[271] Hocking L M 1960 *Mathematika* **7** 1

[272] Gillis J and Kaufman B 1961 *Q. J. Appl. Math.* **19** 301

[273] Kubitschek J P and Weidman P D 2007 *J. Fluid Mech.* **572** 261

[274] Eggers J and Brenner M P 1999 *Proc. IUTAM Symp. on Nonlinear Waves in Multi-Phase Flow (Notre Dame, IN, USA)* ed H C Chang (Dordrecht: Kluwer) p 185

[275] Pedley T J 1967 *J. Fluid Mech.* **30** 127

[276] Ashmore J and Stone H A 2004 *Phys. Fluids* **16** 29

[277] Sallam K A, Aalburg C and Faeth G M 2004 *AIAA J.* **42** 2529–40

[278] Bremond N, Clanet C and Villermaux E 2007 *J. Fluid Mech.* **585** 421–56

[279] Kitamura Y and Takahashi T 1986 *Encyclopedia Fluid Mech.* **2** 474–510

[280] Merrington A C and Richarson E G 1947 *Proc. Phys. Soc.* **59** 1–13

[281] Grant R P and Middleman S 1966 *AICHE J.* **12** 669–78

[282] Hiroyazu H, Shimizu M and Arai M 1982 *Proc. 2nd Conf. on Liquid Atomization and Spray Systems (Madison, WI)* pp 69–74

[283] Engelbert C, Hardalupas Y and Whitelaw J H 1995 *Proc. R. Soc.* **451** 189–229

[284] Rehab H, Villermaux E and Hopfinger E J 1998 *AIAA J.* **36** 867–9

[285] Wu P K and Faeth G M 1995 *Phys. Fluids* **7** 2915–17

[286] Jeans J 1902 *Phil. Trans. R. Soc. Lond.* A **199** 1–53

[287] Derrida B, Godrèche C and Yekutieli I 1996 *Nature* **383** 56–8

[288] Newton I 1687 *Principia Mathematica* (London: Streater)

[289] Chen Y J and Steen P H 1997 *J. Fluid Mech.* **341** 245–67

[290] Papageorgiou D T 1995 *Phys. Fluids* **7** 1529

[291] Barenblatt G I 1996 *Similarity Self-Similarity and Intermedeate Asymptotics* (Cambridge: Cambridge University Press)

[292] Eggers J 2005 *Z. Angew. Math. Mech.* **85** 400

[293] Lister J R and Stone H A 1998 *Phys. Fluids* **10** 2758

[294] Cohen I, Brenner M P, Eggers J and Nagel S R 1999 *Phys. Rev. Lett.* **83** 1147

[295] Eggers J 2002 *Phys. Rev. Lett.* **89** 084502

[296] Wilson S D R 1988 *J. Fluid Mech.* **190** 561

[297] Gordillo J M, Sevilla A, Rodriguez-Rodrigues J and Martinez-Bazan C 2005 *Phys. Rev. Lett.* **95** 194501

[298] Moseler M and Landman U 2000 *Science* **289** 1165–9

[299] Hennequin Y, Aarts D G A L, van der Wiel J H, Wegdam G, Eggers J, Lekkerkerker H N W and Bonn D 2006 *Phys. Rev. Lett.* **97** 244503

[300] Papageorgiou D T 1995 *J. Fluid Mech.* **301** 109

[301] Eggers J 1995 *Phys. Fluids* **7** 941

[302] London R A and Flannery B P 1982 *Astrophys. J.* **258** 260

[303] Brenner M P, Lister J R and Stone H A 1996 *Phys. Fluids* **8** 2827

[304] Kowalewski T A 1996 *Fluid Dyn. Res.* **17**

[305] Giga Y and Kohn R V 1989 *Commun. Pure Appl. Math.* **42** 845

[306] Wegner F J 1972 *Phys. Rev.* B **5** 4529–36

[307] Bernoff A J, Bertozzi A L and Witelski T P 1998 *J. Stat. Phys.* **93** 725–76

[308] Ishiguro R, Graner F, Rolley E and Balibar S 2004 *Phys. Rev. Lett.* **93** 235301

[309] Matano H and Merle F 2004 *Commun. Pure Appl. Math.* **57** 1494

[310] Ishiguro R, Graner F, Rolley E, Balibar S and Eggers J 2007 *Phys. Rev.* E **75** 041606

[311] Angenent S B and Velázquez J J L 1997 *J. Reine Angew. Math.* **482** 15

[312] Longuet-Higgins M S, Kerman B R and Lunde K 1991 *J. Fluid Mech.* **230** 365

[313] Oğuz H N and Prosperetti A 1993 *J. Fluid Mech.* **257** 111

[314] Burton J C, Waldrep R and Taborek P 2005 *Phys. Rev. Lett.* **94** 184502

[315] Eggers J and Fontelos M A 2005 *J. Fluid Mech.* **530** 177

[316] Clasen C, Eggers J, Fontelos M A, Li J and McKinley G H 2006 *J. Fluid Mech.* **556** 283

[317] Renardy M 1994 *Non-Newton. Fluid Mech.* **51** 97

[318] Renardy M 1995 *Non-Newton. Fluid Mech.* **59** 267

[319] Renardy M 2005 *IMA J. Appl. Math.* **70** 353

[320] Rothert A, Richter R and Rehberg I 2001 *Phys. Rev. Lett.* **87** 084501

[321] Fontelos M A 1998 *PhD Thesis* Universidad Complutense de Madrid

[322] Rothert A, Richter R and Rehberg I 2003 *New J. Phys.* **5** 59

[323] Stokes Y M and Tuck E O 2004 *J. Fluid Mech.* **498** 205

[324] Zhang W W and Lister J 1999 *Phys. Rev. Lett.* **83** 1151

[325] Cohen I and Nagel S R 2001 *Phys. Fluids* **13** 3533

[326] Thoroddsen S T, Etoh E G and Takeara K 2007 *Phys. Fluids* **19** 042101

[327] Bergmann R, van der Meer D, Stijnman M, Sandtke M, Prosperetti A and Lohse D 2006 *Phys. Rev. Lett.* **96** 154505

[328] Keim N C, Møller P, Zhang W W and Nagel S R 2006 *Phys. Rev. Lett.* **97** 144503

[329] Levinson N 1946 *Ann. Math.* **47** 704

[330] Gordillo J M and Fontelos M A 2007 *Phys. Rev. Lett.* **98** 144503

[331] Gordillo J M and Perez-Sabroid M 2006 *J. Fluid Mech.* **562** 303

[332] Shi X D, Brenner M P and Nagel S R 1994 *Science* **265** 157

[333] Kawano S 1998 *Phys. Rev.* E **58** 4468

[334] Bonn D 2007 private communication

[335] Brenner M P, Shi X D and Nagel S R 1994 *Phys. Rev. Lett.* **73** 3391

[336] Eggers J 2007 *Thin Films of Soft Matter* ed S Kalliadasis and U Thiele (Berlin: Springer) p 95

[337] Risken H 1984 *The Fokker-Planck Equation* (Berlin: Springer)

[338] Graham R 1973 *Springer Tracts in Modern Physics* vol 66 (Berlin: Springer)

[339] Fogedby H C and Brandenburg A 2002 *Phys. Rev.* E **66** 016604

[340] Janssen H K 1976 *Z. Phys.* B **23** 377

[341] Landau L D and Lifshitz E M 1984 *Quantum Mechanics* (Oxford: Pergamon)

[342] Eggers J and Bonn D 2006 unpublished

[343] Grundy R E 1983 *IMA J. Appl. Math.* **30** 209–14

[344] Sierou A and Lister J 2004 *Phys. Fluids* **16** 1379

[345] Milosevic I N and Longmire E K 2002 *Int. J. Multiph. Flow* **28** 1853

[346] Fenn J B, Mann M, Meng C K, Wong S F and Whitehouse C M 1989 *Science* **246** 64

[347] Pimbley W T and Lee H C 1977 *IBM J. Res. Dev.* **21** 21

[348] Wallace D B 2001 http://www.ima.umn.edu/multimedia/abstract/1-10abs.html#wallace

[349] Williams C 2006 *Phys. World* **19** 24

[350] Hilbing J H and Heister S D 1996 *Phys. Fluids* **8** 1574
[351] Chaudhary K C and Maxworthy T 1980b *J. Fluid Mech.* p 287
[352] Xing J H, Boguslawsky A, Soucemarianadin A, Atten P and Attané P 1996 *Exp. Fluids* **20** 302
[353] Barbet B, Atten P and Soucemarianadin A 1997 *J. Imaging Sci. Technol.* **41** 570
[354] Dong H and Carr W W 2006 *Phys. Fluids* **18** 072102
[355] Xu Q and Basaran O A 2007 *Phys. Fluids* **19** 102111
[356] Gañán-Calvo A M, López-Herrera J M and Riesco-Chueca P 2006 *J. Fluid Mech.* **566** 421
[357] Gañán-Calvo A M 2007 *Phys. Rev. Lett.* **98** 027301
[358] Stone H A, Stroock A D and Adjari A 2004 *Annu. Rev. Fluid Mech.* **36** 381–411
[359] Squires T M and Quake S R 2005 *Rev. Mod. Phys.* **77** 977–1026
[360] Tan V C Y C 2004 *Lab Chip* **4** 257
[361] Zeleny J 1914 *Phys. Rev* **3** 69
[362] Bailey A G 1988 *Electrostatic Spraying of Liquids* (New York: Wiley)
[363] Taylor G I 1964 *Proc. R. Soc. Lond.* A **280** 383
[364] Jackson J D 1975 *Classical Electrodynamics* (New York: Wiley)
[365] Pantano C, Gañán-Calvo A M and Barrero A 1994 *J. Aerosol Sci.* **25** 1065
[366] Clopeau M and Prunet-Foch B 1989 *J. Electrost.* **22** 135
[367] Oddershede L and Nagel S R 2000 *Phys. Rev. Lett.* **85** 1234
[368] Rosell-Llompart J and Fernandez de la Mora J 1994 *J. Aerosol Sci.* **25** 1093
[369] Gabovich M D 1983 *Usp. Fiz. Nauk* **140** 137
[370] Gañán-Calvo A M 1997 *Phys. Rev. Lett.* **79** 217
[371] Hartman R P A, Brunner D J, Camelot D M A, Marijnissen J C M and Scarlett B 1999 *J. Aerosol Sci.* **30** 823
[372] Melcher J R and Taylor G I 1969 *Annu. Rev. Fluid Mech.* **1** 46
[373] Gañán-Calvo A M 2004 *J. Fluid Mech.* **507** 203
[374] Gañán-Calvo A M 1999 *J. Aerosol Sci.* **30** 863–72
[375] Cherney L T 1999 *J. Fluid Mech.* **378** 167
[376] Higuera F J 2003 *J. Fluid Mech.* **484** 303
[377] Eggers J 2001 *Phys. Rev. Lett.* **86** 4290
[378] Lorenceau E, Quéré D and Eggers J 2004 *Phys. Rev. Lett.* **93** 254501
[379] Gañán-Calvo A M 1998 *Phys. Rev. Lett.* **80** 285
[380] Cohen I, Li H, Hougland J, Mrksich M and Nagel S R 2001 *Science* **292** 265
[381] Podgorski T, Flesselles J M and Limat L 2001 *Phys. Rev. Lett.* **87** 036102
[382] Betelú S I, Fontelos M A, Kindelán U and Vantzos O 2006 *Phys. Fluids* **18** 051706
[383] Yang C 2003 Dynamic point-formation in dielectric fluids *Preprint* physics/0303122
[384] Betelú S I, Fontelos M A, Kindelaán U and Vantzos O 2007 (unpublished simulations)
[385] Gañán-Calvo A M 2004 *Phys. Rev. E* **69** 027301
[386] Loscertales I G, Barrero A, Guerrero I, Cortijo R, Marquez M and Gañán-Calvo A M 2002 *Science* **295** 1695
[387] Bentley B J and Leal L G 1986b *J. Fluid Mech.* **167** 241
[388] Zhang W W 2004 *Phys. Rev. Lett.* **93** 184502
[389] Marin A G, Campo-Cortés F and Gordillo J M 2007 submitted
[390] Anna S L, Bontoux N and Stone H A 2003 *Appl. Phys. Lett.* **82** 364
[391] Garstecki P, Stone H A and Whitesides G M 2005 *Phys. Rev. Lett.* **94** 164501
[392] Lagutkin S, Achelis L, Sheikhaliev S, Uhlenwinkel V and Srivastava V 2004 *Mater. Sci. Eng.* A **383** 1–6
[393] Bauer-Agricola G 1556 *De Re Metallica* (Basel: Froben)
[394] Born M 1969 *Atomic Physics* (New York: Dover)
[395] Lavoisier A L 1789 *Traité Élémentaire de Chimie* (Paris: Cuchet)

[396] Coulson J M and Richardson J F 1968 *Chemical Engineering* (Oxford: Pergamon)
[397] Yang V and Anderson W 1995 *Progress in Astronautics and Aeronautics Series* vol 169 *Liquid Rocket Engine Combustion Instability* (Reston, VA: AIAA)
[398] Blanchard D C 1966 *From Raindrops to Volcanoes* (New York: Dover)
[399] Mason B J 1971 *The Physics of Clouds* (Oxford: Clarendon Press)
[400] Seinfeld J H and Pandis S N 1998 *Atmos. Chem. Phys.* (New York: Wiley)
[401] Alidibirov M and Dingwell D B 1996 *Nature* **380** 146–8
[402] Ritter R C, Sterling A M and Zinner N R 1977 *Br. J. Urol.* **49** 293
[403] Mastin L G 2007 *J. Geophys. Res.* **112** B02203
[404] Pilch M and Erdman C A 1987 *Int. J. Multiph. Flow* **13** 741–57
[405] Krzeczkowski S A 1980 *Int. J. Multiph. Flow* **6** 227–39
[406] Ranger A A and Nicholls J A 1969 *AIAA J.* **7** 285–90
[407] Hinze J O and Milborn H 1955 *Trans. ASME: J. Appl. Mech.* **17** 145–53
[408] Lane W R 1961 *Ind. Eng. Chem.* **43** 1312–17
[409] Yule A J and Al-Suleimani Y 2000 *Proc. R. Soc.* A **456** 1069–85
[410] James A J, Vukasinovic B, Smith M K and Glezer A 2003 *J. Fluid Mech.* **476** 1–28
[411] Vukasinovic B, Smith M K and Glezer A 2007 *Phys. Fluids* **19** 012104
[412] Andreas E L, Pattison M L and Belcher S E 2001 *J. Phys. Res.* **106** 7157–61
[413] Anguelova M and Barber R P 1999 *J. Phys. Oceanogr.* **29** 1156–65
[414] Faragó Z and Chigier N 1992 *Atom. Sprays* **2** 137–53
[415] Rayleigh Lord 1883 *Proc. R. Soc. Lond.* **14** 170–7
[416] Taylor G I 1950 *Proc. R. Soc. Lond.* A **201** 192–6
[417] Lewis D J 1950 *Proc. R. Soc. Lond.* A **202** 81–96
[418] Schlichting H 1987 *Boundary Layer Theory* 7th edn (McGraw-Hill: New York)
[419] Faeth G M, Hsiang L P and Wu P K 1995 *Int. J. Multiph. Flow* **21** 99–127
[420] Ashgriz N and Poo Y L 1990 *J. Fluid Mech.* **221** 183–204
[421] Edgerton H E 1977 *Stopping Time: The Photographs of Harold Edgerton* (New York: Abrams)
[422] Stern S A, Weaver H A, Steffl A J, Mutchler M J, Merline W J, Buie M W, Young E F, Young L A and Spencer J R 2006 *Nature* **439** 946–8
[423] Qian J and Law C K 1997 *J. Fluid Mech.* **331** 59–80
[424] Stow C D and Stainer R 1977 *J. Met. Soc. Japan* **55** 518–31
[425] Xu L, Barcos L and Nagel S R 2006 *Preprint* physics/0608079
[426] Antkowiak A, Bremond N, Le Dizes S and Villermaux E 2007 *J. Fluid Mech.* **577** 241–50
[427] Potts H E and Diver D A 2001 *New J. Phys.* **3** 7
[428] Bartolo D, Josserand C and Bonn D 2006 *Phys. Rev. Lett.* **96** 124501
[429] Richtmyer R D 1960 *Commun. Pure Appl. Math.* **8** 297–319
[430] Meshkov E E 1969 *Sov. Fluid Dyn.* **4** 101–8
[431] Zef B W, Kleber B, Fineberg J and Lathrop D P 2000 *Nature* **403** 401–4
[432] Lavrentiev M and Chabat B 1980 *Effets Hydrodynamiques et Modèles Mathématiques* (Moscow: MIR) (translated from the 1977 Russian edition)
[433] Pomeau Y and Villermaux E 2006 *Phys. Today* **3** 39–44
[434] Lenard P 1904 *Meteorol. Z.* **21** 249–62
[435] Laws J O and Parsons D A 1943 *Trans. Am. Geophys. Union* **24** 452–60
[436] Marshall J S and Palmer W M 1948 *J. Meteorol.* **5** 165–6
[437] Low T B and List R 1982 *J. Atmos. Sci.* **39** 1591–606

[438] Falkovich G, Fouxon A and Stepanov M G 2002 *Nature* **419** 151–4

[439] Srivastava R C 1971 *J. Atmos. Sci.* **28** 410–15

[440] Kombayasi M, Gonda T and Isono K 1964 *J. Met. Soc. Japan* **42** 330–40

[441] Hinze J O 1949 *AIChE J.* **1** 289–95

[442] Hanson A R, Domich E G and Adams H S 1963 *Phys. Fluids* **6** 1070–80

[443] Chou W H and Faeth G M 1998 *Int. J. Multiph. Flow* **24** 889–912

[444] Alusa A L and Blanchard D C 1971 *J. Rech. Atmos.* **VII** 1–9

[445] Savart F 1833 *Ann. Chim.* **55** 257–310

[446] Savart F 1833 *Ann. Chim.* **54** 56–87

[447] Savart F 1833 *Ann. Chim.* **54** 113–45

[448] Taylor G I 1959 *Proc. R. Soc. Lond.* **253** 296–312

[449] Taylor G I 1959 *Proc. R. Soc. Lond.* **253** 313–21

[450] Huang J C P 1970 *J. Fluid Mech.* **43** 305–19

[451] Taylor G I 1960 *Proc. R. Soc. Lond.* **259** 1–17

[452] Lin S P 2003 *Breakup of Liquid Sheets and Jets* (Cambridge: Cambridge University Press)

[453] Fraser R P, Eisenklam P, Dombrowski N and Hasson D 1962 *AIChE J.* **8** 672–80

[454] Dombrowski N and Jonhs W R 1963 *Chem. Eng. Sci.* **18** 203–14

[455] Clanet C and Villermaux E 2002 *J. Fluid Mech.* **462** 307–40

[456] Bremond N and Villermaux E 2006 *J. Fluid Mech.* **549** 273–306

[457] Mansour A and Chigier N 1990 *Phys. Fluids* A **2** 706–19

[458] Park J, Huh K Y, Li X and Renksizbulut M 2004 *Phys. Fluids* **16** 625–32

[459] Lozano A, Garcia-Olivares A and Dopazo C 1998 *Phys. Fluids* **10** 2188–97

[460] Kim I and Sirignano W A 2000 *J. Fluid Mech.* **410** 147–83

[461] Heidmann M F, Priem R J and Humphrey J C 1957 *N A C A Tech. note* number 3835

[462] Dombrowski N and Hooper P C 1963 *J. Fluid Mech.* **18** 392–400

[463] Crapper G D, Dombrowski N, Jepson W P and Pyott G A D 1973 *J. Fluid Mech.* **57** 671–2

[464] Dombrowski N and Neale N D 1974 *J. Aerosol Sci.* **5** 551–5

[465] Ryan H M, Anderson W E, Pal S and Santoro R J 1995 *J. Propulsion Power* **11** 135–45

[466] Anderson W E, Ryan H M and Santoro R J 1995 *Progress in Astronautics and Aeronautics Series* vol 169 *Liquid Rocket Engine Combustion Instability* (Reston, VA: AIAA)

[467] Bush J W M and Hasha A E 2004 *J. Fluid Mech.* **511** 285–310

[468] Sovani S D, Sojka P E and Lefebvre A H 2000 *Prog. Energy Combust. Sci.* **27** 483–521

[469] Thoroddsen S T, Etoh T G and Takehara K 2006 *J. Fluid Mech.* **557** 63–72

[470] Keller J B and Kolodner I 1954 *J. Appl. Phys.* **25** 918–21

[471] Bremond N and Villermaux E 2005 *J. Fluid Mech.* **524** 121–30

[472] Markstein G H 1957 *J. Aerosol. Sci.* **24** 238–9

[473] Reiner G 1992 *Phys. Rev. Lett.* **68** 75–8

[474] Elbaum M and Lipson S G 1994 *Phys. Rev. Lett.* **72** 3562–5

[475] Dombrowski N and Fraser R P 1954 *Phil. Trans.* A **247** 101–30

[476] Dan G B and Stokes M D 2002 *Nature* **418** 839–44

[477] Grumpstrup T, Keller J B and Belmonte A 2007 *Phys. Rev. Lett.* **99** 114502

[478] Wu J 1981 *J. Geophys. Res.* **86** 457–63

[479] Loewen M R, O'Dor M A and Skafel M G 1996 *J. Geophys. Res.* **101** 452–60

[480] Kolmogorov A N 1941 *Dokl. Akad. Nauk SSSR* **31** 99–101

[481] Kolmogorov A N 1962 *J. Fluid Mech.* **13** 82

[482] Monin A S and Yaglom A M 1975 *Statistical Fluid Mechanics: Mechanics of Turbulence* vol 2 (Cambridge, MA: MIT Press)

[483] Konno M, Aoki M and Saito S 1983 *J. Chem. Eng. Japan* **16** 313–19

[484] Novikov E A and Dommermuth D G 1997 *Phys. Rev.* E **56** 5479–82

[485] Martinez-Bazan C, Montanes J L and Lasheras J C 1999 *J. Fluid Mech.* **401** 183–207

[486] Gorokhovski M A and Saveliev V L 2003 *Phys. Fluids* **15** 184–92

[487] Ellis R S 1885 *Entropy, Large Deviations, and Statistical Mechanics* (Berlin: Springer)

[488] Halsey T C, Jensen M H, Kadanoff L P, Procaccia I and Shraiman B I 1986 *Phys. Rev.* E **33** 1141

[489] Clay P H 1940 *Proc. R. Acad. Sci. (Amsterdam)* **43** 852–65

[490] Kolmogorov A N 1949 *Dokl. Akad. Nauk SSSR* **66** 825–8

[491] Shinnar R 1961 *J. Fluid Mech.* **10** 259–75

[492] Lemenand T, Della Valle D, Zellouf Y and Peerhossaini H 2003 *Int. J. Mutliph. Flow* **29** 813–40

[493] von Smoluchowski M 1917 *Z. Phys. Chem.* **92** 129–68

[494] Coulaloglou C A and Tavlarides L L 1977 *Chem. Eng. Sci.* **32** 1289–97

[495] Saffman P G and Turner J S 1956 *J. Fluid Mech.* **1** 16–30

[496] Valentas K J and Amundson N R 1966 *Ind. Eng. Chem. Fundam.* **5** 533–42

[497] Derrida B, Godrèche C and Yekutieli I 1991 *Phys. Rev.* A **44** 6241–51

[498] Schumann T E W 1940 *Q. J. R. Meteorol. Soc.* **66** 195–207

[499] Friedlander S K and Wang C S 1966 *J. Colloid Interface Sci.* **22** 126–32

[500] Lifshitz I M and Slyozov V V 1961 *J. Phys. Chem. Solids* **19** 35–50

[501] Mayer J E and Mayer M G 1966 *Statistical Mechanics* (New York: Wiley)

[502] Stockmayer W H 1943 *J. Chem. Phys.* **11** 45–55

[503] Kapur J N 1989 *Maximum Entropy Models in Science and Engineering* (New York: Wiley)

[504] Englman R 1991 *J. Phys.: Condens. Matter* **3** 1019–53

[505] Cohen R D 1990 *J. Chem. Soc. Faraday Trans.* **86** 2133–8

[506] Cohen R D 1991 *Proc. R. Soc. Lond.* A **435** 483–503

[507] Eaton J K and Fessler J R 1994 *Int. J. Multiph. Flow* **20** 169–209

[508] Lei X, Ackerson B J and Tong P 2001 *Phys. Rev. Lett.* **86** 3300–3

[509] Longuet-Higgins M S 1992 *Proc. R. Soc. Lond.* A **439** 611–26

[510] Marmottant P and Villermaux E 2004 *Phys. Fluids* **16** 2732–41

[511] Rayleigh Lord 1880 *Phil. Mag.* **10** 73–8

[512] Massel S R 1996 *Ocean Surface Waves: Their Physics and Prediction* (Singapore: World Scientific)

[513] Roberts J B and Spanos P D 1999 *Random Vibrations and Statistical Linearization* (New York: Dover)

[514] Thoroddsen S T and Takehara K 2000 *Phys. Fluids* **12** 1265–7

[515] Oliveira M S N and McKinley G H 2005 *Phys. Fluids* **17** 071704

[516] Tucker C L and Moldenaers P 2002 *Annu. Rev. Fluid Mech.* **34** 177–210

[517] Mabile C, Leal-Calderon F, Bibette J and Schmitt V 2003 *Europhys. Lett.* **61** 708–14

[518] Simmons H C 1977 *J. Eng. Power* **7** 309–14

[519] Simmons H C 1977 *J. Eng. Power* **7** 315–19

[520] Safran S A 2003 *Statistical Thermodynamics of Surfaces, Interfaces, and Membranes* (Boulder, CO: Westview)

[521] Amarouchene Y, Bonn D, Meunier J and Kellay H 2001 *Phys. Rev. Lett.* **86** 3558

[522] Yildirim O E and Basaran O A 2001 *Chem. Eng. Sci.* **56** 211

[523] Coussot P and Gaulard F 2005 *Phys. Rev.* E **72** 031409

[524] Fel L G and Zimmels Y 2005 *J. Colloid Interface Sci.* **288** 553

[525] Grisenti R E and Toennies J P 2003 *Phys. Rev. Lett.* **90** 234501

[526] Möbius M E 2006 *Phys. Rev.* E **74** 051304

[527] Jin F, Gupta N R and Stebe K J 2006 *Phys. Fluids* **18** 022103

[528] Goldin M, Yerushalmi J, Pfeffer R and Shinnar R 1969 *J. Fluid Mech.* **38** 689

[529] Bird R B, Armstrong R C and Hassager O 1987 *Dynamics of Polymeric Liquids Volume I: Fluid Mechanics; Volume II: Kinetic Theory* (New York: Wiley)

[530] Goren S L and Gottlieb M 1982 *J. Fluid Mech.* **120** 245

[531] Liu Z and Liu Z 2006 *J. Fluid Mech.* **559** 451

[532] Bousfield D W, Keunigs R, Marrucci G and Denn M M 1986 *J. Non-Newton. Fluid Mech.* **21** 79

[533] Anna S L and McKinley G H 2001 *J. Rheol.* **45** 115

[534] Bazilevskii A V, Entov V M and Rozhkov A N 1990 *Proc. 3rd Eur. Rheology Conf. (Edinburgh, UK)* ed D R Oliver (Amsterdam: Elsevier) p 41

[535] Matta J E and Tytus R P 1990 *J. Non-Newton. Fluid Mech.* **35** 215

[536] Tirtaatmadja V and Sridhar T 1993 *J. Rheol.* **37** 1081

[537] Spiegelberg S H, Ables D C and McKinley G H 1996 *J. Non-Newton. Fluid Mech.* **64** 229

[538] Spiegelberg S H and McKinley G H 1996 *J. Non-Newton. Fluid Mech.* **67** 49

[539] Yesilata B, Clasen C and McKinley G H 2006 *J. Non-Newton. Fluid Mech.* **133** 73

[540] Bazilevskii A V, Voronkov S I, Entov V M and Rozhkov A N 1981 *Sov. Phys.—Dokl.* **26** 333

[541] Tirtaatmadja V, McKinley G H and Cooper-White J J 2006 *Phys. Fluids* **18** 043101

[542] Wagner C, Amarouchene Y, Bonn D and Eggers J 2005 *Phys. Rev. Lett.* **95** 164504

[543] Temmen H, Pleiner H, Liu M and Brand H R 2000 *Phys. Rev. Lett.* **84** 3228

[544] Beris A N, Graham M D, Karlin I and Öttinger H C 2001 *Phys. Rev. Lett.* **86** 744

[545] Milner S T 2004 *J. Rheol.* **48** 53

[546] Doi M and Edwards S F 1986 *The Theory of Polymer Dynamics* (Oxford: Oxford University Press)

[547] Larson R G 1999 *The Structure and Rheology of Complex Fluids* (Oxford: Oxford University Press)

[548] Fontelos M A and Li J 2004 *J. Non-Newton. Fluid Mech.* **118** 1

[549] Lindner A, Vermant J and Bonn D 2003 *Physica* A **319** 125

[550] Entov V M and Hinch E J 1997 *J. Non-Newton. Fluid Mech.* **72** 31

[551] Entov V M and Yarin A L 1984 *Fluid Dyn.* **19** 21

[552] Fontelos M A 2003 *Z. Angew. Math. Phys.* **54** 84

[553] Sattler R, Wagner C and Eggers J 2007 submitted

[554] Ramé E 2002 *Encyclopedia of Surface and Colloid Science* (New York: Dekker) pp 3602–18

[555] Renardy M and Losh D 2002 *J. Non-Newton. Fluid Mech.* **106** 17

[556] Chang H C, Demekhin E A and Kalaidin E 1999 *Phys. Fluids* **11** 1717

[557] Li J and Fontelos M A 2003 *Phys. Fluids* **15** 922

[558] Boys C V 1959 *Soap Bubbles, their Colors and Forces which Mold them* (New York: Dover)

[559] Vollrath F and Tillinghast E K 1991 *Naturwissenschaften* **78** 557

[560] Oh M H, So J H and Yang S M 1999 *J. Colloid Interface Sci.* **216** 320

[561] MCheny J and Walters K 1999 *J. Non-Newton. Fluid Mech.* **86** 185

[562] Harrison G M, Mun R, Cooper G and Boger D V 1999 *J. Non-Newton. Fluid Mech.* **85** 93

[563] Zirnsak M A, Boger D V and Tirtaatmadja V 1999 *J. Rheol.* **43** 627

[564] Jones D A R, Leary B and Boger D V 1991 *J. Colloid Interface Sci.* **147** 479

[565] Foss D R and Brady J F 2000 *J. Fluid Mech.* **407** 167

[566] Bach A, Almdal K, Rasmussen H K and Hassager O 2003 *Macromolecules* **36** 5174

[567] Doshi P, Suryo R, Yildirim O E, McKinley G H and Basaran O A 2003 *J. Non-Newton. Fluid Mech.* **113** 1

[568] Renardy M and Renardy Y 2004 *J. Non-Newton. Fluid Mech.* **122** 303

[569] Doshi P and Basaran O A 2004 *Phys. Fluids* **16** 585

[570] McKinley G H 2005 private communication

[571] Al Khatib M A M and Wilson S D R 2005 *J. Fluids Eng.* **127** 687

[572] Burton J C, Rutledge J E and Taborek P 2007 *Phys. Rev.* E **75** 036311

[573] Jaeger H M, Nagel S R and Behringer R P 1996 *Rev. Mod. Phys.* **68** 1259

[574] Lohse D, Bergmann R, Mikkelson R, Zeilstra C, van der Meer D, Versluis M, van der Weele K, van der Hoef M and Kuipers H 2004 *Phys. Rev. Lett.* **93** 198003

[575] Chang C H and Franses E I 1995 *Colloids Surf.* **100** 1

[576] Dravid V, Songsermpong S, Xue Z, Corvalan C A and Sojka P E 2006 *Chem. Eng. Sci.* **61** 3577

[577] Stone H A and Leal L G 1990 *J. Fluid Mech.* **220** 161

[578] Liao Y C, Franses E I and Basaran O A 2006 *Phys. Fluids* **18** 022101

[579] Timmermans M L and Lister J R 2002 *J. Fluid Mech.* **459** 289

[580] Burkholder H C and Berg J C 1974 *AIChE J.* **20** 863

[581] Whitaker S 1975 *J. Colloid Interface Sci.* **54** 231

[582] Skelland A H P and Walker P G 1989 *Can. J. Chem. Eng.* **67** 762

[583] Craster R V, Matar O K and Papageorgiou D T 2002 *Phys. Fluids* **14** 1364

[584] Coyle R W and Berg J C 1983 *Phys. Chem. Hydrodyn.* **4** 11

[585] Hansen S, Peters G W M and Meijer H E H 1999 *J. Fluid Mech.* **382** 331

[586] Kwak S and Pozrikidis C 2001 *Int. J. Multiph. Flow* **27** 1

[587] McGough P T and Basaran O A 2006 *Phys. Rev. Lett.* **96** 054502

[588] Dupré A 1869 *Théorie Méchanique de la Chaleur* (Paris: Gauthier-Villars)

[589] Bechtel S E, Koelling K W, Nguyen W and Tan G 2002 *J. Colloid Interface Sci.* **245** 142

[590] Kochurova N N, Noskov B A and Rusanov A I 1974 *Kolloidn. Zh.* **36** 559

[591] Marmottant P, Villermaux E and Clanet C 2000 *J. Colloid Interface Sci.* **230** 29–40

[592] Lenard P 1910 *Sitzungsber. Heidelberger Akad. Wiss.* **18** paper 3

[593] Bohr N 1910 *Phil. Trans. R. Soc.* A **84** 395

[594] Bond W N and Puls H O 1937 *Phil. Mag.* **24** 864–88

[595] Stückrad B, Hiller W J and Kowalwski T A 1993 *Exp. Fluids* **15** 332

[596] Blake T D and Shikhmurzaev Y D 2002 *J. Colloid Interface Sci.* **253** 196–202

[597] Kochurova N N and Rusanov A I 1981 *J. Colloid Interface Sci.* **81** 297

[598] Eggers J and Evans R 2004 *J. Colloid Interface Sci.* **280** 537

[599] Shikhmurzaev Y D 2005 *IMA J. Appl. Math.* **70** 880

[600] Chen H H and Brenner M P 2004 *Phys. Rev. Lett.* **92** 166106

[601] Goddard J D 2006 *J. Fluid Mech.* **568** 1